Development of a Dynamic LES Model for Premixed Turbulent Flames

by

Sreenivasa Rao Gubba

A Doctoral Thesis

Submitted in partial fulfilment of the requirements for the award of
Doctor of Philosophy of Loughborough University

Loughborough
University

February 2009

Wolfson School of Mechanical and Manufacturing Engineering
Loughborough University

Dedicated to

Lord Krishna

Abstract

In numerical modelling, Large Eddy Simulations (LES) has evolved itself as a powerful tool for the prediction of turbulent premixed flames. In LES, sub-grid scale (SGS) modelling plays a pivotal role in accounting for various SGS effects. Chemical reaction rate in LES turbulent premixed flames is a SGS phenomenon and must be accounted accurately. Flame surface density (FSD) models based on laminar flamelet concepts are simple and efficient in accounting the chemical reaction rate, which is the main motive of this research.

The work presented in this thesis is mainly focused on the development, implementation and evaluation of a novel dynamic flame surface density (DFSD) model for the calculation of transient, turbulent premixed propagating flames using the LES technique. The concept of the dynamism is achieved by the application of a test filter in combination with Germano identity, which provides unresolved SGS flame surface density information. The DFSD model is coupled with the fractal theory in order to evaluate the instantaneous fractal dimension of the propagating turbulent flame front.

LES simulations are carried to simulate stoichiometric propane/air flame propagating past solid obstacles in order to validate the novel model developed in this work with the experiments conducted by the combustion group at The University of Sydney. Preliminary LES investigations are carried using a simple FSD model and thereafter using DFSD model. Various numerical tests are carried to establish the confidence on LES. A detailed analysis has been carried to determine the regimes of combustion at different stages of flame propagation inside the chamber. LES predictions using the novel DFSD model are evaluated and validated against experimental measurements for various flow configurations. The LES predictions are identified to be in excellent agreement with experimental measurements and very much improved when compared to predictions of simple FSD model. The impact of the number and position of the baffles with respect to ignition origin is also studied. LES results are found to be in very good agreement with experimental measurements in all these cases.

Acknowledgements

Firstly, I wish to express my deep sense of gratitude to Professor W Malalasekera, for giving me this great opportunity I am very grateful to my supervisors, Professor W Malalasekera and Dr. Salah S Ibrahim for their invaluable guidance throughout the course of my research work. Their keen interest and personal involvement at all stages of this work is beyond words of gratitude Their invaluable advices and exceptionally thought provoking discussions has improved my knowledge, and helped this thesis to be in good shape.

Secondly, I am thankful to Wolfson School of Loughborough University for the financial support provided to carry out this research work I am very thankful to Dr. M. Kirkpatrick for providing the basic LES code, PUFFIN. I am very grateful to Professor A.R. Masri for providing the experimental data used for model validation and for his invaluable advices on progress of work. I sincerely appreciate the help of Dr. Evatt Hawkes, for his invaluable advices on sub-grid scale modelling during the early stages of my Ph D. I am also thankful to Professor Denis Veynante for his comments regarding the developments of the dynamic flame surface density model

I am thankful to Dr. Ranga-Dinesh for his indebted information on LES, which helped me to understand the subject deeply. Discussions with Dr. M. Ravikanti led me to understand various aspects of combustion, which are quite appreciated I would like to, also, thank my fellow researchers Dr. A. Odedara, Dr. V. Savaryanadam and Mr. Suresh for sharing their invaluable modelling and experimental experiences with me. I would like to thank Dr. I. Sebastian and his family for their moral support provided throughout the course of my research work

I would like to thank my wife Siri, for her hard work, continuous support and moral encouragement, without which this work is impossible Finally, I would like to thank my teachers, project supervisors and colleagues motivating me through their aspiring discussions and great teachings, to choose the correct path in my life. Last but not least, I would like to thank my family for their support in achieving this great success in my life.

Publications

1. **Gubba, S.R.**, Ibrahim, S.S., Malalasekera, W , Masri, A.R.. LES modelling of propagating turbulence premixed flames using a dynamic flame surface density model. 2nd ECCOMAS thematic conference on computational combustion, TU Delft, The Netherlands, 18-20 July (2007), ISBN 978-90-811768-1-1.

2. Ibrahim, S.S., Malalasekera, W , **Gubba, S.R** , Masri, A R LES modelling of explosion propagating flame inside vented chambers with built-in solid obstructions 21st ICDERS, ENSEMA, Poitiers, France, 23-27 July (2007)

3. **Gubba, S.R.**, Ibrahim, S S , Malalasekera, W., Masri, A R : Determination of regimes of combustion in premixed propagating flames using large eddy simulations, Combustion Theory and Modelling, (Accepted for publication)

4. **Gubba, S.R** , Ibrahim, S.S., Malalasekera, W , Masri, A R : LES of premixed turbulent combustion using a dynamic flame surface density model. Submitted to Flow, Turbulence and Combustion December 2007

5. **S.R. Gubba**, S.S. Ibrahim, W. Malalasekera: A dynamic SGS model for LES of turbulent premixed flames, CHT-08, Marrakech, Morocco 11-16 May 2008

6. S.S. Ibrahim, **S.R. Gubba**, AR Masri and W Malalasekera: Calculations of explosion deflagrating flames using a dynamic flame surface density model, Journal of Loss and Prevention in Process Industries, (In press, corrected proof available at http://dx.doi.org/10.1016/j.jlp.2008.05.006)

7. **Gubba, S.R** , Ibrahim, S.S , Malalasekera, W., Masri, A.R.: LES modelling of premixed deflagrating flames in vented explosion chamber with a series of solid obstructions, Combustion Science and Technology, 10 (180), pp. 1936-1955, (2008), DOI: 10.1080/00102200802261852

8. **Gubba, S.R.**, Ibrahim, S S., Malalasekera, W.: LES Study of influence of obstacles on turbulent premixed flames in a small scale vented chambers, Submitted to Mediterranean Combustion Symposium-06 January 2009

Contents

Nomenclature

Latin Letters

A	Area
A_T	Turbulent flame surface area per unit volume
A_L	Laminar flame surface area per unit volume
$\bar{A}$	Projected area of flame on its average surface per unit volume
B_i	Body forces
C_{ij}	Cross stress
Cp	Specific heat at constant pressure
C	Dimensionless coefficient in Smagorinsky model
C_{EBU}	EBU Model constant
C_I	Model coefficient in Smagorinsky mode
C_s	Smagorinsky coefficient
Cs	Model constant used in DFSD equation
c	Reaction progress variable
c_{red}	Reduced progress variable
D	Mass Diffusivity/ Fractal dimension
Da	Damköhler number
D_L	Laminar fractal dimension
D_T	Turbulent fractal dimension
E	Efficiency function
e	Specific internal energy
F	Flame thickening factor
f	Force per unit mass
G	Convolution function or G field
h	Enthalpy
I_0	Mean stretch factor
Ka	Karlovitz number
k	Thermal conductivity
L_{ij}	Leonard stress and

L_y	Length scale of wrinkle flame front
l	Length scale
l_t	Integral length scale
M	Molar mass
Ma	Markstein length
$\dot{m}$	Mass flow rate
M_{ij}	Stress tensor
n	Constant
Pr	Prandtl number
Pr_t	Turbulent Prandtl number
P_{sg}	Probability in PDF equation
p	Pressure
Q	Heat generation
q_c	Chemical source term
R	Mean reaction rate per unit surface area
Re	Reynolds number
R_{ij}	Sub-grid scale Reynolds stress
R_G	Gas constant
R_u	Universal gas constant
S	Stress tensor
Sc	Schmidt number
Sc_t	Turbulent Schmidt number
S_φ	Generic source term
S_{ij}	Strain rate
S^+	Marker field scalar
T	Temperature
T_{ij}	Sub-test-scale stress tensor
t	Time
u	Velocity in x-direction
u'	RMS fluctuations
u'_Δ	SGS velocity fluctuation
u_k	Flame advancement by curvature effects
u_L^0	Un-strained laminar burning velocity

u_L	Laminar burning velocity
u_T	Turbulent burning velocity
$\tilde{u}$	Tangential velocity
V	Volume
v	Velocity in y-direction
W	Functional dependence
w	Velocity in z-direction
Y_{fu}	Fuel mass fraction
Y_{fu}^0	Fuel mass fraction in un-burnt mixture

Greek Symbols

α	Model constant in TFS equation
α_1	Model constant in equation 5 11
α_2	Model coefficient in equation 5 13
α_3	Model constant in equation 5 40
α_4	Filter width coefficient
α_T	Thermal diffusivity
α_{ij}	Traceless tensor
β	Model coefficient simple FSD equation
β_1	Model constant in equation 5 11
β_3	Model constant in equation 5 40
β_{ij}	Traceless tensor
λ	Unresolved flame surface density
μ	Dynamic viscosity
μ'	Bulk viscosity
$\overline{\mu}_{SGS}$	SGS turbulent eddy viscosity
ω_c	Chemical reaction rate
ε	Turbulent kinetic energy
ρ	Fluid density

ρ_u	Unburned gas density
σ	Surface force
δ_{ij}	Kronecker delta
δ_L	Flame thickness
δ_c	Lower cut-off scale
δ_r	Reaction zone thickness
ν	Kinematic viscosity
Φ	Dissipation by viscous stress
φ	Any fluid property
ϕ	Equivalence ratio
τ	Stress tensor
τ_{ij}^{sgs}	Residual stress
τ_t	Turbulent time scale
τ_c	Chemical time scale
τ_k	Kolmogorov time scale
τ_w	Wall shear stress
$\bar{\Delta}$	Filter width
Σ	Flame surface density
η_k	Kolmogorov scale
γ	Ratio of test filter to grid filter
Λ	Unresolved flame surface density at test filter
Ξ	Flame wrinkling factor
Γ_k	Efficiency function in ITFNS equation

Subscripts/Superscripts

fu	fuel
k	Kolmogorov
l	Laminar
o	unburned
s	Smagorinsky

sgs	Sub-grid scale
t	Turbulence

Operations

~	Favre average
^	Test filter
¯	Spatial filter
′	Fluctuations

Abbreviations

AFSD	Algebraic Flame Surface Density
ADI	Alternating-Direction-Implicit
ANN	Artificial Neural Network
BiCGStab	Bi-Conjugate Gradient Stabilized
CFD	Computational Fluid Dynamics
DFSD	Dynamic Flame Surface Density
DFM	Dynamic Fractal Model
DNS	Direct Numerical Simulation
EBU	Eddy-Break-Up
EFM	Empirical Fractal Model
FSD	Flame Surface Density
FPI	Flame Propagation of Intrinsic Low-Dimensional Manifold
GHG	Green House Gases
ISAT	In Situ Adaptive Tabulation
ITNFS	Intermittent Turbulence Net Flame Stretch
LIF	Laser Induced Florescence
LDV	Laser Doppler Velocimeter

LDA	Laser Doppler Anemometry
LEM	Linear Eddy Mixing
LES	Large Eddy Simulation
MSI	Modified Strongly Implicit
NGT	Non-Gradient Transport
Nd.YAG	Neodymium-doped Yttrium Aluminum Garnet
PDF	Probability Density Function
PIV	Particle Image Velocimetry
PLIF	Planar Laser-Induced Fluorescence
PRISM	Piecewise Reusable Implementation of Solution Mapping
PUFFIN	Particles IN Unsteady Fluid Flow
QSSA	Quasi-Steady State Assumption
RANS	Reynolds Averaged Navier-Stokes
RCCE	Rate-Controlled Constrained Equilibrium
RMS	Root Mean Square
SIMPLE	Semi-Implicit Method for Pressure Linked Equations
SGS	Sub-Grid Scale
SSM	Scale Similarity Models
TFS	Turbulent Flame Speed
ZNG	Zero-Normal Gradient

List of Figures

List of Tables

Chapter 1

Introduction

1.1 Introduction

Combustion plays a vital role in converting energy from one form to another and giving the utmost comfort to human life. Over a period of time, due to the industrial revolution and life sophistication, world has suffered many consequences such as global warming, pollution and shortage of conventional fuels etc. These are mainly due to the combustion emissions and green house gases (GHG) emitted due to inefficient exploitation of fossil fuels. Recent implementation of strict regulations on combustion generated emissions by government authorities are prompting the necessity of eco-friendly combustion systems, with optimal design characteristics, essentially in automobile, aircraft, marine and power generation industries. With ever growing demand for eco-friendly, optimised combustion systems, fundamental understanding of the combustion phenomena is vital to lower the impact of emissions on environment and to improve the performance, reliability and safety. The successfulness of understanding the physics of combustion with decades of research is continuous, with many open questions to be answered such as combustion instabilities, extinction, re-ignition, flame-flow interactions etc. Combustion being a complex thermo-chemical process, understanding the presence of unsteadiness and turbulence, formulate a multifaceted problem.

Combustion in many practical systems such as automobile engines as shown in Figure 1.1 (Maly, 1994), gas turbines as shown in Figure 1.2 (Correa et al., 1996) and industrial burners as shown in Figure 1.3 (Hayashi et al., 2000) is very rapid with high turbulence levels and fast chemical reactions. Moreover, most of the aforementioned engineering applications do operate at either fully or partially premixed conditions prior to reaction

Optimal design of such combustion systems demands rigorous experimental investigations, which require expensive experimental setups, where combustor designs are very complex. For instance, a typical gas turbine combustion chamber shown in Figure 1.4 (Staffelbach, 2006) is not realistic for detailed experimental investigation due to the harsh internal flow and combustion characteristics. These internal conditions raise unclosed questions, which are predominant to understand in order to improve the combustor performance, which demands alternative methods of investigations. Consequently computational/numerical modelling provides a potential alternative to difficult experimental investigations.

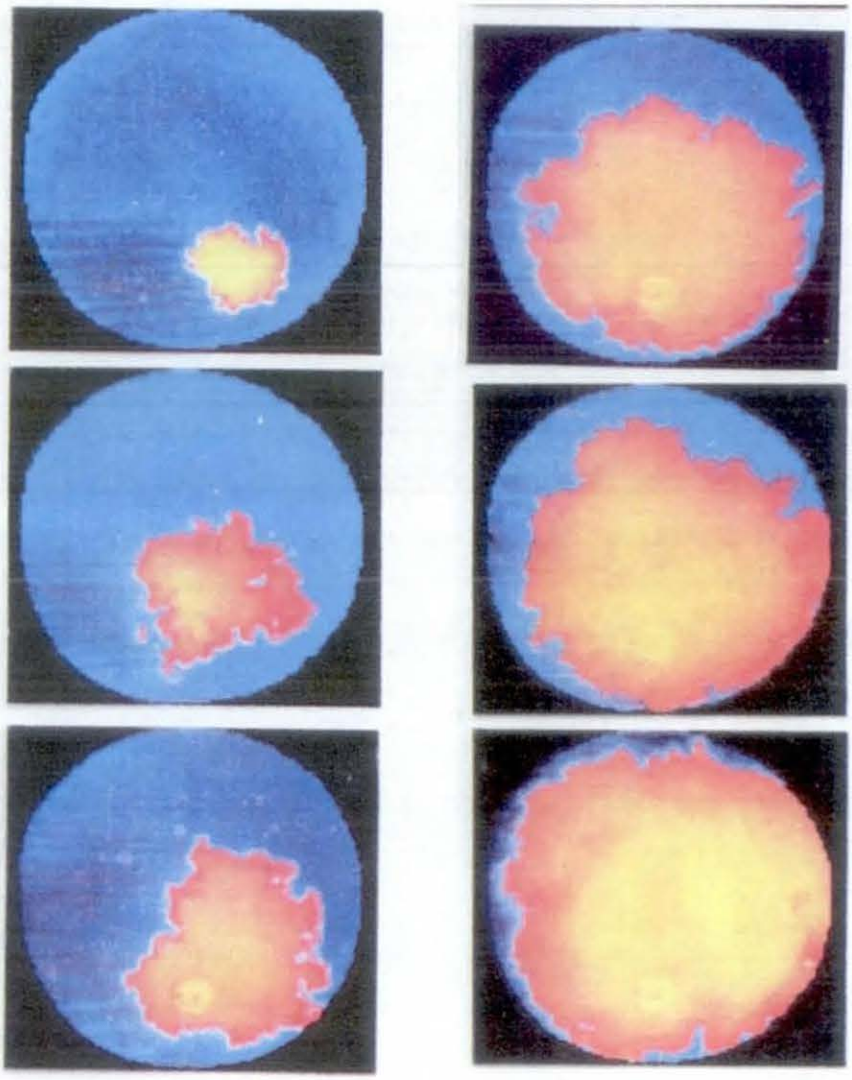

Figure 1.1 Sequence of turbulent premixed propagating flame images in an experimental spark ignition setup (Maly, 1994).

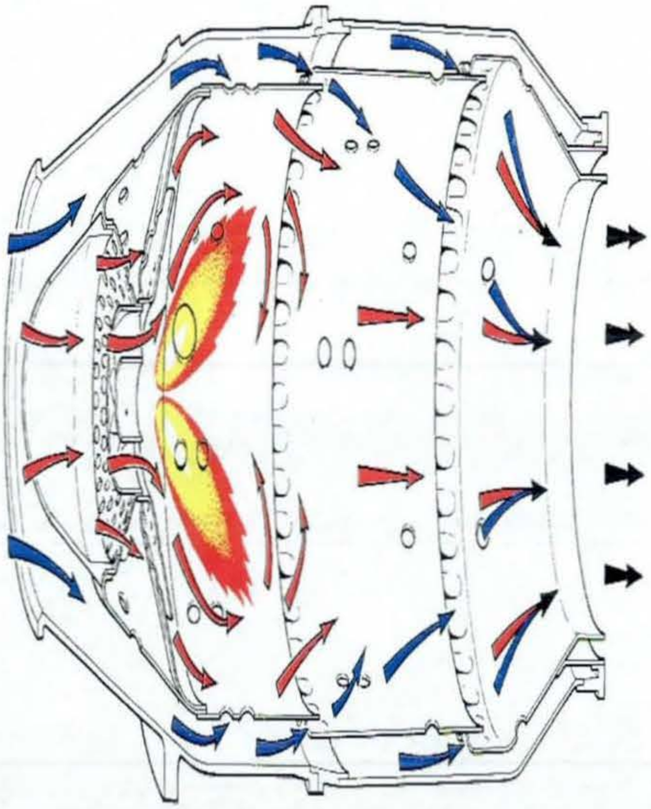

Figure 1.2 Combustion in a gas turbine engine from Rolls-Royce (Correa et al., 1996).

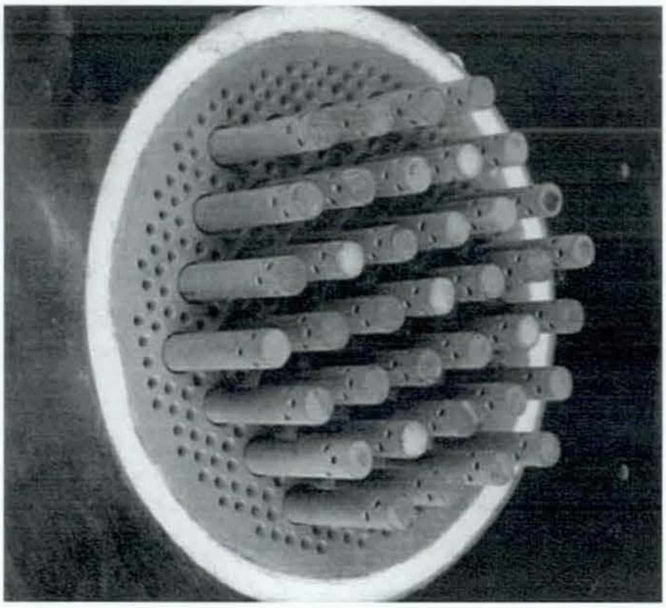

Figure 1.3 Assembly of a burner and perforated flame holder used in combustors at elevated pressures (Hayashi et al., 2000).

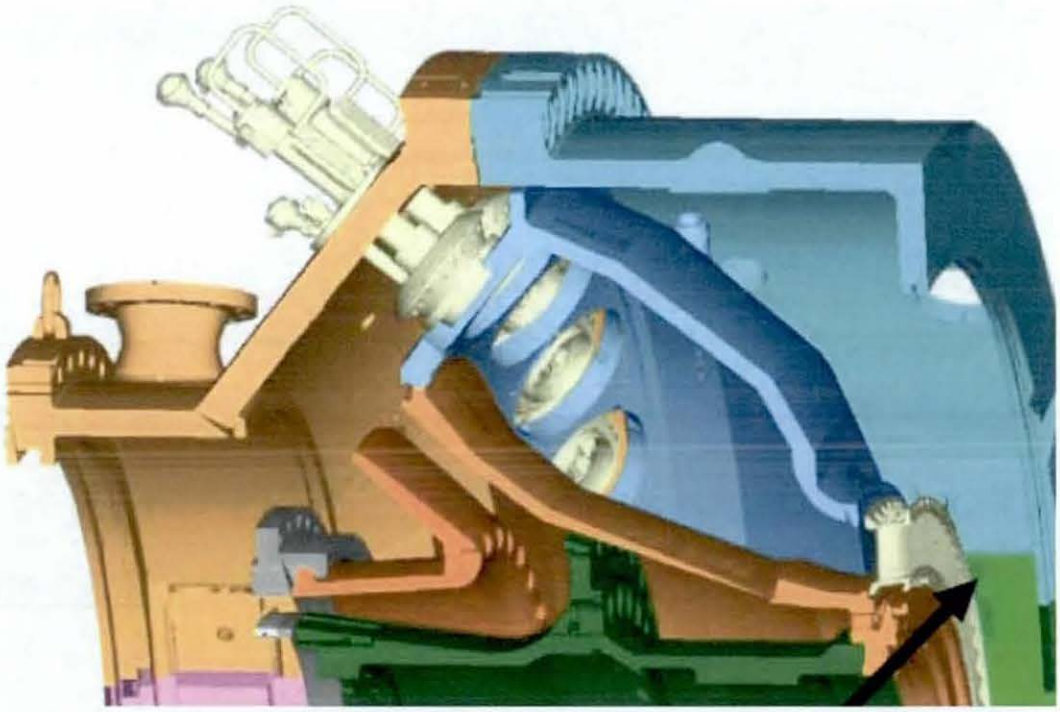

Figure 1.4 Cut view of a 3D annular combustion chamber (Staffelbach, 2006).

Figure 1.5 Accidental explosions at Buncefield oil depot, Hemel Hempstead (Courtesy of Royal Chiltern Air Support Unit, www.buncefieldinvestigation.gov.uk/images/index.htm).

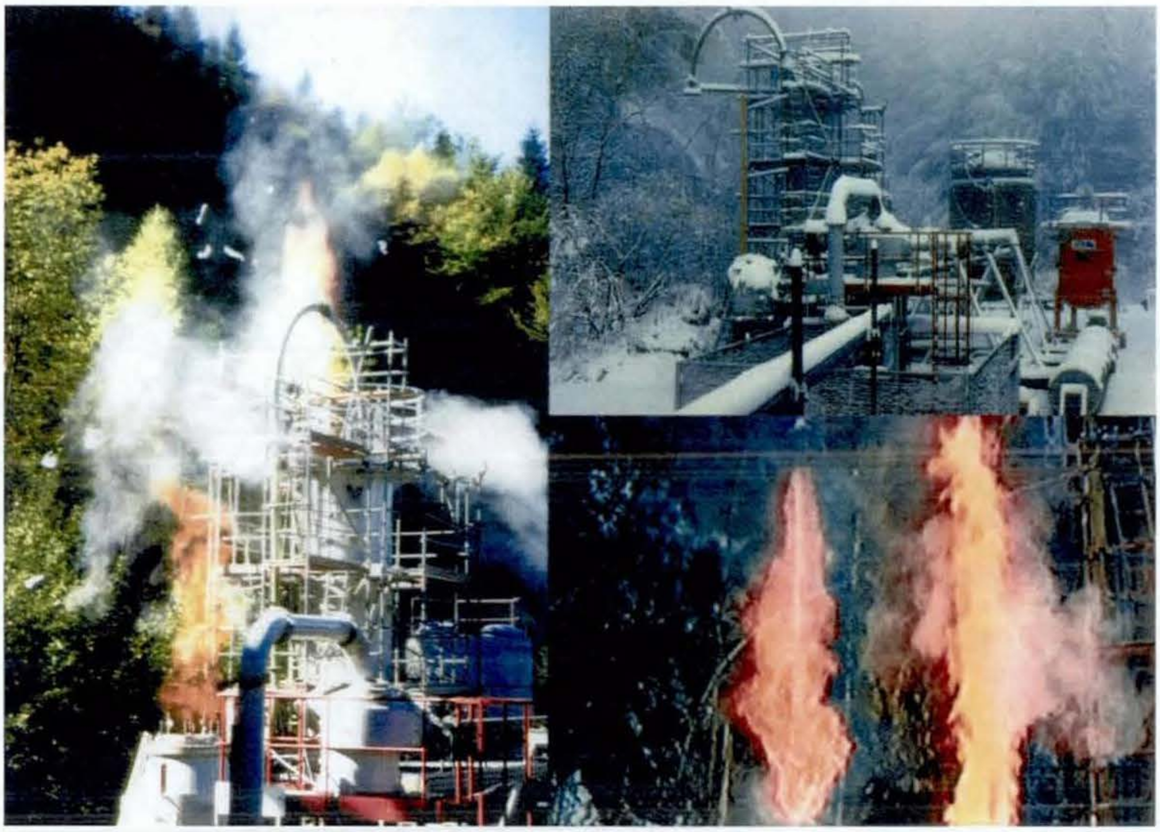

Figure 1.6 Large scale experimental explosion test rig (Malalasekera, private communication).

Apart from aforementioned applications, numerical modelling plays pivotal role in the safe design of on- and off-shore chemical/fuel processing/storage plants. For example, a recent accidental explosion happened on Sunday 11th December 2005 at Buncefield oil depot located near the M1 motorway on the edge of Hemel Hempstead, England (Figure 1.5), the damage caused by the explosion generated overpressure due to flame acceleration and its interactions with the presented equipment/solid obstacles was enormous and highly hazardous. Investigating such large scale explosion experiments as shown in Figure 1.6 (Malalasekera, private communication) in industrial scale vessels are very expensive and risk taking, while yielding limited data.

Computational modelling tools have been proved as an excellent alternative and the methods are adequately developed in the field of aerospace, fluid dynamics, metrology and health engineering even for complex non-reacting flow problems. However, in case of reacting flow problems, where turbulence is involved, the progress made is less satisfactory with many outstanding research issues. With successful prediction of non-reacting flow applications, industrial usage of computational modelling for turbulent combustion is ever growing. Generally, there are three computational modelling techniques available for current use, mainly Direct Numerical Simulations (DNS), Large Eddy Simulations (LES) and Reynolds Averaged Navier Stokes (RANS) equations.

Among the aforesaid numerical techniques, DNS offers the utmost accuracy as all the physical scales involved in a flow problem are completely resolved without modelling. However, despite significant improvements in computational resources, application of DNS is limited to low Reynolds number flows due to the cost and computational resources involved. Hence, the application of DNS to real combustion systems, where the flows are complex and involve higher Reynolds number is unpractical in the foreseeable future. For instance, Moin and Kim (1997) estimated that it will take several thousands of CPU years of the fastest available supercomputer during 1997, to compute the flow around an aircraft for one second of flight time, in order to understand the turbulence with reasonable details using 10^{16} grid nodes. This estimate limits the use of DNS for practical applications However, DNS can still be efficiently utilised to develop and evaluate computational sub-models

On the other hand, Large Eddy Simulation (LES) is now accepted as a feasible computational tool despite added computational cost, as compared with the RANS technique. Several recent works by Charlette et al (2002), Knikker et al. (2004), Fureby et al (2005), Masri et al (2006) and Pitsch (2006) confirmed the high fidelity of LES in predicting key characteristics of turbulent combustion. LES has a clear advantage over classical Reynolds averaged based methods in the capability of accounting for time-varying nature of the flow and this is particularly important in transient processes such as swirling flows or transient propagating premixed flames. LES also allows for detailed description of turbulence-chemistry interactions, which is a common failure in RANS The ever increasing speed of computers is rendering the high computational requirement of LES and shifting the focus towards developing adequate sub-grid-scale (SGS) models for combustion The development of such SGS models is imperative in both premixed and non-premixed combustion and however, the focus of this thesis is only on the former.

1.2 Motivation

LES has been attracting numerical modellers due the fact that, large eddies above a cut-off length scale are resolved and the small ones are modelled using SGS models. Also the cost and accuracy of the solutions lies between the DNS and RANS techniques Hence, the present study is considering LES methodology to understand the outstanding research issues, which are central to the development of advanced physical sub-models that will improve current predictive capabilities for turbulent premixed flames LES has been successfully applied to a variety of reacting cases ranging from simple to complex flames, involved in fundamental and advanced studies such as aircraft engine combustion (Kim et al , 1999), combustion instabilities (Menon and Jou, 1991, Fureby, 2000), small pool fires (Kang and Wen, 2004), swirling flames (Malalasekera et al., 2007) and large scale explosions (Molkov et al , 2004, Makarov et al , 2007) In spite of numerical and computational advancements, crucial issue to the advancement of LES lies in the development of adequate SGS models, which are capable of representing combustion over a wide range of flow and combustion conditions This remains a key challenge, facing the turbulent combustion community.

In LES, as the reaction zone thickness of the premixed flame to be resolved is thin, with a characteristic length scale much smaller than a typical LES filter width, an appropriate SGS model is vital to account for the SGS chemical reactions Several modelling approaches such as flame surface density (Pope, 1988, Bray, 1990), flame tracking technique (G-equation) (Williams, 1985b, Kerstein et al , 1988, Menon and Kerstein, 1992), artificially thickened flame (Veynante and Poinsot, 1997) and probability density function (PDF) (Mòller et al , 1996) are successfully adapted from classical RANS to LES. Recently, Christophe and Laszlo (2007) have numerically modelled turbulent premixed flames by using an S^+ marker field. They developed a new equation for marker field to capture the laminar or turbulent flame propagation via a reactive diffusive balance equation.

Among currently available models for turbulent premixed flames, the FSD approach (Masri et al. 2006) is quite simple, yet efficient in accounting for the chemical reaction rate The FSD, defined as the local flame surface area per unit volume, is computed either by an algebraic model (Boger et al , 1998) or by solving a transport equation (Prasad and Gore, 1999, Hawkes and Cant, 2001) Computing sub-grid FSD by solving a transport equation in LES is an attractive option However this approach results in several unclosed terms which need to be closed by appropriate models and lead to excessive computational cost. Algebraic models are similar to the Bray-Moss-Libby (BML) approach (Bray, 1990) in the context of RANS and have been extended to LES context (Boger et al., 1998, Knikker et al , 2002). These models are fundamentally based on the laminar flamelet concept, which view the reaction zone as a collection of propagating reaction layers thinner than the smallest scales of turbulence and where the laminar flame structures propagate locally at laminar burning velocity

Motivated by the simplicity of the FSD models, this approach is considered in the present study to simulate turbulent premixed flames propagating over repeated solid obstacles. A preliminary study has been conducted for several flow configurations to identify the drawbacks of the simple algebraic model. A recent breakthrough in the FSD models is the dynamic formulation of the flame surface density following similarity ideas of Bardina et al. (1980). Dynamic flame surface density (DFSD) model was originally developed by Knikker et al. (2004) and tested on experimentally extracted reaction progress variable information from OH images of a premixed flame over triangular stabiliser In this work this concept is developed further and numerically implemented in an existing LES code PUFFIN (Kirkpatrick, 2002). This novel DFSD model is evaluated for a laboratory scale premixed combustion chamber with a specific emphasis to predict the deflagrating premixed flame characteristics and their interactions with repeated solid obstacles

1.3 Objectives of the Present Investigation

The specific objective of this investigation is two-folded Firstly, to conduct transient LES simulations of turbulent premixed flames, propagating over repeated solid obstacles in a recently developed novel combustion chamber (Kent et al., 2005). The simulations use an algebraic, simple FSD model for the chemical reaction rate. To confirm the maturity of the LES methodology, extensive grid independency tests were performed In order to uncover the drawbacks of the simple FSD model in predicting premixed flames, various flow configurations have been studied using grid independent solution

The second objective of this study is to develop a dynamic flame surface density model, which accounts for the unresolved SGS contributions of flame surface density to enhance prediction capabilities. The developed model has been incorporated in an in-house LES code in order to evaluate the aforementioned flow configurations and hence achieving a level of confidence.

Finally, a detailed analysis has been performed in order to identify the influence of the number and position of obstacles inside the chamber on overpressure, flame position and speed, which will help to understand an accidental explosion scenario Subsequently the novel DFSD model is expected to contribute towards the advancement of the LES prediction capabilities of turbulent premixed combustion

In addition to the above mentioned objectives, the following supplementary objectives have been accomplished to gain good confidence in the developed model A dynamic model, capable of self-scaling the model coefficient in simple FSD model, based on the local flame and flow characteristics has been identified and evaluated.

1.4 Thesis Outline

This chapter describes the motivation and specific objectives defined to develop dynamic sub-grid scale (SGS) models for LES simulations of chemically reaction flows in turbulent premixed combustion systems. The available numerical approaches and their capabilities in predicting turbulent reacting flows are briefly discussed The rest of the thesis is organised as follows.

Chapter 2 outlines the breakthrough in premixed combustion research and various SGS models available to account for the chemical reaction rate A brief discussion is provided to review the characteristics of combustion through various regimes

Chapter 3 presents the assumptions considered and outlines governing equations for turbulent premixed combustion in their instantaneous and filtered form Favre filtering technique is briefly explained with an overview of closure problem encountered while applying the filter

Chapter 4 presents an overview on LES approach of modelling turbulent flows Various types of filtering techniques and available filters are presented and discussed The LES methodology has been described with details of closing strategies employed for sub-grid scale stresses and scalar fluxes.

Chapter 5 evaluates the combustion models reviewed in chapter 2. Development of the dynamic flame surface density model and its incorporation in the in-house LES code are discussed Details of the empirical and dynamic fractal models employed in calculating the fractal dimensions are outlined.

Chapter 6 describes the numerical implementation of the filtered governing equations outlined in chapter 3. Implementation of the spatial discretization and time advancement schemes through finite volume methodology are discussed A detailed description of the boundary conditions and the working procedure are also presented.

Chapter 7 describes the test case employed in this work for model validation. A detailed description of the influencing factors in designing this test chamber and the novelty of the chamber are explained. A detailed overview of the experimental ignition system and utilised measurement techniques are explained. Classification of the various test case configurations in terms of the number of obstacles and their position in the novel chamber are explained Typical experimental sequence is detailed to outline the procedure followed.

Chapter 8 explains the numerical domain used and various grid resolutions employed in LES simulations LES results using a simple algebraic flame surface density model for chemical reaction rate are presented and examined for grid independency, influence of filter width and the percentage of resolved turbulent kinetic energy. Firstly, LES results using dynamic formulation for the model controlling parameters in case of the simple algebraic model are presented and validated

Secondly, LES results using dynamic flame surface density model are presented and analysed for various complex flow configurations. A comprehensive model analysis is provided for various aspects of the developed DFSD model. Flame characteristics from various flow configurations are analysed and presented in a turbulent premixed combustion regime diagram.

Chapter 9 summarises conclusions from the present research work with key contributions towards the improved prediction capabilities and suggests directions for further improvements

Chapter 2

Literature Review

This chapter reviews some important breakthroughs in the experimental and numerical techniques for turbulent premixed combustion research associated in understanding the turbulent flame interactions and in developing new models A brief discussion is provided in this section to review the characteristics of premixed flames through various turbulent combustion regime diagrams. Section 2.2 describes various RANS and LES models available to account for the chemical reaction rate in computational modelling.

2.1 Background

Premixed turbulent flames are often characterised by their ability to propagate towards the fresh gases Once the flame is initiated due to the ignition source, the reaction advances through the gas with relatively thin-localised flame front until all the fuel is exhausted. Unlike laminar flames, in turbulent flames the flame propagation speed is not equal to the incoming gas velocity The turbulent flame speed has been identified to depend on many parameters such as turbulence levels, mixture reactivity, surface area of the flame and flame stretch etc On the other hand, if the flame propagation is due to thermal conduction i e transporting energy from hot burnt matter to cold fuel mixture, it is known as deflagration. If the flame propagates due to shock wave i.e. increasing the temperature by virtue of compressing the fuel mixture, it is known as detonation. The deflagration may transform into detonation depending on boundary conditions, length and width of the chamber and the generated overpressure etc. Alternatively, the presence of solid obstructions in combustion environment eventually leads to higher flame acceleration with high overpressure, which has severe consequences in many engineering applications As described in chapter 1, simulation of combustion scenarios using numerical modelling would help in designing an efficient combustion system. However, success of any numerical combustion model depends mainly on the competence of the employed chemical reaction rate model in accounting the chemical reaction rate. Hence, development and evaluation of combustion models are very important with ever growing industrial needs and demands for essentially, efficient combustion systems.

The main focus of this thesis is to develop and evaluate the dynamic formulation of flame surface density model for turbulent premixed combustion. The developed model is evaluated and validated for a laboratory scale premixed combustion chamber established at The University of Sydney by Prof. Masri's combustion group (Kent et al , 2005), where highly resolved experimental data has been obtained This rectangular chamber has built-in solid obstacles to enhance the turbulence level and to increase the flame propagating speed, which eventually lead to stronger interactions between the flame and the solid obstacles. These interactions were found to create turbulence both by vortex shedding and local wake/recirculation. As the flame propagates past the solid obstacles, it wraps on itself, which eventually increases the flame surface area available for combustion. More details of the combustion chamber and the various flow configurations considered in the present study are outlined in Chapter 7.

Several experimental and numerical studies have been performed in the past, using laboratory scale chambers, to evaluate the effect of the chamber size, with or without obstacles on accelerating flames (Williams, 1985a, Aldredge et al., 1998, Bradley, 2002, Lee and Lee, 2003, Akkerman et al , 2006, Bauwens et al., 2007). A large number of these experimental studies were aimed at understanding the flame-turbulence interactions in vented explosion chambers with in-built solid obstructions (Moen et al , 1980, Hjertager et al , 1988, Starke and Roth, 1989, Fairweather et al., 1996, Masri et al., 2000, Bradley et al., 2001). The chambers used by Moen et al. (1980), Moen et al (1982), Hjertager et al. (1988) and Bradley et al. (2001) to study the flame interaction issues, yielded limited data because they involved large-scale experiments that did not lend themselves easily to detailed measurements. Starke and Roth (1989), Phylaktou and Andrews (1991), Fairweather et al. (1996), Lindstedt and Sakthitharan (1998), Masri et al (2000) and Ibrahim and Masri (2001) have used laboratory scale chambers utilising simple geometrical configurations that were adaptable to complex diagnostics and the subsequent validation of numerical models. All these studies have involved the use of a variety of obstacles (square/circle/triangular/wall baffles) in the path of propagating flames However, the exact mechanism that correlates flame structure, speed and resulting overpressure are not well understood yet Masri et al. (2000) reported the influence of the size and shape of the solid obstacles and found that both the blockage ratio, as well as the shape of obstacles influences the flame structure and propagation rate. Lindstedt and Sakthitharan (1998) and Fairweather et al. (1999) reported the interaction of flames with baffles and extracted high quality flame structure, mean and fluctuating velocity data using expensive experimental setups. Numerical studies have been reported on a variety of confined and semi-confined chambers using RANS and LES approaches (Patel et al., 2002, Pitsch and Duchamp de Lageneste, 2002, Kirkpatrick et al., 2003, Fureby et al., 2005, Masri et al., 2006). Masri et al. (2006) performed LES studies on a 20 litre volume and found it to be impractical due to the long LES computational times Hence, an alternative design that preserved the same physics and optical access, yet with a reduced volume of less than a litre was developed by Kent et al. (2005) and that geometry is used in this study.

Considerable progress has been made in the modelling of turbulent premixed flames using LES methodology within the last 20 years Modelling of the chemical reaction rate plays a major role and a variety of modelling approaches are available. However, drawbacks still exist due to the complex nature of turbulent premixed flames, insufficient experimental data for validations and failure to predict flames over a range of turbulent premixed combustion regimes and flow configurations. The majority of models are derived from the popular and simple laminar flamelet concepts, where chemistry is separated from turbulence. Some of these models are briefly discussed in following sections

2.1.1 Characteristics of Turbulent Premixed Flames

Turbulent premixed combustion is a very complex thermo-chemical-fluid flow phenomenon, which is usually associated with a range of turbulence, chemical, time and length scales. Fundamentally, these scales can be estimated from flame-flow characteristics such as flame brush thickness, surface area, velocity fluctuations, turbulent and laminar flame speed. These time and length scales are used to form various non-dimensional numbers, which are useful in understanding insight and physics of the combustion phenomenon. Two of these non-dimensional numbers, namely, Damköhler (*Da*) and Karlovitz (*Ka*) numbers are used to characterise the classical regime diagrams for turbulent premixed combustion based on experimental observations and intuitive arguments These diagrams indicate the nature of the flame and approximate the contents, as flamelets, pockets or distributed reaction zones, depending on turbulence characteristics such as integral length scales, turbulent kinetic energy and lend themselves to develop combustion models based on the physical analysis

Damkohler number is one of the classical non-dimensional numbers, this corresponds to the large eddies in combustion and can be defined as a ratio of turbulent time scale, τ_t to chemical time scale, τ_c as

$$Da = \frac{\tau_t}{\tau_c} \tag{2 1}$$

where the chemical time scale, τ_c may be estimated as the ratio between the flame thickness, δ_L and the laminar flame speed, u_L The turbulent time scale τ_t corresponds to the integral length scale, l_t and is estimated as $\tau_t = l_t / u'$ where u' is the RMS velocity Then the Damkohler number becomes:

$$Da = \frac{\tau_t}{\tau_c} = \frac{l_t}{\delta_L}\frac{u_L}{u'} \tag{2 2}$$

The Karlovitz number corresponds to the smallest eddies and is defined as the ratio of the chemical time scale to the Kolmogorov time scales, τ_k as:

$$Ka = \frac{\tau_c}{\tau_k} = \frac{u'(\eta_k)/\eta_k}{u_L/\delta_L} = \left(\frac{l_t}{\delta_L}\right)^{-1/2}\left(\frac{u'}{u_L}\right)^{3/2} = \left(\frac{\delta_L}{\eta_k}\right)^2 \tag{2.3}$$

where η_k is the Kolmogorov micro scale Figure 2 1 shows a classical combustion regime diagram extracted from the works of Peters (1988) based on the velocity scale (u'/u_L) and length scale (l_t/δ_L). This diagram delineates four important regimes as shown in Figure 2.1. However, this classical diagram is known to fail for many combustion situations (Poinsot and Veynante, 2001) due to the assumption of homogeneous and isotropic turbulence by neglecting heat release affects. Later, Peters (2000a) has modified this classical combustion regime diagram by considering the heat release effects based on same velocity and length scales as shown in Figure 2 2.

Figure 2.2 identifies three main combustion regimes; corrugated/wrinkled flamelets, thin reaction zones, and broken reaction zones. These regimes are also pictorially reproduced from the works of Borghi and Destriau (1998) in Figure 2 3, 2.4 and 2 5 respectively. The corrugated/wrinkled flamelet regime is in which, the chemical time scales are shorter than any turbulent time scales i e. $Ka < 1$. Also the flame thickness is smaller than the smallest turbulent scale (smaller than Kolmogorov scales), which means that the flame front is not affected by turbulent motions The flame front in this regime is very thin and wrinkled due to turbulence motions smaller than Kolmogorov length scales, and similar to laminar flame structure

Thin reaction zone regime, is identified where the Kolmogorov length scale becomes smaller than the flame thickness, which implies $Ka > 1$. In this regime, the order of Kolmogorov, chemical and turbulence time scales are of in the fashion $\tau_k < \tau_c < \tau_t$ and Kolmogorov scales are smaller than the flame thickness and are able to modify the inner flame structure. Majority of the engineering combustion devices are operated in the thin reaction zones regime, because mixing is superior at higher Ka numbers, which leads to higher volumetric heat release and shorter combustion times (Pitsch, 2006)

The "broken" reaction zone is defined when the chemical time scale is higher than turbulent time scale i e. $Da \ll 1$. In this regime, turbulent motions becomes sufficiently strong to affect the whole flame structure, which means mixing is faster and the overall reaction rate is limited by chemistry. This subsequently may lead to a local extinction and can cause noise and instabilities Amplification of instabilities may even lead to global extinction in premixed combustion devices (Pitsch, 2006) This regime is also known as "well-stirred reactor" zone

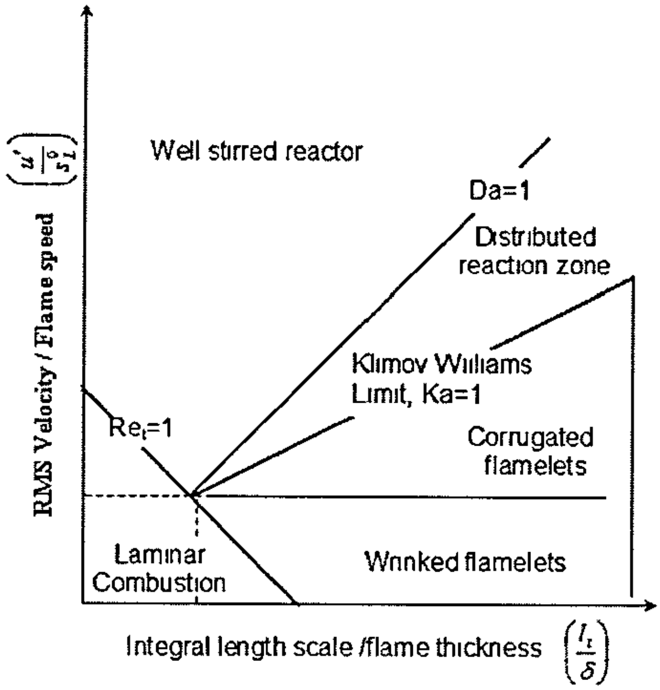

Figure 2.1 Classical Turbulent combustion regime diagram (Peters, 1988).

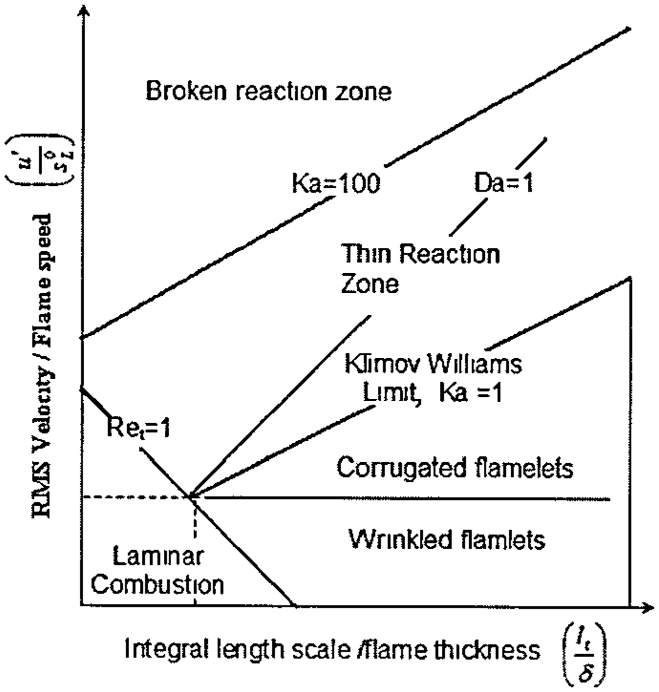

Figure 2.2 Modified turbulent combustion diagram (Peters, 2000a).

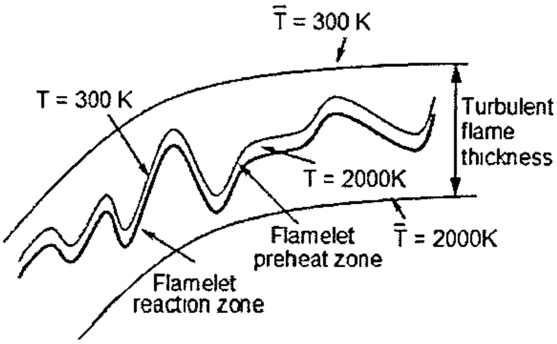

Figure 2.3 Flamelet regime or “thin wrinkled flame regime (Poinsot and Veynante, 2001).

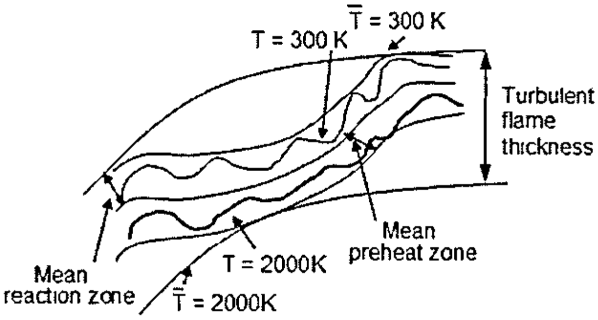

Figure 2.4 Thickened-wrinkled flame regime (Poinsot and Veynante, 2001).

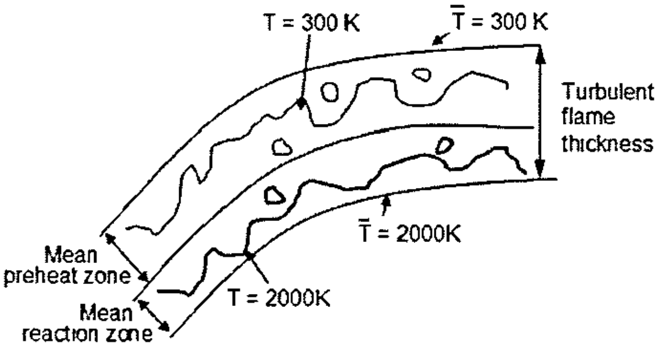

Figure 2.5 Thickened flame regime (Poinsot and Veynante, 2001)

2.1.2 Regimes of LES Turbulent Premixed Combustion

The classical regime diagrams discussed in the previous section are helpful in identifying the combustion phenomenon in various combustion systems, based on relevant velocity and time scales estimates. However in case of LES, the unique parameter which distinguishes other numerical modelling approaches, is the filter width ($\bar{\Delta}$), which plays a vital role in separating large eddies from small eddies in the flow field. This fact has mainly led to a recent development of LES regime diagrams for premixed flames (Pitsch and Duchamp, 2002). Pitsch and Duchamp (2002) exploited the fact that the Karlovitz number, *Ka* is independent of the filter width and introduced a new regime diagram with respect to Karlovitz and Reynolds number. However, sub-grid velocity fluctuations are dependent on filter width and a change in the filter width results in a change in the sub-grid velocity fluctuations, which eventually may change the regime of combustion, provided that the solution is grid independent This identifies that the effect of the filter width, cannot be studied independently as it has significant effect on combustion (Pitsch, 2006)

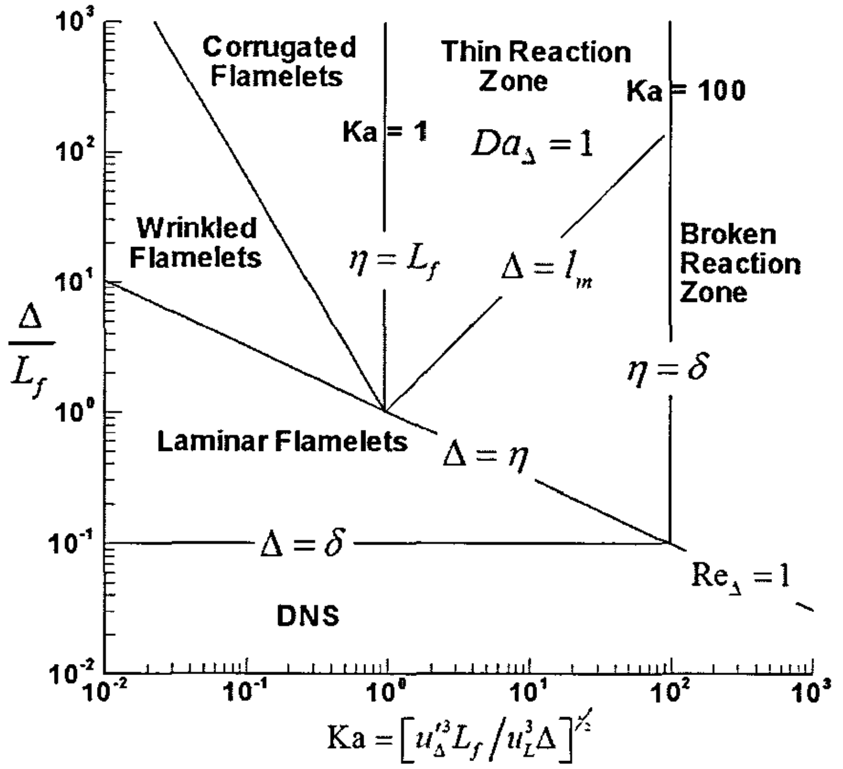

Figure 2.6 Regimes diagram for LES of premixed turbulent combustion (Pitsch and Duchamp, 2002)

Figure 2 6 reproduces the LES regime diagram of Pitsch (2006) with length scale $(\overline{\Delta}/\delta_L)$ and Karlovitz number as co-ordinates. The Karlovitz number describes the physical interactions of flow and combustion at the smallest turbulent scales The sub-grid Reynolds, Damköhler numbers and the Karlovitz number are defined as:

$$\mathrm{Re}_\Delta = \frac{u'_\Delta \overline{\Delta}}{u_L \delta_L},\ \mathrm{Da}_\Delta = \frac{u_L \overline{\Delta}}{u'_\Delta \delta_L},\ \text{and}\ \ \mathrm{Ka} = \frac{\delta_L^2}{\eta_k^2} = \left(\frac{u'^3_\Delta \delta_L}{u_L^3 \overline{\Delta}} \right)^{1/2} \tag{2.4}$$

where u'_Δ is the sub-grid scale velocity fluctuations. In LES, the Karlovitz number is a fluctuating quantity, but for a given flow field and chemistry it is fixed. The effect of changes in filter size can therefore easily be assessed at constant *Ka* number An additional benefit of this regime diagram is that it can be used equally well for DNS (Pitsch, 2006) if $\overline{\Delta}$ is associated with the mesh size.

It can, easily, be noticed from Figures 2.2 and 2.6 that the combustion regimes shown in Figure 2.6 are the same and represented in terms of LES quantities. Hence, the three regimes identified and discussed in the previous section are still valid for LES. However, it should be noticed that the effect of changing the LES filter width can have an impact on the accuracy of the numerical solutions. For instance, by choosing an appropriate $\overline{\Delta}/\delta_L$ ratio, by decreasing the filter width, eventually leads to a smaller sub-filter Reynolds number (Re_Δ) less than one Therefore for a filter size smaller than the Kolmogorov micro scale, no sub-filter modelling for the turbulence is required, which eventually reaches DNS resolution. However, the entire flame including the reaction zone can only be resolved if $\overline{\Delta} < \delta_L$

2.2 Modelling the Reaction Rate

Modelling the reaction rate in turbulent premixed flames is highly challenging due to its non-linear relation with chemical and thermodynamic states, and often characterized by propagating reaction layers thinner than the smallest turbulent scales. The major difficulty in modelling the reaction rate is due to the variation of thermo chemical variables through the laminar flame profile, which is typically very thin (Veynante and Poinsot, 1997). This issue is strongly affected by turbulence, which causes flame wrinkling and thereby forming the most complex three way thermo-chemical-turbulence interactions. However, assuming a single step irreversible chemical reaction and neglecting the Zeldovich instability (thermal diffusion), i e. considering unit Lewis number will reduce the complexity of the whole system Various modelling approaches available can be found in literature (Poinsot and Veynante, 2001). Some of these models are briefly discussed in the following sections

2.2.1 Flamelet Modelling of Premixed Turbulent Flames

Flamelet modelling of turbulent deflagrating premixed flames provides a means to introduce chemical and turbulence time scales by considering a thin laminar flame in a turbulent flow field. The key goal behind laminar flamelet modelling is to incorporate various flamelet stretching mechanisms to account for effective turbulence time scales by assuming that the heat release will only occur within the thin reaction zone. Much of the flamelet modelling literature focuses on deriving effective turbulent burning velocity (e g (Abdel-Gayed et al., 1987)) An alternative modelling strategy has been pursued for the flamelet regime since the introduction of the Bray-Moss-Libby (BML) model (Bray et al., 1985). This model has been extended from its preliminary form since first introduction in premixed turbulent combustion by Bray and Moss (1977) and Bray-Moss-Libby (BML) model (Bray et al., 1981, Libby and Bray, 1981), and subject of many interesting research works thereafter. BML models are derived based on a combination of statistical approaches using probability density functions (PDF) and physical analysis. This combination has led to the development of both complex and simple models using probability functions. For instance, Bradley et al. (1992) used a classical presumed PDF model by assuming a weak flamelet, which considers reduced chemistry through the parameterisation of detailed chemistry. On the other hand, following BML analysis, mean chemical reaction rate can be simply modelled by analysing the flamelet and using modelling tools as (Bray et al., 1985)

$$\dot{\omega}_c = \rho_u u_L^0 I_0 \Sigma \qquad (2\ 5)$$

where ω_c is the chemical reaction rate, ρ_u is unburned gas density, I_0 is the mean stretch factor and Σ is the flame surface density (FSD), defined as flame surface to volume ratio Modelling the chemical reaction rate, using the above approach requires models for FSD and mean flame stretch factor Several models and empirical correlations for the evaluation of flame stretch I_0 can be found in the literature. For example, Bray (1990) identified flame stretch as a function of Karlovitz number Bradley et al. (1992) identified flame stretch as a function of Karlovitz and Lewis numbers and Bray and Cant (1991) deduced an analytical expression from DNS data as a function of Markstein and Karlovitz numbers

The flame surface density, Σ in equation (2 5) represents the balance between turbulence, which wrinkles the flame and laminar flame propagation, which smoothes out the flame wrinkles (Bray and Peters, 1993). The flame surface density can be computed by either solving a transport equation (Pope, 1988, Candel and Poinsot, 1990, Cant et al., 1991) or via an algebraic model (Bray, 1990, Trouvé and Poinsot, 1994). Various models available to compute FSD have been evaluated in the RANS frame work (Duclos et al., 1993, Prasad and Gore, 1999), which is a central problem in establishing a good flamelet model. Duclos and Veynante (1993) reported that solving a transport equation for FSD in its exact form is highly difficult due to the excessive computational times involved However, solving a transport equation for the flame surface density has been the subject of many works in RANS and LES (Prasad and Gore, 1999, Hawkes and Cant, 2001, Patel et al , 2003) and sub models have been developed through the phenomenological arguments (Darabiha et al , 1986, Borghi, 1990). Although solving a transport equation for the flame surface density is an attractive option, this will result in several unclosed terms which need to be closed by appropriate sub-models and restricted to handle extreme cases, where coupling between the flow-field and flame front is intense

The uncertainties involved in the extensive modelling of unclosed terms, in solving the transport equation for Σ, are instigating for an algebraic expression for Σ, which is the main focus of the present study Bray et al. (1985) proposed a simple model to calculate Σ as, $\bar{c}(1-\bar{c})/L_y$, where $\bar{c}$ is the reaction progress variable and L_y is the length scale associated with wrinkled flame The length scale, L_y can be modelled by assuming it to be proportional to the integral length scale (Abu-Orf and Cant, 2000) or by an additional transport equation (Lindstedt and Váos, 1999). Gouldin et al (1989) and Weller et al. (1998) derived an expression for Σ based on fractal theory by viewing the turbulent flame as a fractal surface within the lower and outer cut-off scales and found to be in good agreement (Veynante and Vervisch, 2002) with experimental data for $\Sigma/[\bar{c}(1-\bar{c})]$.

Various other studies (Pope, 1988, Duclos et al, 1993, Veynante et al, 1996) can be found in the literature, modelling the flame surface density either by balancing the production, transport and annihilation terms or developing a correlation from experimental data. On the other hand, Σ can be modelled using turbulent flame speed (TFS) closure as a ratio between the turbulent flame surface area per unit volume A_T to its projection on its average surface per unit volume $\bar{A}$. The ratio of $A_T/\bar{A}$ can be modelled by following the prominent observation of Damkohler (1940). Recently, this approach has been used by Muppala et al (2005) in RANS and by Aluri et al (2006) in LES to predict various turbulent premixed flames

Most of these flamelet models have been successfully transformed from the framework of RANS to LES and applied to a variety of practical problems such as V-flames (Chan and Li, 2005), SI engines (Richard et al, 2007), gas turbines and Ramjets (Menon and Jou, 1991) etc. Boger et al. (1998) deduced a simple algebraic model suitable for LES of turbulent premixed flames This model has been used by Kirkpatrick et al. (2003) and Masri et al. (2006) to predict the turbulent deflagrating flame in an obstructed explosion chamber and found to be predicting reasonably well However, their studies under-predicted explosion overpressures, flame position and structures. Masri et al (2006) reported that using a complex model for flame surface density would provide more accurate predictions for the flame characteristics

Inspired by the works of Masri et al. (2006), the present study intends to develop a dynamic flame surface density model In this work, the simple algebraic model of Boger et al (1998) is used initially to predict the turbulent deflagrating flames in various flow configurations and efforts are made to identify its drawbacks. Subsequently, the present work concludes (see Chapter 8) that the model constant is not universal and depend on many physical parameters such as the LES filter width, fuel/air mixture, turbulence etc. Hence, a model is developed based on wrinkling flame theory and tests are performed to evaluate the self-scaling capabilities of this model. Further to this, the concept of the dynamic flame surface density model, which was proposed by Hawkes (2000) and Knikker et al (2002) is developed and evaluated This model follows the dynamic procedure of Germano et al. (1991) and the similarity concept of Bardina et al. (1980) The dynamic flame surface density model, presented in chapter 5, has been linked with flame wrinkling theory in order to dynamically evaluate the model coefficient. This procedure is followed to calculate the fractal dimension of the turbulent premixed flame, which has been the subject of many interesting research works (Mandelbrot, 1975, Gouldin, 1987, Kerstein, 1988, Gouldin et al , 1989 and Gouldin, Hilton et al , 1989) in past Recently, Fureby (2005) used an empirical model in LES, based on original developments of North and Santavicca (1990). This model is also tested, here, and evaluated against the fractal dimension model developed by Knikker et al. (2004) in calculating the dynamic model coefficient.

2.2.2 Other Modelling Approaches

As described earlier, modelling of chemical reaction rate in turbulent premixed combustion is very complex and there are various modelling approaches ranging from simple to complex available in the literature Most of these approaches have been initially developed for RANS modelling and then extended to LES

2.2.2.1 Turbulent Flame Speed Closure

Chemical reaction rate can be simply modelled by the overall turbulent flame speed S_T as a function of the ratio of turbulent flame surface area to laminar flame surface area. Damkohler (1940) hypothesised a relation given in equation (2 6) and Abdel-Gayed et al. (1987) extended (shown in equation 2.7) this by correlating various experimental measurements of turbulent premixed flames. Since the turbulent flame speed is not a well defined quantity and known to be dependent on many physical and chemical parameters, use of TFS closure is quite questionable. However, TFS closure has been successfully used in RANS (Zimont et al., 1997, Polifke et al , 2000 and Zimont, 2000) for gas turbine combustor and in LES (Flohr and Pitsch, 2000) for industrial burners, with certain limitations. This simple closure has been widely used in flame tracking approach (G-equation) with various modifications. Current models calculate S_T as a function of turbulence intensity alone show significant variations (Bradley, 1992) reflecting the possible influence of other parameters, such as the scalar dissipation rates However, use of TFS closure is debatable in LES as it is not well suited to close Favre averaged transport equations.

$$\frac{u_T}{u_L}=\frac{A_T}{A_L} \tag{2 6}$$

$$\frac{u_T}{u_L}=1+\alpha\left[\frac{u'}{u_L}\right]^n \tag{2 7}$$

Recently this closure has been used in conjunction with the flame surface density model to predict turbulent premixed flames in RANS (Muppala et al , 2005) and LES (Aluri et al , 2006).

2.2.2.2 Eddy-Break-Up Model

The Eddy-Break-Up (EBU) model, originally developed by Spalding (1971), views the reaction zone as a collection of fresh and burnt gas pockets transported by turbulent eddies and can be modelled as:

$$\bar{\dot{\omega}}_c=C_{EBU}\bar{\rho}\frac{\varepsilon}{k}\frac{\tilde{Y}_F}{Y_F^0}\left(1-\frac{\tilde{Y}_F}{Y_F^0}\right) \tag{2 8}$$

where Y_F^0 is the fuel mass fraction in fresh gases, k and ε are respectively the turbulent kinetic energy and its dissipation rate, C_{EBU} is a model constant. EBU models have been extensively used in RANS (Fureby and Lôfstrom 1994, Moller et al , 1996) and LES (Fureby and Lôfstrom, 1994, Moller et al , 1996 and Porumbel and Menon, 2006) for industrial applications, despite over estimation of the reaction rate, due to its simplicity. In this approach, the reaction rate is assumed to be proportional to the intermittency between fresh and burnt gases and inversely proportional to the turbulence time scale. This model is attractive because the reaction rate is simply written as a function of known quantities without any additional transport equations, simply by neglecting the chemistry effects. This results in an overestimate the reaction rate, especially in highly strained flow regions (Cant and Bray, 1989).

In the context of LES, EBU models found to predict reasonably well for bluff body stabilised flames (Fureby and Möller, 1995), without any additional sub-grid scale models Porumbel and Menon (2006) studied bluff body stabilised flame using sub-grid scale EBU model and Linear Eddy Model (LEM) in LES. They concluded that, results using EBU found to under-predict turbulent flame wrinkling, turbulent mixing rate, temperature field, and to over-predict turbulent flame thickness. Kim et al. (2006) have reported results by using EBU model for gas turbine flame holder stabilised flames for various equivalence ratios, with an additional transport equation for turbulent kinetic energy and an algebraic equation for dissipation rate Their studies found to predict stabilised flame very well except few deviations from experimental data at stoichiometric condition. Hence, it can be concluded that the success of EBU models with or without sub-models or additional transport equations is variable

2.2.2.3 Probability Density Function Approach

Probability density function methods have been used in turbulent reacting flows for over 60 years (Kollmann and Schmitt, 1981) and are quite established, especially in turbulent non-premixed combustion (Cook and Riley, 1994) In PDF methodology, the flame front/flow field is described based on statistical properties and probability theories. These methods have close tie-ups in deriving sub-models in flame tracking and flame surface density approaches. There are several methods to describe flow/flame probability functions such as presumed PDF, where a shape is assumed by solving a PDF balance equation, joint PDF, where probability of a set of variables are either solved using a transport equation or modelled and finally, conditional PDF, where PDF is used based on certain local conditions.

Several important studies (Pope, 1985, Givi, 1989, Gao and O'Brien, 1993, Madina and Givi, 1993, Moller et al , 1996, Cook et al , 1997 and Cook and Riley, 1998) can be found reporting development and application of PDF methods for turbulent reacting flames in RANS and LES. The fundamental idea of the PDF method is based on describing the statistical property of thermo-chemical variables For instance, if ϕ represents an arbitrary thermo-chemical variable of interest and the PDF in LES can be defined as

$$P_{sg}(\theta,x,t) = \iiint \delta(\theta-\phi(x',t))G(x'-x)dx' \qquad (2\ 9)$$

where θ is the statistical random variable associated with ϕ, and $\delta(\theta-\phi(x',t))$ is the fine grained density of the variable θ. The value $P_{sg}(\theta, x, t)d\theta$ is the probability of the LES filter-weighted fraction of fluid around x that has ϕ in the range $[\theta, \theta+d\theta]$. The advantage of the PDF approach is that the reaction rate term can be closed exactly through the simple relation as:

$$\bar{\omega}(x,t)=\int\omega(\theta)P_{sg}(\theta,x,t)d\theta \tag{2.10}$$

Using PDF models have produced good results in comparison with DNS data for non-premixed combustion (Moller et al., 1996, Reveillon and Vervisch, 1997, Colucci et al , 1998 and Cook and Riley, 1998) successfully predicted premixed combustion using presumed PDF approach, assuming a multidimensional normal distribution for the scalar variables With this success, PDF of turbulent premixed flames has become an alternative method to predict flames in various combustion regimes. However, the shape of initial PDF may need to be obtained either from experimental data or DNS data.

2.2.2.4 Flame Tracking (G-equation) Approach

The flame tracking approach or G-equation, originally introduced by Williams (1985b) is based on the flamelet assumption. In this approach the flame is assumed to be a thin surface and can be represented or tracked by the level surface of a scalar field *G*, which has a constant value G_o at flame surface and can be described as:

$$\frac{\partial G}{\partial t}+u.\nabla G=w\left|\nabla G\right| \tag{2.11}$$

where w is the local relative propagation velocity of the flame The equation in (2 11) can be used to represent a surface of chosen variable such as temperature, reaction progress variable or any other variable of interest Pitsch (2006) argued that this approach is not modelling the flame front, rather a numerical method, which can resolve the flame front Several studies reported, successful prediction of turbulent flames using G-equation in RANS and LES Yakhot (1988) was the first to suggest this equation to be used in LES combustion Following Yakhot (1988), several authors (Kim and Menon, 2000, Pitsch and Duchamp, 2002 and Huang et al., 2003) proposed LES formulation of the G-equations and applied to various combustion chambers such as ramjet (Menon and Jou, 1991), IC engines (Naitoh et al., 1992), Bunsen burner experiment (Pitsch and Duchamp, 2002) etc.

Pitsch (2005) argued that the G-equation for the filtered flame front used in the above studies, did not consider the special character while filtering the G-equation, which has caused inconsistency with generalised scaling symmetry Pitsch (2005) derived a new filtering technique for G-equation and reported that the filtered G-equation (equation 2.12) is valid in corrugated flamelet and the thin reaction zones.

$$\frac{\partial \breve{G}}{\partial t}+\hat{u}.\nabla\breve{G}=-(u_L+u_k)\text{n}.\nabla\breve{G} \tag{2.12}$$

where n is the flame front normal vector, and u_L and u_k describe laminar flame propagation and flame advancement by curvature effects respectively, which requires sub-models to close. Pitsch (2006) proposed models for u_L and u_k based on production-dissipation balance assumption and found to fit well in LES, with certain drawbacks near the flame holder, where the flame is not fully established. Also he described that $\breve{G}$ in the above equation is not the filtered G-field, but a level set representing the flame front position This is clearing the concerns raised by Hawkes and Cant (2000) regarding this approach in tracking the level set of flame front. However, the G-equation employed in the above studies appears to still have some drawbacks.

Modelling the flame structure is a major challenge in G-equation, as the flame surface can only be tracked and not resolved in numerical space This can be achieved by the sub-models derived either from experiments or DNS data Filtered G-equation (2 12) does not include any diffusion terms, which may lead to numerical difficulties. Finally, there is no theoretical lower limit for the radius of the flame front curvature. As the flame front propagates, cusps can form with zero radius of curvature (Pope, 1988), which cannot be resolved on the computational mesh Cusps are not expected for the filtered LES field since these would be smeared out by the filtering process. This problem is usually overcome in an ad-hoc manner by the introduction of artificial diffusion (Piana et al , 1997)

2.2.2.5 Artificially Thickened Modelling

It can be noticed from the above modelling strategies, that the premixed flame is very thin i e. about 0.1 to 1mm (Colin et al., 2000) and cannot be resolved on LES numerical grid This difficulty in resolving flame on numerical grid, associated with the stiffness of the progress variable has lead to the development of an alternative approach of "thickened flame modelling" by Butler and O'Rourke (1977) originally for laminar flame calculations This method has been extended to LES by Veynante and Poinsot (1997) and Thibaut and Candel (1998) for turbulent premixed flames.

The basic idea of this approach is thickening of the flame brush by a factor F and dividing the reaction rate by the same factor, while keeping the laminar flame speed constant, so that its structure is resolved by LES. The flame thickening is accomplished by a modification of the scalar transport equations, following the simple theories of laminar premixed flames (Kuo, 1986), such that the flame speed $u_L \propto \sqrt{\alpha_T \omega}$, and the flame thickness $\delta_L \propto \alpha_T / u_L$. Where $\dot{\omega}$ is the total reaction rate and α_T is the thermal diffusivity. This results in a flame of thickness $F\delta_L$ that propagates at a speed u_L The advantages of the approach are that it is simple to implement and, due to the Arrhenius law, it can handle some effects associated with ignition and flame-wall interaction processes (Colin et al , 2000). This approach models both the reaction rate and sub-grid transport terms simultaneously.

The flame thickening approach seems to be very attractive for flows in which the turbulence-flame interactions are governed mainly by very large scale flow structures. However, there are several drawbacks when applied to many common scenarios Firstly, this approach assumes implicitly that the reaction rate is controlled by chemistry rather than diffusive processes and hence the use of detailed chemical kinetics is recommended for better accuracy (Poinsot et al , 1991). This is numerically unattractive compared to the laminar flamelet approach where fast chemistry is considered and reaction is assumed to be controlled by transport processes. Secondly, the thickening of the flame decreases the sensitivity towards turbulent motions. Therefore the turbulent and chemical time scales are altered, which need to be accounted separately. The turbulent eddies smaller than the size of thickened flame are found to have no significant effect in stretching the flame (Poinsot et al., 1991). This effect was observed for the thickened flame model in comparison with DNS results by Veynante and Poinsot (1997). Thirdly, the sensitivity of the laminar flame velocity to stretch and curvature is increased by the transformation since the Markstein length is proportional to the flame thickness. The thickened flame will react to a stretch of k/F, as the actual flame would react to a stretch of k. This may influence flame quenching and may be prone to quench thickened flame much easily.

To counteract the over-response of flame stretch, an efficiency function E relating the actual flame stretch to the stretch felt by the thickened flame has been proposed by Meneveau and Poinsot (1991) based on DNS results. Similarly, Charlette et al., (2002) developed a dynamic model based on local flame conditions to overcome the over-response of the flame stretch in thickened flame modelling.

2.2.2.6 Marker Field Approach

The *S*+ marker field (Bilger, 2004) model in LES is fairly a new derivative of above discussed laminar flamelet models, which captures flame propagation by balancing reactive, diffusive fluxes in combustion space. Originally, the concept of the marker field *S* (a scalar) was introduced by Bilger (2004) in DNS and extended to RANS by Bilger et al., (2004) Recently, this model has been extended in the frame work of LES (Christophe and Laszlo, 2007) to predict stabilised turbulent premixed flame behind a back-facing step

2.3 Summary

This chapter has described some fundamentals and characteristics of turbulent premixed flames. A survey of a wide range of experimental and numerical studies, which employed similar forms of the combustion chamber employed in the present investigation, has been presented. Various regimes of turbulent premixed combustion have been discussed in general and in LES context Various reaction rate modelling approaches suitable for RANS and LES were presented and discussed. A brief history and evolution of the flamelet models, employed in this study for mean chemical reaction rate was presented. Some of the interesting features and drawbacks of the existing models were also presented and discussed.

Chapter 3

The Governing Equations

This chapter presents the instantaneous governing equations for the conservation of mass, momentum, energy, reaction progress variable, *c* and the equation of state, which govern turbulent premixed flames. In numerical modelling, it is necessary to impose simplifying assumptions to these governing equations to avoid non-linearity issues, which are detailed in section 3 1 Predicting turbulent reacting flows is usually involved in some form of averaging, which is briefly explained Also discussed is the application of the ensemble averaging (Favre) to the instantaneous governing equations and the resulting unclosed terms. A summary of the filtered governing equations are detailed in section 3 2 1

3.1 Instantaneous Conservation Equations

Governing equations of fluid flows can be derived by considering an infinitesimal control volume fixed in space and applying the conservation laws of physics The derivation of equations can be found in many text books (Turns, 1996) and are not repeated here. The governing equations shown in the following sections are derived for Cartesian coordinate system by considering the following assumptions.

- Low Mach number
- Soret and Dufour effects are neglected
- Unity Lewis number (neglecting Zeldovich instability)
- Newtonian fluid
- Negligible bulk viscosity from Stokes hypothesis
- Ideal gases
- Fully premixed reactants with one-step irreversible chemistry

3.1.1 Conservation of Mass

Conservation of mass physically imposes the condition that, neither creation, nor destruction of the mass within the control volume is possible. Application of this conservation law with convective transportation of mass across the control surface eventually leads to the well known continuity equation·

$$\frac{\partial \rho}{\partial t}+\frac{\partial(\rho u_j)}{\partial x_j}=0 \tag{3.1}$$

where ρ is fluid density in kg/m^3 and u_j is the velocity in x_j direction. The equation (3.1) is for unsteady, compressible and three-dimensional mass conservation, which can be simplified as per the problem specifications.

3.1.2 Conservation of Momentum

Conservation of momentum is based on Newton's second law, which states that the rate of change of momentum of a fluid particle equals the sum of the forces on the particle and can be expressed by the famous Navier-Stokes equation:

$$\frac{\partial \rho u_i}{\partial t}+\frac{\partial\left(\rho u_i u_j\right)}{\partial x_j}=-\frac{\partial P}{\partial x_j}+\frac{\partial}{\partial x_j}\left(2\mu\left[S_{ij}-\frac{1}{3}\delta_{ij}\frac{\partial u_k}{\partial x_k}\right]\right)+B_i \tag{3 2}$$

where P is the static pressure, μ is the dynamic viscosity, S_{ij} is the strain rate, δ_{ij} is the Kronecker delta and B_i is other body forces such as gravity, centrifugal and Coriolis forces acting on the fluid. The strain rate can be express as.

$$S_{ij}=\frac{1}{2}\left(\frac{\partial u_i}{\partial x_j}+\frac{\partial u_j}{\partial x_i}\right) \tag{3.3}$$

It is worth noting at this stage that the momentum equation given in 3.2 is balancing the various forces in the fluid flow. Even though equation 3 2 does not have any implicit or explicit reaction rate term, the flow generally behaves differently in reacting and non-reacting cases. In case of turbulent reacting flows, combustion influences the flow dynamics, which has immense influences on density, temperature and dynamic viscosity variations, which are found to be approximately 10 times higher than in non-reacting flows. Subsequently, the local Reynolds number varies much more than in non reacting situations Hence, the whole treatment of the governing equations is different and more details are provided in Chapter 6

3.1.3 Conservation of Energy

Conservation of energy can be derived from the fist law of thermodynamics and usually used to evaluate the temperature, T and enthalpy, h for a chemical reacting flow. Many forms of this equation exist, having static temperature, specific enthalpy, stagnation enthalpy or internal enthalpy as the principal variable However, in case of low-Mach number flows, it is typical to use the energy equation in terms of specific enthalpy as follows:

$$\frac{\partial \rho h}{\partial t}+\frac{\partial(\rho u_j h)}{\partial x_j}=\frac{\partial P}{\partial t}+2\mu\left(S_{ij}-\tfrac{1}{3}\delta_{ij}\frac{\partial u_k}{\partial x_k}\right)\cdot\frac{\partial u_j}{\partial x_i}+\frac{\partial}{\partial x_j}\left(\frac{\mu}{\mathrm{Pr}}\frac{\partial h}{\partial x_j}\right)+q_c \qquad (3.4)$$

where Pr is the mixture Prandtl number and $\dot{q}_c$ is the chemical source term In the above equation, the first three terms on the right hand side are contributions due to pressure work, viscous dissipation and flow dilation Thermal dissipation is written in terms of the fluid viscosity and Prandtl number. In order to simplify the system of equations, Zeldovich instability (thermal diffusion) is neglected by considering the unity Lewis number. The last term in the RHS of equation (3.4) is the chemical source term, which represents the enthalpy added to or removed from the fluid as a result of chemical reaction and is given as:

$$\dot{q}_c=\Delta h_f^o w_c Y_{fu}^o \qquad (3\ 5)$$

where Δh_f^o is the enthalpy of combustion taken as 2.22*10^6 kJ/kmol for stoichiometric propane in air mixture (Wark, 1977), Y_{fu}^o is the fuel mass fraction in unburned mixture and $\dot{w}_c$ is the chemical reaction rate

3.1.4 The Reaction Progress Variable Equation

In premixed flames, the chemical status of the mixture can be typically addressed by assuming a single step irreversible reaction between reactants and products, and a progress variable c, defined such that it is zero where the mixture is unburned and unity where it is fully burned Mathematically reaction progress variable is defined as.

$$c = 1 - \frac{Y_{fu}}{Y_{fu}^{o}} \tag{3 6}$$

where Y_{fu} is the local fuel mass fraction. The transportation equation for the reaction progress variable which balances production and destruction of the chemical reaction can be written as

$$\frac{\partial \rho c}{\partial t} + \frac{\partial \left(\rho u_j c \right)}{\partial x_j} = \frac{\partial}{\partial x_j} \left(\frac{\mu}{\mathrm{Sc}} \frac{\partial c}{\partial x_j} \right) + \dot{\omega}_c \tag{3.7}$$

where Sc is the Schmidt number considered to be equal to the Prandtl number to give a unity Lewis number and $\dot{\omega}_c$ is the mean chemical reaction rate, which is required to be modelled Modelling reaction rate in turbulent premixed flames is highly challenging due to its non-linear relation with chemical and thermodynamic states. More details about the reaction rate modelling are detailed in Chapter 5.

3.1.5 The Equation of State

Classically, many thermodynamic problems assume a chemical and thermodynamic equilibrium state to derive the gas properties from the ideal gas state equation The state equation used to close the system of equations described in previous sections and relate pressure, temperature, density as·

$$P / \rho = MRT \tag{3.8}$$

where the gas constant R is defined as R_u/M, R_u is universal gas constant and M is the molar mass (Kg/Kgmol).

3.2 Favre Averaging

In turbulent flows, the flow consists of random fluctuations of the various flow properties such as density, temperature, velocities etc. As explained in section 3.1.2, in case of reacting flows, the density is subjected to fluctuations due to thermal heat release. In order to account for these fluctuations some sort of statistical averaging is required, where all quantities are expressed as the sum of mean and fluctuating parts. Conventional Reynolds-averaging or time averaging will only consider velocity and pressure fluctuations in the fluid flow. This is appropriate for steady turbulence i.e. a turbulent flow that, on the average does not vary with time. Using Reynolds averaging in an unsteady, reacting problems leads to several complexities, which eventually involve the explicit modelling of velocity-density correlation due to high fluctuations, which is not recommended.

Alternatively, Favre averaging or mass weighted averaging accounts for density and temperature fluctuations in addition to velocity and pressure fluctuations, when the medium is a compressible fluid. In Favre averaging, all the instantaneous values of velocity and scalars except for pressure and density are decomposed into steady and fluctuating part as:

$$\phi = \tilde{\phi} + \phi'' \tag{3.9}$$

where ϕ is generic flow property, $\tilde{\phi}$ is mass-weighted mean, defined as $\tilde{\phi} = \overline{\rho\phi} / \bar{\rho}$ and ϕ'' is superimposed fluctuations. Favre mean is denoted by a tilde while the fluctuation about the Favre mean is given by double prime. Additionally, $\overline{\rho u_i''} = 0$, and $\overline{\rho\phi''} = 0$ while $\overline{\phi''} \neq 0$ and $\overline{u_i''} \neq 0$. Insertion of this decomposition into the continuous form of the governing equations with subsequent ensemble averaging, results in Favre averaged equations for the mean flow quantities as shown in next section.

3.2.1 Favre Averaged Governing Equations

Application of Favre averaging to the instantaneous governing equations shown in Eq. 3.1, 3.2, 3.4, 3.7 and 3.8 leads to the following set of equations, which have unclosed terms and must be closed by modelling

- Conservation of mass

$$\frac{\partial \bar{\rho}}{\partial t}+\frac{\partial\left(\bar{\rho}\tilde{u}_j\right)}{\partial x_j}=0 \tag{3.10}$$

- Conservation of momentum

$$\frac{\partial\left(\bar{\rho}\tilde{u}_i\right)}{\partial t}+\frac{\partial\left(\bar{\rho}\tilde{u}_i\tilde{u}_j\right)}{\partial x_j}=-\frac{\partial \bar{P}}{\partial x_i}+\frac{\partial}{\partial x_j}\left(2\bar{\mu}\left[\tilde{S}_{ij}-\frac{1}{3}\delta_{ij}\tilde{S}_{kk}\right]\right)+\tilde{B}_i-\frac{\partial \tau_{ij}}{\partial x_j} \tag{3.11}$$

$$\tilde{S}_{ij}=\frac{1}{2}\left(\frac{\partial \tilde{u}_i}{\partial x_j}+\frac{\partial \tilde{u}_j}{\partial x_i}\right) \tag{3.12}$$

$$\tau_{ij}=\bar{\rho}\widetilde{u_i'' u_j''}=\bar{\rho}(\widetilde{u_i u_j}-\tilde{u}_i\tilde{u}_j) \tag{3.13}$$

- Conservation of energy

$$\frac{\partial\left(\bar{\rho}\tilde{h}\right)}{\partial t}+\frac{\partial\left(\bar{\rho}\tilde{u}_j\tilde{h}\right)}{\partial x_j}+\frac{\partial\left(\overline{\rho u_j'' h''}\right)}{\partial x_j}=\frac{\partial \bar{P}}{\partial t}+2\bar{\mu}\left[\tilde{S}_{ij}-\frac{1}{3}\delta_{ij}\tilde{S}_{kk}\right]\frac{\partial \tilde{u}_j}{\partial x_i}+\frac{\partial}{\partial x_j}\left(\frac{\bar{\mu}}{\mathrm{Pr}}\frac{\partial \tilde{h}}{\partial x_j}\right)+\bar{q}_c \tag{3.14}$$

$$\bar{q}_c=\Delta h_f^o\bar{w}_c Y_{fu}^o \tag{3.15}$$

- Reaction progress variable equation

$$\frac{\partial \bar{\rho}\tilde{c}}{\partial t}+\frac{\partial\left(\bar{\rho}\tilde{u}_j\tilde{c}\right)}{\partial x_j}+\frac{\partial\left(\overline{\rho u_j'' c''}\right)}{\partial x_j}=\frac{\partial}{\partial x_j}\left(\frac{\bar{\mu}}{\mathrm{Sc}}\frac{\partial \tilde{c}}{\partial x_j}\right)+\bar{\omega}_c \tag{3.16}$$

- The equation of state

$$\bar{P}/\bar{\rho}=MR\tilde{T} \tag{3.17}$$

By observing the above Favre averaged governing equations, it can be noticed that some of the transport terms such as Reynolds stress, heat flux can not closed in the solution space However these terms are very important in order to close the equations and must be obtained by modelling. Some of these closing strategies are discussed in Chapter 4.

3.3 Summary

This chapter has outlined the set of instantaneous governing equations for turbulent premixed flames and the assumptions considered in evaluating them The technique of Favre averaging has been described, which generally employed in turbulent flows. List of Favre averaged governing equations has been described.

Chapter 4

Large Eddy Simulations

This chapter reviews the large eddy simulation technique and discusses the main issues that have to be accounted for before implementation Some fundamentals such as, spatial filtering technique, mathematical description of filters and decomposition of velocity components are briefly explained. The governing equations detailed in the previous chapter are spatially filtered using the box filter and are presented with unclosed terms. Various models and methodologies available to close the sub-grid scale momentum fluxes and the choice of model considered in the present simulations are discussed Simple and widely used gradient transport model is used to account for the sub-grid scalar turbulent fluxes in filtered energy and reaction progress variable equations. Sub-grid scale reaction rate can be modelled based on modelling strategies discussed in chapter 2 However a short discussion is provided in this chapter and detailed discussion can be found in chapter 5, which is dedicated to the modelling of the SGS reaction rate.

4.1 A Short Survey

Large eddy simulations (LES) have been proved to be an extremely powerful and highly reliable modelling technique for the last couple of decades, following the pioneering works of Smagorinsky (1963) and the first successful application to turbulent channel flows by Deardorff (1970). Since then, LES has been vividly used to develop underlined theories and to understand various flow problems ranging from simple to complex flow configurations such as fluid flow over bodies, turbulence-transition modelling, forecasting weather conditions, understanding the aerodynamics of vehicles and combustion dynamics etc. LES is basically a numerical technique, which separates large eddies from small eddies by the application of a low-pass filtering technique. In most turbulent flows, large eddies above certain cut-off scale are expected to be responsible for most of the transportation of mass, momentum and energy. However, the smaller eddies formed due to the interactions of these large eddies are generally expected to be isotropic in nature and eventually die out in due course, while dissipating energy fluctuations, which slightly affect the mean characteristics of the flow. This unique observation propounds to resolve separated large eddies explicitly and to model small eddies/scales that are smaller than a chosen filter width by using suitable sub-grid scale (SGS) model.

Numerical modelling of turbulent flows, usually involves defining the flow properties in terms of mean and fluctuations, corresponding to the instantaneous values associated with turbulence The way these quantities are predicted or calculated will in general calibrate the accuracy of numerical approaches LES lies between DNS, in which the whole of the turbulence spectrum is resolved, and RANS, where equations are solved in combination with a turbulence model to give a solution for the time-averaged flow-field. DNS is able to predict instantaneous and statistical flow information by resolving all flow scales ranging from the integral to Kolmogorov and provides a high degree of accuracy. However, DNS requires high-end computational resources and is restricted to simulate simple, low-Reynolds number flows. The use of the DNS technique is currently very limited to model development and will remain challenging in the foreseeable future to simulate real complex flow situations

On the other hand, RANS requires only modest resources, where all flow scales are modelled and has been applied to a wide range of flow configurations with varying degrees of success. The accuracy of a RANS simulation depends on how well the model predicts the flow and generally model parameters must be 'tuned' in order to achieve acceptable accuracy. Modelling the whole spectrum of flow turbulence scales poses a great difficulty, which eventually piloted to develop the concept of LES In LES, the large scales explicitly resolved are in fact equal to that of DNS large scales and gives both instantaneous and statistical information of the flow, while the effect of small scales are modelled. Since, only the sub-grid, dissipative scales, which are usually expected to be universal and homogeneous are modelled, the accuracy of the LES solution is less dependent on the accuracy of the model. Hence, LES demands greater computational resources than RANS, as involved in resolving the large eddies.

Despite the advancements in available computational resources, key challenges remained in LES are sub-grid scale turbulence modelling and the scale separation SGS or unresolved turbulence modelling in LES has matured to a greater level and usually modelled by the classical eddy viscosity model of Smagorinsky (1963). Smagorinsky model has been widely used in many interesting works in early stages of LES (Lilly, 1967, Deardorff, 1970, Schumann, 1975, Moin et al, 1978 and Moin and Kim, 1982) and continuing to be used with much remarkable advancements (Kirkpatrick et al., 2003 and Malalasekera et al., 2007). Several other models are also available to account for SGS turbulence For example, Yakhot and Orszag (1986) and Yakhot and Orszag (1987) proposed a model based on a renormalisation theory, details of which are not discussed here and can be found in the author's original work or in published reviews (Rogallo and Moin, 1984 and Lesieur and Metais, 1996)

The classical Smagorinsky eddy viscosity model though widely used by turbulence modellers, however, it is found to fail for various reasons. The Smagorinsky model was failed to predict the energy backscatter to the resolved scales and found to have improper asymptotic behaviour of the Smagorinsky model coefficient. These failures have been rectified by the development of the dynamic procedure (Germano et al., 1991) to calculate the Smagorinsky model coefficient using local instantaneous flow conditions, which is detailed in the following sections of this chapter. The procedure typically involves the application of a test filter to the velocity field to extract information from the resolved scales based on scale similarity ideas of Bardina et al (1980), which are then used to calculate the coefficient. Ghosal et al. (1992) and Piomelli and Liu (1995) extended this using a localized dynamic procedure to calculate the model coefficient Moin et al (1991) extended the Germano dynamic procedure for compressible flows, which has been found to be successful in predicting model coefficient and energy backscatter, and is used in the present study.

The second challenge posed by LES, is in separating the large scales from the small ones. This can be achieved by separating the scales in the exact solution by defining a cut-off length based on Ferziger (1977) and Rogallo and Moin (1984) in spectral space or applying a spatial filter of Leonard (1974) in physical space The scales that are of a characteristic size greater than the chosen cut-off length are called large or resolved scales, and others are called small or sub-grid scales (SGS). But defining the cut-off length and the scale-separation mathematical operator are very difficult tasks in LES The difficulty comes from the fact that many parameters contribute to the definition of the effective scale-separation operator. Recently, Debliquy et al. (2004) reported a novel sampling technique, replacing the traditional filtering in LES by sampling operators, which is not yet very popular, but seems to be promising in avoiding numerical errors

4.2 Spatial Filtering

Scales are filtered either in physical space or spectral space by applying a scale high-pass filter, i e. low-pass in frequency, to the exact solution. The sub-grid scale fluctuations below chosen cut-off scale are modelled by assuming isotropic The application of scale separation or spatial filtering in LES can be mathematically represented by a convolution product, first due to the Leonard (1974), can be defined for any flow variable $\phi(x,y,z,t)$ to separate large eddies from flow motions as:

$$\overline{\phi}\left(x,y,z,t\right)=\int_{v}G\left(x-x',y-y',z-z'\right)\phi\left(x',y',z',t\right)dx'dy'dz' \tag{4.1}$$

In the above equation G is a filter function, which is associated with the cut-off length $\overline{\Delta}$ in space, generally taken in between Kolmogorov and integral length scales. Eddies of size larger than $\overline{\Delta}$ are classified as large eddies, while those smaller than $\overline{\Delta}$ are classified as small eddies which need to be modelled. The integration is carried out over the entire computational domain v. Selection of the correct spatial filter in equation (4.1) is very important in LES as it must commute with differentiation, once filtered Navier-Stokes equation are developed for the flow field The most commonly used filter functions are the sharp cut-off filter (Fourier), the Gaussian filter and the box filter.

Sharp cut-off filter is applied in spectral space and generally known as ideal low-pass filter, in which flow contributions greater than cut-off wave number (k_c) are removed without affecting the contributions of small wave numbers. This filter reduces the number of degrees of freedom and also known as "projective filter" (Carati and Wray, 2000), which is defined as:

$$G(x-x')=\frac{\sin\left(k_c(x-x')\right)}{k_c(x-x')} \tag{4 2}$$

$$G(k)=\begin{cases}1 & \text{if } |k|\le k_c=\pi/\Delta \\ 0 & \text{otherwise}\end{cases} \tag{4.3}$$

Gaussian filter, which is generally applied in physical space, is widely used for homogeneous and inhomogeneous turbulence in the direction of homogeneity, often with separate cut-off scales in each direction. This filter simply transforms turbulent field u_i into a new field v_i and reduces the noise Hence, called "smooth filter" and is defined as·

$$G(x-x')=\left(\frac{6}{\pi\bar{\Delta}^2}\right)^{\frac{1}{2}}\exp\left(\frac{-6|x-x'|^2}{\bar{\Delta}^2}\right) \tag{4.4}$$

Box or top-hat filter is the other most commonly used implicit spatial filter applied in physical space, with a characteristic cut-off scale of $\bar{\Delta}$, generally defined in terms of grid spacing Since this filter wipes out the small scales by filtering operation, this is also considered as a smooth filter and typically defined as:

$$G(x-x')=\begin{cases}\frac{1}{\bar{\Delta}} & \text{if } |x-x'|\le\frac{\bar{\Delta}}{2} \\ 0 & \text{otherwise}\end{cases} \tag{4.5}$$

In the present work, top-hat filter is employed as it naturally fits into the finite volume discretization. The filtered governing equations in finite volume format can be simply rewritten by the application of equivalent box filter width of:

$$\bar{\Delta}=\left(\Delta x\Delta y\Delta z\right)^{1/3} \tag{4 6}$$

where Δx , Δy and Δz denotes the width of a computational cell in the three co-ordinates Accuracy of LES simulations depends on many factors and yet, filter width is one of the most important. Choice of the filter width is critical to resolve the appropriate amount of energy in the computational domain. For instance, Figure 4.1 illustrates the use of two different filter widths in obtaining the filtered velocity It is clear that the use of larger filter width has resulted in a smoother curve compared to that of smaller filter width. Using a large filter width may save computational time; however, Figure 4.1 confirms the loss of information while using large filter width. In a conceptual study, Pope (2004) hypothesises that the solution may reach an intermediate asymptote when the filter width lies within the inertial sub-range. However, using a box filter (4.6) simplifies the difficulty of choosing appropriate cut-off scales, yet associated with grid resolution employed.

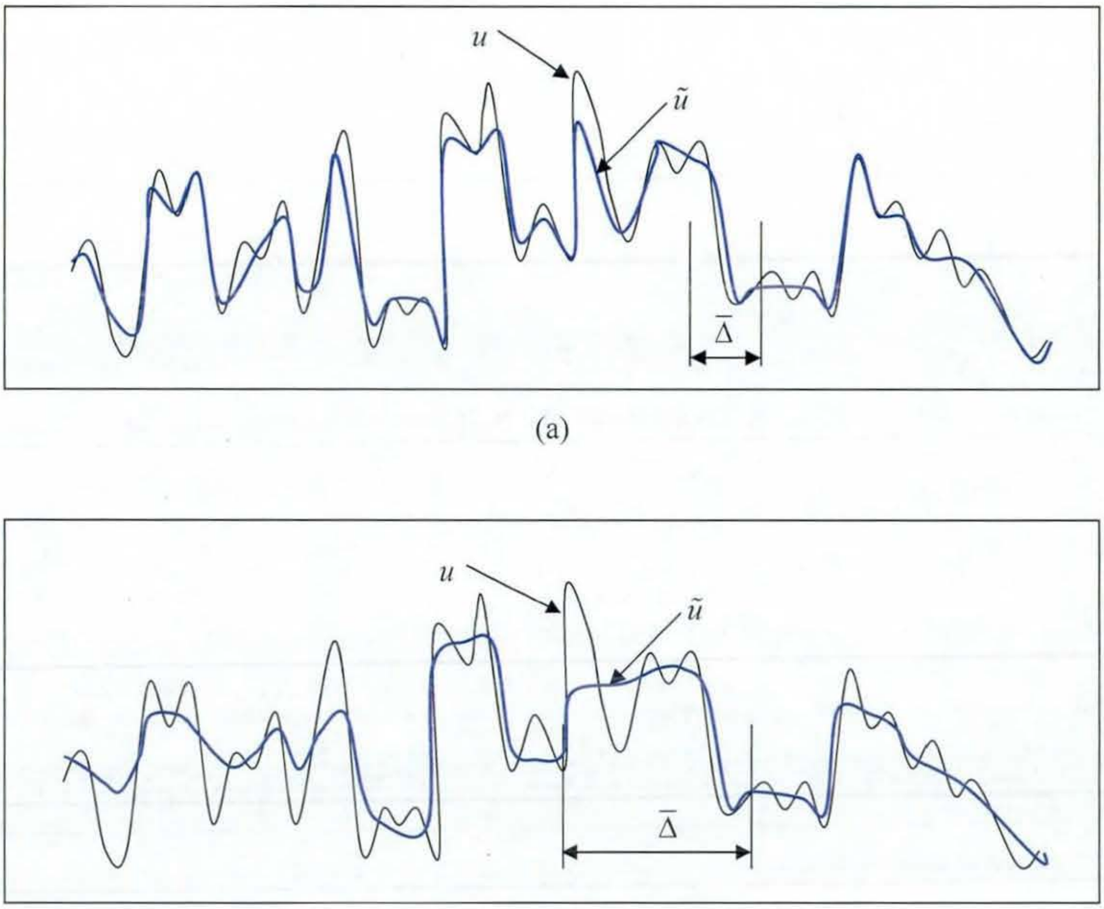

(a)

(b)

Figure 4.1 Application of top-hat filter to velocity signal *u(x)* (a) Narrow filter (b) Wide filter (reproduced from (Fröhlich and Rodi, 2002))

In general, the above filters can be classified into two categories as either implicit or explicit filters. Both filtering approaches have their own advantages and disadvantages. However, most of the LES simulations reported so far have been carried out using implicit filtering technique (Schumann, 1989), due to its simplicity and ability to fit naturally into discretization schemes employed. Another advantage is that the definition of discrete unknown amounts to an implicit filtering i.e. any scales smaller than the grid are automatically discarded. This facilitates the implicit filter to fit naturally in the numerical discretization and the notations looks similar to that of RANS technique.

Contrary to the implicit filtering, one can change filter width and grid size independently while using explicit filtering This explicit filtering has recently been advocated by several authors such as Moin (1997), Chow and Moin (2003) and Klein (2005), since it considerably reduces numerical discretization errors and there is a possibility to achieve a grid independent LES solution. On the other hand, it increases the modelling demands, since for the same number of grid points, more scales of turbulent motion have to be modelled and it is not yet completely clear, which approach is more advantageous (Lund and Kaltenbach, 1995).

4.2.1 Filtered Governing Equations

As described in section 3.2, turbulent reacting flows are associated with large density variations, which must be properly accounted for. As Jones (1993) argued, considering these sub-grid density fluctuations in filtered conservation equations seems to be possible by the application of Favre-filtering. A Favre or mass-weighted spatial filter in LES is shown in equation (4 7) and similar to equation (4.1). Application of equation (4.7) to the conservation equations yields Favre-filtered conservation equations, which look very similar to that of Favre-averaged equations shown in equations (3 10) to (3 17)

$$\bar{\rho}\tilde{\phi}(x,t)=\int_{v}\rho G(x-x')\phi(x',t)dx' \qquad (4.7)$$

- Favre-filtered continuity equation:

$$\frac{\partial\bar{\rho}}{\partial t}+\frac{\partial(\rho\tilde{u}_j)}{\partial x_j}=0 \qquad (4.8)$$

- Favre-filtered Navier-Stokes equation

$$\frac{\partial(\bar{\rho}\tilde{u}_i)}{\partial t}+\frac{\partial(\bar{\rho}\tilde{u}_i\tilde{u}_j)}{\partial x_j}=-\frac{\partial\bar{P}}{\partial x_i}+\frac{\partial}{\partial x_j}\left(2\bar{\mu}\left[\tilde{S}_{ij}-\frac{1}{3}\delta_{ij}\tilde{S}_{kk}\right]\right)+\tilde{B}_i-\frac{\partial\tau_{ij}^{sgs}}{\partial x_j} \qquad (4.9)$$

where the filtered strain rate tensor $\tilde{S}_{ij}$ is defined as

$$\tilde{S}_{ij} = \frac{1}{2}\left(\frac{\partial \tilde{u}_i}{\partial x_j} + \frac{\partial \tilde{u}_j}{\partial x_i}\right) \tag{4.10}$$

The filtered NS equation yields an unclosed term, τ_{ij}^{sgs} due to the decomposition of non-linear convective terms, which must be closed using models available from simple linear eddy viscosity based to complex second moment closures, where transport equations are solved. In LES, the term τ_{ij}^{sgs} is generally referred to as residual stress and represents the impact of the unresolved velocity components on the resolved ones Mathematically these terms arises from the non-linearity of the convection term which does not commute with the linear filtering operation. In the present work, this term is modelled by widely used, classical Smagorinsky turbulence model based on linear eddy viscosity

$$\tau_{ij}^{sgs} = \overline{\rho u_i'' u_j''} = \bar{\rho}(\widetilde{u_i u_j} - \tilde{u}_i \tilde{u}_j) \tag{4 11}$$

- Favre-filtered energy equation

$$\frac{\partial(\bar{\rho}\tilde{h})}{\partial t} + \frac{\partial(\bar{\rho}\tilde{u}_j\tilde{h})}{\partial x_j} + \frac{\partial(\overline{\bar{\rho} u_j'' h''})}{\partial x_j} = \frac{\partial \bar{P}}{\partial t} + 2\bar{\mu}\left[\tilde{S}_{ij} - \frac{1}{3}\delta_{ij}\tilde{S}_{kk}\right] : \frac{\partial \tilde{u}_j}{\partial x_i} + \frac{\partial}{\partial x_j}\left(\frac{\bar{\mu}}{\mathrm{Pr}}\frac{\partial \tilde{h}}{\partial x_j}\right) + \bar{q}_c \tag{4.12}$$

The above equation is very similar to the Favre averaged equation shown in (3 14) and needs to be closed for SGS scalar fluxes, $\overline{\bar{\rho} u_j'' h''} = \bar{\rho}(\widetilde{u_j h} - \tilde{u}_j \tilde{h})$ and filtered energy source term Modelling the scalar fluxes is quite difficult as compared to the momentum fluxes, since they are of dissipative nature Also, the SGS residual stresses shown in equation (4 11) are assumed to be isotropic, however, SGS scalar fluxes are anisotropic in nature and involve sharp variations due to large density variations.

- Favre-filtered reaction progress variable equation:

$$\frac{\partial \bar{\rho}\tilde{c}}{\partial t} + \frac{\partial(\bar{\rho}\tilde{u}_j\tilde{c})}{\partial x_j} + \frac{\partial(\overline{\rho u_j'' c''})}{\partial x_j} = \frac{\partial}{\partial x_j}\left(\frac{\bar{\mu}}{\mathrm{Sc}}\frac{\partial \tilde{c}}{\partial x_j}\right) + \bar{\omega}_c \tag{4.13}$$

The above Favre-filtered reaction progress variable equation yields two unclosed terms. The last term on the LHS of equation (4.13) is due to the scalar fluxes, similar to that of NS equation, which can be usually decomposed as $\overline{u_j'' c''} = \widetilde{u_j c} - \tilde{u}_j \tilde{c}$. This is usually modelled based on the gradient diffusion and turbulent eddy viscosity hypothesis. The second term is the filtered chemical reaction rate $\overline{\omega}_c$, which represents the SGS mean chemical reaction rate. Since the turbulent flame thickness is thinner than the LES grid, most of the turbulent combustion is sub-grid phenomenon, hence, must be accounted for appropriately.

4.3 Modelling of SGS Residual Stresses

Modelling of the SGS residual stress τ_{ij}^{sgs} has gained great deal of attention by turbulence modellers and a large collection of SGS models are available in literature. The primary concern of any SGS model is to account for the local and instantaneous momentum transportation effects of small scales on large scales and vice versa (generally known as energy back-scatter in certain flows). However, it may not be always necessary for the SGS models to mimic the detailed interaction between resolved and small scales, yet essential to expect correct representation of energy at the correct location. A few important modelling strategies are briefly outlined in the following sections.

4.3.1 Residual Stress Decomposition

It is clear from equation (4.9) that the sub-grid stress, τ_{ij}^{sgs} resulted due to the commutation of Favre filtering on convective term of NS equation, which must be closed by modelling as a function of known resolved values. Ferziger (1982) identified that the models developed following Leonard decomposition of velocity field into mean and fluctuating quantities, are effective and efficient in accounting sub-grid scale effects. Hence, velocity component in i direction can be decomposed as:

$$u_i = \tilde{u}_i + u_i' \tag{4.14}$$

where u_i' is the sub-grid scale component of u_i. Following the above, decomposition of the $\widetilde{u_i u_j}$ yields:

$$\widetilde{u_i u_j} = \widetilde{\tilde{u}_i \tilde{u}_j} + \widetilde{u_i' \tilde{u}_j} + \widetilde{\tilde{u}_i u_j'} + \widetilde{u_i' u_j'} \tag{4.15}$$

Rearranging the above equation as

$$\widetilde{u_iu_j} = \tilde{u}_i\tilde{u}_j + L_{ij} + C_{ij} + R_{ij} \tag{4.16}$$

where

$$L_{ij} = \widetilde{\tilde{u}_i\tilde{u}_j} - \tilde{u}_i\tilde{u}_j,\ C_{ij} = \widetilde{u'_i\tilde{u}_j} + \widetilde{\tilde{u}_iu'_j} \text{ and } R_{ij} = \widetilde{u'_iu'_j} \tag{4.17}$$

Now we can rewrite equation (4.11) as

$$\tau_{ij}^{sgs} = \widetilde{u_iu_j} - \tilde{u}_i\tilde{u}_j = \bar{\rho}(L_{ij} + C_{ij} + R_{ij}) \tag{4.18}$$

In the above equation, L_{ij} is the Leonard stress, C_{ij} is the cross stress and R_{ij} is the sub-grid scale Reynolds stress. The Leonard stress represents interactions between resolved scales that results in sub-grid scale contributions The cross terms represent interactions between resolved and unresolved scales, whereas the sub-grid scale Reynolds stress represent interaction between the small unresolved scales.

Various approaches (Smagorinsky, 1963, Lilly, 1967, Deardorff, 1970, Schumann, 1975 and Bardina et al., 1980) have been delineated in literature to model the above stress terms, based on either explicit or implicit filtered resolved values Among the available, representation of these turbulent stresses through the use of simplified linear models based on the eddy viscosity approach are well known and widely used The classical model of this category introduced by Smagorinsky (1963) is, from a historical point of view, and subject of many changes later on. The introduction of the dynamic modelling concept by Germano et al (1991) has spurred significant progress in the sub-grid scale modelling in non-equilibrium flows (see section 4.5.4). In dynamic modelling, model coefficients are determined as the calculation progresses, based on the energy contents of the smallest resolved scales rather than input a priori as standard Smagorinsky model. A detailed discussion of this method is given in the following section.

4.3.2 The Smagorinsky Model

Representation of the turbulent stresses using scalar eddy viscosity is a well-known approach since its introduction by Boussinesq (1877). Smagorinsky (1963) was the first to propose a similar model to Boussinesq for turbulent stresses in LES, which is still widely employed in turbulence modelling. Smagorinsky model assumes that the anisotropic part of the residual stress tensor is inline and proportional to the anisotropic part of the resolved strain tensor, while the normal stresses are isotropic. This model assumes that the scales in unresolved turbulence are approximately in equilibrium with energy cascaded down from the large scales. Accordingly, the SGS stress tensor, τ_{ij}^{sgs} can be modelled as:

$$\tau_{ij}^{sgs} - \tfrac{1}{3}\delta_{ij}\tau_{kk}^{sgs} = -2\bar{\mu}_{\mathrm{SGS}}\left(\tilde{S}_{ij} - \tfrac{1}{3}\delta_{ij}\tilde{S}_{kk}\right) \tag{4.19}$$

where μ_{SGS} is the eddy viscosity, which can be expressed as a function of the filter size and the strain rate as:

$$\mu_{\mathrm{SGS}} = \bar{\rho} C \bar{\Delta}^2 \left|\tilde{S}\right| \tag{4.20}$$

where $\left|\tilde{S}\right| = \sqrt{2\tilde{S}_{ij}\tilde{S}_{ij}}$ and C is a dimensionless coefficient and often used to be specified in classical models as the Smagorinsky coefficient $C_s = \sqrt{C}$. The isotropic part of the SGS stress tensor in equation (4.19), τ_{kk}^{sgs} is modelled using the relation of Yoshizawa (1986) as

$$\tau_{kk}^{sgs} = 2\bar{\rho} C_I \bar{\Delta}^2 \left|\tilde{S}\right|^2 \tag{4.21}$$

where the model coefficient C_I is very small and usually expected to be around 0.01. The classical Smagorinsky model is quite simple and widely used, despite certain drawbacks. One of the major drawbacks is a prior requirement to specify the model coefficient, though it is dependent on local flow conditions. For instance, Lilly (1966) suggested a value of $C_s \approx 0.23$ for homogeneous isotropic turbulence, Deardorff (1970) used a value of 0.1 in turbulent channel flow simulations, where as for the same flows Piomelli et al. (1988) found 0.0065 as an optimal value. Rogallo and Moin (1984) and Germano et al. (1991) identified that C_s value ranges between 0.1 and 0.25 and there is no general agreement on how it influences/depends on the flow.

Secondly, the model does not predict correct asymptotic behaviour near a wall and requires ad-hoc treatment. Simulations of transitional wall boundary flows show that the model over-damps the flow, leading to incorrect prediction of growth rates of initial disturbance. Due to the dissipative nature of the model, Piomelli et al. (1990) identified that the model over predicts dissipation by 35% in laminar channel flows. Also it has been identified (Piomelli et al., 1990) that it fails to predict the energy transfer from small to large scales, which is generally known as energy back-scatter and important in certain flows. Finally, the model does not vanish in a fully resolved “laminar" flow even though $\widetilde{u_i u_j} = \tilde{u}_i \tilde{u}_j$.

In order to compensate these drawbacks, several researchers employed ad-hoc procedures (Ferziger, 1993, Fureby et al., 1997 and Fureby, 1998) to calculate the appropriate model coefficient and found to achieve good confidence in using Smagorinsky model. Motivated by its simplicity, Germano et al. (1991) developed a dynamic procedure to calculate the model coefficient using local instantaneous flow conditions. The procedure involves the application of a test filter (^) to the equations and to extract information from the smallest resolved scales, which is then used to calculate the coefficient. This procedure was found to be a great success in predicting the correct model coefficient and extended to compressible flows by Moin et al. (1991).

4.3.3 The Dynamic SGS Flow Model

The limitations outlined in the above section, while using Smagorinsky model inspired Germano et al. (1991) to propose the dynamic procedure to calculate C_s based on local flow conditions and similarity ideas of Bardina et al. (1980). Later, Moin et al. (1991) extended this procedure for compressible flows, which is used in the present simulations to calculate the model coefficient. The central idea of the dynamic procedure is in using information from the smallest resolved scales to model the sub-grid scales effects. In order to obtain information from the smallest resolved scales, a test filter, is generally represented by $\hat{\bar{\Delta}}$, which is larger than the grid filter, $\bar{\Delta}$, and is applied to velocity field. Application of the test filter to the filtered Navier-Stokes equations results in sub-test-scale stress tensor analogous to sub-grid-scale stress tensor.

$$T_{ij} = \widehat{\widetilde{u_i u_j}} - \hat{\tilde{u}}_i \hat{\tilde{u}}_j \qquad (4.22)$$

Applying the test filter to the equation (4.14) and rearranging will result in the resolved turbulent stress as:

$$\mathcal{L}_{ij} = \widehat{\tilde{u}_i \tilde{u}_j} - \hat{\tilde{u}}_i \hat{\tilde{u}}_j \qquad (4.23)$$

The resolved turbulent stresses also known as Leonard stress, represent the contribution of the Reynolds stresses by scales whose length is intermediate between the test and grid filter width Identifying the relation between equations (4.18), (4.22) & (4 23) and rearranging will result in what is called Germano identity.

$$\mathcal{L}_{ij} = T_{ij} - \hat{\tau}_{ij}^{sgs} \tag{4 24}$$

The Germano identity in the above equation (4.24) can be used to compute, explicitly, the sub-grid scale stresses at the test and grid levels, T_{ij} and τ_{ij}^{sgs}.

$$T_{ij} - \tfrac{1}{3}\delta_{ij}T_{kk} = -2\bar{\rho}C\hat{\Delta}^2 \,|\hat{\tilde{S}}|\left(\hat{\tilde{S}}_{ij} - \tfrac{1}{3}\delta_{ij}\hat{\tilde{S}}_{kk}\right) = -C\alpha_{ij} \tag{4.25}$$

$$\tau_{ij}^{sgs} - \tfrac{1}{3}\delta_{ij}\tau_{kk}^{sgs} = -2\bar{\rho}C\bar{\Delta}^2 \,|\tilde{S}|\left(\tilde{S}_{ij} - \tfrac{1}{3}\delta_{ij}\tilde{S}_{kk}\right) = -C\beta_{ij} \tag{4.26}$$

where the traceless tensors α_{ij} and β_{ij} are:

$$\alpha_{ij} = -2\bar{\rho}\hat{\Delta}^2 \,|\hat{\tilde{S}}|\left(\hat{\tilde{S}}_{ij} - \tfrac{1}{3}\delta_{ij}\hat{\tilde{S}}_{kk}\right) \tag{4.27}$$

$$\beta_{ij} = -2\bar{\rho}\bar{\Delta}^2 \,|\tilde{S}|\left(\tilde{S}_{ij} - \tfrac{1}{3}\delta_{ij}\tilde{S}_{kk}\right) \tag{4 28}$$

Substituting equations (4 25) & (4.26) in the anisotropic part of equation (4.24) gives:

$$\mathcal{L}_{ij}^{a} = C\left(\hat{\beta}_{ij} - \alpha_{ij}\right) \tag{4.29}$$

To obtain a scalar equation for the model coefficient *C*, the above equation is contracted with $\tilde{S}_{ij}$ tensor as:

$$C = \frac{\mathcal{L}_{ij}^{a}\tilde{S}_{ij}}{\left(\hat{\beta}_{ij} - \alpha_{ij}\right)\tilde{S}_{ij}} \tag{4 30}$$

From the above equation one can obtain *C*, however, observing the fact that the terms within parentheses in equation (4 30), can become zero, which may create ill-posed problem. To improve this, *C* was considered to vary in only the *y*-direction, normal to the wall. Since, equation (4.30) is a tensor, it can only be satisfied in some average sense, which can be carried in the *y*-direction where the test filter is not applied. This results in an expression for *C* as:

$$C(y,t)=\frac{\langle \mathcal{L}^{a}_{ij}\tilde{S}_{ij}\rangle_{y}}{\langle \hat{\beta}_{ij}\tilde{S}_{ij}\text{-}\alpha_{ij}\tilde{S}_{ij}\rangle_{y}} \tag{4.31}$$

Since, equation (4.29) is a set of five independent equations, a single value of C is seldom to be obtained simultaneously. To alleviate this situation, Lilly (1992) proposed a tensor M_{ij} instead $\tilde{S}_{ij}$ in equation (4 29), which locally minimizes the sum of the square of residuals as:

$$\mathcal{L}_{ij}-\tfrac{1}{3}\delta ij\mathcal{L}_{kk}=2CM_{ij} \tag{4.32}$$

where $M_{ij}=(\hat{\overline{\Delta}}/\overline{\Delta})^{2}\hat{\overline{\rho}}\left|\hat{\tilde{S}}\right|\hat{\tilde{S}}_{ij}-\widehat{\overline{\rho}\left|\tilde{S}\right|\tilde{S}_{ij}}$, which is obtained by explicitly evaluating the stresses at test scale and comparing locally by subtracting the test-scale average of equation (4.26) from equation (4 25) Re-arranging equation (4.32) for C yields:

$$C=-\frac{\mathcal{L}_{ij}M_{ij}-\frac{1}{3}\mathcal{L}_{ll}M_{mm}}{2\overline{\Delta}^{2}\left(M_{ij}M_{ij}-\frac{1}{3}M_{ll}M_{mm}\right)} \tag{4.33}$$

Accordingly, the Smagorinsky model coefficient can be calculated using the dynamic procedure at every spatial grid point and time by considering the localised flow conditions, which has the correct behaviour near to solid wall and in laminar flow and also allows for energy back-scatter However, the model coefficient found to fluctuate in space and time, and some form of averaging is usually required to avoid stability problems. Typically, L_{ij} and M_{ij} are averaged in spatially homogeneous directions in space However, this requires the flow to have at least one homogeneous direction. However, if there is no direction to perform averaging, alternative approaches may be used such as localised models of Ghosal et al. (1992) and Piomelli and Liu (1995), dynamic mixed models of Zang et al. (1993) and relaxation procedure of Breuer and Rodi (1994) i.e. co-efficient from previous time step are used.

4.3.4 Scale Similarity Models

The concept of the scale similarity was first proposed by Bardina et al (1980) and expected to overcome the aforementioned drawbacks of eddy viscosity models. The key idea of scale similarity is to identify and correlate the smallest resolved scales to the sub-grid scales of the flow. Filtering the decomposed velocity component in equation (4.14) yields

$$\overline{u'_i} = \overline{u}_i - \overline{\overline{u}}_i \tag{4.34}$$

This can be reasonably estimated equal to the largest contributions of u'_i and the smallest contributions of $\overline{u}_i$. Furthermore, this equality will facilitate velocity decompositions as.

$$\overline{u'_i u'_j} \approx \overline{u'_i}\,\overline{u'_j} \text{ and } \overline{u'_i \overline{u}_j} \approx \overline{u'_i}\,\overline{\overline{u}}_j \tag{4.35}$$

Which in turn facilitates to model the residual stress given in equation (4.18) as:

$$\tau_{ij}^{sgs} = \rho\left(\underbrace{\overline{\overline{u}_i\overline{u}_j} - \overline{\overline{u}}_i\overline{\overline{u}}_j}_{L_{ij}} + \underbrace{K_C[(\overline{u}_i - \overline{\overline{u}}_i)\overline{\overline{u}}_j + (\overline{u}_j - \overline{\overline{u}}_j)\overline{\overline{u}}_i]}_{C_{ij}} + \underbrace{K_R(\overline{u}_i - \overline{\overline{u}}_i)(\overline{u}_j - \overline{\overline{u}}_j)}_{R_{ij}}\right) \tag{4.36}$$

where the model coefficients K_C and K_R in the above equation should be carefully chosen such that, the expression observes Galilean invariance (Zang et al., 1993, Salvetti and Banerjee, 1995 and Horiuti, 1997). The scale similarity models (SSM) allows back-scatter, i.e. transfer of energy from small to large scales and does not impose alignment between the SGS stress tensor and the strain rate. Piomelli et al. (1996) identified that the scale similarity models in conjunction with dynamic procedure perform quite well for low-order finite-difference or finite-volume methods.

4.4 Modelling of SGS Scalar Fluxes

Modelling sub-grid scalar fluxes in turbulent reacting flames is highly challenging due to their non-linear relation with chemical and thermodynamic states. The major difficulty in modelling is due to the anisotropic behaviour of scalar fluxes. This is strongly affected by the turbulent velocity fields, through the large increase in specific volume and viscosity, which causes large temperature rise in reacting flows. Modelling could be further complicated due to the large pressure gradients and density variations associated with heat release, which may cause non-gradient transport (NGT) or counter gradient diffusion.

Several models are available in literature to account for SGS scalar fluxes, such as simple gradient transportation assumption, scale similarity model (Fureby and Moller, 1995), linear eddy model (LEM) (Kerstein, 1991) etc In a recent LES analysis by Boger and Veynante (1999) of DNS database, Boughanem and Trouvé (1998), revealed that the gradient or counter gradient diffusion of scalar fluxes are observed similar to RANS. However, unresolved scalar fluxes are identified to be less in LES, which supports that the use of simple model will have fewer consequences on the end solution. To support this observation, Boger and Veynante (2000) performed LES of turbulent premixed flames on a V-shaped flame holder using simple gradient transport assumption and able to recover counter gradient transport at resolved scales without any extra effort, which is not the situation in RANS. Hence, in the present simulations the simple gradient transport model in equations (4.12) & (4 13) for scalar fluxes is adopted.

$$\bar{\rho}\overline{u_j''h''} = \frac{\bar{\mu}_{\mathrm{SGS}}}{\mathrm{Pr}_t}\frac{\partial \tilde{h}}{\partial x_j} \tag{4.37}$$

$$\bar{\rho}\overline{u_j''c''} = \frac{\bar{\mu}_{\mathrm{SGS}}}{\mathrm{Sc}_t}\frac{\partial \tilde{c}}{\partial x_j} \tag{4 38}$$

where Pr_t is the turbulent flow Prandtl number, Sc_t is the turbulent flow Schmidt number and $\bar{\mu}_{\mathrm{SGS}}$ is the SGS eddy viscosity.

4.5 Modelling of Mean Chemical Reaction Rate

Modelling the chemical reaction rate is another crucial task in LES of premixed turbulent combustion, as it is generally involved in complex thermo-chemical-turbulence interactions. One major difficulty is to predict the random, non-linear behaviour of chemical reaction rate as a function of available scalar variables. Another difficulty especially in LES is the laminar flame thickness, which is typically thinner than the characteristic flow turbulence length scale much smaller than a typical LES filter width, $\bar{\Delta}$. Hence it is a prerequisite of any SGS combustion model in LES, to address the above issue with an accurate, yet computationally efficient model. One way of modelling the filtered mean chemical reaction rate term is by solving transport equations of the detailed or reduced chemical kinetic mechanism of the fuel. This generally includes tens of species and several hundreds of elementary reactions Solving these transport equations directly in RANS itself are quite complex and solving them in LES is unthinkable. However, several alternative strategies are available to implement detailed chemistry effects. These include techniques such as, the "skeletal mechanism" obtained due to the elimination of inconsequential species from detailed chemical mechanism, "dimension reduction techniques" due to low-dimensional manifold systems such as QSSA (quasi-steady state assumption), RCCE (rate-controlled constrained equilibrium) and FPI (flame propagation of intrinsic low-dimensional manifold), "storage and retrieval systems" such as look-up table, repro-modelling, artificial neural network (ANN), in situ adaptive tabulation (ISAT) and piecewise reusable implementation of solution mapping (PRISM) and finally, adaptive chemistry technique. All of the above techniques required extraordinary computational resources

On the other hand, mean chemical reaction rate term can be simply modelled by considering a single step, irreversible chemistry, which is widely used due to the long turbulent time scales compared to chemical time scale (Bray, 1980) in turbulent premixed combustion applications and greatly reduces the complexity of the whole system of equations. Several modelling strategies are available and briefly delineated in section 2 2 For example the laminar flamelet based models gained wide attention due to their flexibility in decoupling chemistry from turbulence. There has been some recent interest on FSD models as they are fundamentally based on the laminar flamelet concepts, which view the reaction zone as a collection of propagating reaction layers thinner than the smallest scales of turbulence and where the laminar flame structures propagate locally at the laminar burning velocity. The FSD, defined as the local flame surface area per unit volume and may be computed using either an algebraic model or by solving a transport equation for the FSD. Algebraic models are simple, yet well established and are similar to the Bray-Moss-Libby (BML) approach in the context of RANS. These models are considered in the present study to account for the filtered mean chemical reaction rate term with a dynamic formulation for the flame surface density More details of this model are described in Chapter 5.

4.6 Summary

This chapter summarises use of LES concept for turbulent premixed flames. A brief history of the LES and the pioneering developments since its first use by Deardorff (1970) has been detailed. The spatial filtering technique, which distinguishes LES from other modelling techniques, has been discussed with a variety of spatial filters Advantages of implicit filtering over explicit filtering was briefly discussed and applied to the flow governing equations described in the previous chapter. Various modelling strategies to close the resulted unclosed terms from Favre-filtered governing equations were discussed. Especially for momentum fluxes, various classical and dynamic modelling techniques/strategies were discussed. Suitability of the simple non-gradient transportation (NGT) strategy for SGS scalar fluxes in scalar equations has been discussed in LES. Various approaches available to close the mean chemical reaction rate term in the filtered reaction progress variable equation were briefly discussed More details of chemical reaction rate model development will be discussed in the next chapter.

Chapter 5

Flame Surface Density Modelling

Following recent efforts of Knikker et al. (2004) in developing a dynamic formulation for the FSD of premixed turbulent flames, the present work is carried out by implementing and validating a novel dynamic flame surface density (DFSD) model in an existing LES code PUFFIN (Kirkpatrick, 2002) The FSD models are well established in the context of LES and are the subject of many interesting developments. In this chapter, brief introduction of the flamelet and flame surface density concepts are outlined. A short survey of available algebraic models and the exact transport equation of FSD in LES are detailed in section 5.1. Details of a simple algebraic FSD model derived based on DNS data and its use with a novel self-scaling model coefficient are explained in section 5 2. Section 5 3 presents the concept and development of the dynamic FSD (DFSD) model, together with the dynamic evaluation of the fractal dimension and the flame wrinkling theory of Weller et al. (1998). Finally, section 5.4 provides brief details of the fractal concept and the empirical and dynamic fractal models used in the present simulations to calculate the fractal dimensions of turbulent premixed flames Available outer and inner cut-off scale models and their choice in the present work are also presented and discussed

5.1 Introduction

The concept of FSD in RANS is very well established but relatively new in LES framework The FSD models proposed in LES are very similar to that of RANS and can be derived from the laminar flamelet fundamentals. Based on the laminar flamelet assumptions for many turbulent premixed applications, the reaction zone/flame front is viewed as a collection of asymptotically thin wrinkled, propagating layers between fresh and burnt gases. Within the limit of high Damkohler number, these layers can be assumed to propagate at local laminar flame speed. Therefore, these layers can be considered as laminar flamelets. The concept of the laminar flamelets in turbulent premixed combustion greatly reduces the complexity of the problem by decoupling turbulence from chemistry. Following the laminar flamelet concept, the wrinkling of the flame front surface by turbulence can be described by the mean flame-surface area per unit volume i.e. flame surface density, Σ. Therefore, the filtered mean chemical reaction rate in equation (4.13) can be expressed as a function of the FSD, Σ as follows:

$$\bar{\dot{\omega}}_c = R\bar{\Sigma} = \langle \rho_u S_d \rangle_s \bar{\Sigma} \qquad (5.1)$$

In the above equation, R is expressed as $\langle \rho_u S_d \rangle_s$, which is the surface averaged-Favre filtered displacement speed of the propagating flame into the fresh gases. Assuming that the individual flamelet is propagating with the laminar flame speed u_L, into the fresh gases having density ρ_u, the mean reaction rate can be modelled as $\rho_u u_L$.

The filtered FSD, $\bar{\Sigma}$ in the above equation is accounted for via either solving a transport equation, known as Σ-equation or by using an empirical algebraic expression. The Σ-transport equation was first formulated by Marble and Broadwell (1977) and further developed by Pope (1988). The transport equation developed by Pope (1988) is based on filtering the basic equation with a filter width sufficiently larger than the grid spacing such that the thin turbulent dynamic premixed flame is smeared out sufficiently to be resolved on a LES grid. Recently, Hawkes and Cant (2001) provided a transport equation for FSD, similar to the typical RANS equation, which includes resolved contributions neglected by the typical RANS equations. However, this equation has resulted in several unclosed terms, leading to excessive computational requirements (reaching DNS limit for fully resolved flows (Pitsch, 2005)) during computation. The exact, unclosed equation proposed by Hawkes and Cant (2001) is presented below and its details are available in the original publication.

$$\frac{\partial \Sigma}{\partial t} + \frac{\partial(\tilde{u}_i \Sigma)}{\partial x_i} + \frac{\partial((\overline{(u_i)_s} - \tilde{u}_i)\Sigma)}{\partial x_i} = \overline{(a_T)_s}\Sigma - \frac{\partial}{\partial xi}(\overline{(wN_i)_s}\Sigma) + \overline{\left(w\frac{\partial N_k}{\partial x_k}\right)_S}\Sigma \qquad (5.2)$$

Alternatively, FSD can be modelled by an empirical algebraic model, by considering the balance between production and destruction of flame surface density in the transport equation. Boger et al. (1999) were the first to develop a simple algebraic model for FSD in LES, based on extensive DNS database of infinitely thin planar flame using a Gaussian filter This model is given in equation (5 3), which is simple and very similar to the BML model in the context of RANS. This model has been used by several researchers to model turbulent premixed flames (see for example; Kirkpatrick et al (2003), Masri et al (2006) and Richard et al. (2007))

$$\overline{\Sigma} = 4\frac{\tilde{c}(1-\tilde{c})}{L_{\Sigma}} \tag{5 3}$$

Here $\tilde{c}$ is the filtered reaction progress variable and L_{Σ} refers to the flame wrinkling scale formulated as $(\overline{\Delta}/\beta)$. The model coefficient, β in the above equation can be either considered as a constant or modelled based on a flame wrinkling factor

Charlette et al (1999) proposed a model similar to BML and EBU expression, including a term to account for the resolved flame surface density as

$$\overline{\Sigma} = |\nabla\overline{c}| + a\Gamma_k\left(\frac{\delta_L}{\overline{\Delta}}, \frac{\sqrt{2k/3}}{u_L}\right)\frac{\sqrt{k}}{u_L}\frac{\tilde{c}(1-\tilde{c})}{\overline{\Delta}} \tag{5.4}$$

where Γ_k is the efficiency function of Intermittent Turbulence Net Flame Stretch (ITNFS) model of Meneveau and Poinsot (1991), k is the sub-grid kinetic energy and a is a model constant.

Angelberger et al., (1998) proposed another model based on sub-grid RMS fluctuations and expressed as·

$$\overline{\Sigma} = |\nabla\overline{c}| + a\Gamma_k|\nabla\overline{c}|\left(\frac{\delta_L}{\overline{\Delta}}, \frac{u'}{u_L}\right)\frac{u'}{u_L} \tag{5 5}$$

Weller et al. (1998) and Tabor and Weller (2004) used an additional equation to solve for flame surface wrinkling factor, Ξ in their work as·

$$\Xi = \frac{\overline{\Sigma}}{|\nabla\overline{b}|} \tag{5 6}$$

where $|\nabla\overline{b}|$ is the area of grid scale surface and the flame surface density is derived using conditional filtering method.

Recently, Knikker et al (2004) proposed a dynamic flame surface density model following their a priori work (Knikker et al., 2002) in deriving a mathematical formulation for LES. Although this model was never implemented numerically, it was tested on the data extracted from experimental OH images and found to work well with LES. The work presented in this thesis is carried out by employing two different models for $\overline{\Sigma}$, the first is a simple algebraic FSD (AFSD) model (i e equation 5 3) and the second is a dynamic FSD (DFSD) model described in the following sections. Details of the numerical implementation of the novel DFSD model are provided in Chapter 6

5.2 The Algebraic Flame Surface Density (AFSD) Model

As mentioned earlier, Boger et al. (1999) were first to deduce an algebraic expression for FSD for use in LES codes. A 3-D DNS database developed by Boughanem and Trouvé, (1998) has been used for decaying isotropic, homogeneous turbulence, with an assumption of evolving thin flame front into the fresh gases. The key idea behind their expression is in identifying the sub-grid surface density, $\overline{\Sigma}$ (i e, the sub-grid flame surface per unit volume) of the flame surface defined by $c = c^*$ and the conditionally averaged displacement speed of the propagating flame of the surface c^* into the fresh gases, $\overline{\langle R\rangle}_s$ as:

$$\overline{\Sigma} = \int_{-\infty}^{\infty} |\nabla \overline{c}\, |\delta(c-c^*)G(x-x')dx' \tag{5.7}$$

$$\overline{\langle R\rangle}_s = \langle \rho_u S_d \rangle \tag{5 8}$$

A generalised sub-grid flame surface density and displacement speed, which do not depended on specific c^* isosurface are defined as:

$$\Sigma_{gen} = \int_0^1 \overline{\Sigma}\, dc^* = \overline{|\nabla c\,|} \tag{5 9}$$

$$\langle R\rangle_s = \frac{1}{\Sigma_{gen}} \int_0^1 \overline{\langle R\rangle}_s dc^* = \frac{\overline{R\,|\nabla c\,|}}{\Sigma_{gen}} \tag{5 10}$$

Following the laminar flamelet concepts, assuming the reaction zone to be very thin, the sub-grid flame surface density $\overline{\Sigma}$ of $c{=}c^*$ isosurface is no more dependent on isosurface chosen and becomes equal to generalised flame surface density Σ_{gen}. The displacement speed $\langle R\rangle_s$ can be approximated as $\rho_u u_L$ considering, that the laminar flamelets are steadily propagating Boger et al. (1999) have validated this approximation for turbulent premixed combustion by filtering the DNS data. The laminar flame speed in the above equation is calculated by the following expression of Metghalchi and Keck (1980) and

Metghalchi and Keck (1982), which accounts the effects of local pressure and temperature and is given as:

$$u_L = u_L^0 \left(\frac{T_R}{T_o}\right)^{\alpha_1} \left(\frac{P}{P_o}\right)^{\beta_1} \tag{5 11}$$

where u_L^0 is the reference or un-strained laminar burning velocity taken as 0 45 m/s for stoichiometric propane/air mixture, T_o and P_o are reference temperature and pressure 298 15 K and 1.01 bar respectively, T_R is the reactant temperature, and α_1, β_1 are constants calculated from the following expressions of Metghalchi and Keck (1980) and Metghalchi and Keck (1982)

$$\alpha_1 = 2.18 - 0.8(\phi - 1\ 0) \text{ and } \beta_1 = -0\ 16 + 0\ 22(\phi - 1\ 0) \tag{5 12}$$

where ϕ is the mixture equivalence ratio. However, Poinsot et al. (1995) identified that the process of filtering will average the effects of variation in flame strain and curvature on the flame speed.

Boger et al (1999) chose $c^* = 0.8$ to define the flame surface and introduced a reduced progress variable, c_{red} as 0 if $c \le c^*$ otherwise 1. Accordingly, they extracted a simple expression for $\bar{\Sigma}$ from DNS as

$$\bar{\Sigma} = 4\alpha_2 \frac{\tilde{c}_{red}\left(1 - \tilde{c}_{red}\right)}{\bar{\Delta}} \tag{5.13}$$

where α_2 is the model coefficient, analytically derived by assuming infinitely thin flame front (i e. $|\nabla c| = \delta(c - c^*)$) as:

$$\alpha_2 = \sqrt{\frac{6}{\pi}}\Xi \tag{5.14}$$

In the above expression, α_2 becomes 1.4 for a unity sub-grid scale flame wrinkling factor, Ξ. Alternatively, Boger et al (1999) proposed another expression similar to equation (5.13) by replacing c_{red} with c, which is the instantaneous value of the reaction progress variable as:

$$\bar{\Sigma} = 4\beta \frac{\tilde{c}\left(1 - \tilde{c}\right)}{\bar{\Delta}} \tag{5.15}$$

where β is a model coefficient which has a value equal to α_2 in equation (5.13) for sufficiently large values of $\bar{\Delta}/L_f$ i e infinitely thin flames compared to grid width. The above expression has a similar format as the Bray-Moss-Libby (BML) expression for flame surface density in RANS (Bray et al, 1989) and only accounts for the so called resolved contributions. The ratio $\Delta/4\beta$ represents the wrinkling length scale of the sub-grid flame surface.

In general, the model coefficient β is not universal and known to be dependent on many physical parameters such as grid resolution, turbulence levels and chemistry. A range of values for the model coefficient β, in RANS and LES ranging from 1 0 to 2.6 can be found in literature However, choosing a constant value for β resembles the Eddy-Break-Up (EBU) model in RANS, which is inappropriate and alters the solution based on model coefficient To avoid the problems associated with selecting value for β, one of the following two options may be followed.

a) Choosing a constant value either by doing parametric studies based on appropriate filter width and chemistry or iterating/tuning in order to get the qualitative agreement with experimental values.
b) Deriving a dynamic or self-scalable model for the model coefficient β using local flame characteristics.

As a first approximation, one can use a constant value for β following first option. However, fine tuning to achieve desired results in LES is inappropriate Hence, the present study has been carried initially using a constant value for β from the parametric studies of Kirkpatrick (2002) and Masri et al (2006) and later derived a simple expression capable to self-scale model coefficient based on local flow conditions as shown in next section

5.2.1 Dynamic Evaluation of the Model Coefficient β

The basic idea here is to derive the model coefficient β from filtered reaction progress variable at test filter by applying Germano identity (4.24) to equation (5.15) However, following the work of Charlette et al (2002), it has been identified that the model coefficient in equation (5.15) is multiplicative in nature and fails for the application of Germano identity (Germano et al, 1991). Considering equations (5.1) and (5.15) for mean SGS chemical reaction rate and defining γ as a ratio of test filter to grid filter (i e. $\hat{\bar{\Delta}}/\bar{\Delta}$)

such that the test filter $\hat{\bar{\Delta}}$ is greater than grid filter $\bar{\Delta}$ Applying test filter to flame surface density (equation 5 15) using the Germano identity (Germano et al , 1991) and averaging over the volume leads to

$$\left\langle \widehat{4\rho_u u_L \beta \frac{\tilde{c}(1-\tilde{c})}{\bar{\Delta}}} \right\rangle = \left\langle 4\rho_u u_L \beta \frac{\hat{\tilde{c}}(1-\hat{\tilde{c}})}{\hat{\bar{\Delta}}} \right\rangle \tag{5.16}$$

Assuming that β is a model coefficient in the volume over which averaging has been performed and solving for β reduces to.

$$4\rho_u u_L \beta \left\langle \frac{\widehat{\tilde{c}(1-\tilde{c})}}{\bar{\Delta}} \right\rangle = 4\rho_u u_L \beta \left\langle \frac{\hat{\tilde{c}}(1-\hat{\tilde{c}})}{\hat{\bar{\Delta}}} \right\rangle \tag{5.17}$$

From the above equation, it is apparent that β cancels out from each side of the equation (5 17) and the Germano identity becomes ineffective to determine β

5.2.2 Modelling β using a Flame Wrinkling Factor

The model coefficient β can be modelled using a wrinkling flame factor as observed in equation (5.14) rather choosing unity The sub-grid flame wrinkling factor Ξ in equation (5 14) is defined as the ratio between the flame surface density and its projection in the normal direction of the flame propagation (Knikker et al , 2004). Identifying the flame surface as a fractal surface between the inner and outer cut-off scales leads to:

$$\Xi = \left[\frac{\bar{\Delta}}{\delta_c} \right]^{D-2} \tag{5 18}$$

In the above equation, $\bar{\Delta}$ is the filter width considered as the outer cut-off scale, δ_c is the inner cut-off scale and D is the fractal dimension. In deriving the fractal dimension in equation (5.18), we have used an empirical relation (see section 5 4.1) based on sub-grid velocity fluctuations, which is based on fractal properties of the sub-grid flame surface area (Kronenburg and Bilger, 2001) However, it is not yet been experimentally determined, whether sub-grid flame surface area is fractal or not, since the flame wrinkling process may not be scale-independent. However, this approach has been implemented successfully in the thickened flame modelling (Charlette et al , 2002). The critical assumption involved in choosing such an expression for wrinkling flame factor is that vortices of all sizes between outer and inner cut-off scales contribute to the wrinkling of flame surfaces. In general, outer cut-off length represents the largest eddies of integral length scales and the inner cut-off length represents eddies of the size Kolmogorov length scales. In LES, filter width $\bar{\Delta}$ is generally considered as outer cut-off scale and for inner cut-off scale there are several expressions available in the literature related to Gibson scale or Kolmogorov scale or laminar flame thickness as discussed in section 5.4.3. In the present study, the inner cut-off scale is assumed to be equal to three times the laminar flame thickness following the work by Knikker et al. (2004). Hence, β is calculated as.

$$\beta = \sqrt{\frac{6}{\pi}}\Xi = \sqrt{\frac{6}{\pi}}\left[\frac{\bar{\Delta}}{\delta_c}\right]^{D-2} \tag{5.19}$$

5.3 The Dynamic Flame Surface Density (DFSD) Model

The limitation of the AFSD model as outlined in the above section is that, it can only account for the resolved contributions, using a model constant which is not universal To overcome this limitation, Hawkes (2000) proposed a dynamic model for the flame surface density and Knikker et al (2002) developed a conceptual similarity FSD model, involving a combination of test filter application and the similarity ideas (Bardina et al. 1980) to account for the SGS reaction rate This approach has been coupled with the fractal theory to identify the flame surface as a fractal surface and to determine the model constant Cs, which is given in equation (5.27) below. However, this model has failed to determine the fractal dimension, D The similarity FSD model has been tested against experimental data published by Nottin et al (2000) The data were extracted from OH images obtained from planar laser-induced fluorescence (PLIF) measurements of propane/air turbulent premixed flames The FSD model was successful, in predicting specific regions where the sub-grid scale contribution to the flame surface density is high. However, this model failed to calculate fractal dimension dynamically, which resembles the failure of the AFSD model in using constant model coefficient.

To overcome this limitation, a DFSD model has been developed by Knikker et al. (2004) The basic idea is based on modelling the unresolved FSD by applying Germano identity (4.24) to the flame surface density and to model the fractal dimension dynamically. In this approach, a flame wrinkling factor Ξ is introduced as a ratio of flame surface density to its projection in the normal direction of the flame propagation as

$$\Xi = \frac{\int_v |\nabla c| G(x-x')dx'}{\mathbf{N}\cdot\int_v |\nabla c|\,\mathbf{n}G(x-x')dx'} = \frac{\overline{|\nabla c|}}{|\nabla \bar{c}|} = \frac{\bar{\Sigma}}{|\nabla \bar{c}|} \tag{5 20}$$

where **n** and **N** are the normal vectors to the instantaneous c and to the filtered $\bar{c}$ iso-surface pointing towards the unburnt gases Knikker et al (2004) identified that gradient of filtered progress variable $|\nabla\bar{c}|$ becomes zero due to high wrinkled nature of the flame front To avoid this problem, they assumed flame to be locally planar and infinitely thin surface They defined a sharp progress variable c_l using Heaviside function and expressed $|\nabla\bar{c}|$ as $|\nabla\bar{c}_l| = \Pi(\bar{c}_l,\bar{\Delta})$, which becomes zero only far away from the flame front This facilitates to redefine the flame wrinkling factor Ξ as

$$\Xi = \frac{\bar{\Sigma}}{\Pi(\bar{c},\bar{\Delta})} \tag{5.21}$$

Knikker et al (2004) coupled the above equation with the fractal theory to identify the flame surface as a fractal surface between the inner and outer cut-off scales In the present analysis, $\bar{\Delta}$ and δ_c are considered as outer and inner cut-off scale respectively Several models are available in the literature corresponding to the smallest scales such as Kolmogorov and Bachelor scales Hence, the wrinkling factor at outer cut-off scales can be present as

$$\Xi(\bar{\Delta}) = \left(\frac{\bar{\Delta}}{\delta_c}\right)^{D-2} \tag{5 22}$$

In this approach, the term, mean filtered flame surface density $\bar{\Sigma} = \overline{|\nabla c|}$ (in equation 5 20), can be split into two terms as resolved and unresolved

$$\bar{\Sigma} = \overline{|\nabla c|} = \underbrace{\Pi(\bar{c},\bar{\Delta})}_{\text{Resolved}} + \underbrace{f\left(\bar{c},\bar{\Delta},\Pi(\bar{c},\bar{\Delta})\right)}_{\text{Unresolved}} \tag{5.23}$$

The resolved term in the above equation is evaluated using the expression given by Knikker et al. (2002) and the unresolved term is calculated as:

$$\lambda = \bar{\Sigma} - \Pi(\bar{c},\bar{\Delta}) = \overline{|\nabla c|} - \Pi(\bar{c},\bar{\Delta}) \tag{5.24}$$

Defining γ as a ratio of the test filter to grid filter, i e. $\hat{\bar{\Delta}}/\bar{\Delta}$, such that the test filter $\hat{\bar{\Delta}}$ is greater than the grid filter $\bar{\Delta}$. Applying the test filter to flame surface density (5.23) leads to

$$\hat{\bar{\Sigma}} = \widehat{\overline{|\nabla c|}} = \underbrace{\Pi(\hat{\bar{c}},\hat{\bar{\Delta}})}_{\text{Resolved@testfilter}} + \underbrace{\left[\widehat{\overline{|\nabla c|}} - \Pi(\hat{\bar{c}},\hat{\bar{\Delta}})\right]}_{\text{Unresolved@testfilter}} \qquad (5\ 25)$$

From the above equation, unresolved flame surface density contributions at the test filter level can be written as.

$$\Lambda = \left[\widehat{\overline{|\nabla c|}} - \Pi(\hat{\bar{c}},\hat{\bar{\Delta}})\right] \qquad (5\ 26)$$

Following the similarity ideas (Bardina et al., 1980), assuming the sub-grid scale contribution of unresolved flame surface density at test filter is the same as that at grid filter and relating λ and Λ by using the Germano identity (Germano et al., 1991):

$$\Lambda - \hat{\lambda} = \left[\widehat{\overline{|\nabla c|}} - \Pi(\hat{\bar{c}},\hat{\bar{\Delta}})\right] - \left[\widehat{\overline{|\nabla c|}} - \widehat{\Pi(\bar{c},\bar{\Delta})}\right] \qquad (5.27)$$

$$\Lambda - \hat{\lambda} = \left[\widehat{\Pi(\bar{c},\bar{\Delta})} - \Pi(\hat{\bar{c}},\hat{\bar{\Delta}})\right] \qquad (5\ 28)$$

The sub-grid scale flame surface density contributions from the above equation can be added to the resolved flame surface density (5.25) with a model coefficient *Cs* in order to obtain total flame surface density Hence the flame surface density can be expressed as:

$$\bar{\Sigma} = \Pi(\bar{c},\bar{\Delta}) + Cs\left[\widehat{\Pi(\bar{c},\bar{\Delta})} - \Pi(\hat{\bar{c}},\hat{\bar{\Delta}})\right] \qquad (5\ 29)$$

Using equation (5 21) & (5 22), the two terms in the unresolved equation (5 28) may be expressed as:

$$\widehat{\Pi(\bar{c},\bar{\Delta})} = \hat{\bar{\Sigma}}\left(\frac{\bar{\Delta}}{\delta_c}\right)^{D-2} \text{ and } \Pi(\hat{\bar{c}},\hat{\bar{\Delta}}) = \hat{\bar{\Sigma}}\left(\frac{\hat{\bar{\Delta}}}{\delta_c}\right)^{D-2} \qquad (5.30)$$

The above terms can be combined with the similarity concept in order to derive the model coefficient *Cs* as:

$$Cs = \frac{\widehat{\Pi(\bar{c},\bar{\Delta})} - \Pi(\hat{\bar{c}},\hat{\bar{\Delta}})}{\widehat{\Pi(\hat{\bar{c}},\hat{\bar{\Delta}})} - \Pi(\hat{\hat{\bar{c}}},\hat{\hat{\bar{\Delta}}}) - \widehat{\overline{\Pi(\bar{c},\bar{\Delta})}} + \widehat{\Pi(\bar{\bar{c}},\bar{\bar{\Delta}})}} \qquad (5\ 31)$$

The above equation can be simplified by using equation (5.30) by identifying the sub-grid scale flame surface as a fractal surface (Knikker et al., 2004) as:

$$Cs = \frac{1}{1-\gamma^{2-D}}\left[\left(\frac{\bar{\Delta}}{\delta_c}\right)^{D-2} - 1\right] \qquad (5.32)$$

In the above equation, δ_c is the lower cut-off scale, taken equal to three times of the laminar flame thickness following Knikker et al. (2004) The fractal dimension *D* can be calculated using either an empirical relation (North and Santavicca, 1990 and Fureby et al., 2005) described in 5 4 1 or calculated dynamically by combining Germano identity with the fractal theory for wrinkled flames as described in section 5 4 2.

The above model for *Cs* with the fractal model described in section 5 4.2 have been tested by Knikker et al. (2004) for experimentally extracted data of PLIF-OH images (Nottin et al., 2000). Good predictions were obtained for the global mean flame surface density together with realistic values for the fractal dimension. However, this model has never been tested numerically In the present investigation, this dynamic flame surface density model is implemented in an in-house LES code PUFFIN (Kirkpatrick, 2002) and the numerical predictions are validated against experimental data from a laboratory scale premixed combustion chamber as described in chapter 7.

5.4 Modelling the Fractal Dimension

In this section, two models, based on the classical fractal theory, are presented and discussed to examine the fractal nature of turbulent premixed flames Since the successful introduction of the fractal theory by Mandelbrot (1975) in homogeneous, isotropic turbulence, fractal concepts have been widely used for various diverse applications (Batty, 1985) Application of the fractal concept to turbulent premixed flames has been a subject of interest, while understanding the flame structure by many researchers such as Gouldin (1987) and Kerstein (1988). Gouldin (1987) characterised turbulent flame surface as a passive scalar surface dominated by the fractal nature of turbulent flow field. Kerstein (1988) represented turbulent flame structure as a fractal surface based on dynamic similarity of the flame front. However, both studies have concluded a value of 2.37 for the fractal dimension, *D* for turbulent premixed flames. Later, North and Santavicca (1990) carried out an extensive experimental study of a freely propagating turbulent premixed flame over a wide range of turbulent Reynolds and Damköhler numbers. From their experimental observations, they devised a heuristic, empirical relation as a function of turbulence intensity and laminar flame speed.

The basic principle of the fractal theory is to identify and characterise the flame front structure as a fractal surface, which cannot be described by conventional methods. Since turbulent flames come under the category of naturally occurring fractals as shown in

Figure 5 1, there exist a wide range of self-similar shapes and forms of different scales between outer and inner cut-off scales as shown in Figure 5 2 The similarity between different size scales implies that the dynamic processes operating at each scale of similar size is the same and facilitates to calculate the fractal dimension of the fractal surface. As mentioned earlier, Mandelbrot (1975) was the first to suggest a value of 2.5 to 2 67 for *D* in case of isotropic, homogeneous turbulence, but subsequent experiments (Lovejoy, 1982, Sreenivasan and Meneveau, 1986) and mathematical analysis (Hentschel and Procaccia, 1984) suggested a value of 2 35 to 2 41 However, Gouldin (1987) considered an intermediate value of 2.37 based on experimental studies of clouds and jet boundaries in free shear flows in his turbulent premixed modelling studies. Kerstein (1988) also suggested the same value for *D*, while deriving it using dynamic similarity approach Hence, it is evident that there exist various values for fractal dimensions based on intuitive arguments, experimental analysis or mathematical derivation in literature

Numerical modelling of turbulent premixed flames, based on fractal theory generally requires a value for fractal dimension of the fractal surface, which can be either modelled, based on local flow conditions or a prior value can be taken as an input. Nevertheless, most of current research studies found to follow the later approach due to either loss of information in numerical simulations or to avoid the complexity of the whole problem. However, in the present work, fractal dimension of the turbulent premixed flame front is modelled using two different models, namely, the empirical fractal model (EFM) due to North and Santavicca (1990) and the dynamic fractal model (DFM) of Knikker et al. (2004) The first is based on an empirical relation, parameterised based on the local flow conditions, while the second is based on the outcome of recent mathematical derivation of the dynamic evaluation and Germano identity of the resolved filtered flame surface density at test and grid filter. These two models are presented and discussed in following two sections.

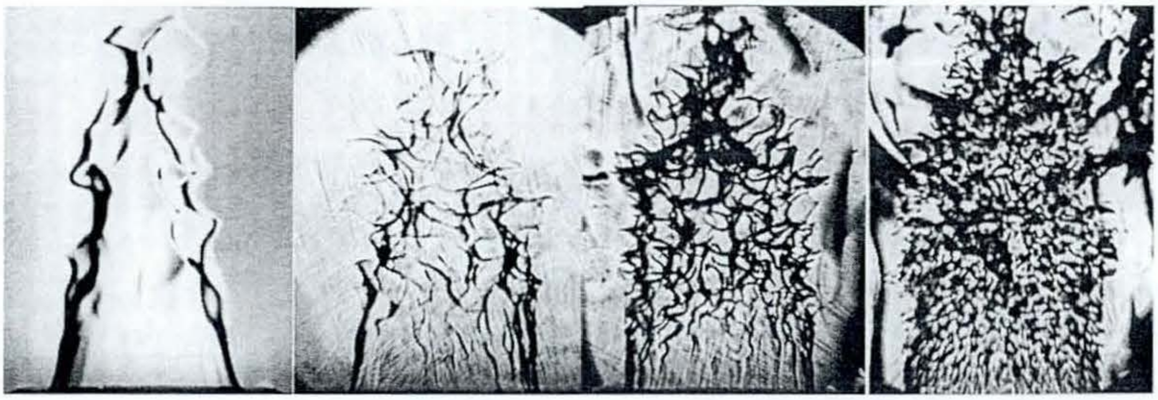

Figure 5.1 Instantaneous Schlieren images of typical lean premixed flame at different pressures showing the fractal nature of the flame (Kobayashi et al., 1996).

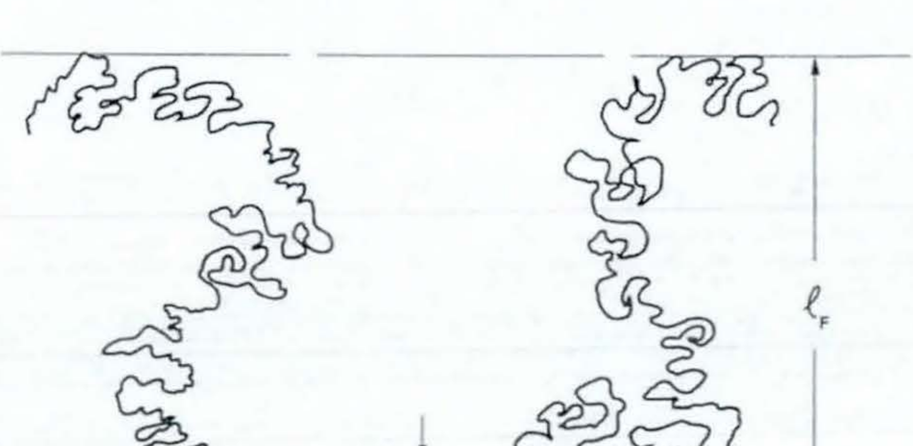

Figure 5.2 Fractal nature of flame front showing various length scales (Gouldin, 1987).

5.4.1 Empirical Fractal Model (EFM)

North and Santavicca (1990) considered various turbulent premixed flame configurations over a wide range of Reynolds and Damköhler numbers, such as rod-stabilised V-flame (Dandekar and Gouldin, 1981), rim stabilized conical flames (Murayama and Takeno, 1989), edge stabilised oblique flame (Gulati and Driscoll, 1986) and wall stabilized stagnation flames (Cho et al., 1988). They also developed a pulsed-flame flow reactor, which is able to generate freely propagating turbulent premixed flame over a wide range of conditions. After careful examination of images taken from the experimental flame, it was observed that the fractal dimension increases with increasing turbulence intensity and decreasing laminar flame speed. This phenomenon is explained as "the turbulent velocity fluctuations act to convectively distort the flame front at a rate proportional to the characteristic velocity scale, u' and the laminar burning process acts to smooth the flame surface at a rate proportional to the laminar burning speed, u_L" [See (North and Santavicca, 1990)]. They quantified this equilibrium situation as, the wrinkling of flame within turbulent fractal limit i.e. D_T, due to the convective process by u', as a measure of distortion of the flame sheet by turbulent motions and smoothing of the flame within laminar fractal limit i.e. D_L, due to the control of burning process by u_L, to eliminate the flame wrinkles. Based on the combined, equilibrium effects of the turbulent intensity and laminar burning speed, they parameterised a model to evaluate fractal dimension as:

$$D = \frac{D_L}{\left(\frac{u'}{u_L} + 1\right)} + \frac{D_T}{\left(\frac{u_L}{u'} + 1\right)} \tag{5.33}$$

It is evident from the above equation that the fractal dimension, D is automatically clipped between chosen lower and upper fractal limits for a particular flame. However, these values are not definite and depend on the flow configuration. In the present investigation, the laminar fractal limit, D_L and the turbulent fractal limit, D_T are considered as 2.19 and 2.35 respectively, following the recent analysis of wrinkling length scales of propane/air flames of Patel and Ibrahim (1999). Recently, Fureby (2005) has successfully implemented this empirical model in LES modelling of propane/air turbulent flames in a dump combustor by replacing u' with the SGS velocity fluctuations, u'_Δ as:

$$D = \frac{D_L}{\left(\frac{u'_\Delta}{u_L} + 1\right)} + \frac{D_T}{\left(\frac{u_L}{u'_\Delta} + 1\right)} \tag{5.34}$$

It is evident from the above equation that the use of SGS velocity fluctuation instead of turbulence intensity is quite straight forward and do not required any further explanation in the case of LES. Using the equation (5.34), one can calculate the fractal dimension at every grid point for each time step.

5.4.2 Dynamic Fractal Model (DFM)

The dynamic fractal model (DFM) can be considered as continuation to the DFSD model described in section 5.3, which identify the fractal dimension of the turbulent premixed flame. Considering the flame kernel as a fractal surface, the fractal dimension, D is extracted by coupling the wrinkling flame factor (equation 5.21) with Germano identity (Germano et al., 1991), while conserving the averaged filtered flame surface at test and grid filter as:

$$\widehat{\Xi(\bar{\Delta})\Pi(\bar{c},\bar{\Delta})} = \Xi(\hat{\bar{\Delta}})\Pi(\hat{\bar{c}},\hat{\bar{\Delta}}) \tag{5.35}$$

Using equations (5.22) and (5.30) the above expression can be rewritten as:

$$\widehat{\left(\frac{\bar{\Delta}}{\delta_c}\right)^{D-2}\bar{\Sigma}\left(\frac{\bar{\Delta}}{\delta_c}\right)^{2-D}} = \left(\frac{\hat{\bar{\Delta}}}{\delta_c}\right)^{D-2}\hat{\bar{\Sigma}}\left(\frac{\hat{\bar{\Delta}}}{\delta_c}\right)^{2-D} \tag{5.36}$$

The above expression can be solved for fractal dimension, D for each time step at every grid point in the computational domain. However, some form of averaging is usually required to avoid numerical stability issues, similar to that used to dynamically evaluate the Smagorinsky constant. Hence, volume average of equation (5.36) is carried out for every time step as

$$\left\langle\widehat{\left(\frac{\bar{\Delta}}{\delta_c}\right)^{D-2}\bar{\Sigma}\left(\frac{\bar{\Delta}}{\delta_c}\right)^{2-D}}\right\rangle = \left\langle\left(\frac{\hat{\bar{\Delta}}}{\delta_c}\right)^{D-2}\hat{\bar{\Sigma}}\left(\frac{\hat{\bar{\Delta}}}{\delta_c}\right)^{2-D}\right\rangle \tag{5.37}$$

Rearranging the above equation results in:

$$\left(\frac{\hat{\bar{\Delta}}}{\bar{\Delta}}\right)^{D-2} = \frac{\langle\widehat{\Pi(\bar{c},\bar{\Delta})}\rangle}{\langle\Pi(\hat{\bar{c}},\hat{\bar{\Delta}})\rangle} \tag{5.38}$$

Applying logarithm on both sides of the above equation and rearranging will lead to:

$$D = 2.0 + \frac{\log\left(\langle\widehat{\Pi(\bar{c},\bar{\Delta})}\rangle / \langle\Pi(\hat{\bar{c}},\hat{\bar{\Delta}})\rangle\right)}{\log\left(\hat{\bar{\Delta}}/\bar{\Delta}\right)} \tag{5.39}$$

The above equation can be solved at each grid point in the computational domain at every time step. To alleviate the ill-posed problems due to strong local variations or to avoid irrelevant values, the maximum value of the fractal dimension is clipped to 2.5 in simulations. It is worth mentioning at this stage that, the DFM can only be applied in conjunction with dynamic flame surface density procedure described in section 5.3, where the values of $\Pi(\overline{c},\overline{\Delta})$ at grid and test filter, at every grid point in time are available. Where as, the empirical model described in section 5.4.1 can be applied to any turbulent premixed flame situation, as the turbulent intensity and laminar burning velocity information can easily be extracted.

5.4.3 Outer and Inner Cut-off Scales

It is evident from the above fractal models that there is a necessity to define correct outer and inner cut-off scales, which facilitates to evaluate correct fractal dimension of the flame. In case of EFM, outer cut-off scale is important since it is required to determine the SGS velocity fluctuations based on filter width used in LES studies. Similarly in case of DFM, it is evident, that the wrinkling flame factor and flame surface density in equation (5.35) are derived based on filter width, which is considered as outer cut-off scale. In case of LES studies, it is appropriate to consider filter width Δ as outer cut-off scale. Hence, in the present simulations, filter width has been considered as outer cut-off scale.

Inner cut-off scale, commonly represents the smallest scale of wrinkling flame is predominant in evaluating overall reaction rate apart from fractal dimension There are several hypotheses available in choosing appropriate inner cut-off scales based on physical and intuitive arguments. However, interactions between the smaller turbulent eddies and local flame front are not well established in defining inner cut-off scale through experiments (North and Santavicca, 1990) Among the available, predominantly used cut-off scales are the Kolmogorov length scale (Gouldin, 1987), the Gibson scale (Peters, 1988) and the laminar flame thickness (Murayama and Takeno, 1989, Knikker et al., 2002 and Knikker et al., 2004).

Kolmogorov scale is the smallest physical length scale in any turbulent flow and it has been widely exploited by Gouldin (1987), who identified that smoothing action in numerical simulations will generally wipe out the information regarding smallest scales and increases the inner cut-off scale. Also, at high values of u'/u_L, the Kolmogorov scale can become smaller than the laminar flame thickness (North and Santavicca, 1990). Where as, Peters (1988) identified the Gibson scale as the smallest scale, which remains in the reaction region long enough to alter the flame structure and is appropriate to consider as inner cut-off scale However, Murayama and Takeno (1988) argued that it is impossible for an object to have wrinkles smaller than its thickness, which eventually implies laminar flame thickness should be appropriate to consider as the inner cut-off scale while using laminar flamelet concepts. Experimental studies of Gulder and Smallwood (1995) supports this concept by relating inner cut-off scale as, $\delta_c \propto \delta_L$ Gülder and Smallwood (1995) proposed a relation based on DNS data by considering the chemistry effects as·

$$\delta_c = \delta_L(\alpha_3 + Ka^{\beta_3}) \tag{5 40}$$

In the above equation *Ka* is Karlovitz number, α_3 and β_3 are model constants Equation (5 40) can be applicable for u'/u_L values in between 0 5 to 6 2 However, we identified that u'/u_L values are reaching a maximum of 13 4 (as discussed in results) in the combustion chamber discussed in Chapter 7 and hence, the above relation may not be useful in defining the appropriate inner cut-off scale Similar opinion has been expressed by Fureby (2005) and they used a model based on sub-grid scale wrinkling length scale as the inverse of surface averaged curvature of the flame as, $\delta_c = |\langle \nabla \cdot \mathbf{n} \rangle|^{-1}$. However, recently Knikker et al. (2002 and 2004) used inner cut-off scale equal to three times of laminar flame thickness, which they identified to predict good results from experimental extractions Accordingly, a lower cut-off scale equal to three times of laminar flame thickness is used in the present work.

5.5 Summary

This chapter mainly described various models considered and developed for the present investigation, are summarized in Table 5 1. The existing challenges in accounting for the mean chemical reaction rate, in turbulent premixed flames using flame surface density model were discussed. One of such a main challenge in LES described was, accounting the unresolved flame surface density, which can be either obtained by solving the exact FSD equation or modelling by dynamic procedure It was identified that solving exact equation in RANS itself used to be complex and solving it in LES will lead to many unclosed terms. Alternatively, a dynamic flame surface density (DFSD) model based on Germano identity and the similarity concept by Knikker et al (2004), has been developed and implemented in the current work.

	Model-1 (M1)	**Model-2 (M2)**	**Model-3 (M3)**	**Model-4 (M4)**
Chemical Reaction	AFSD	AFSD	DFSD	DFSD
Fractal Dimension	-n/a-	EFM	EFM	DFM
Model Coefficient	Constant	Self-scaling	Dynamic	Dynamic

AFSD Algebraic flame surface density, DFSD Dynamic flame surface density
EFM Empirical fractal model, DFM Dynamic fractal model

Table 5 1 Different sub-grid scale models used in the present study

Prior to DFSD model, it was concluded that dynamic evaluation of the model coefficient in algebraic FSD model may be the best choice. However, it was identified that the application of Germano identity in deriving model coefficient fails and alternatively, a model based on flame wrinkling factor was identified Preliminary studies using this model revealed (details are explained in chapter 8) that the flame wrinkling model is capable to self scale the model coefficient, based on local flow conditions and is a much better option rather than using a constant value. However, this study also identifies that algebraic FSD can be further improved by calculating the unresolved flame surface density by additional formulation Consequently, DFSD model based on simple FSD has been identified as a best available option and a detailed derivation was provided

DFSD derivation provides certain challenges in calculating the fractal dimension and a model for lower cut-off scale Two models were used to calculate fractal dimension based on experimental studies and dynamic similarity ideas respectively with a choice of lower cut-off scale. However, following the simple experimental thought, it is concluded that lower cut-off scale corresponding to laminar flame thickness would result in best predictions and hence is used in the present study

Chapter 6

Numerical Implementation

The dynamic flame surface density model and other sub models developed in this work are numerically implemented in an available in-house LES code PUFFIN, originally developed by Kirkpatrick (2002) and thereafter extended for compressible flows (Kirkpatrick et al., 2003). PUFFIN was developed using sophisticated, state of the art programming techniques in FORTRAN 90, which is capable of handling 2-D and 3-D, non-reacting and reacting (specifically premixed), LES numerical simulations of various industrial flow problems. Recently, PUFFIN has been extended to compute, non-premixed (Ranga-Dinesh, 2007) and partially premixed (Ravikanti, 2008) industrial problems as well. However, the work presented in this thesis is, mainly in relation to premixed flames and aims to gain confidence, in using simple and dynamic FSD models for unsteady turbulent flames, especially for stagnant propane/air mixture of equivalence ratio of 1.0, ignited and allowed to propagate over multiple solid obstacles LES findings are validated against available experimental measurements. This chapter briefly describes various numerical aspects and solution methodologies implemented in LES code PUFFIN.

In any numerical simulation tool, the primary concern is to outline the partial differential equations, governing the fluid flow, as described in Chapter 3 and 4. The governing equations are then carefully discretized, to achieve error free/most accurate numerical results Finally, spatially discretized equations are solved in computational space and time, which is very important to achieve results of desired and decent accuracy, within the available computational resources.

PUFFIN uses finite volume spatial discretization methodology, on a forward staggered, non-uniform, Cartesian grid, which is detailed in section 6.1. Spatial discretization of individual terms in a generic governing equation, using finite volume methodology is discussed in section 6 2. Section 6 3 describes various aspects of the code such as, time advancement scheme, pressure correction scheme, solver and typical solution iteration procedure for models described in Table 5.1 employed in the present work Section 6 4 presents the details of outflow and solid boundary conditions employed in the present investigation. Finally, a brief summary of the chapter is given in section 6 5

6.1 Finite Volume Method

In the finite volume method, the computational domain is divided into finite number of control volumes (CVs) Conservation equations described in chapter 3 and 4 for turbulent premixed flames are numerically integrated in each of these CVs, which eventually leads to a set of simultaneous algebraic equations, whose solution is an approximation to the solution of the continuous equations at a set of discrete points or nodes Centroid of the individual control volume is generally considered as a node and the solution at this node represents the solution within the control volume. One main advantage of the finite volume methodology is that it can accommodate any type of grid, which is quite suitable for complex geometries Also, as discussed in chapter 4, application of box filter in LES, naturally fits into the finite volume formulation

Hence, the work presented here uses finite volume methodology, based on a forward, staggered Cartesian grid and defines the boundaries of the rectangular finite volumes as shown in Figure 6 1 Scalars such as pressure and reaction progress variable are calculated at the scalar nodes as shown in Figure 6 1 However, the velocity components are calculated at the velocity nodes i.e. centroid of scalar cell faces, forming a staggered grid, which means that the velocity cells are staggered with respect to the scalar cells. Staggering of the velocity avoids physically non-realistic predictions for oscillating pressure fields. Also, since the velocities are generated at scalar cell faces, it has the added advantage of avoiding interpolation of velocities for scalar transport computations. Extension of the grid shown in Figure 6 1 in 3-D uses the same structure in the z direction, with an addition of velocity component in z-direction i.e. w.

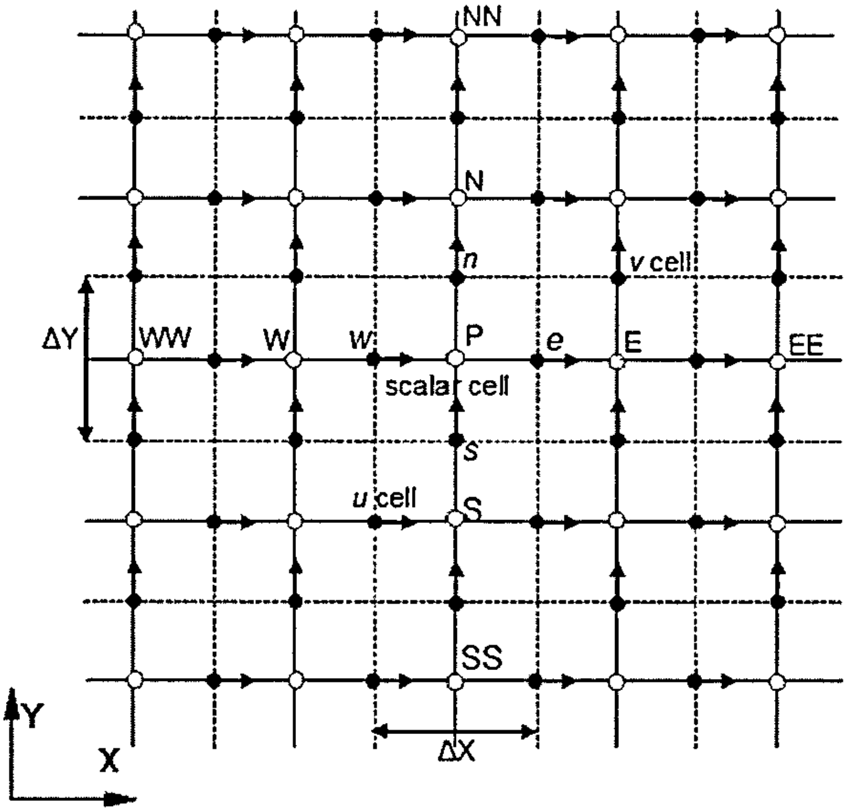

Figure 6.1 Two dimensional forward staggered grid Circles are scalar nodes, horizontal arrows are nodes of the *u* velocity component and vertical arrows the nodes of the *v* velocity component. Examples of a *u*, *v* and scalar cells are highlighted.

6.2 Discretization of the Conservation Equations

The conservation equations of mass, momentum, energy and reaction progress variable detailed in chapter 3 and 4 are in similar format and therefore, can be expressed using a generic variable ϕ as:

$$\frac{\partial(\rho\phi)}{\partial t}+\frac{\partial(\rho u_j\phi)}{\partial x_j}=\frac{\partial}{\partial x_j}\left(\Gamma\frac{\partial\phi}{\partial x_j}\right)+S_\phi \qquad (6\ 1)$$

For instance, in the above equation, ϕ equals to one represents continuity, u represents momentum in x-direction, h represents specific enthalpy (energy) and c represents reaction progress variable equation. The equation (6.1) can be rearranged as:

$$\frac{\partial(\rho\phi)}{\partial t}=-\frac{\partial(\rho u_j\phi)}{\partial x_j}+\frac{\partial}{\partial x_j}\left(\Gamma\frac{\partial\phi}{\partial x_j}\right)+S_\phi \qquad (6\ 2)$$

In the above equation, Γ is the diffusion coefficient and S_ϕ is the source term The equation (6 2) is integrated over a control volume *V* bounded by an arbitrary shape as:

$$\int_V \frac{\partial(\rho\phi)}{\partial t}dV = -\int_V \frac{\partial(\rho u_j\phi)}{\partial x_j}dV + \int_V \frac{\partial}{\partial x_j}\left(\Gamma\frac{\partial\phi}{\partial x_j}\right)dV + \int_V S_\phi dV \tag{6 3}$$

The convection and diffusion terms in the above equation can be transformed into surface integrals by using Gauss divergence theorem, which yields the integral form of the equation as

$$\frac{\partial}{\partial t}\int_V (\rho\phi)dV = -\int_S \rho u_j\phi dS_j + \int_S \Gamma\frac{\partial\phi}{\partial x_j}dS_j + \int S_\phi dV \tag{6 4}$$

The differential surface area vector *dS* has a magnitude equal to the area of the segment of surface and direction corresponding to the direction of the outward normal to the segment The terms in the equation (6 4) represents, unsteady term on LHS and advection, diffusion and the source terms on RHS respectively Spatial discretization of the equation (6 4) involves approximating the volume and surface integrals within the finite volume to obtain a set of simultaneous linear algebraic equations in ϕ.

A schematic representation of 2-D forward staggered grid shown in Figure 6 1 elucidates the details of a scalar cell *P* for which the integrals are to be calculated and surrounded by its northern (*N*), eastern (*E*), southern (*S*), western (*W*) neighbours and one level away from it as north of northern (*NN*), east of eastern (*EE*), south of southern (*SS*), west of western (*WW*) Figure 6 2 extends this structure in 3-D for the same scalar and shown neighbouring cells in *z*-direction as up (*U*) and down (*D*), which can be extended thereafter as upper of up (*UU*) and down of down (*DD*). The surfaces separating two cells are denoted as A_n, A_e, A_s, A_w, A_u and A_d, the associated fluxes are F_n, F_e, F_s, F_w, F_u and F_d. Small letters *e*, *n* etc refer to the points at the centroid of the respective cell faces In the following section, *nb* is used as a generic subscript for neighbour cell and *f* is a generic subscript for a quantity evaluated at a cell face. To reduce the complexity of the notation, the fluxes are given for a particular face such as the east or north face All results can be applied in a similar manner to other faces.

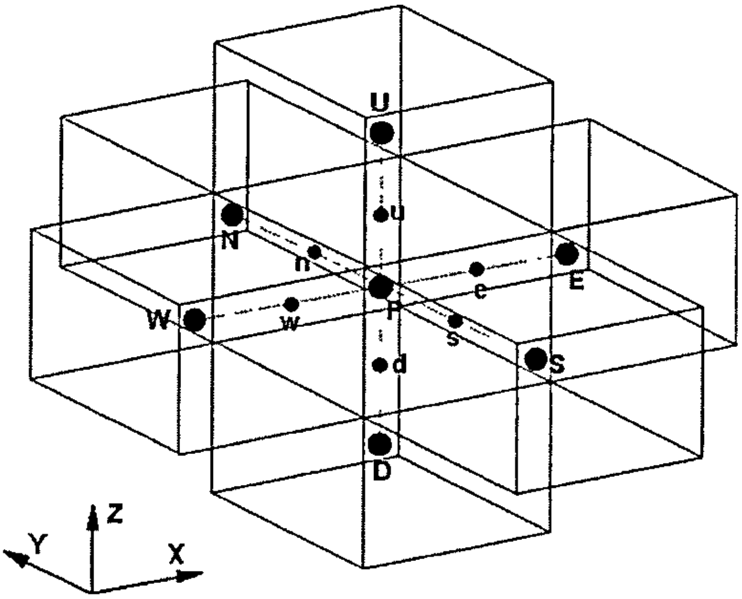

Figure 6 2 Three dimensional view of a finite volume cell and its neighbours.

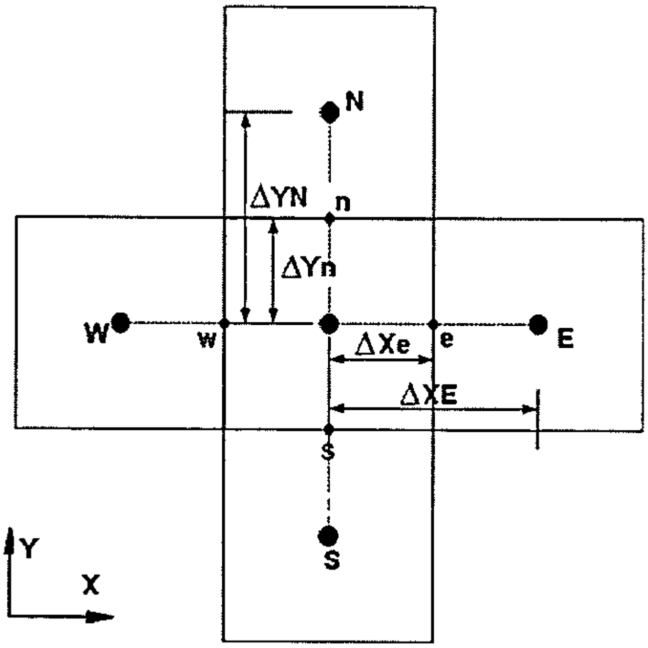

Figure 6.3 A finite volume cell and its neighbours in the *xy*-plane.

6.2.1 The Unsteady Term

The unsteady term on the left hand side of the conservation equation (6 4) can be discretized by considering the value of ϕ at the central node, which is considered to be representing the value throughout the control volume Using the central difference approximation for the time derivative at $n+1/2$ it can be derived as:

$$\int_V \frac{\partial(\rho\phi)}{\partial t} dV \approx \frac{(\rho\phi)^{n+1} - (\rho\phi)^n}{\Delta t} \Delta V \tag{6.5}$$

where n is the time level. The value n indicates that the values are taken at the start of the current time step, where as $n + 1$ indicates the end of the time step

6.2.2 The Convection Term

The convective fluxes are very important in any turbulent reacting flows and hence, their description is essential in numerical simulations In order to achieve appropriate numerical stability and accuracy, a special treatment for the convective fluxes is required Numerical discretization employed for convective fluxes is explained as follows·

Considering a control volume and representing convective fluxes as:

$$\int_S \rho u_j \phi dS_j = \sum_{n,e} F_{conv} \tag{6.6}$$

The convection flux across a cell face is given by.

$$F_{conv} = \left(\rho u_{normal} \Delta A \phi\right)_f \tag{6.7}$$

where u_{normal} is the velocity component normal to the surface A and ΔA is the area of the face. The convection for the east face can be written as:

$$F_{conv} = \left(\rho u \Delta A\right)_e \phi_e \tag{6 8}$$

The application of weighted, linear interpolation of the neighbouring cells at the centre of the face leads to:

$$\phi_e = (1-\theta)\phi_P + \theta\phi_E \tag{6.9}$$

Here the weighting factor for the interpolation is

$$\theta = \frac{\Delta x_e}{\Delta x_E} \tag{6.10}$$

Δx_e and Δx_E are the distances from the node P to the face of the centroid e and the east neighbour node E, as shown in Figure 6 3

In the staggered grid it is required to find the convective velocity u_e at the face and the density ρ_e at the face depending on whether the variable ϕ is a scalar or velocity component. When ϕ is a scalar, the convective velocity is available, as u is established at the cell face. However, density must be interpolated using an equation similar to (6 9) such as:

$$\rho_e = (1-\theta)\rho_P + \theta\rho_E \tag{6.11}$$

Contrary to that, when ϕ is a velocity component, linear interpolation is required to find the convective velocity, however, ρ is directly available. Finally the resulting formulation for the convection fluxes can be described using a second order central difference scheme as:

$$F_{conv} = (\rho u \Delta A)_e [(1-\theta)\phi_P + \theta\phi_E] \tag{6 12}$$

This linear interpolation based numerical scheme used to calculate the variables at cell faces of the finite volumes is equivalent to a second order central difference scheme in finite difference method. This scheme is second order accurate, computationally efficient and simple to implement This accuracy is desirable for LES since numerical damping acts as an extra un-quantified contribution to the eddy viscosity and contaminates the effects of the sub-grid scale model. However this scheme tends to give solutions containing non-physical oscillations or 'wiggles' in areas of the field containing high gradients. The convection terms in the scalar equations are particularly problematic due to the large gradients which often occur in the scalar fields Because scalars are often coupled with the velocity field through density, wiggles which result from use of the central difference for the scalar convection terms cause problems with the numerical stability of the overall solution. Hence this scheme is hardly suited for scalar transport, especially when they have to remain bounded For example, reaction progress variable is limited to a range from 0 to 1 From this scheme, wiggles may lead to unphysical results such as predictions of reaction progress variable outside the range 0 and 1, which do not yield any sensible meaning. For this reason, the convection term for the scalar equation is discretized using non-centred schemes such as QUICK of Leonard (1979) or SHARP of Leonard (1987)

QUICK is a third order upwind scheme and can reduce numerical oscillations by introducing fourth order dissipation. Quadratic interpolation is used to find the value ϕ at the centre of the cell faces. The formula for the east face can be written as

$$\phi_e = \left[(1-\theta)\phi_P + \theta\phi_E\right] - \frac{1}{8} CRV \times \Delta x_E^2 \tag{6.13}$$

Here the upwind biased curvature term define as

$$CRV = \frac{\phi_P - 2\phi_E + \phi_{EE}}{\Delta x_E^2}, \qquad u < 0 \tag{6.14}$$

$$CRV = \frac{\phi_E - 2\phi_P + \phi_W}{\Delta x_E^2}, \qquad u > 0 \tag{6.15}$$

The double subscript such as *EE* refers to the cell east of the eastern neighbour as described in section 6.2. The weighting factor θ can be calculated from equation (6.10). The first term in equation (6.13) is the value of ϕ at the cell face calculated using linear interpolation. The second term is an upwind biased curvature term which makes the overall interpolation quadratic.

The linear interpolation term accounts for the non-uniform grid through the weighting factor θ, while the curvature terms have no grid weighting included. Castro and Jones (1987) have shown that the uniform grid formula for QUICK gives negligible errors for grid expansion ratios ($r_x = \Delta x_i+1/\Delta x_i$) between 0.8 and 1.25. Substituting equation (6.13) into equation (6.5) gives the convective flux of ϕ across the east face as

$$F_{conv} = (\rho u \Delta A)_e \left[\left((1-\theta)\phi_P + \theta\phi_E\right) + S_{QUICK}\right] \tag{6.16}$$

where $S_{QUICK} = -1/8\ CRV\ \ \Delta x_E^2$. The source term S_{QUICK} indicates the curvature of the field. In PUFFIN, the term S_{QUICK} is included as part of the source term S_ϕ.

However, QUICK scheme can reduce the wiggles but does not remove them completely. In this case another scheme called SHARP (Leonard, 1987), which is a modification to QUICK is used. SHARP introduces second order diffusion where local conditions are such that oscillations will not occur, thereby ensuring that the solution remains monotonic. An outline of this scheme can be found in (Leonard, 1987). Finally, summation of the convective fluxes across all faces can be added and described as:

$$\int_S \rho u_j \phi \, dS_j \approx \sum (\rho u \Delta A)_f \left[\left(1-\theta_f\right)\phi_P + \theta_f \phi_{nb} + \sum S_{QUICK}\right] \tag{6.17}$$

6.2.3 The Diffusion Term

The diffusive flux is proportional to the gradient of ϕ across a cell face f and is given as:

$$F_{diff} = \left[\Gamma \Delta A \left(\frac{\partial \phi}{\partial \mathrm{n}} \right) \right]_f \tag{6.18}$$

where n is the direction normal to the face, Γ is the kinematic diffusion coefficient and ΔA the area of the face. The flux at the centre of the east cell face is then computed from the values at the two neighbouring points and their distance from central difference approximation as

$$F_{diff} = \left(\Gamma \Delta A \right)_e \frac{\phi_E - \phi_P}{\Delta x_E} \tag{6.19}$$

The diffusion coefficient at the centre of the face Γ_e is calculated by linear interpolations same as density calculation in the preceding section of the convection term. Summation of the diffusive fluxes across all faces can be described as a discrete diffusion operator as:

$$\int_S \Gamma \frac{\partial \phi}{\partial x_j} dS_j \approx \sum \frac{\left(\Gamma \Delta A \right)_e}{\Delta x_E} \left(\phi_{nb} - \phi_P \right) \tag{6.20}$$

It is worth noting at this stage, that the discrete diffusion operator does not suffer from numerical instability as observed in the case of convective fluxes. Therefore, no special treatment is required for diffusion terms in conservation equation.

6.2.4 The Source Term

Source terms are different for each variable in individual conservation equations and dependent of the variable being transported. For instance, in case of momentum equation, source term represents the effect of the pressure gradient and the gravitational force. Where as, in case of energy equation, source term include contributions due to pressure work, viscous dissipation and flow dilatation as well as a chemical source term. Chemical source term is also presented in the reaction progress variable equation.

Spatial discretization of the source term in all the transport equations is in the same manner. They are calculated by evaluating the function representing the source term S_ϕ at the node and multiplying by the volume of the cell as

$$\int_V S_\phi dV \approx S_{\phi P}\Delta V \tag{6.21}$$

Gradients are evaluated using second order central differences, while interpolations utilize a linear profile similar to that used in evaluating convection and diffusion terms. In general, source terms can be expressed as a combination of implicit and explicit components as.

$$S_{\phi P}\Delta V = S_{imp}\phi_P + S_{\exp} \tag{6.22}$$

The implicit component of the above equation is integrated using implicit time advancement scheme, whereas the explicit component is integrated using explicit time advancement scheme. The time advancement schemes employed in the present work are described in section 6.3.

6.2.5 The Complete Discretized Conservation Equation

It is evident from the above sections, that the complete discretized conservation equation for a generic variable ϕ can simply written by summing the individual discretized terms as

$$\begin{aligned}\frac{(\rho\phi)^{n+1}-(\rho\phi)^{n}}{\Delta t}\Delta V = {} & \left\{\sum(\rho u\Delta A)_f\left[(1-\theta_f)\phi_P+\theta_f\phi_{nb}\right]\right\}^{(n-2,n-1,n,n+1)} \\ & + \left\{\sum\frac{(\Gamma\Delta A)_e}{\Delta x_E}(\phi_{nb}-\phi_P)\right\}^{(n-1,n,n+1)} \\ & + \left\{S_{imp}\phi_P\right\}^{(n-1,n,n+1)} + \left\{S_{\exp}\right\}^{(n-2,n-1,n,n+1)}\end{aligned} \tag{6.23}$$

Here the curly brackets {} with superscripts ($n-2$, $n-1$, n, $n+1$) represent a weighted average of the term evaluated at the listed time intervals, which gives an estimate of the term at the ($n+1/2$) time level, which will be discussed in next section. Collecting the coefficients and rearranging the above equation results in the final form equation as:

$$\begin{aligned}A_P^{n+1}\phi_P^{n+1} = {} & \sum_{nb}\left(A_{nb}^{n+1}\phi_{nb}^{n+1}\right) + S_{imp}\phi_P^{n+1} + S_{exp}^{n+1} \\ & + \left[\sum_{nb}\left(A_{nb}^{n}\phi_{nb}^{n}\right) - A_P^{n}\phi_P^{n} + S_{imp}\phi_P^{n} + S_{\exp}^{n}\right] \\ & + \left[\sum_{nb}\left(A_{nb}^{n-1}\phi_{nb}^{n-1}\right) - A_P^{n-1}\phi_P^{n-1} + S_{imp}\phi_P^{n-1} + S_{\exp}^{n-1}\right] \\ & + \left[\sum_{nb}\left(A_{nb}^{n-2}\phi_{nb}^{n-2}\right) - A_P^{n-2}\phi_P^{n-2} + S_{\exp}^{n-2}\right]\end{aligned} \tag{6.24}$$

where the coefficients corresponding to the node A_P and its neighbours A_{nb} are formed due to the contributions from convection and diffusion terms. More details of spatial discretization methods can be found in Kirkpatrick (2002) and Kirkpatrick et al. (2003).

6.3 Time Advancement Scheme

The discretized transport equation described in the above section must be solved in space and time in order to simulate reacting flows. To obtain time-accurate and unsteady simulations, time integration schemes are developed using second and third order numerical accuracy. The time integration schemes for scalar equation uses the Crank-Nicolson scheme and the momentum equations are advanced using either Crank-Nicolson or the second- and third- order hybrid Adams-Bashforth scheme

6.3.1 Time Integration of Scalar Equation

In the present work, Crank-Nicolson scheme is employed to achieve time integration of the scalar equation. The time dependent conservation equation, integrated in time using Crank-Nicolson scheme can be written as

$$\begin{aligned}\frac{(\rho\phi)^{n+1}-(\rho\phi)^{n}}{\Delta t}\Delta V = &-\frac{1}{2}\left[H^{n+1}\left(\phi^{n+1}\right)+H^{n}\left(\phi^{n}\right)\right]\\ &+\frac{1}{2}\left[L^{n+1}\left(\phi^{n+1}\right)+L^{n}\left(\phi^{n}\right)\right]\\ &+\frac{1}{2}\left[S_{imp}^{n+1}\phi^{n+1}+S_{imp}^{n}\phi^{n}\right]\\ &+\frac{1}{2}\left[S_{\exp}^{n+1}\phi^{n+1}+S_{\exp}^{n}\phi^{n}\right]\end{aligned} \tag{6.25}$$

where H is the discrete convection term, expressed as:

$$H(\phi)=\sum(\rho u\Delta A)_f\left[\left(1-\theta_f\right)\phi_P+\theta_f\phi_{nb}\right] \tag{6.26}$$

L is the discrete diffusion term, expressed as:

$$L(\phi)=\sum\frac{(\Gamma\Delta A)_e}{\Delta x_E}\left(\phi_{nb}-\phi_P\right) \tag{6.27}$$

$S_{imp}\phi$ and S_{exp} are discrete implicit and explicit source terms respectively. It is to be noted that S_{imp} is a coefficient of ϕ rather a function of ϕ.

In the above equation (6 25), each term is evaluated at the n and n+1 time levels, and employs linear interpolation to estimate their value at n+1/2. Therefore, this scheme is second order accurate. At least two iterations of scalar equation per time step are required due to the contributions of terms containing ϕ^{n+1} to the explicit source term which result from the use of the QUICK and SHARP spatial discretization schemes It should be noted at this stage that in turbulent premixed combustion, density and diffusivity vary significantly in time Hence to maintain the stability of the solution, a number of outer iterations of the entire time advancement scheme per time step are required to ensure that the values of ρ^{n+1} and Γ^{n+1} are second order accurate. This non-oscillatory criterion for Crank-Nicolson scheme can be achieved by enforcing a condition on time as:

$$\Delta t \le \frac{(\Delta x)^2}{\Gamma} \tag{6.28}$$

While the above criterion poses a rather stringent limitation on the improvement that could be achieved on spatial accuracy, it results from an error term in the Taylor series expansion which contains the second derivative in space $\partial^2\phi/\partial x_i^2$. However this term is relatively small in most flow problems and the scheme remains stable for considerably large time steps

6.3.2 Time Integration of Momentum Equations

Time integration of the momentum equations uses either Crank-Nicolson or the second and third order hybrid Adams schemes In the hybrid schemes, Adams-Bashforth methods are used for the advection terms and Adams-Moulton methods for the diffusive terms The momentum equations are integrated by using Crank-Nicolson scheme can be expressed as:

$$\begin{aligned}\frac{\rho^{n+1}u^{*}-\rho^{n}u^{n}}{\Delta t}\Delta V = &-\frac{1}{2}\left[H^{n+1}(u^{*})+H^{n}(u^{n})\right]\\ &+\frac{1}{2}\left[L^{n+1}(u^{*})+L^{n}(u^{n})\right]\\ &+\frac{1}{2}\left[S_{imp}^{n+1}u^{*}+S_{imp}^{n}u^{n}\right]\\ &+\frac{1}{2}\left[S_{\exp}^{n+1}u^{*}+S_{\exp}^{n}u^{n}\right]-Gp^{n-\frac{1}{2}}\end{aligned} \tag{6.29}$$

It is evident from the above equation, that it has similar form of the scalar equation employing Crank-Nicolson scheme (equation 6 25) However, an additional term can be noticed, added as a pressure gradient term $Gp^{n-1/2}$, which considers n-1/2 time level concerning the pressure correction scheme, which will be discussed in next section Here the approximate velocity obtained before pressure correction step at n+1 time level is specified with superscript u*.

The advection terms in the momentum equations are integrated using explicit time advancement scheme, as Crank-Nicolson requires several iterations to retain second order accuracy In PUFFIN, second and third order hybrid schemes are used such that advection terms are treated explicitly using an Adam-Bashforth scheme while diffusion term is treated implicitly using Adams-Moulton. The additional terms such as gravitational terms are treated explicitly using Adams-Bashforth

The second order Adams-Bashforth/Adams-Moulton scheme for the momentum equations can be written as:

$$\begin{aligned}\frac{\rho^{n+1}u*-\rho^{n}u^{n}}{\Delta t}\Delta V=&-\frac{1}{2}\left[3H^{n}\left(u^{n}\right)-H^{n-1}\left(u^{n-1}\right)\right]\\&+\frac{1}{2}\left[L^{n+1}\left(u^{*}\right)+L^{n}\left(u^{n}\right)\right]\\&+\frac{1}{2}\left[S_{imp}^{n+1}u^{*}+S_{imp}^{n}u^{n}\right]\\&+\frac{1}{2}\left[3S_{\exp}^{n}u^{n}-S_{\exp}^{n-1}u^{n-1}\right]-Gp^{n-\frac{1}{2}}\end{aligned}\tag{6.30}$$

and the third order Adams-Bashforth/Adams-Moulton scheme can be written as:

$$\begin{aligned}\frac{\rho^{n+1}u*-\rho^{n}u^{n}}{\Delta t}\Delta V=&-\frac{1}{12}\left[23H^{n}\left(u^{n}\right)-16H^{n-1}\left(u^{n-1}\right)+5H^{n-2}\left(u^{n-2}\right)\right]\\&+\frac{1}{12}\left[5L^{n+1}\left(u^{*}\right)+8L^{n}\left(u^{n}\right)-L^{n-1}\left(u^{n-1}\right)\right]\\&+\frac{1}{12}\left[5S_{imp}^{n+1}u^{*}+8S_{imp}^{n}u^{n}-S_{imp}^{n-1}u^{n-1}\right]\\&+\frac{1}{12}\left[23S_{\exp}^{n}u^{n}-16S_{\exp}^{n-1}u^{n-1}+5S_{\exp}^{n-2}u^{n-2}\right]-Gp^{n-\frac{1}{2}}\end{aligned}\tag{6.31}$$

The non-linear advection terms and explicit source terms in this case are calculated at previous time steps where all necessary information is known Hence these schemes do not require any iteration procedure, as in Crank-Nicolson scheme to maintain the accuracy. However, when the density and viscosity vary significantly, for instance such as “turbulent premixed propagating flame”, iteration of the overall solution procedure is required to include the correct value of density in the unsteady term and viscosity in the diffusion term at the n+1 time step The advection term within one time step has to be limited to at least satisfy the Courant number, $C = u_i\Delta t/\Delta x_i < 1.0$. Simply, this criterion requires that, within a time step, information may only travel to the neighbouring cell but no further. For advection terms, the maximum time step is proportional to the characteristic convection time $\Delta x_i/u_i$, which is usually described in terms of the Courant number. For diffusion term the maximum usable time step is proportional to the characteristic diffusion time $\Delta x_i^2/v$. However, Adams methods require some treatment for the initial steps where no information about previous time step is available. Therefore, the Crank-Nicolson is used for the initial time steps to enable the calculation of the n-1 and n-2 source terms for the Adams schemes.

6.3.3 The Pressure Correction Equation

In the present study, pressure correction of unsteady compressible flow simulations have been carried out using the fractional step method based, incompressible flow pressure correction of Vankan (1986) and Bell and Colella (1989), which has been recently extended by Kirkpatrick (2002) for compressible flows It is well known that in case of compressible reacting flows, pressure and density remain coupled through the state equation and large density variations exist. Hence, it is essential to correct velocity, density and pressure simultaneously by enforcing the mass conservation of the fluid flow. Since density depends on both pressure and temperature, an iterative method is required to correct it Accordingly, considering the m^{th} iteration of the time step from $t = n$ to $t = n+1$, the transport equations of energy and reaction progress variable are solved for temperature field T^m. An approximate density field ρ^* for the m^{th} iteration is then found using the equation of the state with the temperature T^m and the pressure from the previous iteration P^{m-1} as

$$\rho^* = \frac{RT^m}{P^{m-1}} \tag{6.32}$$

The momentum equations for three velocity components are then integrated using ρ^* and P^{m-1} to find an approximate solution for the velocity field u_i^* as:

$$\frac{\left(\rho^* u_i^*\right)^{n+1} - \left(\rho u_i\right)^n}{\Delta t} = \Upsilon\left(u_i^*, u_i^n\right) - \frac{1}{2}\left[\frac{\delta P^n}{\delta x_i} + \frac{\delta P^{m-1}}{\delta x_i}\right] \tag{6.33}$$

where Υ is an operator representing the remaining terms in the momentum equation In order to correct u_i^*, P^{m-1} and ρ^* mass conservation is thus enforced through the obtained velocity field as:

$$\frac{\left(\rho^m u_i^m\right)^{n+1} - \left(\rho u_i\right)^n}{\Delta t} = \Upsilon\left(u_i^*, u_i^n\right) - \frac{1}{2}\left[\frac{\delta P^n}{\delta x_i} + \frac{\delta P^m}{\delta x_i}\right] \tag{6.34}$$

which eventually satisfies conservation of mass as:

$$\frac{\rho^m - \rho^n}{\Delta t} + \frac{\delta\left(\rho^m u_i^m\right) P^n}{\delta x_i} = 0 \tag{6.35}$$

Subtracting equation (6.33) from (6.34) gives:

$$\rho^m u_i^m - \rho^* u_i^* = -\frac{\Delta t}{2}\frac{\delta p'}{\delta x_i} \tag{6.36}$$

where the pressure correction is defined as $p' = p^m - p^{m-1}$. Taking the divergence of equation (6.36) yields:

$$\frac{\delta\left(\rho^m u_i^m\right)}{\delta x_i} - \frac{\delta\left(\rho^* u_i^*\right)}{\delta x_i} = -\frac{\Delta t}{2}\frac{\delta^2 p'}{\left(\delta x_i\right)^2} \tag{6.37}$$

Substituting equation (6.35) in the above results in:

$$\frac{\rho^m - \rho^*}{\Delta t} + \frac{\rho^* - \rho^n}{\Delta t} + \frac{\delta\left(\rho^* u_i^*\right)}{\delta x_i} - \frac{\Delta t}{2}\frac{\delta^2 p'}{\left(\delta x_i\right)^2} = 0 \tag{6.38}$$

Finally, writing the density correction in terms of the pressure correction using the state equation as:

$$\rho^m - \rho^* = \frac{p'}{RT^m} \tag{6.39}$$

Substituting equation (6.39) in (6.38) results in pressure correction equation as:

$$\frac{p'}{\Delta t R T^m} - \frac{\Delta t}{2}\frac{\delta^2 p'}{\left(\delta x_i\right)^2} = -\left[\frac{\rho^* - \rho^n}{\Delta t} + \frac{\delta\left(\rho^* u_i^*\right)}{\delta x_i}\right] \tag{6.40}$$

Once the pressure correction is evaluated, it is used to correct pressure, velocity and density as.

$$P^m = P^{m-1} + p' \tag{6.41}$$

$$\rho^m = \rho^* + \frac{p'}{RT^m} \tag{6.42}$$

$$u_i^* = \frac{1}{\rho^*}\left[\rho^m u_i^m + \frac{\Delta t}{2}\frac{\delta p'}{\delta x_i}\right] \qquad (6\ 43)$$

Hence, the pressure correction equation is spatially discretized in the similar manner to the discretization of the generic transport equation described in the earlier sections. Integrating the equation (6.40) over a control volume and applying the Divergence theorem gives:

$$\frac{p'}{\Delta t R T^m}\Delta V - \frac{\Delta t}{2}\sum\left(\Delta A\frac{\delta p'}{\delta x_i}\right)_f = -\left[\frac{\rho^* - \rho^n}{\Delta t}\Delta V + \sum\left(\rho^* u_i^* \Delta A\right)_f\right] \qquad (6.44)$$

where summation is performed over each of the faces of area ΔA, and ΔV is the volume of the cell Second order central differences are used to calculate the gradients $\delta p'/\delta x_i$ It is important to use same discretization for the pressure gradient in momentum equation and the pressure correction in pressure correction equation (6 40) This minimizes the projection error and ensures convergence if an iterative scheme is used.

The boundary condition for pressure correction equation at solid boundaries uses zero-normal gradient condition, since the mass flux across these boundaries is constant. However for outflow boundaries, a special treatment is required to reduce the pressure reflections as discussed in later sections of this chapter.

6.3.4 Solution of the Algebraic Equations

The system of algebraic equations, obtained through numerical discretization, is generally solved using linear equation solvers. The flow simulation code, PUFFIN has two solvers, namely Alternating-Direction-Implicit (ADI) solver and Bi-Conjugate Gradient Stabilized (BiCGStab) solver with a Modified Strongly Implicit (MSI) pre-conditioner. Current work has been carried out using BiCGStab to solve the momentum, scalar and pressure correction equations, which is more efficient and requires ten times less number of iterations to achieve same level of convergence by ADI (Kirkpatrick, 2002).

Convergence of the solvers is measured using the L_2 norm of the residual (L_2 norm is a vector norm that is commonly encountered in vector algebra and vector operations such as dot product). The residual was set to be less than 10^{-10} for the solution of the momentum and scalar equations, which typically required one or two sweeps of the solver to obtain convergence At each time step, a number of iterations of the pressure/velocity correction steps are generally required to ensure adequate mass conservation.

Pressure correction equation is solved for all iterations with a condition, either to reduce the residual to 10% of its original value or the BiCGStab solver has performed 7 sweeps. Each sweep of the solver includes 2 sweeps of the pre-conditioner. The solution is then used to correct the pressure and velocity field and the divergence of the corrected velocity field is calculated. The process is repeated until the L_2 norm of the divergence error is less than pre-set value. Typically, 6 to 8 projections are required to attain the minimum divergence error.

6.3.5 Typical Iteration Procedure

In case of unsteady, compressible reacting flows, where density and pressure variations are predominant, it must be ensured that the pressure, density and velocity are corrected simultaneously by enforcing mass conservation The overall solution procedure for each time step follows similar to that of Kirkpatrick (2002) for compressible flows and however, combustion modelling capabilities in LES has been enhanced using dynamic modelling of flame surface density (FSD) A typical iteration procedure requires information at current and previous time steps represented by superscripts n and n-1 respectively. In the following, superscript k refers to the iteration cycle within the time step and the superscript 0 indicates the initial guess for the first iteration with a time step i e k=0

Step 1: Predict or choose appropriate initial values for the variables at time = 0. In the present work, a straightforward choice is adopted by choosing the solution values at the current time level as:

$$u_k^0 = u_k^n,\quad \phi_k^0 = \phi_k^n,\quad \text{etc}$$

Step 2: Solve scalar transport equations to obtain provisional values, which will facilitates better estimate of the density early in the iteration process.

Step 3: Calculate the fluid properties such as temperature, density, molecular viscosity according to the combustion model implemented.

Step 4: Update the scalar field information, based on the new density available from preceding step and solve for momentum equation

Step 6: Solve the pressure correction equation.

Step 7: Correct pressure, velocity and density fields

Step 8: Check mass conservation error and repeat steps 6 and 7 as required

Step 9: Calculate eddy viscosity

Step 10: Calculate dp/dt, S_{kk}, etc

Typically 8-10 outer iterations of this procedure are required to obtain satisfactory convergence at each time step. The time step is limited to ensure that the Courant number (CFL number), C remains less than 0 5 by enforcing a limit on time advancement, δt as

$$C = \frac{\delta t u_i}{\delta x_i}$$

However, to avoid un-realistic times an extra condition has been imposed such that the upper limit for δt is 0 3 ms The solution for each time step requires around 8 iterations to converge, with residuals for the momentum equations less than 2 5e-5 and scalar equations less than 2.0e-3. The mass conservation error is less than 5.0e-8.

6.3.5.1 Numerical implementation of FSD/DFSD models

The flame surface density models detailed in Table 5.1 are implemented in the LES code, PUFFIN to calculate the sub-grid scale reaction rate and other numerical parameters such as model coefficients and fractal dimensions The SGS reaction rate calculated by these models will be added to the source term of reaction progress variable equation at every grid point and at each time step All the models are programmed in a separate subroutine and invoked during step 1 and 4, while calculating and updating scalar field iteration. It should be noted that for every time step, 8-10 outer iterations and several inner iterations are required to achieve desired accuracy At each of these inner and outer iterations, the reaction rate is calculated from the reaction progress variable information stored.

From the equations (5.15), (5.18), (5 23), (5 32), (5.34) and (5 39), it is evident that the information required is filtered reaction progress variable, filter width, test filter width, laminar flame width and SGS velocity fluctuations It is worth mentioning here that most of the information except SGS velocity fluctuations is available at step 2 at time = 0, and can be calculated without any difficulty However, calculating fractal dimension at initial step using equation (5 34) may be slightly difficult due to unavailability of the SGS velocity at that time However, due to the upper and lower fractal limitations in equation (5.34), initial values will be within these limits and will be used as initial guess. Since the solution requires a minimum number of outer iterations, the fractal dimension in case of (5 34) will be reasonable at the initial time step

6.4 Boundary Conditions

It is well recognized that besides the mathematical model and the numerical scheme, appropriate boundary conditions are important for successful LES predictions. From a mathematical point of view the imposition of exact boundary and initial values are prerequisite for unique solution of the set of partial differential equations to be solved. However, the later is not discussed in this section and will be dealt separately in chapter 7.

In the present investigation, the problem considered is a propagation of turbulent premixed flame, evolved from stagnant condition in a rectangular chamber having multiple solid obstacles. Solving premixed flames requires the boundary conditions for all the dependent variables such as density, velocity, pressure, temperature and reaction progress variable Since density is dependent on the pressure and temperature, the boundary condition for density can be specified from pressure and temperature. Continuity requires that mass conservation be satisfied over the complete domain at all times, and the boundary conditions for the velocity field must therefore ensure that:

$$\int_\Omega \frac{\partial \rho}{\partial t} dV + \int_S \rho u_i n_i S = 0 \qquad (6.45)$$

For the combustion configuration under investigation, we imposed outflow boundary conditions at outlet (top) of the chamber and solid wall boundary conditions at rest of the walls (four vertical and one bottom) and solid obstacles. The details of these boundary conditions are described in the following sections.

6.4.1 Outflow Boundary Conditions

The outflow boundary conditions generally use a zero normal gradient (ZNG) condition or a convective outlet boundary condition. The use of a zero gradient condition at an outflow boundary is generally given by:

$$\frac{\partial \phi}{\partial n} = 0 \qquad (6.46)$$

where $\partial/\partial n$ denotes the gradient taken normal to the outflow boundary. Alternatively, the convective boundary condition is also given by:

$$\frac{\partial \phi}{\partial t} + U_b \frac{\partial \phi}{\partial n} = 0 \qquad (6.47)$$

where U_b is the bulk velocity across the boundary. It is very important in case of compressible flow that the pressure wave generated within the chamber must be allowed to leave smoothly without reflection. Since the pressure field is dependent on the velocity field, the boundary conditions applied for velocity will determine the pressure wave behaviour. The outflow boundary conditions described in equation (6.46) & (6.47) work well when the dominant force on the fluid flow is due to advection and diffusion. However, in the present case (see chapter 7 for description of test case) due to the compressible nature of the propagating flame, the dominant force is the pressure gradient resulting from pressure waves radiating from the chamber. Consequently, both the above boundary conditions would result in significant pressure reflections. Hence, to overcome this problem, Kirkpatrick (2002) developed a new non-reflecting boundary condition for velocity, analogous to commonly used convective boundary condition in incompressible LES as

$$u_i = \left(u_{i-1} - \frac{\Delta x_i}{C} \frac{\partial u_{i-1}}{\partial t} \right) \frac{R_{i-1}^3}{R_i^3} \qquad (6.48)$$

where u_t is the velocity on the boundary, u_{t-1} is the velocity in the adjacent cell within the domain, Δx_t is the distance between the two nodes, R_t and R_{t-1} are the distance from the two nodes to the centre of the open end of the chamber and C is the speed of sound, which is convective velocity To ensure that this boundary condition is accurate, the numerical domain has to be extended with far-field boundary conditions from outlet of the chamber.

6.4.2 Solid Boundary Conditions

The natural boundary condition for velocity at solid wall boundaries is to set the normal and tangential velocity components to zero at the wall. These conditions correspond to the impermeable and the no-slip conditions ideally. At the domain boundaries coinciding with a stationary impermeable wall, the no-slip condition can be applied as:

$$u_i(x,t) = 0 \tag{6.49}$$

It is very important in case of turbulent reacting flows, that the near wall treatment should be accurate enough to account the boundary layer effects. In general, the flow near wall exhibits substantially different than away from it due to shear forces within the vicinity of wall. The predominant structures capable to determine the flow properties within this region are of the order of boundary layer thickness. Hence, in high Reynolds flows, it is very important to employ fine grid in the domain near wall, which eventually reaches DNS limit in order to resolve energy carrying scales Refining grid near wall in LES is not possible due to the computational limitations and alternative methods, such as wall functions are required to model the overall dynamics of the near wall effects Hence, in the present investigation, wall shear is calculated by the $1/7^{th}$ power-law wall function of Werner and Wengle (1991) as:

$$\tau_w = W(\tilde{u}, y) \tag{6 50}$$

where τ_w is the wall shear stress, W is a functional dependence, y is the distance of the grid point form the wall and $\tilde{u}$ is the tangential velocity at y. Solid boundary conditions with this wall function are applied at the bottom, vertical walls, and for solid obstacles in the chamber.

6.5 Summary

This chapter described various numerical aspects of the simulation code PUFFIN in LES. PUFFIN uses finite volume methodology, which generally allows complex geometries to form grids and solve successfully. Spatial discretization and numerical implementation of a generic transport equation of variable ϕ has been detailed Several challenges were discussed while dealing the individual terms of the generic equation Since the fluid flow numerically marches into time, time advancement of the spatially discretized equations are very important for accurate predictions Mainly, Crank-Nicholson time advancement scheme was discussed as it was used for momentum and other scalar equations Pressure correction is critical as the fluid flow involved mainly is unsteady, compressible, which generally involved in large density variations and directly coupled with pressure via state equation. Hence, a new methodology developed by Kirkpatrick (2002) is used to correct the pressure, velocity and density fields simultaneously by enforcing the mass conservation.

Various linear solvers available in the present numerical code PUFFIN were briefly outlined and the choice of BiCGStab to solve system of linear equations has been explained. Typical iteration procedure used by PUFFIN was outlined with possible modifications carried out while accounting the chemical reaction rate of the propagating flame Various boundary conditions such as solid and outflow used in the present study were also presented and discussed

Chapter 7

Test Cases and the Numerical Domain

This chapter presents description of the experimental test cases used for model validation in the present investigation. Section 7.1 describes the importance of the experimental turbulent flames and the influencing factors in design of any experimental combustion configuration. Section 7.2 describes the novel chamber established at The University of Sydney, which is a revised version and third inline to test turbulent premixed propagating flames. This chamber has reconfigurable capability, which facilitates to generate 9 configurations. A brief introduction and some technical details of the various measuring techniques and Laser ignition system are provided. Typical experimental procedure and sequence of operations are detailed in section 7.3. Finally, a numerical domain with initial conditions and ignition details are discussed in section 7.4 along with various grids employed in the numerical simulations

7.1 Influencing Factors in Designing the Combustion Chamber

Turbulence being an unsolved problem for several decades with available analytical and experimental techniques, turbulence-flame interactions complicated premixed turbulent flames as one of the very interesting and most challenging area of research. In this series, with the advancement of the numerical prediction tools and computational power, numerical techniques became an alternative method of solving turbulent fluid flow and combustion problems. In order to capture the correct physics and chemical properties of fluid flow problems, it is compulsory to validate the numerical model, method and the technique implemented against a valid experimental test case. Since the introduction of laser technology for the flow measurements into combustion studies, such as Laser Induced Florescence (LIF), Laser Doppler Velocimeter (LDV), Laser Doppler

Anemometry (LDA) and Particle Image Velocimetry (PIV), extracting the more accurate information regarding turbulence intensity and various other flow parameters made possible. However, the major challenge is to quantify these measurements of turbulence and its interactions with flame in a transient process of approximately, 10 to 20 ms duration

As described in Chapter 1, turbulent premixed flames have significant practical importance in real engineering applications. Experimental studies of turbulent premixed flames have been carried by several researchers with a variety of chambers and turbulence generating devices as detailed in chapter 2. The work presented here, mainly aims to simulate a real explosion situation, where multiple solid obstacles are presented in the path of a propagating flame, which is expected to facilitate to understand some of the remaining key challenges such as complex feedback system formed due to flame-flow interactions, local quenching due to abnormal flame stretch, flame dynamics with respect to position and number of obstacles etc However, one of the main objectives of this work is validating the novel DFSD model against experimental studies, which is expected to improve the predictions of combustion characteristics.

Since, one main objective of the current work is experimental validation of the developed model, it is ideal to choose a combustion chamber, which could provide sufficient optical access for measurements and affordable for computational modelling. It is worth mentioning here, that the original experimental chamber used by combustion groups at both Loughborough and the University of Sydney (Masri et al , 2000, Ibrahim and Masri, 2001 and Masri et al., 2006) was a big chamber of 20 litres in volume and, found to be impractical for LES modelling studies due to the long computational times Hence, an alternative design (Kent, Masri et al , 2005), that preserved the same physics and optical access, yet with a reduced volume of less than one litre is adopted in this study.

Essentially the present experimental combustion chamber is designed to represent many of the most realistic situations of the propagating turbulent premixed flames in a confined chamber, such as in a SI engine, accidental explosion situation, bluff body combustion etc. Understanding the turbulence generation, flame propagation speed and the flame interactions will help to design a better combustion device. This allows analysis of the relationship between turbulence levels and flame surface density, and the associated influence/dependence of flame front structure on turbulent burning rates to be related to other real world applications, such as prevention of loss and damage in case of accidental explosions in built-up areas. One important factor influencing the design of any experimental chamber is that, it should be easily applicable for model validations and numerical simulations. This requires well defined initial and boundary conditions and also the physical size must be affordable for numerical simulations in order to resolve the length scales (Masri et al , 2006) Additionally, good optical access is required to allow the imaging experiments to be easily performed Considering the factors stated above, the experimental chamber designed in this investigation has a simple rectangular chamber with a provision to hold a maximum of three baffle plates and a solid obstacle in the path of propagating flame.

7.2 Experimental Setup

As described in the preceding section, the experimental setup adopted in this investigation is originally developed by (Kent, Masri et al , 2005) at The University of Sydney. This vessel is the latest and third iteration (Masri and Ibrahim, 2007) of the combustion chambers used in similar experimental investigations Figure 7.1 & 7 2 illustrates the schematic representation of the vessel used in this study The combustion chamber is a Perspex square prism, with internal dimensions of 50 x 50 mm, and an overall length of 250 mm giving an experimental volume of 0.625L. The external prism is constructed from 20 mm thick Perspex walls, is used to enclose the thinner 5 mm Perspex combustion chamber. External prism encapsulates the inner chamber rigidly and adds additional strength to withstand the shock waves encountered during the explosion. The external and internal prisms are placed in between a Perspex base plate and an open vented aluminium top plate, the entire rig is then held firmly together using draw bolts.

Horizontal grooves (stations) are cut into the sidewalls at locations of 20 mm (S1), 50 mm (S2) and 80 mm (S3) downstream of the ignition point in which turbulence inducing baffle plates can be housed For this investigation, baffle plates are situated at various combinations of these locations in order to alter the turbulence generating characteristics of the flame and the flow properties The plates are constructed from 3 mm thick aluminium sheet placed perpendicular to the propagating flame front, and consist of five 4

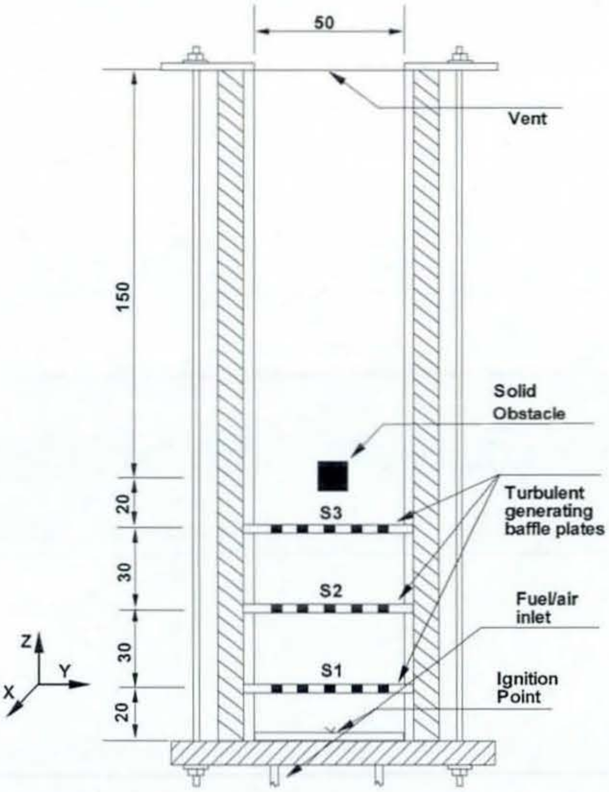

Figure 7.1 Schematic diagram of the premixed combustion chamber. All dimensions are in mm.

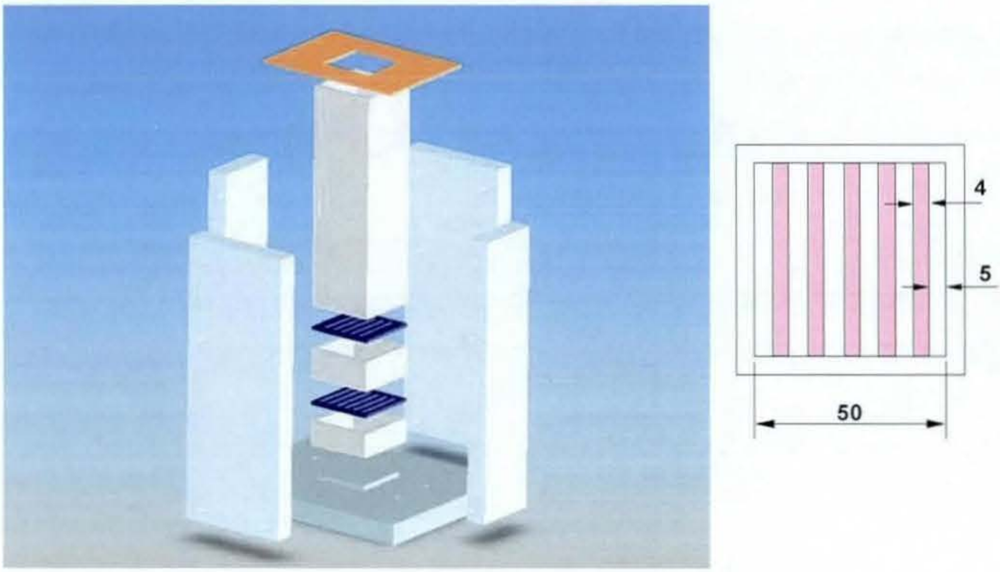

Figure 7.2 Solid diagram showing baffles, internal and external structure of setup.

mm wide strips evenly separated by six 5 mm wide spaces, rendering a blockage ratio of 40% as shown in Figure 7 2. A solid square obstacle of 12 mm in cross section with a blockage ratio of 24% is centrally located at 96 mm from the ignition point running through out the chamber, causing significant disruption to the flow. The influence of the individual obstacle in generating turbulence and flame propagation is detailed in the following section Several configurations were extracted by Kent, Masri et al. (2005), Hall (2006 & 2008) based on the number and position of baffle plates, are illustrated in Figure 7.3. Initially, LES simulations are carried using Model-1 (M1) for chemical reaction rate to establish the modelling capabilities for five configurations Later, LES simulations are carried using other models detailed in Table 5 1 for chemical reaction rate for possible flow configurations Table 7.1 presents the details of the LES simulations carried for various configurations using various models Table 7 2 presents a check list of available experimental data used in this investigation to compare LES simulations.

All experiments conducted by Kent et al. (2005) and Kent, Masri et al. (2005) are using liquefied petroleum gas (88% C_3H_8, 10% C_3H_6 and 2% C_4H_{10} by vol.), which enters through a non-return valve in the base plate at a flow rate of ~20 g/min and equivalence ratio of 1 0 To ensure all the products from previous combustion runs are cleared from the vessel, it is flushed with air before each test. The fuel air mixture then flows into the test rig for long enough time such that more than three times the volume of the vessel is supplied to purge the flame chamber and to ensure the mixture is homogenous A hinged flap closes the top of the vessel during filling. This flap, actuated via a pneumatic valve, is opened prior to ignition to allow the exhaust gases to escape, and remains open until the completion of the combustion process. The entire experimental sequence from initial filling of the vessel to opening of the flap, ignition of the mixture and operation of the LIF components is automated using computer software.

Recently, Hall (2006 & 2008) studied flow field measurements using LDV for propane/air flames of various equivalence ratios using the experimental rig shown in Figure 7.1, for number of configurations with two different (size) solid square obstacles These studies were very successful in measuring the transverses and longitudinal velocity components of the flow field. From these experiments, turbulence intensity was deduced by calculating the root mean square of the transverses and longitudinal velocity components Data from these experiments are also used here to validate LES simulations

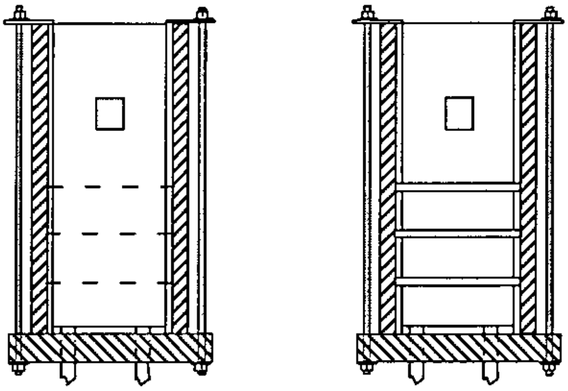

Configuration 0 **Configuration 1**

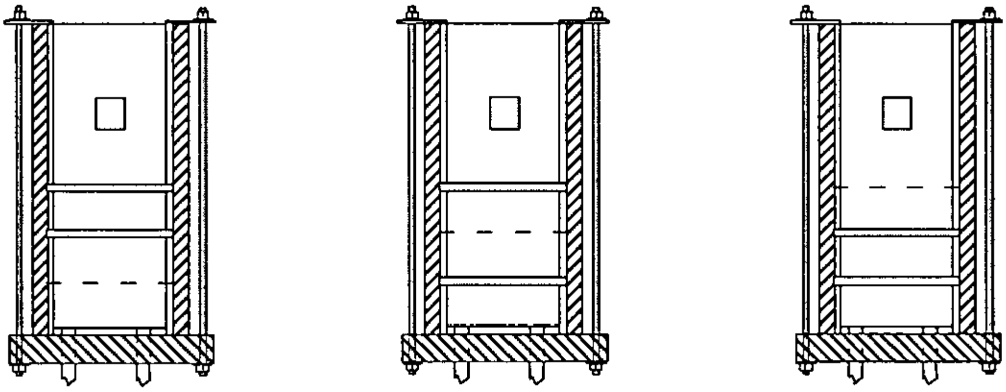

Configuration 2 **Configuration 3** **Configuration 4**

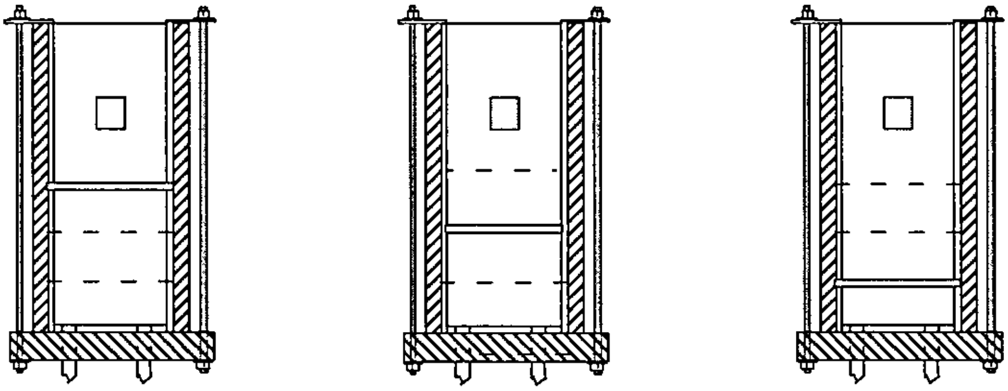

Configuration 5 **Configuration 6** **Configuration 7**

Figure 7 3 Illustration of various combustion configurations employed in the present simulations. The diagrams are not to scale.

7.2.1 Arrangement of Baffles and Solid Obstacle

Introduction of baffle plates and obstacles into the flow inside the combustion chamber serve to increase the turbulence level and flame propagation speed The position and number of the baffle plates employed with respect to the square obstacle significantly alters the generated peak pressure, flame speed and structure (Kent, Masri et al , 2005 and Masri et al., 2006) From these experimental investigations, it is found that the addition of baffle plates increases the overpressure, speeds up the flame and causes significant level of stretching in the flame front as it jets through the baffles. Higher turbulence levels increase the burning rates and hence the overpressures at an even faster rate than the flame speed. Hence large increase in overpressure can be gained through only a small increase in flame speed. In the present work, the influence of individual baffle plates and square obstacle on the flow is discussed with particular relevance on how the solid obstructions placed inside the chamber change the turbulence level and the regime of combustion.

Baffle Plate One (S1) This plate is located at 20mm downstream from the ignition closed end Due to the close proximity to the ignition point the flame speed is still relatively low, thus this obstacle only has a small affect on turbulence generation Hence re-laminarisation of the flame front shortly after this obstruction can be observed The main purpose of this baffle plate is to increase the initial propagation speed of the flame front, hence leading to a faster time to peak pressure

Baffle Plate Two (S2) This plate is located at 50mm downstream from the ignition closed end. This serves both to increase the pressure and increase the propagation speed of the flame In particular it affects the positioning of the flame front at peak overpressure.

Baffle Plate Three (S3) This plate is located at 80mm downstream from the ignition closed end. This is most effective at increasing the amount of turbulence generated within the combustion chamber. Flame accelerates at its greatest after hitting this baffle, thus increasing the amount of turbulence and flame propagation speed.

Square Obstacle (Sq. Ob.) The solid square obstacle is located at 96 mm downstream from the ignition close end. This is not a turbulence-inducing device as such but does serve to increase the blockage ratio and hence alter the development of the flame front.

Rapid acceleration of the flame is recorded past this obstruction followed by the wrapping of the flame in the recirculation region, which enhances the mixing and distortion at the flame front

Configuration	**Obstacle Positions**				**LES Simulations**			
	S1	**S2**	**S3**	**Sq. Obs.**	**M1**	**M2**	**M3**	**M4**
0	--	--	--	Y	--	--	--	✓
1	Y	Y	Y	Y	✓	✓	✓	✓
2	--	Y	Y	Y	✓	--	--	✓
3	Y	--	Y	Y	✓	--	--	✓
4	Y	Y	--	Y	✓	--	--	✓
5	--	--	Y	Y	✓	--	--	✓
6	--	Y	--	Y	--	--	--	✓
7	Y	--	--	Y	--	--	--	✓

Table 7.1 Details of LES simulations carried out for the possible configuration shown in Figure 7.3 Y indicates presence of baffle or solid obstacles

Configuration	**Overpressure**	**Flame Position**	**Velocity Measurements**	**OH images**
0	✓	✓	✓	--
1	✓	✓	--	--
2	✓	✓	✓	✓
3	✓	✓	✓	✓
4	✓	✓	✓	✓
5	✓	✓	--	--
6	--	--	--	--
7	--	--	--	--

Table7.2 A check list of experimental data available to validate LES simulations.

7.2.2 Ignition System

The fuel/air mixture in experimental chamber is ignited by using a focused laser pulse to ionize atoms in the chamber in order to create a spark. The laser system used in the present experiment allowed for a precise and repeatable ignition point with an easily definable reference time (Hall, 2006). To avoid the surface interference and to attain a higher level of consistency, laser beam are supposed to be focused just above the bottom of the combustion chamber. Two prisms are used to direct the laser beam to the focusing lens fitted into the Perspex wall as shown in Figure 7.4.

A Neodymium-doped Yttrium Aluminum Garnet ($Nd{:}Y_3Al_5O1_2$) laser is used to ignite the fuel/air mixture by focusing the infrared output onto the centre surface of the base plate. The Nd:YAG laser produces two simultaneous beams of varying wavelength, the first is the infrared spectrum and the second is a green beam (532nm). The primary role of green beam is to track the path taken by the pulse for aligning purposes as the infrared spectrum is not visible to the naked eye. An external control console is used to adjust the intensity and the frequency of the laser pulse.

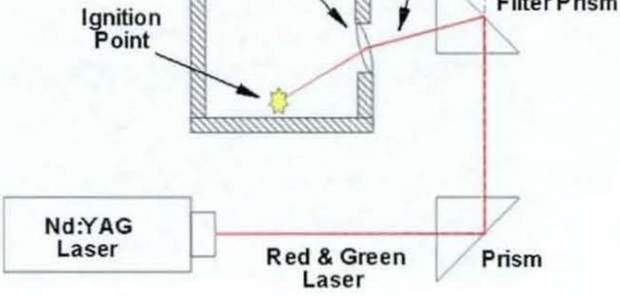

Figure 7.4 Arrangement of the Laser assisted ignition system. (Hall, 2006)

7.2.3 High Speed Imaging System

A Redlake high-speed digital camera is used to obtain images of the propagating flame. The full resolution of the camera (480x420 pixels) may be obtained at framing rates of up to 250 frames per second (fps) Due to the quick nature of the explosion event the camera was operated at 2000 fps with a shutter speed of 1/2000 seconds and an image resolution of 304x72 pixels. This resolution is convenient for the elongated chamber used in the present study, with each pixel is having about 0.8mm by 0.7mm respectively along the length and width of the chamber. After its origination the flame takes approximately 13 ms to come out of the chamber (typically in case of Configuration 1) MIDAS software is employed to records the flame images simultaneously with the pressure data, which is logged at a rate of 10 kHz. This ensures that, for the matching configurations, the same reference point with respect to timing from the ignition point is used in both experiments.

7.2.4 Pressure Transducers

The pressure is measured using piezo-resistive pressure transducers with a range of 0-1bar and a response time of 0 1ms These devices utilize quartz crystals that develop a charge relative to the pressure applied. The piezo-resistive sensor is particularly sensitive to rapid changes in pressure and hence makes it an ideal choice for this experiment. Two pressure transducers are employed to measure the pressure, one is positioned at the ignition end of the vessel and other one is positioned after the square obstruction from ignition point The pressure signals measured from both the transducers confirms to follow the same trend with slight variations However, overpressure details used in this work to compare LES simulations used the base pressure transducer, unless otherwise stated.

7.2.5 Laser Doppler Velocimeter

Recently, Hall (2006) employed Laser Doppler Velocimeter (LDV) technique to extract the flow field measurements. LDV allows a direct qualitative analysis of particles in a flow as they enter the focal area Each realisation of the LDV measures the instantaneous transverse and longitudinal components of velocity Root mean square (RMS) velocity can be calculated from these instantaneous velocity components, which indicates the turbulence intensity present in the flow.

LDV system consists of an Argon Ion Laser, which produces the beams will be directed into a separate box to turn the wavelength and focus the laser. After the laser has been filtered, a fibre optic cable is used to transfer the laser to the combustion chamber. The LDV system requires two beams to focus inside the combustion chamber at the location of interest perpendicular to the direction of propagation. Both wavelengths, 488nm (blue light) and 514.5nm (green light) are then scattered by the seeding particles, which is Talcum Powder (Hydrous Magnesium Silicate – $Mg_3\ [Si_4O_{10}](OH)_2$) in this case and received by the photo detector which is mounted at 180° to the emitter

7.2.6 Laser Induced Fluorescence of OH

Planar Laser Induced Fluorescence from the hydroxyl radical, OH (LIF-OH) is performed using a typical arrangement with a Pulsed YAG laser (Spectra-Physics DCR-2A) used to pump a Pulsed Dye Laser (Spectra-Physics PDL-2). The beam is then passed through cylindrical optics to form a thin sheet of approximately 200μm thick which illuminates the viewing region. The laser is positioned 110mm downstream pointing through a 1-inch diameter quartz-viewing window with the CCD camera placed at a right angle with the lens pointing through a second quartz-viewing window The experimental test rig with CCD camera and viewing windows can be seen in Figure 7.5 & 7 6

The exciting wavelength is 282.93nm with the LIF being collected at 310nm on a CCD camera using 648x595 pixels imaging an area of 28x23mm (Kent, Masri et al , 2005). The timing is such that the LIF measurement is made just when the flame front is crossing the imaging window. Since the OH is formed in the reaction zone of the flame and is rapidly quenched by cold un-reacted gases, it is a good indicator of the flame front position in flames where the reaction zone is thin (Kaminski et al., 2001). Hence this technique is suitable for use with a premixed turbulent flame front, giving negligible perturbation of the flow whilst attaining high temporal and spatial resolution (Kaminski et al., 2000).

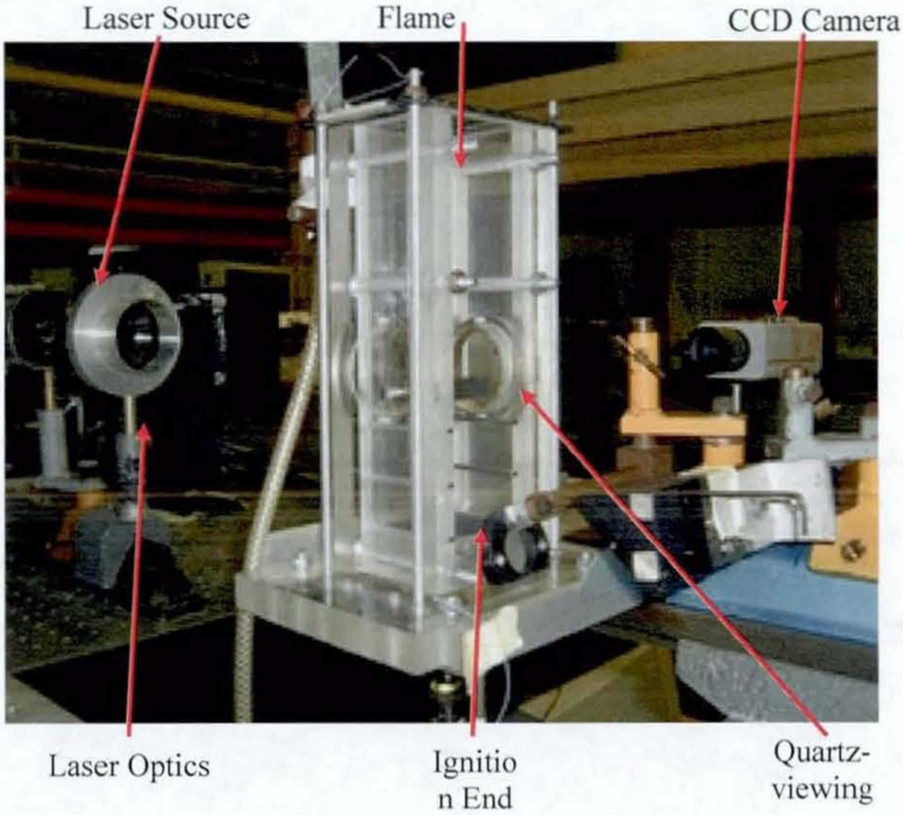

Figure 7.5 Experimental Setup of LIF-OH (Kent et al. (2005)).

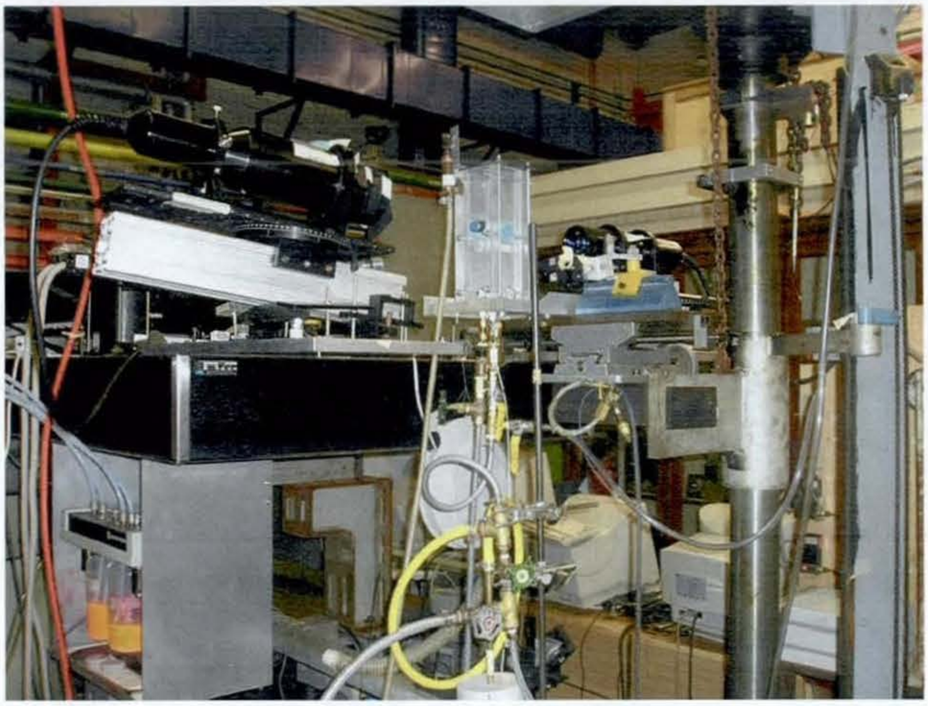

Figure 7.6 Plate showing the experimental rig of turbulent premixed combustion chamber (Hall, 2008).

7.3 Experimental Procedure

The entire experimental sequence is controlled by a computer, operating all equipment and solenoid valves in a predetermined sequence. The fuel/air mixture is directed to the combustion chamber either directly or bypassing via the seeding vessel and finally straight out to the exhaust The technical issue involved in directing the fuel/air mixture through the various way points as the experiment progresses, arises due to the seeding of the fuel before it enters the chamber. This may corrupt the outcome of the experiment. However to avoid the risk of corruption of the results, two sets of two-way valve are used in series as shown in Figure 7.7, which are also operated by the computer. Both the ignition laser and the LDV system are also controlled by a computer to enable a base timeframe for the collection of the data.

7.3.1 Typical Experimental Sequence

As a typical experimental procedure is involved in co-ordinating several systems, such as fuel direction system, high speed imaging system, pressure transducers, Laser system for ignition and for flow measurements, entire sequence is controlled and the data is collected by three computers.

Step 1: Before starting the experiment, the LDV system needs to be prepared by warming up, and will remain on indefinitely as long as the cold cooling water is continually supplied. Power output of the LDV can be controlled by an external console by setting the current to 25 amps to maintain a power of 4.5 W.

Step 2: Cooling of the ignition system should be initiated before firing the laser into the combustion chamber. Laser must be fired at the centre of the chamber approximately 2 mm above the lower surface to avoid the interference and damage to the base Perspex plate The frequency of the Laser should be adjusted by an external control box, to ensure a spark is produced every pulse

Step 3: To ensure the fuel/air mixture supply into the combustion chamber, turn on the fuel at the gas bottle and the compressed air.

Step 4: Turn on the mass flow meter and confirm the pipes and valves are not leaking A digital flow controller controls the quantity of the fuel/air mixture entering the combustion chamber Sufficient time is allowed to settle the fuel/air mixture in order to achieve quiescent conditions before ignition

The entire system works from three independent computers, a Mac and two PC's, which are not networked and must be operated simultaneously to collect the data for each run. The Mac is responsible for running the experiment from the programmed macro, while the first PC was connected to the LDV system and the second connected to the pressure sensor and high speed imaging system Both PC's are responsible for correlating all the results.

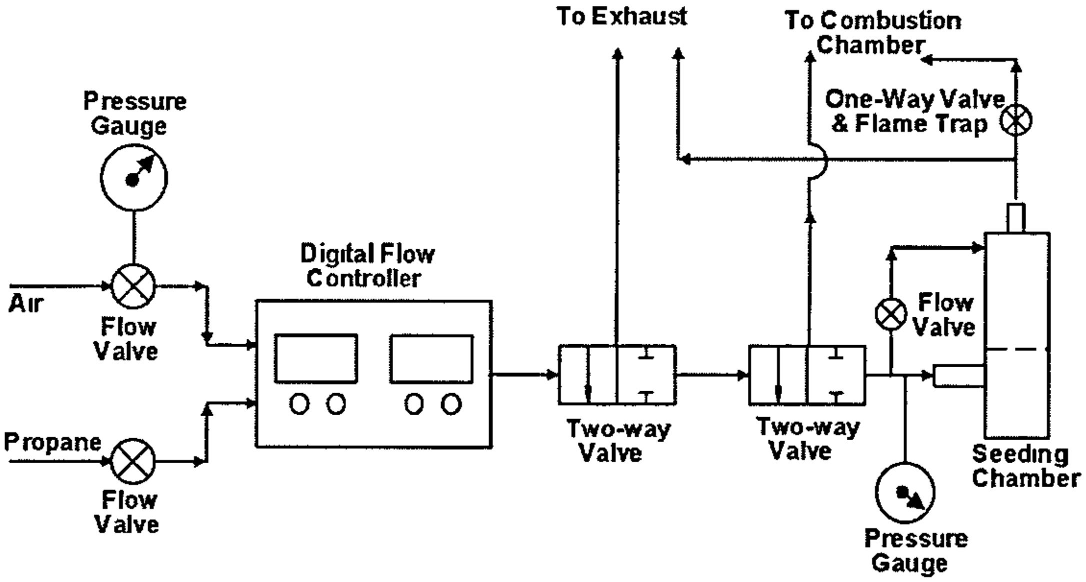

Figure 7.7 Two-way valve fuel/air direction system (Hall, 2006).

7.4 Numerical Domain

In order to simulate the turbulent premixed flame of stoichiometric propane/air flame, in the combustion chamber shown in Figure 7.1, a computational domain with initial and boundary conditions is required. As described in preceding chapter that in case of compressible flows, the domain must extended in the direction normal to outflow boundary to avoid the pressure reflections. However, to avoid certain numerical instabilities, in general, the domain is extended in the other two directions as well A typical computational domain, superimposed with numerical combustion chamber and obstacles is shown for clarity in Figure 7.8. The combustion chamber has dimensions of 50 x 50 x 250 mm where the flame propagates over the baffles and solid obstacle surrounded by solid wall boundary conditions To ensure that the pressure wave leaves the chamber smoothly, without reflections, the open end of the domain is extended to 250 mm in *z*-direction with far-field boundary conditions. Similarly, the domain is extended to 325 mm in *x*, *y* directions with large expansion ratios, approximately equal to 1.25 outside the combustion chamber.

The simulations are carried out for 3-D, non-uniform, Cartesian co-ordinate system for a compressible flow, having low Mach number In order to examine the solution dependence on grid resolution, simulations are performed with four different grid resolutions as detailed in Table 7.3 All calculations are performed on a Viglen Genie computer having a Xeon® processor, with 3 GB RAM Typical running times are also provided in Table 7 3 for clarity

7.4.1 Initial Conditions

Initially i e. at the time of starting new simulations, the energy and reaction progress variable are set to zero everywhere in the computational domain. The initial velocity field is quiescent, with random perturbation field to allow for development of turbulence. In order to achieve the initial quasi-laminar flame phase corresponding to experiments, ignition is modelled by setting the reaction progress variable to 0.5 within the radius of 4 mm (Bradley and Lung, 1987) at the bottom centre of the chamber.

7.5 Summary

This chapter summarizes influencing factors in designing an experimental combustion chamber and the challenges faced in the past due to large scales experimental test rigs. A novel chamber that has recently been developed by The University of Sydney Combustion group that can retain the combustion physics with good optical access has been discussed. Details of the individual obstacles used and their influence in generating turbulence and overpressure of the propagating premixed flame were discussed. Brief details of various measurement devices such as LDV, LIF-OH and techniques such as ignition control, image capturing were presented and discussed. A typical experimental sequence controlled by computer has been illustrated through a flow diagram. Finally, the numerical domain, initial condition and various grid resolutions employed in the present simulations were described and justified for use in the current work.

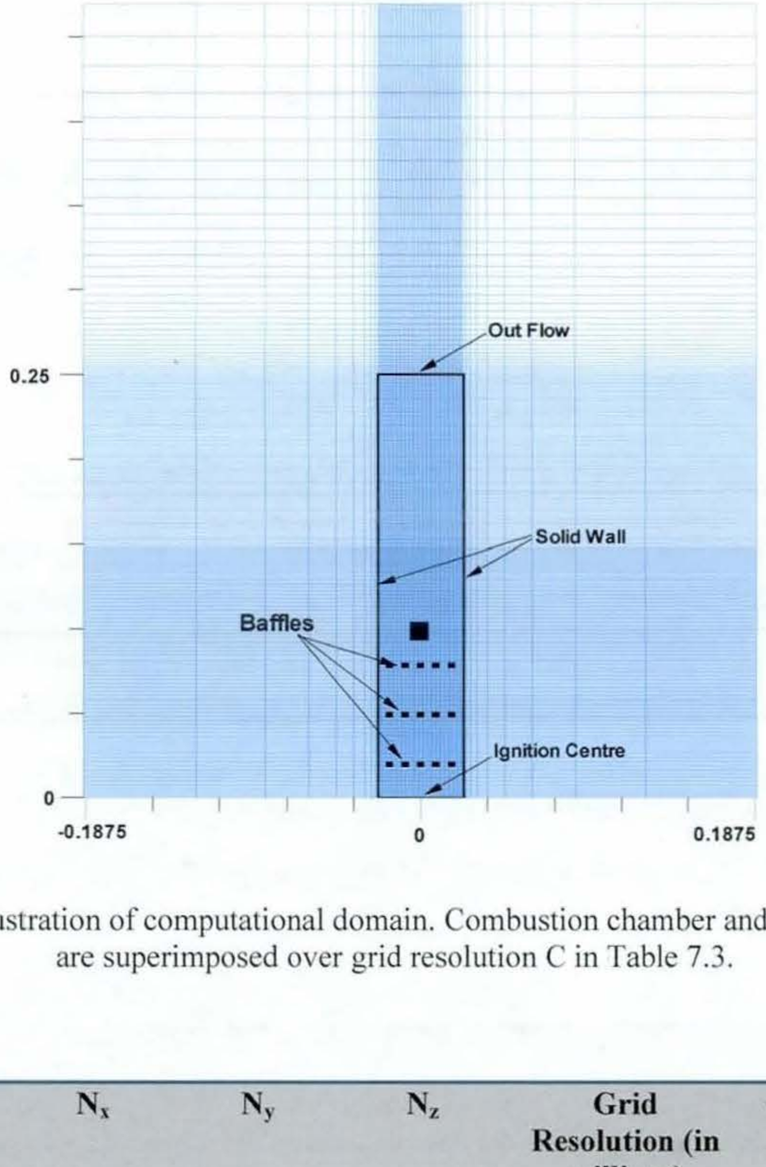

Figure 7.8 Illustration of computational domain. Combustion chamber and other obstacles are superimposed over grid resolution C in Table 7.3.

Grid	N_x	N_y	N_z	Grid Resolution (in millions)	Cost in days of computational time
A	40	40	156	0.25	3
B	54	54	190	0.55	6
C	90	90	336	2.70	32
D	90	90	448	3.62	68

Table 7.3 Grid resolutions employed in the present study. N_x, N_y and N_z are the number of nodes in the x, y and z direction respectively.

Chapter 8

Results and Discussions

8.1 Introduction

This chapter presents results from the LES simulations of stoichiometric propane/air turbulent premixed flame, propagating over various solid obstacles in a confined chamber As discussed in the previous chapter, model validation is made against experimental data obtained from Kent et al (2005) and Hall (2006 & 2008) This chapter is structured as follows:

First, LES simulations have been carried out using FSD model (Eq. 5 15) for configuration 1 to identify the influence of solid obstacles on turbulence generation and flame characteristics. Further numerical optimisation studies are also considered using configuration 1.

Secondly, grid independency tests have been carried out using the FSD model for configuration 1. Furthermore, other numerical aspects such as influence of filter width and the energy resolved in LES are studied and discussed.

The grid independent solution is then used to analyse the flow and flame structure during different phases of flame propagation from ignition to completion of combustion Various velocity and length scales have been extracted from the LES simulations in order to identify the turbulent premixed combustion regime in the current combustion chamber

More model validation has been carried out for a wide range of experimental configurations. Advancement to the simple FSD model has been implemented by adopting a self-scaling model based on fractal theory Detailed analysis of the turbulent flame using self-scaling of the model coefficient has been discussed

The newly developed dynamic FSD model (DFSD), which is the main motive of this research has been validated against various flow configurations shown in Figure 7 3

Finally, parametric studies have been carried to examine the influence of the position and number of the solid baffles on the flame structure and the generated overpressure.

8.2 Results from the Algebraic FSD Model

In this section, results from LES simulations of turbulent premixed flames, propagating past solid obstructions built inside in an open end rectangular combustion chamber, shown in Figure 7.1 are presented Here, the model used is the algebraic FSD model (Model-1) Various parametric studies have been carried out to establish confidence in using the LES methodology to simulate turbulent premixed flames From experimental studies of Kent et al (2005), it has been identified that the overpressure and turbulence levels are very low in configuration 0 and not much insight was extractable, when compared to a more complex configuration such as configuration 1 shown in Figure 7 3. Hence, this analysis has been carried out using the complex configuration 1 having three baffles and a square solid obstacle shown in Figure 7.1. Kent et al (2005) identified that configuration 1 has yielded maximum overpressure with a highly stretched turbulent flame. This was due to the presence of multiple solid obstacles. For this reason, configuration 1 has been chosen to simulate and optimise various parameters such as grid resolutions, filter width etc Further to this, studies have been extended to simulate other flow configurations to understand flame flow interactions.

8.2.1 Grid Independency Tests

The grid independency, in numerical simulations is a much debatable and controversial topic (Klein, 2005) as it depends on many numerical and physical aspects, especially in LES. However, in numerical modelling, it is desirable to achieve substantial uniqueness of results, independent of the grid resolution employed. Hence, in the present investigation, LES simulations of turbulent propagating premixed flames have been carried out by refining the grid employed for configuration 1, as detailed in Table 7.3. Case A consists of 0 25 million, case B has 0 55 million, case C has 2.7 million and case D has 3 6 million grid points in the computational domain shown in Figure 7 8. All these simulations are carried out using the simple algebraic flame surface density model (Model-1) with the model coefficient, $\beta = 1.2$. The pressure-time histories of the overpressure near the closed ignition end of the chamber are considered here as bench mark to assess the grid dependence of the LES results. Pressure-time histories for cases A, B, C and D are presented together with the experimental data (Kent et al , 2005) in Figure 8 1.

From Figure 8.1, it is evident that grids A and B show an initial increase in overpressure at 5 and 6ms after ignition, respectively, while this instant correspond to 8 ms for grid C and D, which is in reasonable agreement with experimental measurements. This initial increase in overpressure in cases of grid C and D correspond to the time where the flame is due to interact with the third baffle plate (see Figure 7.1) It can also be noticed, that the slope of the peak overpressure using grids C and D is well calculated Evidently, these calculations are confirming the peak overpressures of 110 and 102 mbar, occurring at the same time i.e 11 1 ms for grids C and D, respectively. Based on the peak overpressure and its time of incidence, LES results can be considered grid independent, beyond the grid resolution C However, LES calculations with grids C and D found to under-predict the experimental peak pressure of 138 mbar occurring at 10 3 ms after ignition It is identified that this may be mainly due to two reasons; firstly due to the usage of a constant for the model coefficient β and secondly due to the use of the algebraic flame surface density model, which is further discussed in later sections of this chapter However, grids C and D are in reasonable agreement with the experimental data in terms of the rate of pressure rise and overpressure trend. Further to this, influence of the filter width on the grid independency is studied and discussed in the following section.

8.2.2 Influence of the Filter Width

The accuracy of the solution in LES is associated with several numerical and modelling parameters such as grid spacing *h*, filter width $\bar{\Delta}$, discretization schemes, solver, initial and the boundary conditions employed. For a given discretization scheme, solver, initial and boundary conditions, the remaining critical numerical parameters that affect the LES solution are the grid spacing and the filter width. Filtering the flow field for large eddies by choosing an appropriate and optimal filter width does resolve the maximum amount of turbulence kinetic energy, which is a unique concept and distinguishes LES from other modelling techniques such as RANS and DNS. In the present investigation, a box filter presented in equation (4.6) is used.

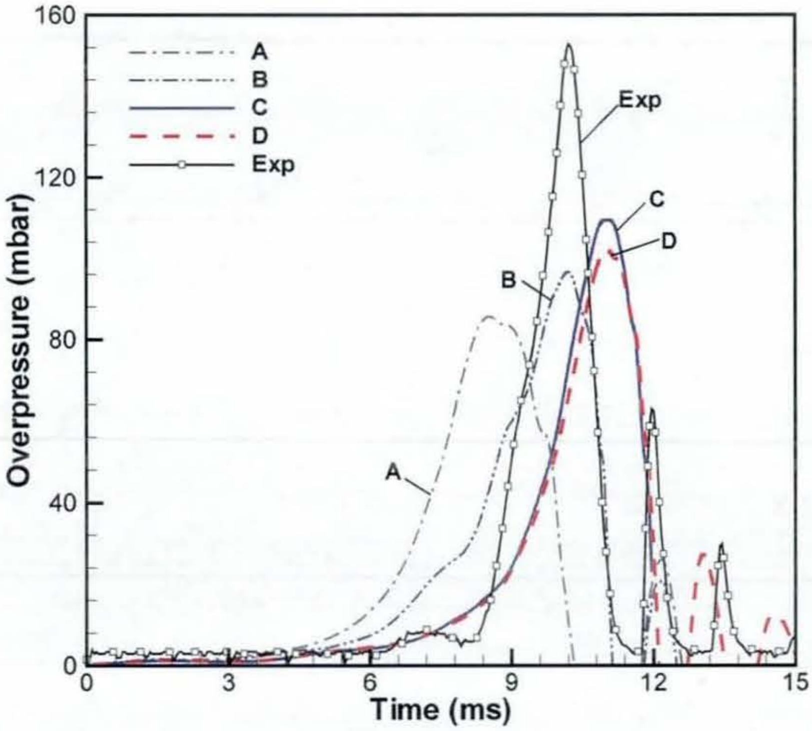

Figure 8.1 LES predictions of overpressure-time histories using various grid resolutions detailed in Table 7.3 are compared with experimental measurements.

In a conceptual study, Pope (2004) hypothesizes that LES solution may reach an intermediate asymptote when the filter width lies within the inertial sub-range. The relationship between grid spacing and filter width has been studied as a ratio of $h/\overline{\Delta}$ by Vreman et al. (1996) and Chow and Moin (2003) for non-reacting cases. Their studies concluded that small values of $h/\overline{\Delta}$ correspond to excellent numerical accuracy and the higher values correspond to resolving a greater range of turbulence motions with less numerical accuracy. Vreman et al. (1996) and Chow and Moin (2003) identified that, with a specified SGS model for turbulence, $h/\overline{\Delta} \leq 0.25$ with second order spatial accuracy or $h/\overline{\Delta} \leq 0.5$ with sixth order spatial accuracy has given numerically accurate solutions.

Parameters	**A**	**B**	**C**	**D**
δx (mm)	2.0	1.47	0.75	0.75
δy (mm)	2.0	1.47	0.75	0.75
δz (mm)	1.0 – 2.0	1.0 – 1.75	0.75 – 1.0	0.48 – 0.75
$\bar{\Delta}$ (mm)	3.17 – 4.0	2.60 – 3.12	1.5 – 1.65	1.29 – 1.5
$h/\bar{\Delta}$	0.32 – 0.5	0.39 – 0.56	0.5 – 0.6	0.37 – 0.5
L_f (mm)	0.294	0.294	0.294	0.294
$\bar{\Delta}/L_f$	10.8 – 13.6	8.78 – 10.6	5.10 – 5.61	4.40 – 5.10
Peak pressure (mbar)	85.6	96.7	110.0	102.0
Time (ms)	8.5	10.2	11.1	11.1
Flame speed (m/s)	62.3	88.3	81.8	81.0
Flame position (cm)	12.0	17.8	17.9	18.2

Table 8.1 Details of the numerical parameters employed and results deduced from LES simulations with various grid resolutions for the configuration shown in Figure 8.1.

Examination of this fact in case of reacting flows is computationally very expensive and requires an extensive experimentally validated DNS solution.

In the present work, numerical investigation has been made to examine the dependency of the numerical accuracy on the filter width. Two important ratios associated with the filter width, $\bar{\Delta}$ have been selected. Firstly, the grid spacing to the filter width as discussed earlier and second is the filter width to the laminar flame thickness. Grid spacing, h in the present study is not uniform and generally varies in the direction of flame propagation i.e. z-axis. Therefore all the relevant estimates used here are calculated using the grid spacing in flame propagating direction and are presented in Table 8.1.

For grids A, B, C and D, the $h/\bar{\Delta}$ ratio is plotted against filter width as shown in Figure 8.2. Correlating Figures 8.1 and 8.2, elucidates the fact that the accuracy of the solution is improved in terms of overpressure inside the chamber, as $h/\bar{\Delta}$ ratio tends to zero with respect to filter width. Referring the time traces of the overpressure shown in Figure 8.1 for all the four grids, the dependency of the numerical accuracy on grid spacing is very clear. Considering the $h/\bar{\Delta}$ ratio from the Table 8.1 for grids A, B and D, it can be noticed that, they are identical in range and the accuracy of the solution D is in close agreement with the experimental measurements. From the time history of overpressure for case C and D shown in Figure 8.1, it is evident that the solution is grid independent in terms of occurrence of peak overpressure. However, the $h/\overline{\Delta}$ ratio for grid C is 0.5 to 0.6 and is different from the values from grid D, which vary from 0 37 to 0.5 This analysis clearly shows the dependency of the numerical accuracy on the filter width It is evident from Table 8.1, that even a small change in $h/\overline{\Delta}$ is affecting the accuracy of the solution. Clearly the $h/\overline{\Delta}$ ratio is demonstrating the fact of improvement in the accuracy of the solution as the value of $h/\overline{\Delta}$ starts diminishing.

Considering the second ratio from Table 8.1, i e the filter width to laminar flame thickness, $\overline{\Delta}/L_f$ for grid A, it ranges from 10 8 to 13 6, and for grid B it ranges from 8 78 to 10.6 compared to 5.10 to 5 16 for grid C and 4.40 to 5 10 for grid D. Here L_f is the calculated strained laminar flame thickness and this is different from the unstrained laminar flame thickness, L_{f0} which is a specified input parameter (L_{f0} = 0.3mm). Figure 8.3 shows $\overline{\Delta}/L_f$ ratio with filter width for four grids employed in this simulations By correlating Figure 8.3 with Figure 8.1, it should be noted, that the accuracy of the solution improved as the $\overline{\Delta}/L_f$ ratio diminishes Further analysis can be carried by halving the mesh size ($\delta_{x2}, \delta_{y2}, \delta_{z2}, \Delta_2$) such that $\overline{\Delta}/L_f$ is also halved but remains larger than about 3.0. At $\overline{\Delta}/L_f \sim 3$, it is expected that the DNS limit is reached and this is not practical when dealing with real combustors It should be pointed at this stage that, as $\overline{\Delta}/L_f$ changes from 5 10-5.16 in grid C to 4 40-5.10 in grid D, the total cost of solutions (CPU time in days) has doubled (Table 7.3) So it is essential to ensure that the filter width remains sufficiently larger than the strained laminar flame thickness It can be seen from the estimates presented in Table 8 1 that L_f is more or less constant for propane/air flame and the filter width is one of the critical parameter, which can control the numerical accuracy.

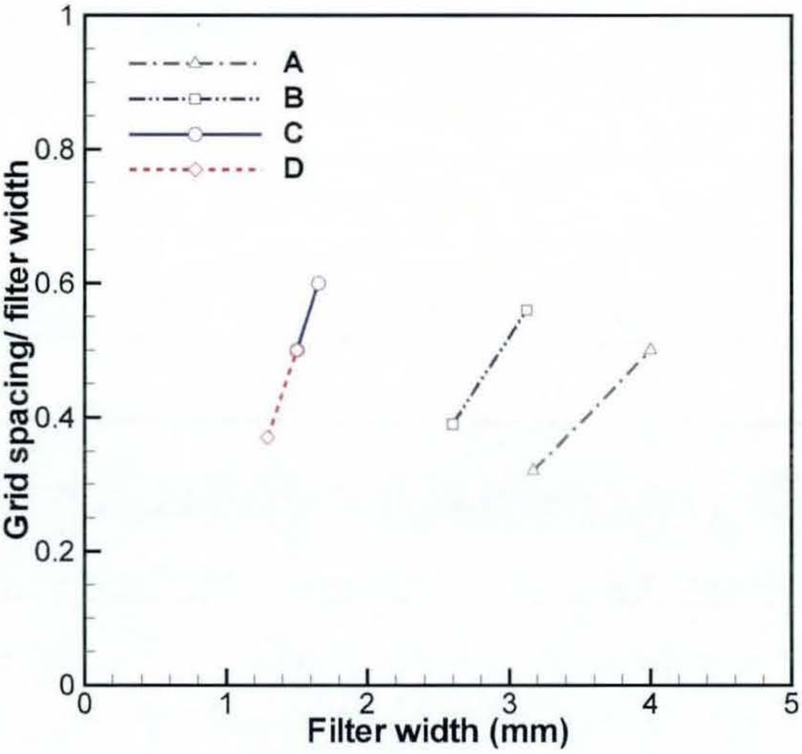

Figure 8.2 Ratio of grid spacing to filter width ($h/\overline{\Delta}$) versus filter width. Estimates are shown in Table 8.1.

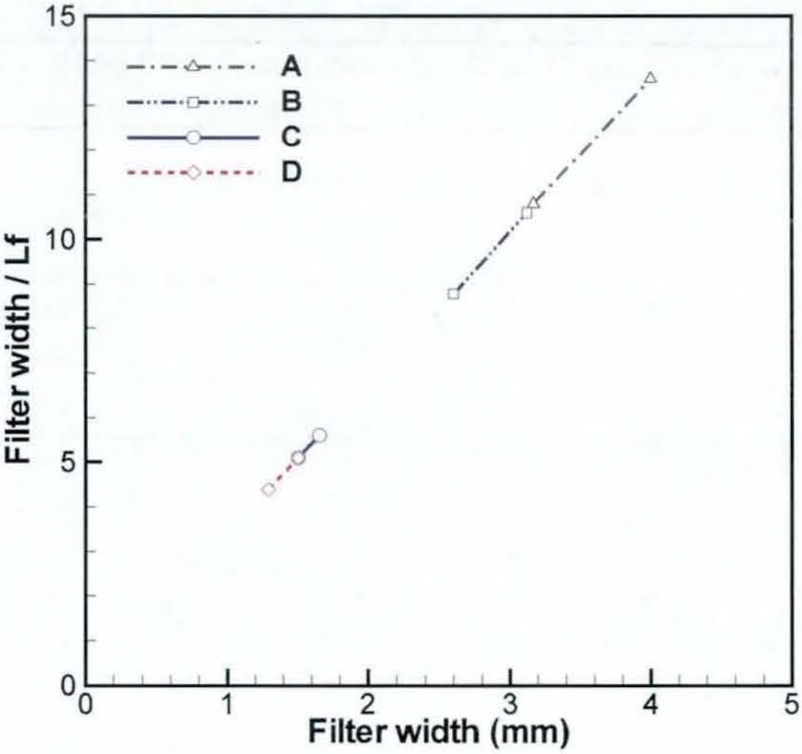

Figure 8.3 Ratio of filter width to strained laminar flame thickness ($\overline{\Delta}/L_f$) versus filter width.

8.2.2.1 Influence of Filter Coefficient, α_4

Given an optimal and affordable grid resolution, one can obtain better numerical accuracy by reducing the filter width. However it should be noted here that the LES simulations under investigation are involved in "implicit filtering" (Schumann, 1989) and is difficult to achieve in practice without the refinement of grid, as it is directly associated with grid resolution as given in equation 4.6. An alternative and more feasible approach is explicit filtering (Chow and Moin, 2003) which involves decoupling the filter width from the grid resolution. For turbulent premixed combustion, the explicit filter width may be expressed in terms of the sub-grid scale flame and flow structures such as laminar flame thickness, flame speed and characteristic sub-grid scale velocity fluctuations.

Just to verify the above fact, we introduced a filter coefficient α_4 in the filter width formulation as:

$$\overline{\Delta} = \alpha_4 \left(\Delta x \Delta y \Delta z \right)^{1/3} \tag{8.1}$$

The filter coefficient α_4 can be any value ≥ 1 such that it satisfies the ratio $\overline{\Delta}/L_f \geq 3$ in order to avoid the DNS limit. Nevertheless, four additional simulations have been carried out using grid C to verify the influence of filter width coefficient on numerical accuracy by varying the value of α_4 from 1.0 to 2.0 with an interval of 0.25. Figure 8.4 shows the pressure-time histories from LES simulations using various filter coefficient values.

Figure 8.4 clearly indicates that, there is no significant improvement in the pressure-time history, by changing the value of the filter width coefficient. It can be seen that, the pressure-time histories from the simulations using α_4 from 1.0 to 1.75 are overlapping when α_4 is equal to 2.0. As explained earlier, this phenomenon is due to the implicit filtering approach used in the present simulations.

From the above analysis, the ratios $h/\overline{\Delta}$ and $\overline{\Delta}/L_f$ have identified the filter width, as a key factor in assessing the numerical accuracy of LES. It is also identified that, in governing the numerical accuracy, filter width has a restricted role due to the type of filtering approach employed, which is directly linked to the grid resolution. However, filt-

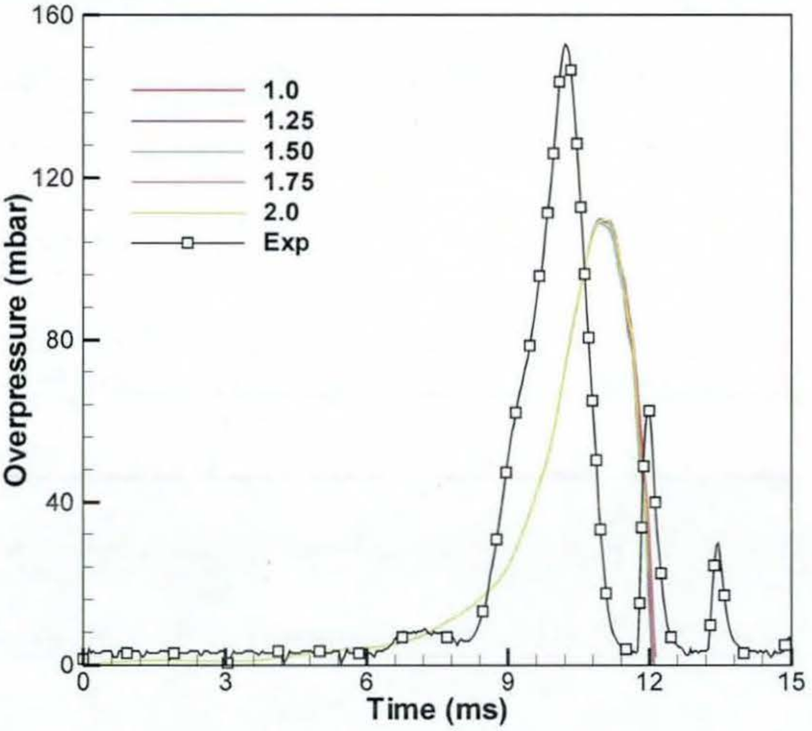

Figure 8.4 Pressure-time histories from LES simulations using grid C, with various filter coefficient values as shown in legend.

er width determines the portion of turbulence kinetic energy resolved, irrespective of the type of filtering approach, which is another key ingredient for good LES. In the present investigation, calculations have been made to estimate the resolved turbulence kinetic energy as described in the next section.

8.2.3 Turbulent Kinetic Energy Resolved in LES

Based on the definition of LES, the quality of any LES simulation is dependent on the percentage of the resolved turbulence kinetic energy. Recently, Pope (2004) hypothesised the importance of the resolved turbulent kinetic energy and identified that a qualitative, valid LES solution must resolve above 80% of all the flow scales. Encouragingly Kempf et al. (2006) tested this fact for LES of non-premixed flames over bluff bodies. However, there is no evidence to substantiate and correlate the percentage of resolved kinetic energy with grid independency. In the present work, the quality of LES simulation is tested and correlated with grid independency by calculating the resolved and modelled kinetic energy for grids C and D at various realizations. At any realization the "percentage of resolved turbulent kinetic energy, η" can be calculated as:

$$\eta = \frac{k_{res}}{k_{tot}} = 1 - \frac{k_{sgs}}{k_{tot}} \tag{8.2}$$

where k_{res} is resolved turbulent kinetic energy, k_{sgs} is SGS or modelled kinetic energy and k_{tot} is total kinetic energy, which is summation of resolved and modelled kinetic energy. As the SGS kinetic energy is not directly accessible, it can be extracted from the SGS eddy viscosity given in equation (4.22) (Kempf et al., 2006) as:

$$k_{sgs} = \frac{1}{\left(C_s\bar{\Delta}\right)^2}\nu_{sgs}^2 \tag{8.3}$$

It is worth noting at this stage that, C_s is the dimensionless Smagorinsky coefficient and is dynamically calculated from the instantaneous flow conditions. These values are stored and post-processed to evaluate modelled kinetic energy.

The percentage of the resolved turbulence kinetic energy from grids C and D at five instants between 8.0 to 10.0 ms as shown in Figure 8.5 is considered. The overpressure and rate of pressure rise during this period is overlapping for both the grids as shown in Figure 8.1, so this time-phase might have influenced the development of different pressure peaks at later stages of flame propagation. Evidently it is observed that, both grids have captured more than 75% energy during these instants and the pattern of the resolved energy is more or less similar with very few differences. This is again confirming the grid independency of the LES solution beyond grid resolution C. However the difference in the peak overpressures might be due to the use of the simple algebraic FSD model.

8.2.4 Flame Characteristics: Configuration 1

From the grid independency tests it is identified that results of grid C with 90x90x336 grid points in the *x*, *y*, *z* computational domain, is in reasonable agreement with experimental measurements and beyond this grid resolution, the solution is considered as grid independent. Hence, LES calculations using grid C are considered in the present section for further analysis of flame structure, location and speed. In order to facilitate a detailed analysis of the flame structure and identify the regimes of combustion, the combustion chamber has been divided into five regions of interest as shown in Figure 8.6. Within these regions, data from the LES simulations has been extracted as provided in Table 8.2 to verify the applicability of the laminar flamelet concept for the present study.

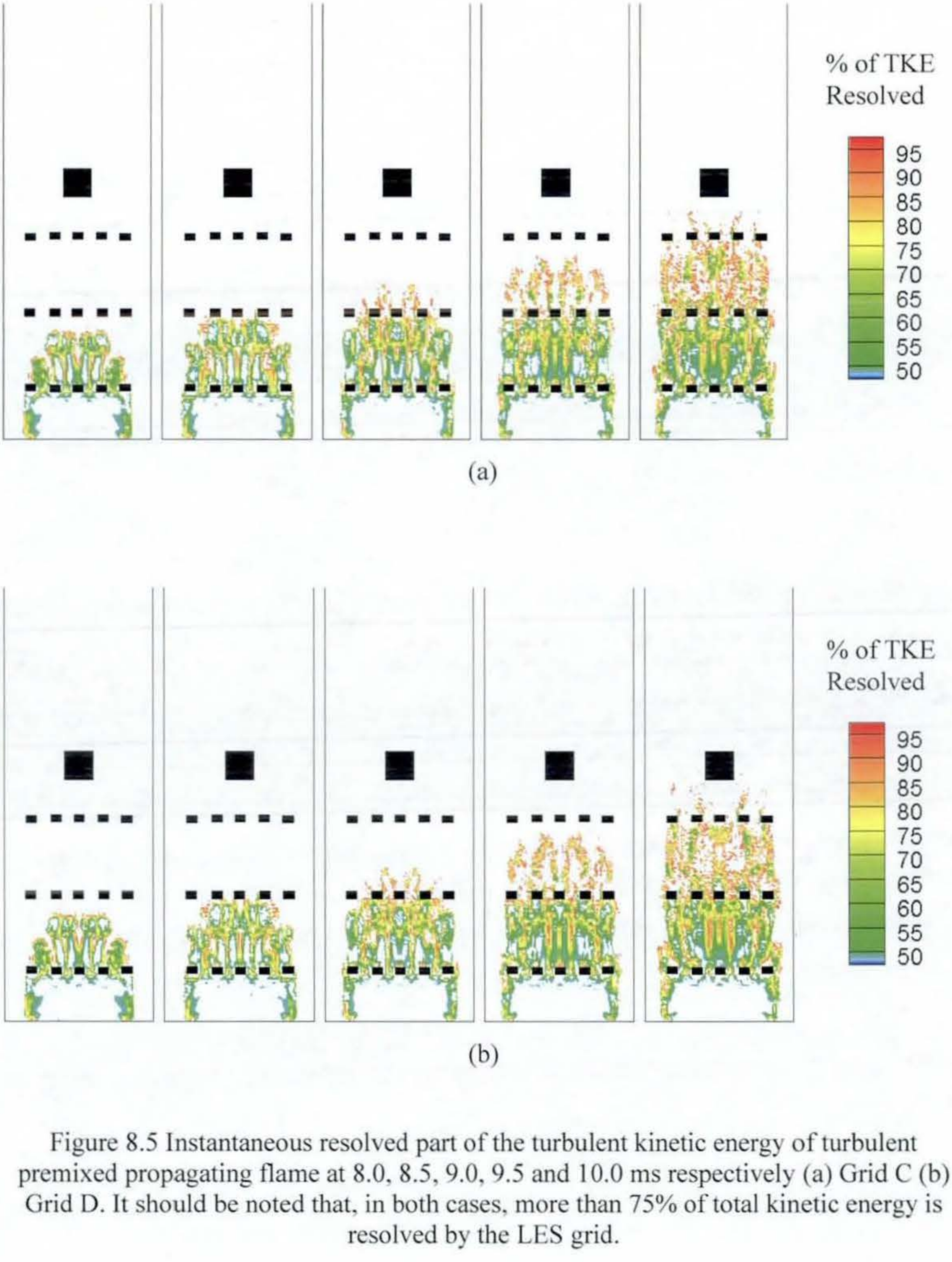

(a)

(b)

Figure 8.5 Instantaneous resolved part of the turbulent kinetic energy of turbulent premixed propagating flame at 8.0, 8.5, 9.0, 9.5 and 10.0 ms respectively (a) Grid C (b) Grid D. It should be noted that, in both cases, more than 75% of total kinetic energy is resolved by the LES grid.

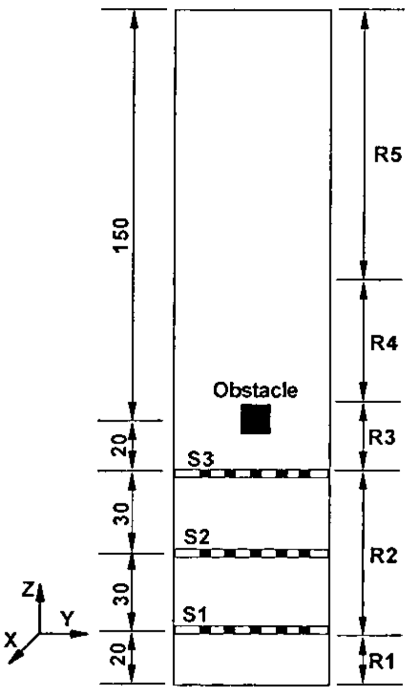

Figure 8 6 Region of interest along the combustion chamber. All dimensions are in mm.

8.2.4.1 Flame Characteristics and Generated Overpressure

Results from LES simulations together with experimental measurements are shown in Figures 8.1, 8.7, 8 8 and 8 9. The time histories of the overpressure for various grids are shown in Figure 8 1 As shown, grids C and D provide reasonably accurate values for the overpressure and its trend with time. As discussed earlier, since there is no significant improvement beyond grid resolution C, further analysis is carried out using grid C only.

In order to validate the LES predictions, flame characteristics such as flame location, speed and structure are extracted from experimental video images Figures 8 7, 8 8 and 8 9 show LES and experimental data for the flame position, speed with time, and flame speed with position respectively. From LES calculations, the flame position is obtained by locating the farthest point of the leading edge of the flame front, from the ignition bottom end (defined here as the most down stream location of the flame from the ignition point, where $\tilde{c}$ = 0 5) The flame speed is derived from the rate of change over successive images of the flame location at the leading edge of the flame furthest from the ignition point It should be noted here that the experimental measurements are analyzed from high speed video recorded (2000 fps) images, where there is a time limitation of 0 5 ms between two consecutive frames, which is considered here as the bin size for relevant LES estimates

From Figure 8.7 it can be seen, that the flame position at various stages of the flame propagation is well predicted. Similarly from Figure 8.8 & 8.9, it can be identified that the flame speed either with respect to time or flame position is well reproduced by grid C and is in very good agreement with experimental measurements The calculated and measured data confirm that the peak overpressure occurs during the reconnection of the flame (see Figures 8 10 & 8.11), downstream of the square obstacle in the blow down region. The higher pressure is induced by consuming the trapped mixture around the square obstacle as discussed later in this section. It should be noted, however, that the peak overpressure is slightly under predicted and there is a slight difference in the time of its occurrence

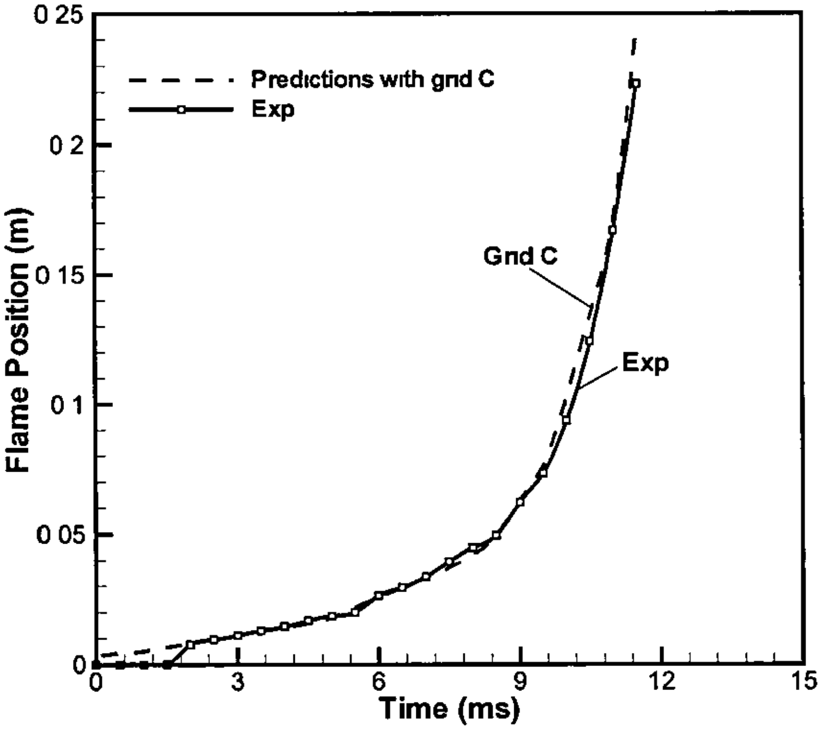

Figure 8.7 Flame position versus time from LES simulations using grid C along with experimental measurements.

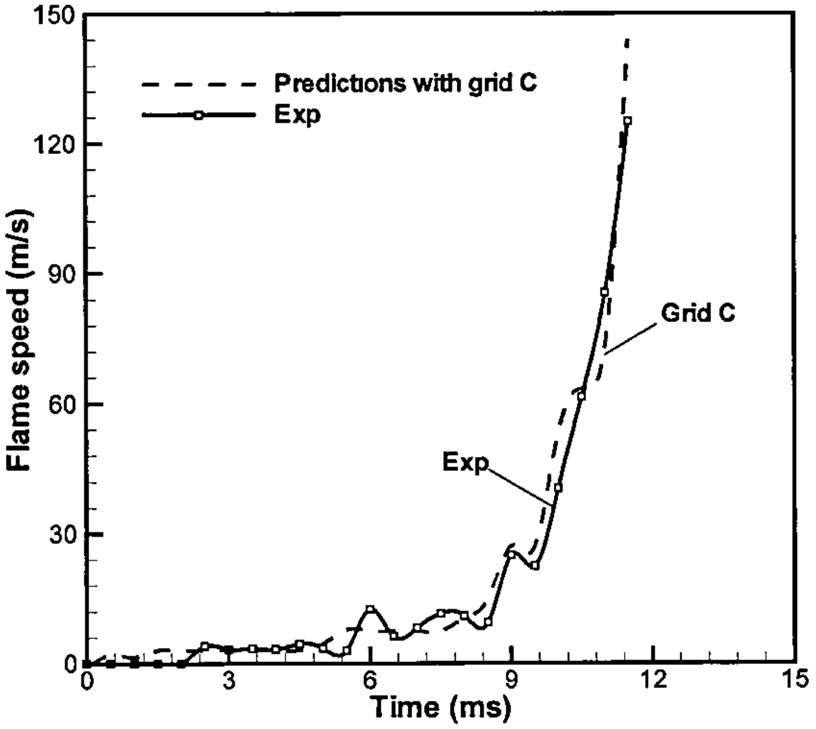

Figure 8 8 Derived flame speed verses time from LES simulations using grid C along with experimental measurements

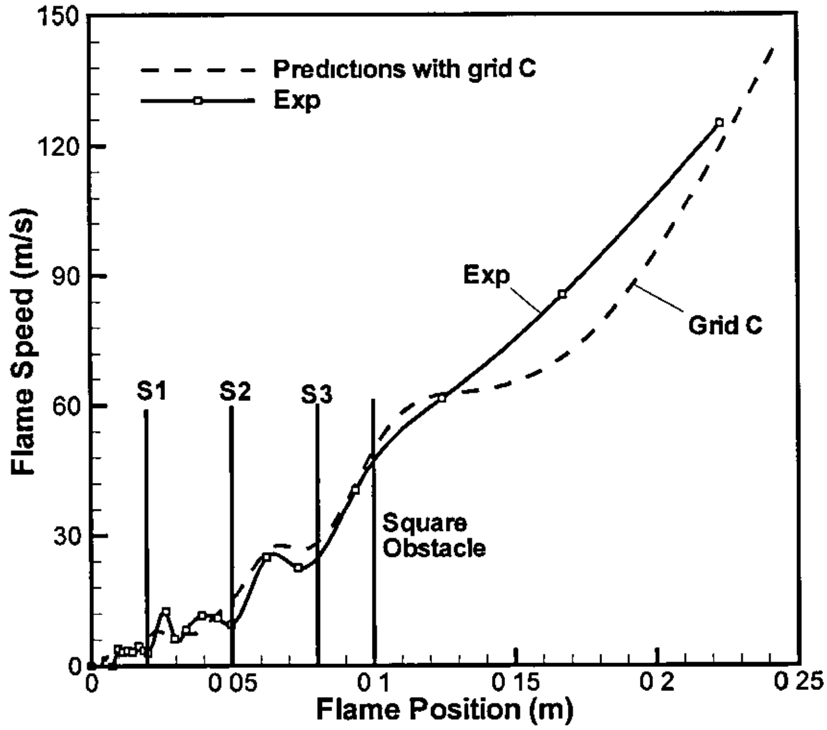

Figure 8.9 Derived flame speed verses flame positions from LES and experiments Baffle and obstacle positions are marked to indicate the influence.

Figures 8.10 and 8 11 provide snap-shot sequence of turbulent propagating flame at particular times from LES and experiments. It is worth mentioning at this stage, that experimental snap-shots are taken from the front end of the combustion chamber However, numerical snap-shots are extracted from the central plane of the chamber in *x*-direction shown in Figure 7.1 It can be observed from these snap-shots, that the flame goes through different phases (or regimes) of turbulent premixed combustion, while interacting and propagating with solid obstacles inside the chamber. To identify these phases or regimes, the combustion chamber is divided into five regions of interest as shown in Figure 8 6 to examine the progress of flame characteristics from ignition at the closed end until the flame exits the chamber at other end. Three possible realizations in every region are considered from LES predictions to demonstrate the flame structure, wrinkled nature, turbulence levels and other flame characteristics as tabulated in Table 8 2. Due to the limitation of frame speed in case of experimental video images, it is not possible to compare LES snap-shots exactly at the same time reference. However, minimum of one experimental video image is considered from each region as shown in Figure 8.11.

Region1 (R1): This region is extended to 20 mm from the ignition end of the chamber. In this region, the flame is thin and quasi laminar and propagates at almost the laminar burning velocity ~0.45m/s until it start to approach the first baffle plate. This is confirmed from both numerical and experimental snap-shots shown in Figure 8.10(R1) & 8.11(a) respectively.

Region 2 (R2): This region extends from 20 to 80 mm as shown in Figure 8 6, downstream of the ignition point. Within this region the flame propagates through three baffle plates and traps a small amount of unburnt fuel/air mixture as it evolves from the baffle plates. The flame is then stretched further as it moves from one baffle plate after the other. The entrapment of the flame around the baffles and its evolution through jetting can be noticed from numerical and experimental images shown in Figure 8.10(R2) & 8 11(b) respectively. From Table 8 2, a progressive increase from 1.0 to 4 m/s of calculated turbulent burning velocities can be noticed.

Region 3 (R3): This region extends from 80 to 112 mm downstream from the ignition closed end. This region has the square obstacle running through chamber having 12 mm side. As shown in numerical and experimental images in Figure 8.10(R3) & 8 11(c), the turbulent flame encounters square obstruction and propagates at a speed of 7.5 m/s from the third baffle plate. This has led to have a highly stretched and distorted flame as it interacts with the solid square obstacle and achieves a maximum of 9 m/s of turbulent burning velocity. A rapid rise of overpressure from 40 to 70 mbar with a steep pressure gradient and a sharp increase in flame propagation speed from 15 to 50 m/s is observed during this interaction

Region 4 (R4): Region 4 extends from 112 to 150 mm downstream of ignition point. This region may be viewed as start of the blow-down region, where flame starts exiting from the chamber. Due to the presence of square obstacle in region 3, a significant amount of unburnt fuel/air mixture is trapped around the obstacle as shown in Figure 8 10(R4) & 8 11(d). The flame is stretched further and reconnected within the recirculation zone. The reconnected flame has an increase in the surface area, which eventually consumes more unburnt mixture. As a result, the pressure and flame propagation speed are found to increase further to 103 mbar and 80 m/s respectively as the turbulent burning velocity increases to 10 m/s

Region 5 (R5): This region covers the remainder of the chamber, where the blow-down phase continues and the flame propagates further to outside of the chamber. In this region flame gets reconnected completely as shown in Figure 8 10(R5) & 8.11(e) The overpressure is found to increase and achieves its maximum of 110 mbar further in this region due to the burning of the remaining fuel/air mixture trapped inside the chamber Experimentally it is observed that the maximum overpressure is reached to 138 mbar by consuming the trapped mixture around the solid obstacles. It is also found that flame propagates at its maximum speed of around 140 m/s driving towards the chambers exit. The generated pressure oscillates while the remaining trapped mixture is burning in the chamber.

Relevant estimates from LES predictions at various instants of flame propagation within the above regions are calculated and presented in Table 8.2. It is very interesting to note, that the level of agreement in case of flame position, propagating speed and the flame structure as shown in Figures 8.7, 8 8, 8.9,8 10 and 8.11 at different instants are very convincing and confirm the validity of the LES predictions. Further to this, various regimes of combustion are calculated based on non-dimensional groups and identified them on two standard combustion regime diagrams as discussed in the following section.

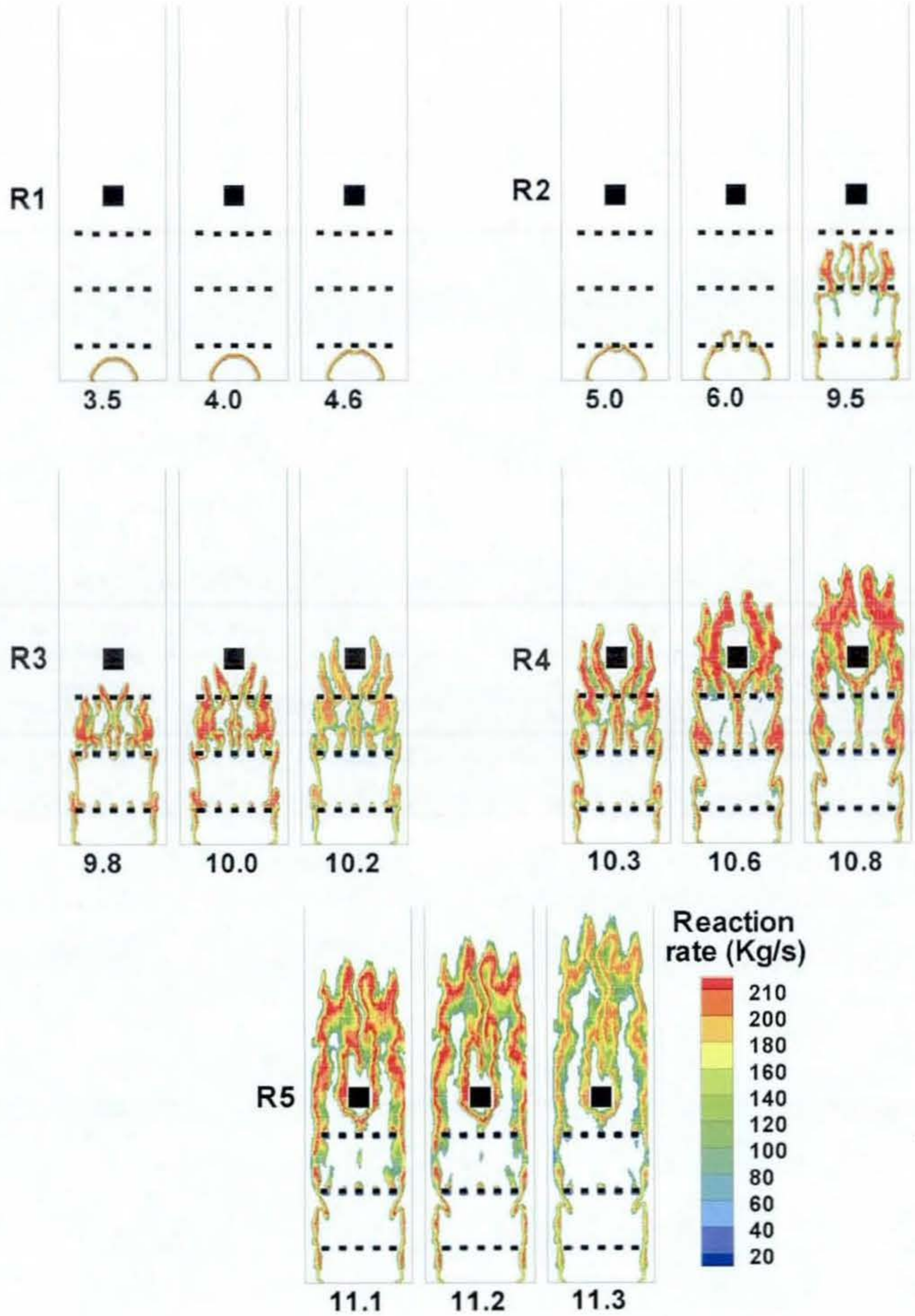

Figure 8.10 Flame structure derived from reaction rate contours from grid C, showing the flame propagation at different times after ignition with in the five regions. The time mentioned at the bottom of each chamber is in ms.

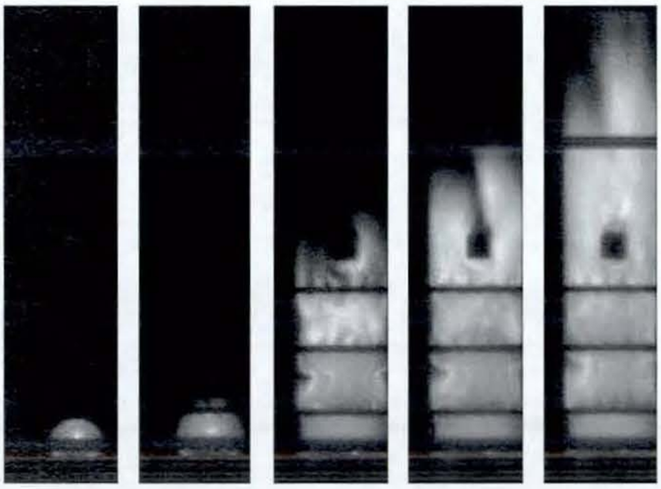

Figure 8.11 Sequence of experimental images to show flame structure at different times after ignition (a) 4.5, (b) 6, (c) 10, (d) 10.5 and (e) 11.0 ms.

	Time (ms)	u' (m/s)	u_L (m/s)	L_f (mm)	u_t (m/s)	u'/u_L	u_t/u_L	Zp (cm)	Da	Re_{LI}	Ka	Regime
R1	3.5	2.10	0.450	0.294	0.45	4.66	0.99	1.181	1.10	1050	4.5	TRZ
	4.0	2.62	0.450	0.294	0.45	5.82	0.99	1.333	0.88	1310	6.2	TRZ
	4.6	4.43	0.450	0.294	0.51	9.84	1.125	1.562	0.53	2215	13.6	TRZ
R2	5.0	6.06	0.450	0.294	1.14	13.47	2.54	1.717	0.38	3030	21.7	TRZ
	6.0	2.0	0.450	0.294	1.34	4.42	2.99	2.488	1.16	995	4.10	TRZ
	9.5	5.23	0.447	0.296	3.96	11.70	8.87	7.213	0.44	2615	17.7	TRZ
R3	9.8	4.55	0.447	0.296	6.27	10.18	14.02	8.283	0.50	2275	14.3	TRZ
	10.0	4.0	0.446	0.296	7.80	8.90	17.50	9.040	0.57	1985	11.8	TRZ
	10.2	5.93	0.446	0.297	8.40	13.29	18.82	10.17	0.38	2965	21.5	TRZ
R4	10.3	5.63	0.445	0.297	8.69	12.65	19.54	10.70	0.40	2815	20.0	TRZ
	10.6	4.78	0.444	0.298	9.58	10.77	21.57	13.03	0.47	2390	15.7	TRZ
	10.8	5.05	0.443	0.298	10.05	11.40	22.66	14.39	0.44	2525	17.1	TRZ
R5	11.1*	5.04	0.443	0.298	10.77	11.38	24.31	16.75	0.49	2520	16.3	TRZ
	11.2	3.70	0.444	0.298	11.61	8.333	26.16	17.75	0.67	1850	10.2	TRZ
	11.3	4.90	0.444	0.298	12.46	11.04	28.05	18.75	0.51	2450	15.5	TRZ

TRZ = Thin reaction zone
Zp = Flame position along z-axis
* = Peak over pressure

Table 8.2 Estimates of velocity and length scale from LES predictions using grid C. The flame structures at these chosen times is produced from reaction rate contours as shown in Figure 8.10 and these estimates are fitted into known combustion regime diagrams as shown in Figure 8.12 (a) & (b).

8.2.4.2 Regimes of Combustion in the Current Chamber

Data from LES simulations employing grid C is used to identify the regime(s) of the turbulent premixed combustion in the current chamber Summary of the data, extracted from LES calculations is presented in Table 8.2. All controlling parameters in this analysis are evaluated at the leading edge of the flame front as defined in earlier section

The classical regime diagram for turbulent premixed flames as developed by Peters (2000b) is plotted for u'/u_L with L_I/L_f An LES regime diagram for turbulent premixed flames has been developed further by Pitsch and De Lagenste (2002) in terms of Karlovitz number (Ka) and the ratio of $\bar{\Delta}/L_f$. The objective of the current analysis is to identify the regimes of the flame at different stages of its propagation during interaction with the solid obstacles Significant importance is given while the flame is ramming and evolving from the obstacles. Relevant non-dimensional numbers at filter width, such as Karlovitz, Reynolds and Damköhler number are calculated using equation (2 4) Reynolds number based on the integral length scale, L_I is calculated as:

$$\mathrm{Re}_{LI} = \frac{u'_{\Delta} L_I}{\nu} \qquad (8\ 4)$$

The integral length scale is estimated to be 10% of the chamber width (Masri et al., 2006), i.e. L_I is taken to be 5 mm. The length scales and dimensionless number estimated as stated above at various time steps of the flame propagation are summarized in Table 8.1. Data from the LES simulation are plotted on two regimes of combustion diagrams to get adequate confirmation of the combustion model used in the present calculations as shown in Figure 8 12 (a) & (b). Both regime diagrams confirm that the leading edge of the flame is always within the thin reaction zone irrespective of its position and interactions with the solid obstacles.

A rapid increase in the Karlovitz and Reynolds numbers is observed at the end of region 1 (R1) where the flame starts approach the first solid baffle plate. This is confirmed by observing the abrupt increment of the flame speed from LES predictions (sudden hike from experimental measurements also can be clearly seen) from Figure 8 9 The same trend of Karlovitz and Reynolds numbers can be observed until the flame starts evolving

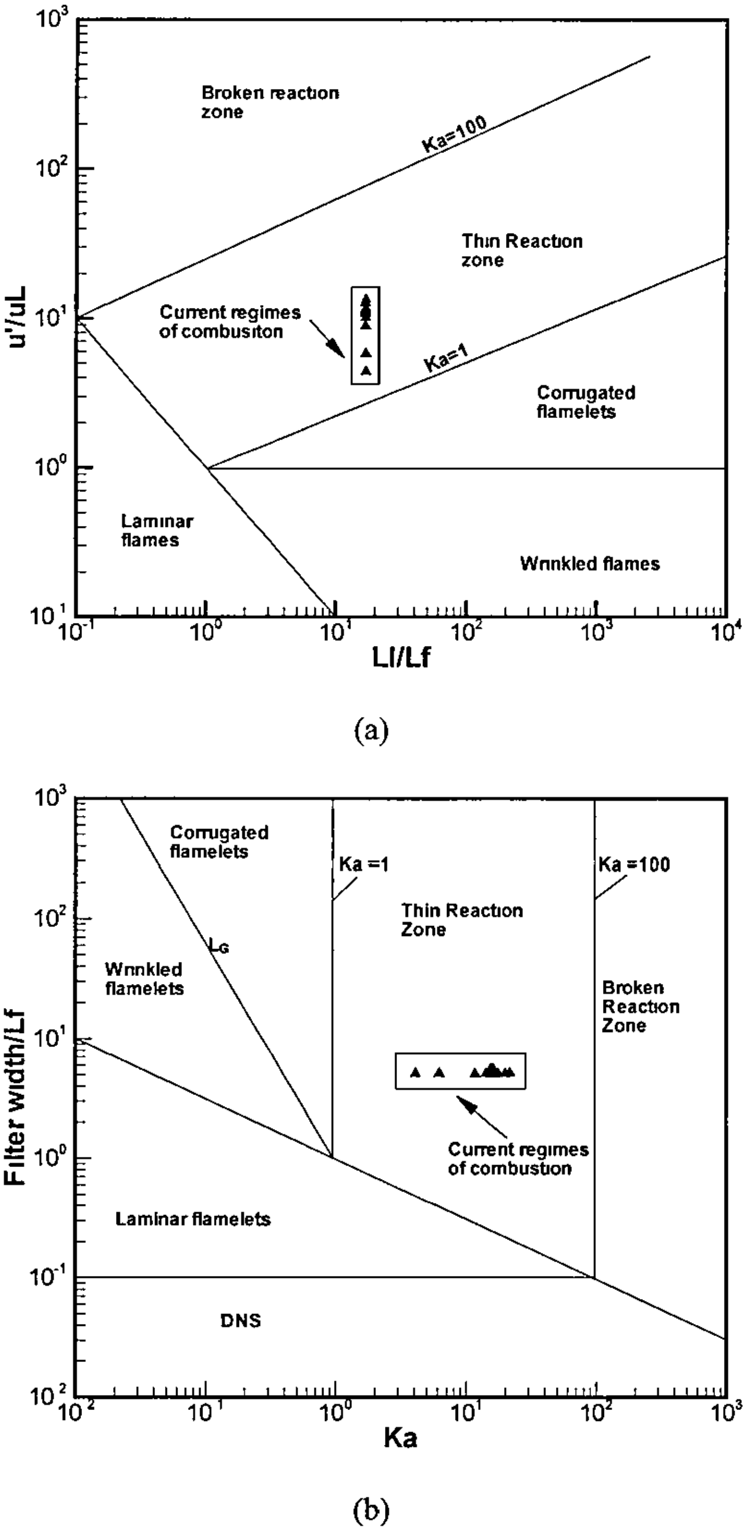

(a)

(b)

Figure 8 12 Estimates from grid C of the LES simulations presented in Table 8.1 are fitted into the regimes of combustions (a) Turbulent premixed combustion reported by Peters (2000b) (b) LES turbulent premixed combustion reported by Pitsch & De Lageneste (2002).

from the first baffle plate. A sudden fall in Karlovitz and Reynolds numbers is noticed as the flame propagates through first turbulence generating grid At this point the flame is experiencing re-laminarisation due to the local flow conditions As the first turbulence generating baffle is very near to the ignition end, it is not influencing much by the increase in turbulence level in the combustion chamber Similar fluctuations trend of Karlovitz and Reynolds numbers is noticed as the flame propagates past second and third baffle plates However the range of fluctuations of Karlovitz and Reynolds numbers is lowered as the turbulence level increases.

8.2.5 Flame Characteristics: Other Configurations

The above analysis is very convincing in employing the algebraic FSD model to predict turbulent propagating flames Hence, LES simulations are performed using grid resolution C for additional configurations in order to get more insight To facilitate a meaningful discussion, configurations shown in Figure 7.3 are classified into a total of four families as shown in Figure 8 13. However, only five configurations detailed in Table 8 3, which can fit into two families are simulated and discussed in following sections Table 8.3 presents the details of flame positions, flame speeds corresponding to the peak overpressures

	Experimental Data				**LES Predictions**				**Time Shift**
Configuration	**Peak over pressure (mbar)**	**Time (ms)**	**Flame position (cm)**	**Flame speed (m/s)**	**Peak over pressure (mbar)**	**Time (ms)**	**Flame position (cm)**	**Flame speed (m/s)**	**LES-Exp (ms)**
1	138 28	10.3	15 0	54.0	109.5	11.0	17 85	81.8	0 74
2	118.46	11.96	15 0	50.7	95.7	12.5	18 15	76.6	0.57
3	80.47	11 42	13 0	50.0	82 0	12 0	18 05	80 8	0 57
4	77.15	9.79	8.0	30.0	80.0	11.0	15.55	65.0	1.16
5	82.03	13 25	17.6	75.0	63 8	14.0	16 75	63 3	0.72

Table 8.3 Experimental measurements & LES predictions for various configurations.

8.2.5.1 Results: Family 1

The evolution of the turbulent flame is shown in terms of isotherms for Family 1 (from 500 to 2200 K) in Figure 8.14 at different instants after ignition Five instants are chosen, which are relatively significant in the development of propagating flame and the generation of overpressure inside the chamber. Family 1 uses a square solid obstacle running through the chamber, with varying number of baffles plates. Configuration 1 uses three baffle plates (S1, S2 & S3), configuration 2 uses two baffle plates (S2 & S3) and configuration 5 uses only one baffle plate (S3) near the solid square obstruction. The time traces of over pressure, flame speed and position for these three configurations with experimental measurements are shown in Figure 8.15, 8.16 & 8 17 Flame speed is plotted against flame position together with experimental measurements for Family 1 as shown in Figure 8 18. These plots give quantitative difference of flame characteristics at any chosen time or flame front position.

It is evident from configuration 1 shown in Figure 8.14(c), that after initialisation of ignition, leading edge of the flame starts to expand hemi-spherically (isotherm A) with a velocity Θu_L (Θ is the thermal expansion factor defined as density ratio of the fresh and burned fuel/air mixture) in the axial direction and the flame skirt elongates with laminar burning velocity, u_L in the radial direction. The leading edge of the flame front propagates at the same speed i e. Θu_L until it reaches the first baffle plate. Once the flame hits the baffle plate, a rapid increase in flame speed followed by a sharp decrease is observed in Figure 8 16 because of the local obstructions. After hitting the first baffle, the laminar hemispherical structure is distorted and flame starts protruding through narrow vents As a result, the surface area of the flame brush increases, hence, consumes more fuel/air mixture per unit time and propagates at relatively higher velocity through the un-burnt fuel/air mixture

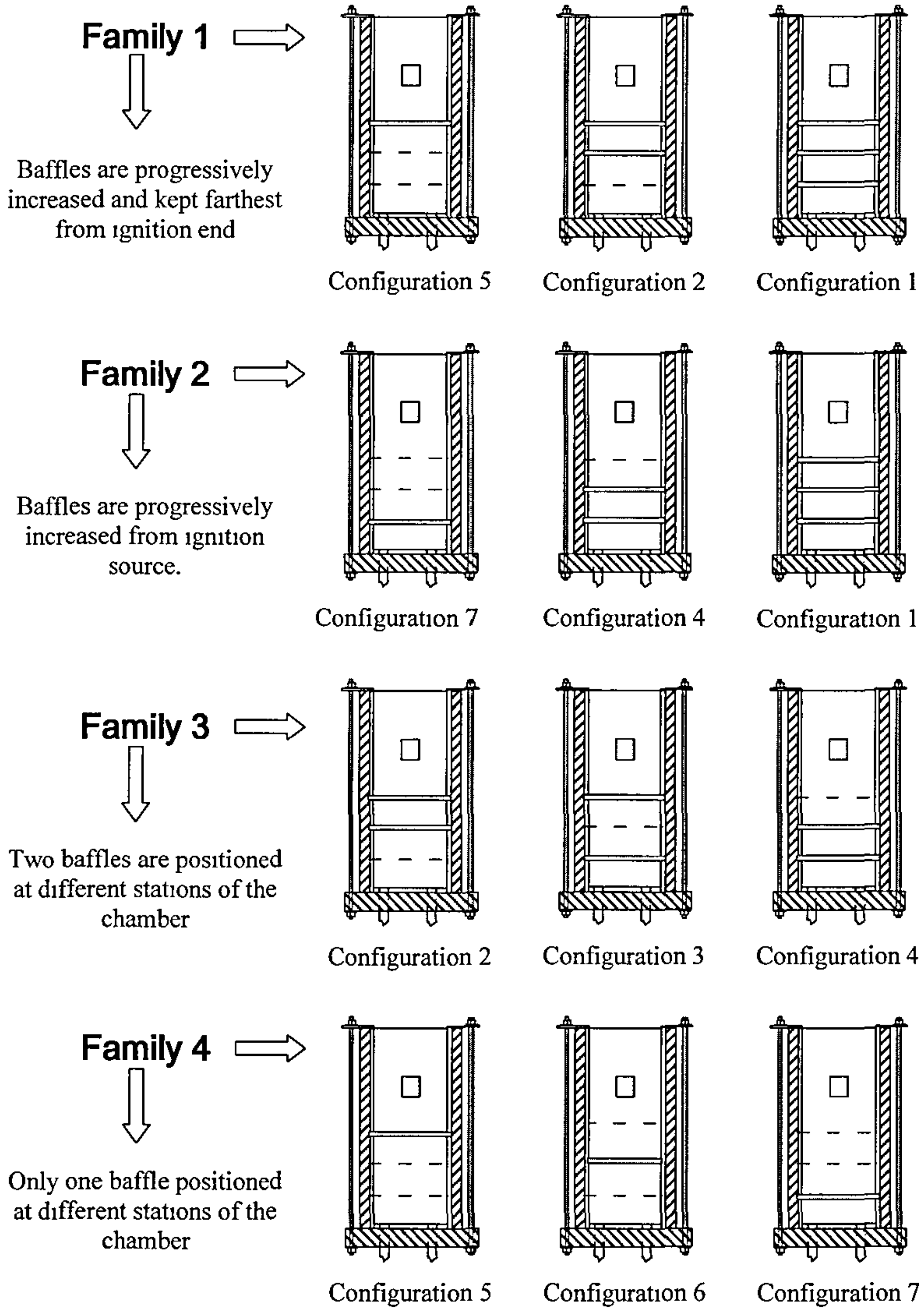

Figure 8 13 Classification of configurations into families.

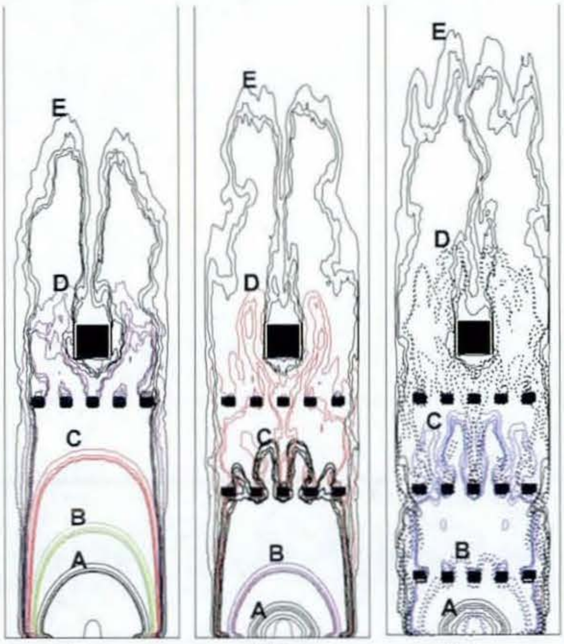

(a) (b) (c)

Figure 8.14 Development of the turbulent propagating flame in three different configurations (Family 1) are presented (a) Configuration 5; isotherms at 6.0, 8.0, 10.5, 13.0 and 14.0 ms corresponding to positions A to E respectively. (b) Configuration 2; isotherms at 3.0, 6.0, 10.0, 11.5 and 12.5 ms corresponding to the positions A to E respectively. (c) Configuration 1; flame isotherms at 3.0, 6.0, 9.5, 10.5 and 11.3 ms corresponding to the positions A to E respectively.

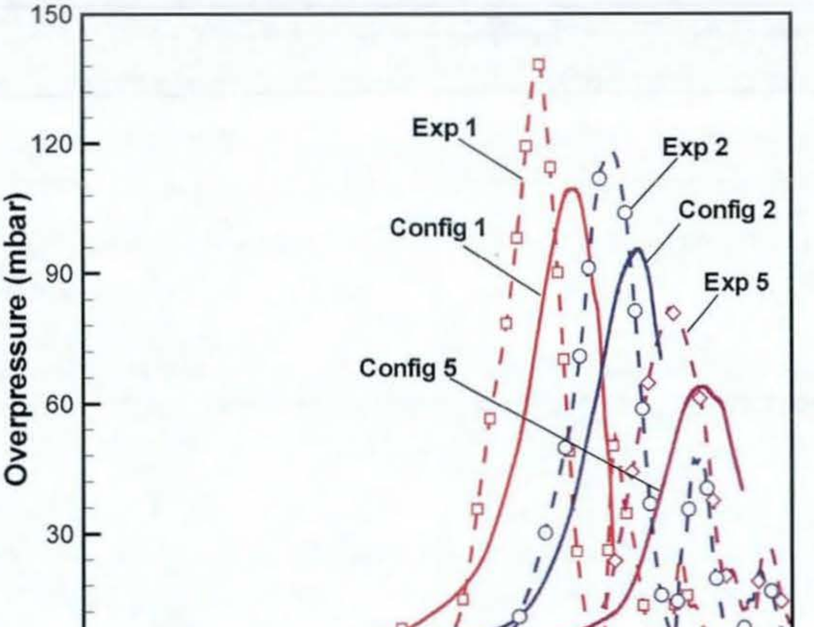

Figure 8.15 Overpressure time histories for Family 1; LES simulations are compared with experimental measurements.

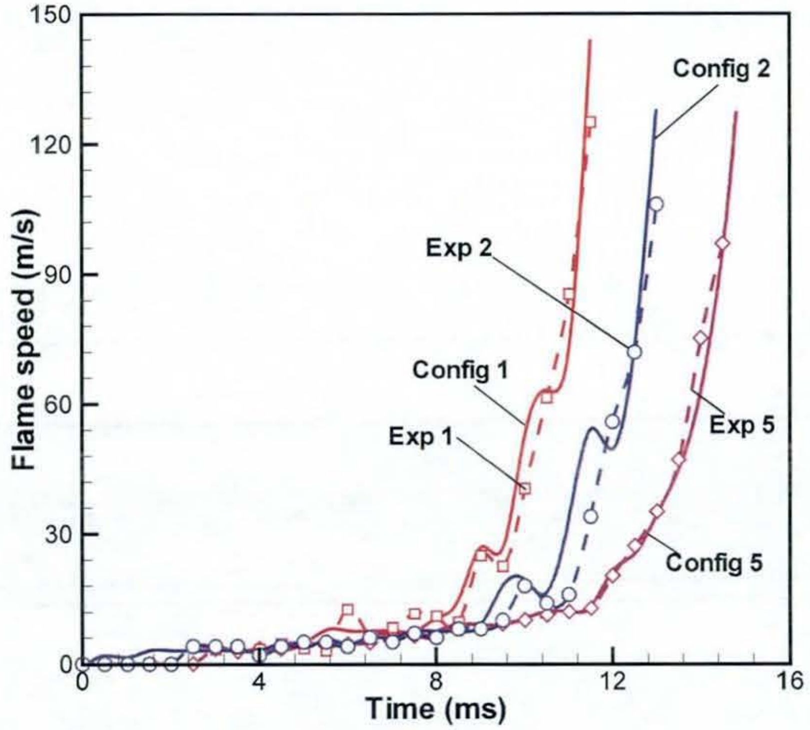

Figure 8.16 Flame propagation speeds versus time for Family 1; LES simulations are compared with experimental measurements.

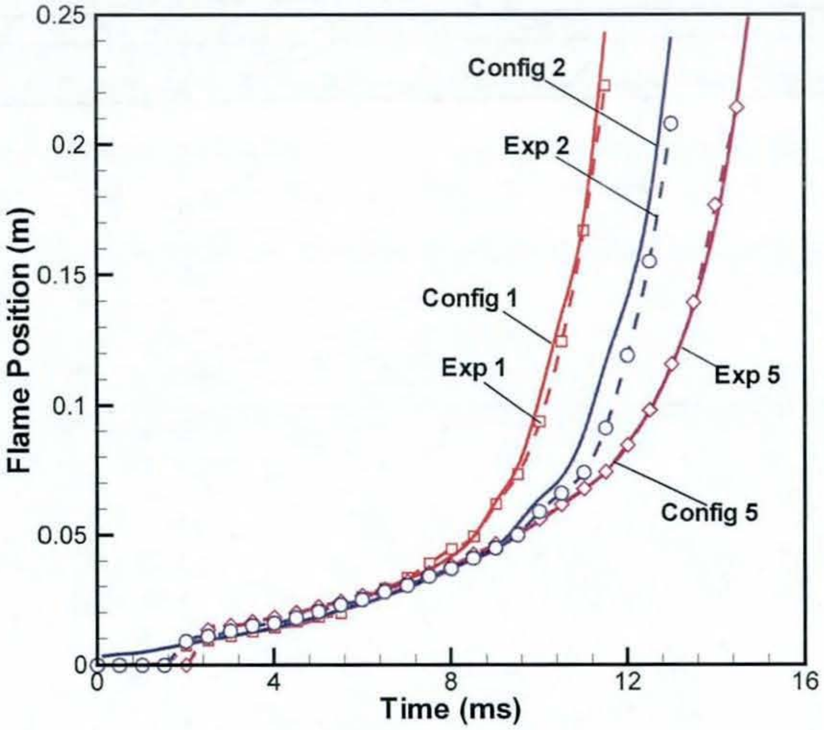

Figure 8.17 Flame position versus time for Family 1; LES simulations are compared with experimental measurements.

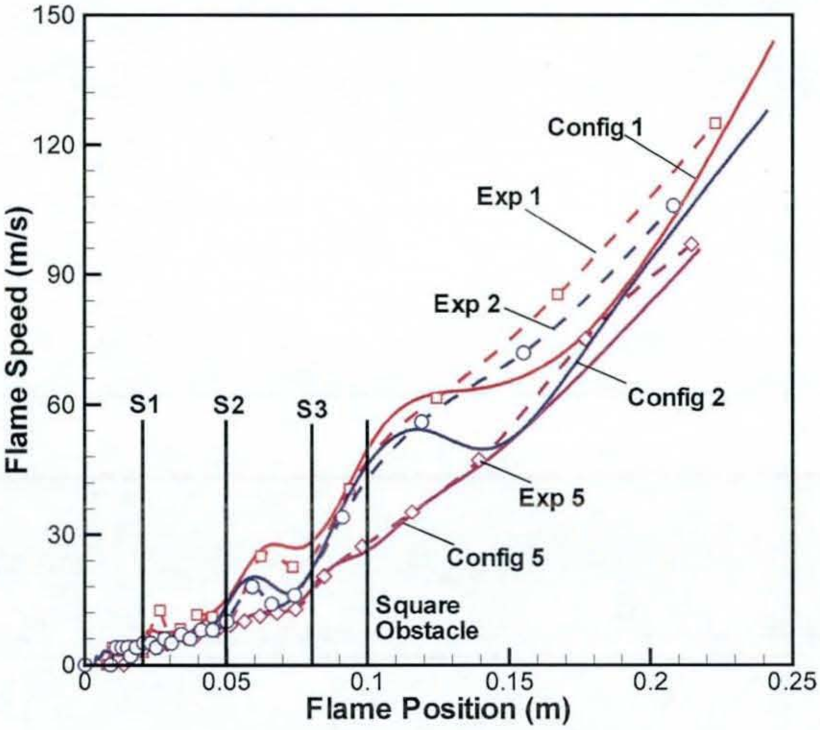

Figure 8.18 Flame speed versus flame position for Family 1; LES simulations are compared with experimental measurements.

From isotherm B in Figure 8.14 (c) it can be clearly seen that, the flame jetting has resulted in wrapping and wrinkling of the flame around the local obstruction and around itself, which lead to trap unburnt mixtures by burnt gases on the obstacles face. The trapped unburnt mixtures will have significant contribution in increasing the overpressure at later stages (after third baffle plate). The flame front reaches the second plate at a progressive speed and creates pockets of fresh fuel/air mixture which eventually help to increase the overpressure at later stages of propagation. Surprisingly, this pocketing phenomenon is only observed in case of configuration 1 and this is believed to be related to the high level of turbulence generated in the chamber. Eventually, the flame experiences wrinkling, stretching and a significant increase in surface area as it propagate further. At this stage, it can be noticed that the flame propagation speed increases rapidly and the flame front appears to be more turbulent and corrugated as it accelerates towards the third baffle. Increase in the propagation speed due to the local turbulence causes further stretching and wrinkling of the flame. At this stage, the flame jets out of third baffle plate and encounters the solid square obstacle, where the flame is further distorted and wrinkled, followed by an increase in surface area thereby boosting the reaction rate.

Highly wrinkled flame starts wrapping around the solid square obstacle, which subsequently results in trapping of a high volume of unburnt fuel/air mixture by flame at the up and down stream of the square obstacle within the recirculation zone. The highly stretched flame propagates past the obstacle and gets reconnected quickly within the recirculation zone. The trapped gases will starts burning as the flame combines together and this has significant contribution in increasing the overpressure. The snapshots of the reaction rate at various instants after ignition from LES simulations are compared with the recorded high speed video images collected experimentally as shown in Figure 8.19 (c). The flame structure and the entrapment of the un-burnt gases are very well predicted at various stages by LES simulations.

Considering the configuration 2 with two baffles at S2 and S3 along with a solid square obstacle shown in Figure 8.13 & 8.14(b), initial flame kernel propagating at a speed of approximately 4 m/s can be observed similar to that of configuration 1. As the flow encounters the baffle plate, laminar flame front get distorted by creating several individual flame fronts protruding through the narrow vents. Due to this distortion, the thin flame front wraps around the individual baffles by trapping certain amount of the unburnt fuel/air mixture. The reaction rate increases due to the enhanced surface area, which in turn suddenly accelerates and then decelerates the flame. Individual flame humps will attempt to merge and propagate together as shown in the snap-shots of the reaction rate in Figure 8.19(b). With a progressive flame speed (can be seen in Figure 8.16 & 8.18), flame encounters the second baffle plate, which intend to generate higher turbulence levels. Due to the increase in the turbulence levels, flame is highly stretched and traps a huge amount of unburnt mixture up- and down- stream of the square solid obstacle.

Configuration	Experimental		LES simulations		
	Over pressure (mbar)	**% Pressure loss**	**Over pressure (mbar)**	**% Pressure loss**	**% Pressure loss based on individual experimental configuration**
1	138.28	0.0	109.53	0.0	20.79
2	118.46	14.33	95.70	12.62	19.21
3	80.47	41.80	82.21	25.0	-2.16
4	77.15	44.20	80.11	26.86	-3.84
5	82.03	40.67	63.82	41.73	22.19

Table 8.4 Percentage of pressure losses calculated and tabulated based on the overpressure of the configuration 1.

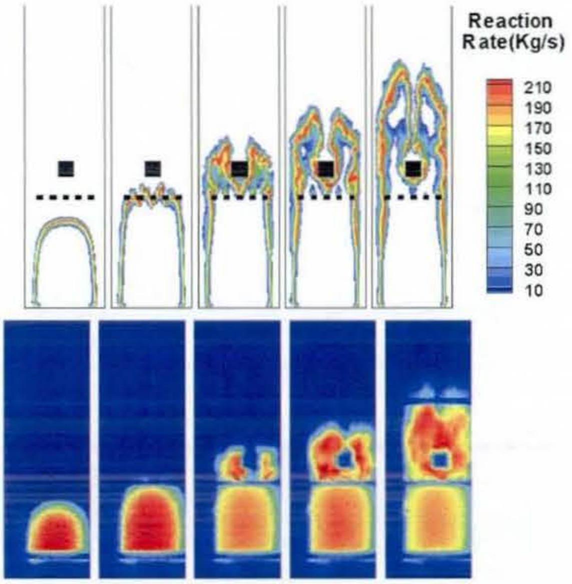

(a) Configuration 5

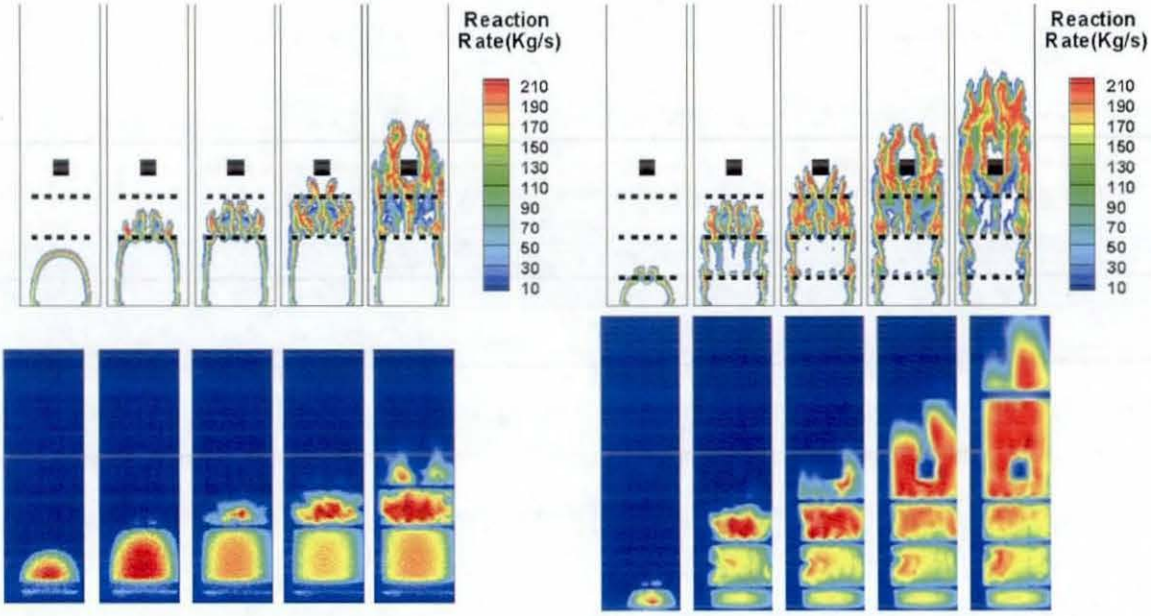

(b) Configuration 2

(c) Configuration 1

Figure 8.19 Sequence of images showing flame structure at different instants after ignition. Reaction rate contours generated from LES predictions are presented against high speed recorded video images of experiments. (a) Numerical snap shots for configuration 5 at 10.5, 12.0, 13.0, 13.5, and 14.0 ms are compared with experimental images at 10.5, 12.0, 13.0, 13.5, and 14.0 ms. (b) Numerical snap shots for configuration 2 at 8.0, 10.0, 11.0, 11.5 and 11.8 ms are compared with experimental images at 8.0, 10.0, 11.0, 11.5 and 12 ms.(c) Numerical snap shots for configuration 1 at 6, 9.5, 10.0, 10.5, and 11.0 ms are compared with experimental images at 6, 9.5, 10, 10.5 and 11.0 ms.

In configuration 5 with only one baffle plate, just upstream the square obstruction shown in Figure 8.13 & 8.14(a), the propagating flame maintains laminar profile indicated by isotherm A, B and C corresponding to 6, 8 and 10.5 ms until it reaches the baffle plate near the square obstacle. The flame surface area then increases due to the augmentation in flame curvature, which subsequently raises the consumption of the fuel/air mixture and the reaction rate. As shown in Figure 8.16 & 8.18, a gradual increase in the flame speed (~15m/s) is observed until the flame hits the baffle plate which increases the surface area due to the flame distortion. Similar tendency of wrinkling as explained in the case of configuration 1 can be observed as shown in Figure 8.14(a) for isotherm D. Unlike in configuration 1, the variation in the flame speed is minor as the flame has enough time to interact with the baffle plate. Also it can be noticed from the snapshots of LES predictions and experimental images shown in Figure 8.19(a), that the hemispherical structure of the flame started changing before hitting the baffle plate. Flame is less stretched in this situation and evidently can be seen from the isotherms D of Figure 8.14 (a), (b) & (c). Distorted flame propagates further and encounters the square obstacle, which further distorts by wrinkling the flame surface due to the generated vortices, which subsequently traps the unburnt gases upstream and down stream of the square obstacle. It is noteworthy at this point, that the volume of the trapped unburnt fuel/air mixture is less than that of the configuration 1. This is because of the strength of local turbulence encountered due to the flow conditions.

It is identified that the volume of the trapped unburnt mixture, mainly around the square obstacle is liable to increase overpressure during blow-down phase. In order to visualise the extent of volume, streamlines are superimposed over reaction rate contours at various instants as shown in Figure 8.20 for configuration 1 and 5 only. All the streamlines originates at the ignition end of the chamber and tend to perpetuity in the fresh fuel/air mixture. It can be clearly seen that streamlines are deflected due to the local obstructions to form a trap and to push the fresh mixture. The amount of trapped mixture is directly proportional to the strength of the turbulence and the number of local obstructions used in the chamber.

The calculated peak overpressure for configuration 1 as shown in Figure 8.15, is about 110 mbar at 11.1 ms against the experimental values of 138 mbar at 10.3 ms. From both, LES and experiments, the peak overpressure is observed during reconnection of the flame

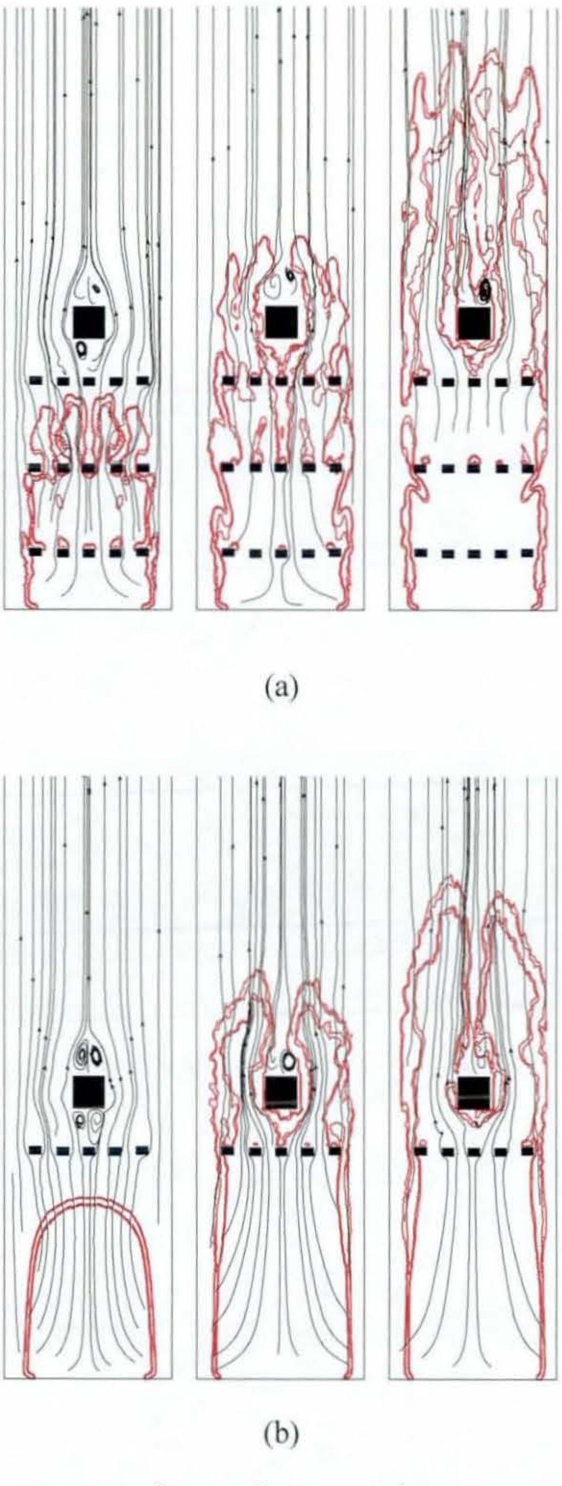

(a)

(b)

Figure 8.20 Streamlines are superimposed over reaction rate contour at various instants after ignition. (a) Configuration 1; at 9.5, 10.5, 11.3 ms. (b) Configuration 5; at 10.5, 13.0, 14.0 ms.

front in region 5 (Figure 8.6). As discussed earlier, this is due to the consumption of unburnt gases down and upstream of the solid obstacles. In configuration 2, the predicted peak over pressure from LES simulations is 96 mbar at 12.5 ms and this is roughly 13% less than the overpressure observed in configuration 1. From the experimental measurements, a peak overpressure of 119 mbar is observed at 12 ms. In case of configuration 5, the calculated peak overpressure is 64 mbar occurring at 14 ms, which is much less than in configuration 1 (approx. 41% lesser). Experimental measurements of the peak overpressure for configuration 5 is 82 mbar occurring at 13.2 ms. The experimental peak pressure for configuration 5 is 41% less than for configuration 1 and occurs at a later time. In this case, the peak overpressure is occurring as the flame propagates furthest from the square obstacle and half way through to the exit of the chamber. This is because the flame has travelled inside the chamber with near to laminar speed until it encounters the first baffle plate.

8.2.5.2 Results: Family 3

All configurations in Family 3 have two baffle plates and however, positioned at different down stream locations at S2-S3, S1-S3 and S1-S2 in configuration 2, 3 and 4 respectively along with a solid square obstacle as shown in Figure 8.13. As discussed in preceding section, growth of flame kernel, its distortion due to the presence of baffles, flame interactions with solid obstacles and the consumption of fuel/air mixture due to the increase in surface area are very similar except the magnitude and occurrence of the peak overpressure inside the chamber (maximum overpressure is observed to induce in Region 4 in case of configuration 3 & 4). Time histories of the flame characteristics from simulations are compared against experimental measurements for Family 3 and shown in Figures 8.21, 8.22, 8.23 & 8.24.

It is evident from Figure 8.21 and Table 8.3 that, the peak overpressure predicted as 96 mbar against experimental measurement of 119 mbar in configuration 2, which is higher from experiments and LES simulations than the peak overpressures of the other two configurations (i.e. 3 & 4). The time of peak overpressure occurrence from LES is identified to be 12.5 ms, which is lagging behind the other two configurations (3 & 4) and this lag is due to the laminar nature of the approaching flame towards the first baffle as it is situated far from ignition end. This phenomenon is duly confirming the impact of the position of baffles or obstructions with respect to the origin of the ignition. Even though, flame takes longer time to reach any reference location in configuration 2, turbulence levels have been relatively increased due to the presence of consecutive baffles, which has greater impact on peak overpressure.

Similarly, in the case of configuration 4, baffles at S1 & S2 progressively increase the flame speed. However, due to the presence of the gap between baffle at S2 and square obstacle, turbulence levels are relatively low and cause to generate lower peak overpressure. In the case of configuration 3, relatively higher overpressure has generated than in configuration 4. It is also interesting to note that, the flame leaves the chamber relatively little later in configuration 3.

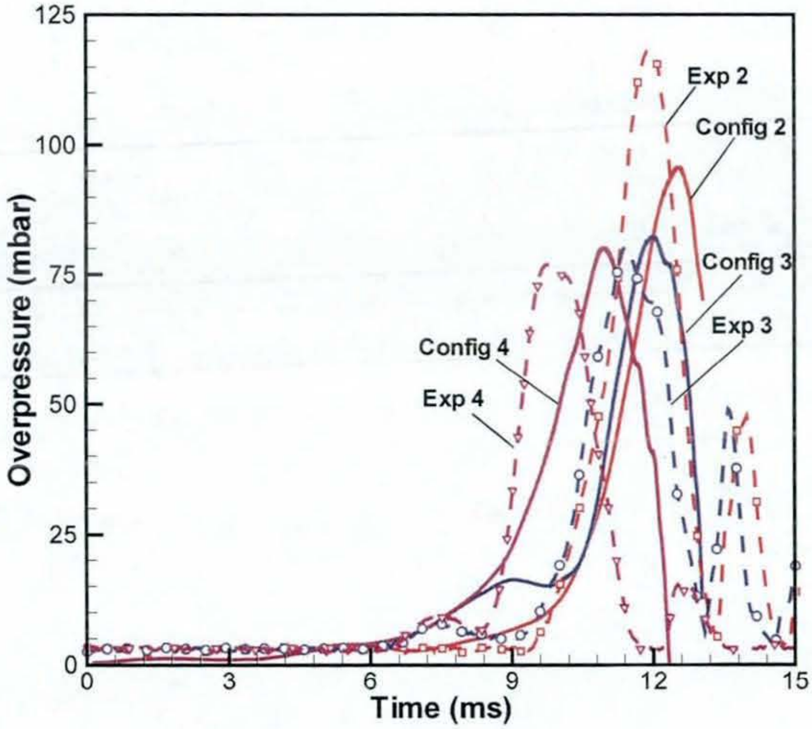

Figure 8.21 Time histories of overpressure from LES and experimental measurements using Model-1 for Family 3.

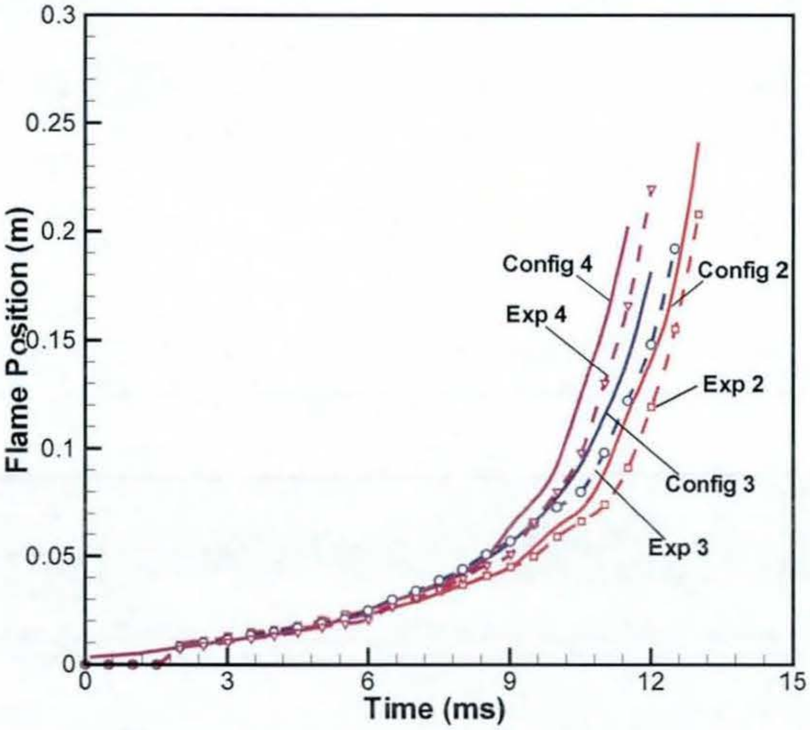

Figure 8.22 Time histories of flame position from LES and experimental measurements using Model-1 for Family 3.

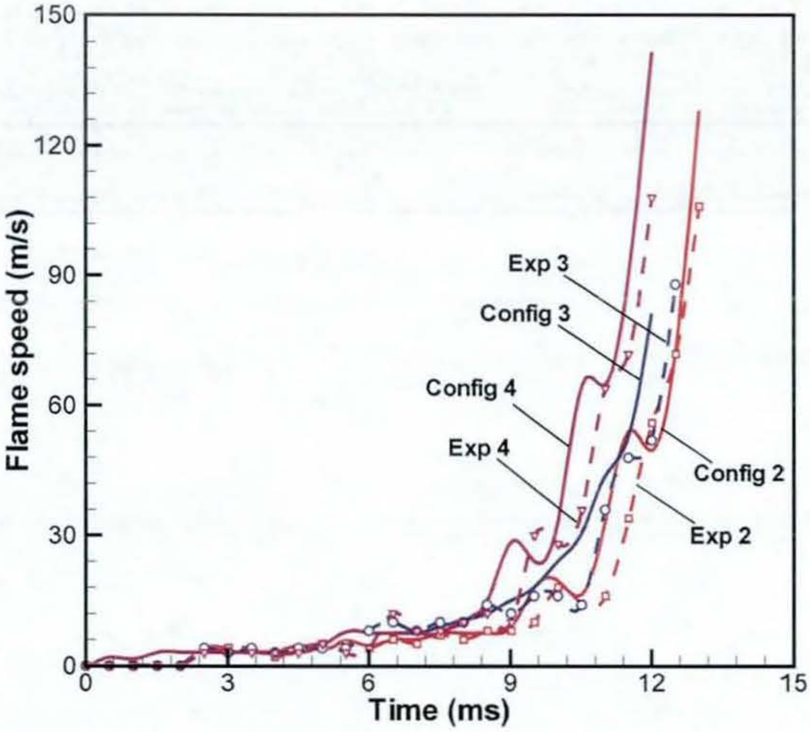

Figure 8.23 Time histories of derived flame speed from LES and experiments using Model-1 for Family 3.

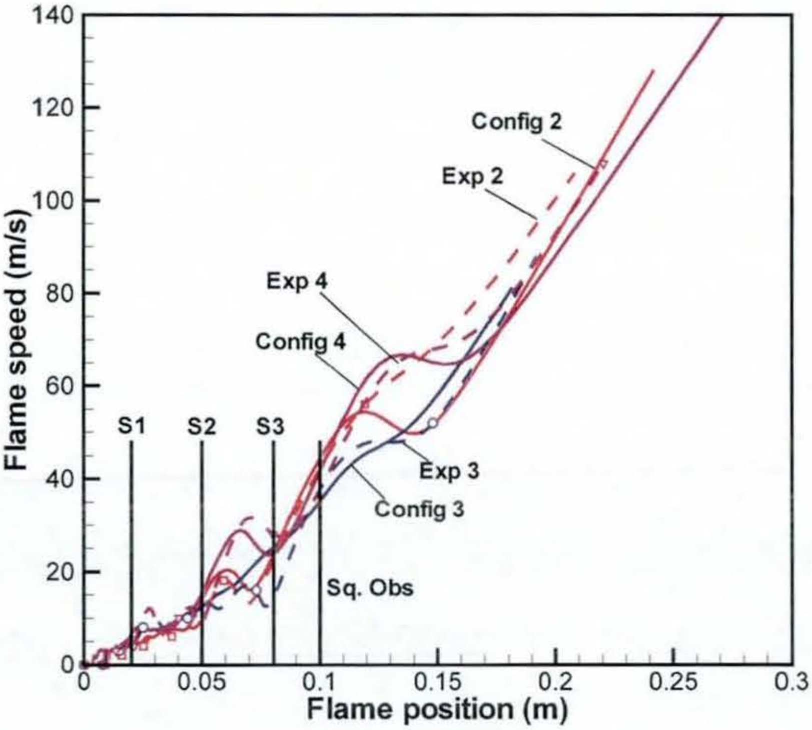

Figure 8.24 Flame speed verses flame position from LES and experiments using Model-1 for Family 3.

8.2.5.3 Under-prediction of Overpressure and the Time Shift

It is very clear from the above LES simulations using algebraic FSD model, that the overall global features are well predicted. However, it should be noted that, the magnitude of overpressure and its time of occurrence is consistently under-predicted. To clarify this, the percentage loss in overpressure prediction compared to that of experiments is given in Table 8.4 (last column). Also overpressures are plotted based on families and shown in Figure 8.25 (a) & (b), which eventually gives a very good idea of impact of obstacles on overpressure and percentage loss of overpressure in LES predictions. Evidently, LES simulations are under-predicting overpressures by about 20% in most cases except in configurations 3 and 4, where a slight over-prediction can be noticed.

Mainly, two possible reasons are identified for the under-prediction of overpressure and its time of incidence in the present LES analysis. Firstly, the simple sub-grid scale model (M1) which is employed to account for the reaction rate is failing to capture unresolved flame surface density. In case of thin premixed flames, chemical reaction takes place in thin propagating layers, referred to as flamelets and is mostly a SGS phenomenon. From

Table 8.1 and 8.2, it is evident that the flame is thinner than the grid resolution employed in the present simulations and hence, a more complex model may be needed to calculate the chemical reaction rate more accurately. Two possible solutions are identified to overcome this problem and are discussed in the next section of this chapter. Secondly, the reason for the time shift of the peak overpressure may be due to experimental uncertainties in establishing the time zero that marks the occurrence of ignition. As discussed in Chapter 7, repeatable ignition reference was established using Nd:YAG laser and however, establishing an accurate zero reference is very difficult due to the quickest nature of the experiment (approximately 13 ms). Nevertheless, ignition in LES is modelled by setting reaction progress variable to 0.5 within the radius of 4 mm to achieve quasi-laminar nature of the turbulent flame.

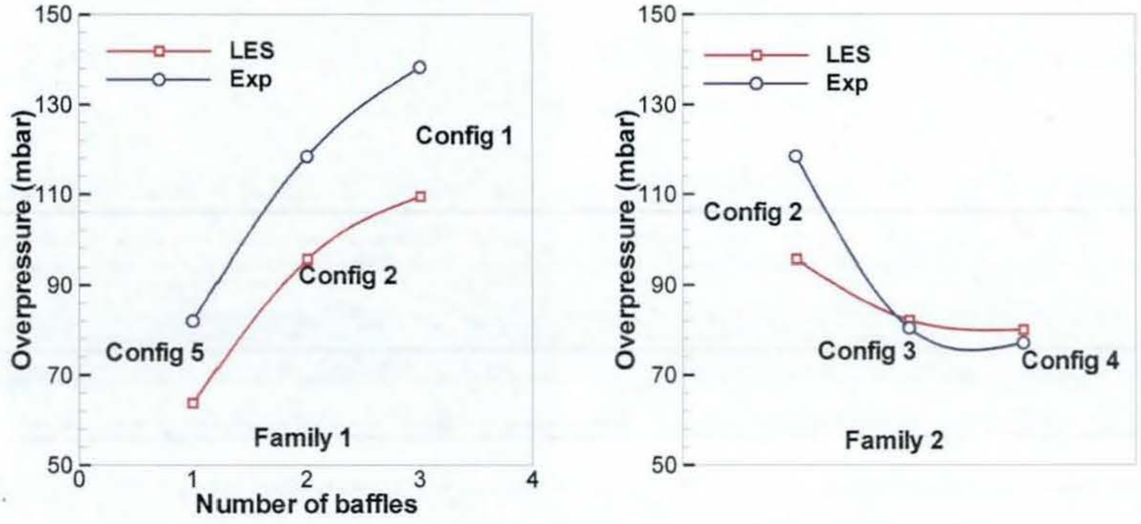

(a) (b)

Figure 8.25 Maximum overpressures inside the combustion chamber for (a) Family 1 and (b) Family 3.

8.3 Dynamic Evaluation of the Model Coefficient

To overcome the drawbacks of under-predicting the overpressure, a natural and first choice could be self-scaling or dynamic modelling of the model coefficient β. This coefficient is not considered to be universal and expected to be dependent on many physical and modelling parameters in the simple algebraic FSD model (equation 5.15). The dynamic calculation procedure, explained in section 5.2.2 has been implemented in the in-house LES code and examined for an additional run employing grid C for configuration 1.

Results from LES simulations using grid C with constant $\beta = 1.2$ and a dynamic model coefficient in the flame surface density equation are compared against the experimental measurements and discussed in this section. It should be noted here that, the LES results using the model coefficient of 1.2 shown in Figure 8.1, 8.7, 8.8 and 8.9 are used to compare present simulation. In order to assess the dynamic model, initial time histories of the overpressure are shown in Figure 8.26. Solid red line in Figure 8.26 represents overpressure with the dynamic model coefficient and the blue dash double dotted line represents overpressure from constant model coefficient, compared with dashed line representing experiments. It is evident from Figure 8.26, that the simulation with dynamic model coefficient has predicted similar pressure trend and the rate of pressure rise equal to that of constant model coefficient. A slightly higher peak overpressure i.e. 114 mbar at 11.0 ms is predicted with dynamic model compared to 110 mbar at 11.1 ms in case of constant value for β. Though, overpressure trend is slightly better and however, still under-predicted by 17% approximately compared to experiments.

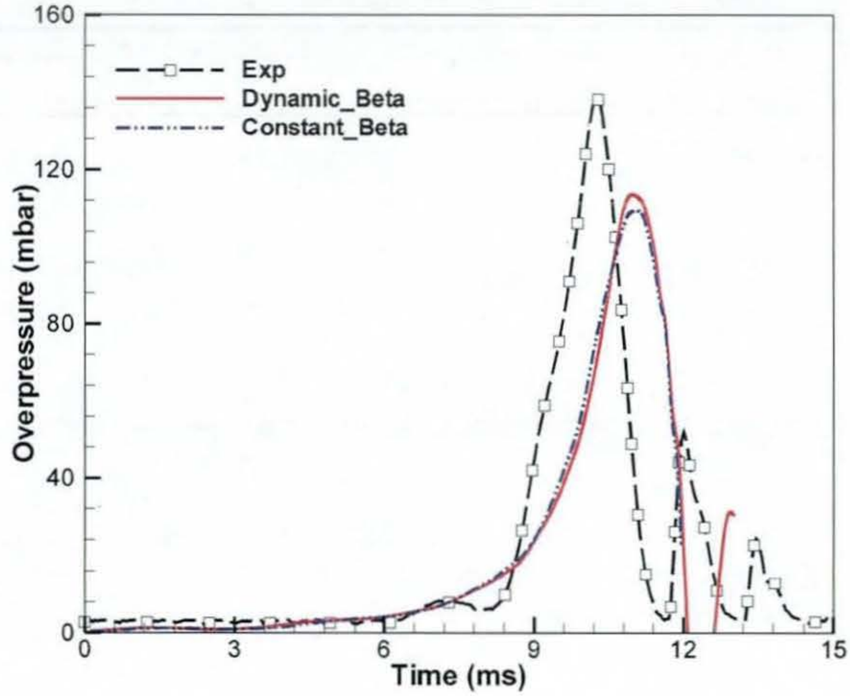

Figure 8.26 Comparison of overpressure time trend between experimental measurements and numerical predictions.

Flame characteristics such as position and speed are shown in Figures 8.27, 8.28 and 8.29. Evidently, Figure 8.27 shows a very good overlapping of the LES predictions (for both simulations) with experiments, which are in excellent agreement. Calculated time histories of flame speed are presented and compared with experimental flame speed in Figure 8.28. Figure 8.29 presents flame speed against flame position for both numerical predictions and experimental measurements. Figures 8.28 and 8.29 are confirming the excellent agreement (based on time scale) at all stages of flame propagation, while encountering the solid obstacles. For instance, at time 11 ms, after ignition, experiments recorded 55 m/s where as LES predicted ~ 57 m/s. However, based on the peak over pressure reference, the flame characteristics are slightly different.

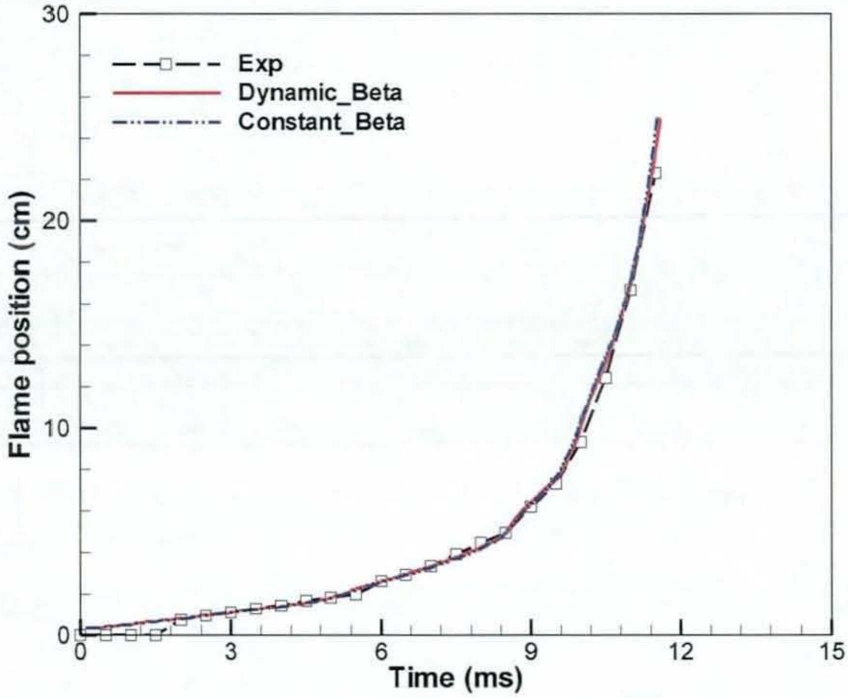

Figure 8.27 Comparisons of flame position between LES simulations and experimental measurements after ignition.

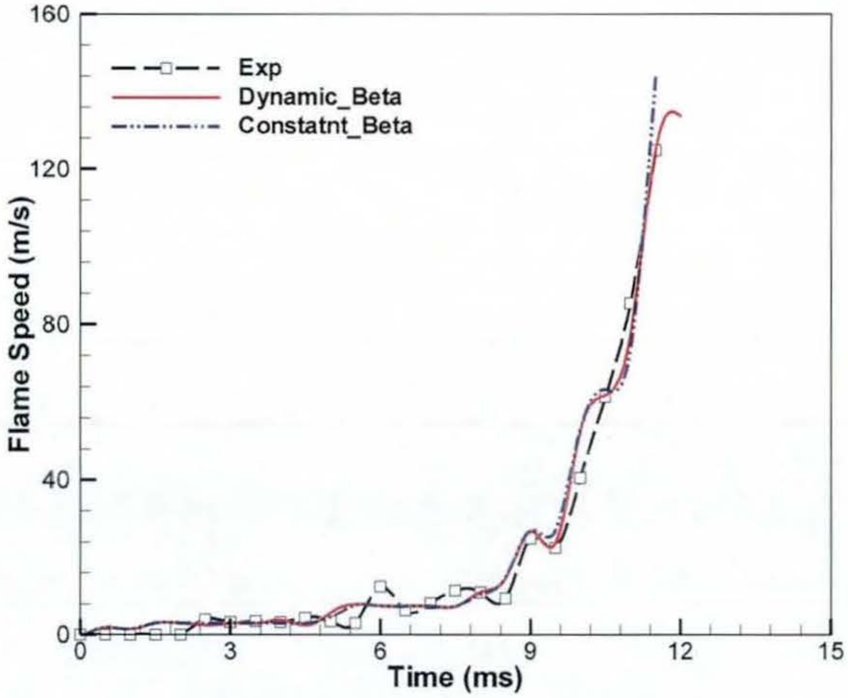

Figure 8.28 Comparison of derived flame speed between LES simulations and experimental measurements.

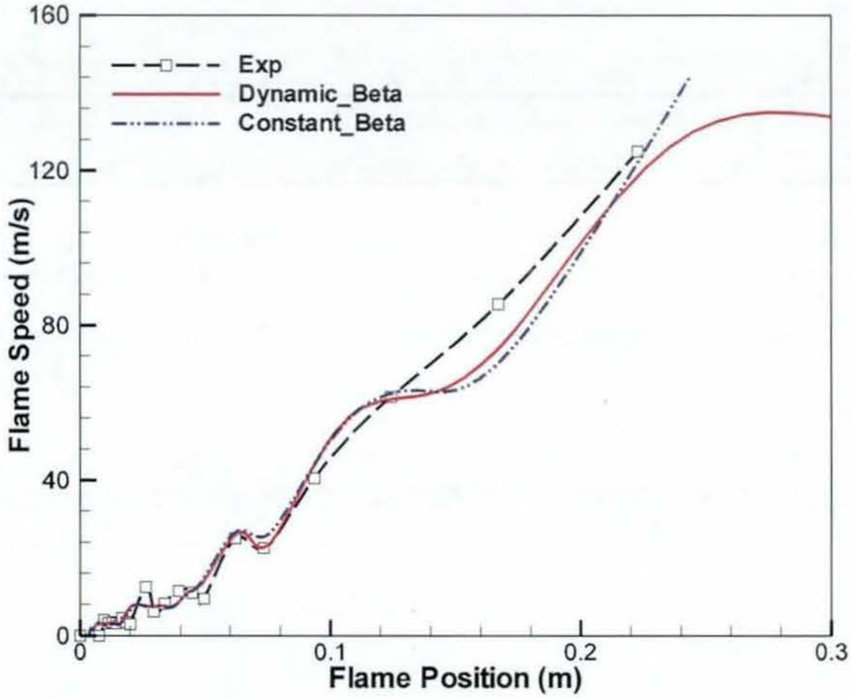

Figure 8.29 Comparison between LES simulations and experimental data for the variation of the flame speed with flame position.

Figure 8.30 shows time histories for the model coefficient β, for LES simulations with both constant and dynamic formulation. The value of the model coefficient has been extracted from LES data at the leading edge of the propagating flame front. The solid red line in Figure 8.30 represents the model coefficient calculated by the dynamic formalism and the blue dashed line represents constant β value i.e. 1.2 used in the simulation. It is noted at this stage that, the model coefficient calculated by the wrinkling flame factor is dynamic in nature, yet very close to the constant value ($\beta = 1.2$) before reaching the peak overpressure i.e. < 11 ms. After the peak overpressure, it should be noticed that the model coefficient has reached a maximum value of about 1.6, which is due to the change in the local flow conditions. It should also be noticed that, the model coefficient has suddenly increased at around 11ms from 1.2 to 1.25. This has caused a slightly higher SGS chemical reaction rate, leading to a slightly higher peak pressure.

Figure 8.30 also shows the fractal dimension D (calculated from equation 5.34) represented by a dash doted red line corresponding to the right hand scale. These values have also been extracted at the leading edge of the flame and representing the wrinkled nature of flame at any given time. It is very interesting to identify the fractal nature of the turbulent flame, which is dynamically calculated based on local flow information. A sudden increase in the fractal dimension from 2.28 to 2.35 at around 8ms can be observed in Figure 8.30, which is due to the protruding flame through the third baffle plate, before hitting the square solid obstacle. However, there is not much impact noticed due to the sudden jump of fractal dimension on the model coefficient, as lower cut-off scale is acting as a damping function.

Figure 8.31 shows the chemical reaction rate plotted against reaction progress variable for both models at peak overpressure reference. The scattered data shown in symbols (Red dots) is obtained from dynamic modelling of the model constant and dashed line represents spatially averaged reaction rate from FSD using constant value for β. The reason for showing averaged reaction rate instead of scattered data in the later case is just to distinguish between reaction rates from both the models. It can be noticed that, a slightly higher chemical reaction rate (~210 kg/s) is obtained at reaction progress variable of 0.5, which is used to define flame position in the combustion chamber.

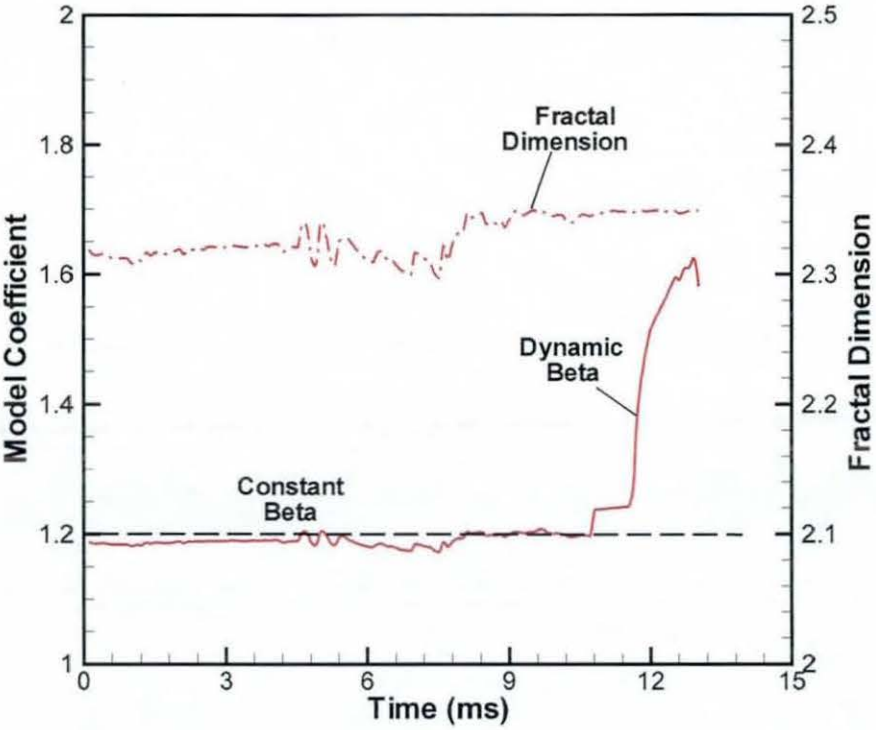

Figure 8.30 Time series of the model coefficient using dynamic procedure and the fractal dimension at the leading edge of the propagating flame.

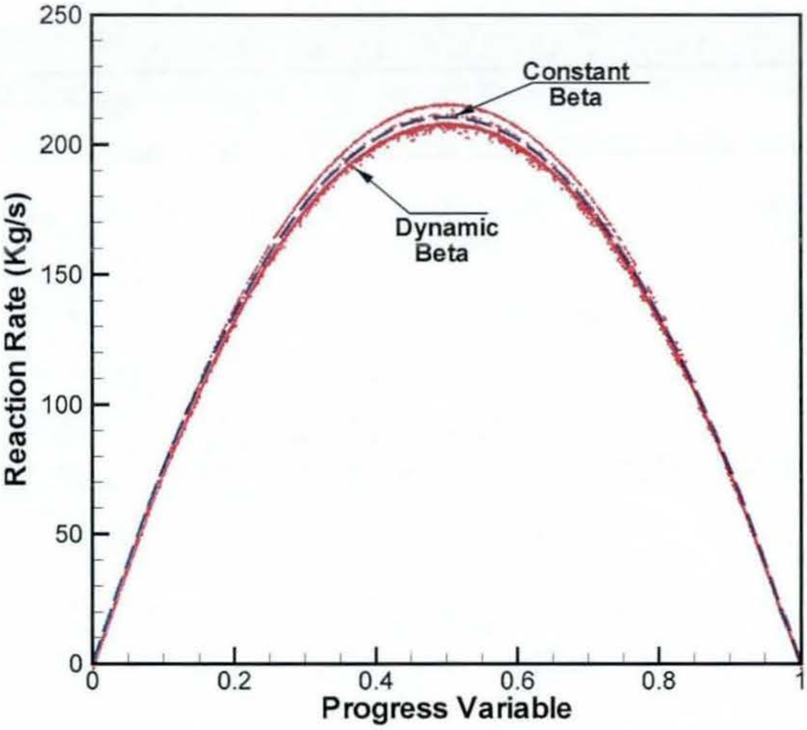

Figure 8.31 Variation of the reaction rate with the reaction progress variable, calculated by the FSD model at peak pressure.

Dynamic modelling of the model coefficient in the simple FSD equation (equation 5.19) though did predicted the global features of flame characteristics at various stages well, still there is a lot of room for improvement. It should be noted at this stage, that the improvement in the predictions is not very significant and should be considered as an encouraging lead to implement the dynamic procedure for the calculation of the SGS flame surface density. It can also be concluded that, using a constant value for the model coefficient, based on the choice of specific fuel and turbulence levels is not a bad choice for preliminary investigations.

8.4 Results from the DFSD Model

In this section, results from LES simulations employing the newly developed dynamic flame surface density (DFSD) model for turbulent premixed flames are presented. The DFSD formulation discussed in section 5.3 is implemented in the in-house code and examined for configuration 1 using grid C. As discussed earlier, accounting for SGS chemical reaction rate using the DFSD model involves the calculation of the fractal dimension of the propagating wrinkled flame. The DFSD model has been used in conjunction with two models for the fractal dimension, namely the empirical fractal model (EFM) and dynamic fractal model (DFM) as detailed in Table 5.1. Results from Model 3 (DFSD with EFM) and Model 4 (DFSD with DFM) are plotted together with Model 1 (AFSD) to validate against experimental measurements.

Figures 8.32, 8.33, 8.34 and 8.35 show comparison of time histories of overpressure, flame position, flame speed and flame speed with flame position for LES simulations with experimental measurements, respectively. Comparison of the predicted peak overpressures using AFSD (M1) and DFSD (M3 & M4) models clearly shows higher predictions with the DFSD formulation. This is mainly due to the contribution of unresolved flame surface density, which is captured by the DFSD formulation while calculating the SGS chemical reaction rate. The peak overpressure as presented in Table 8.5 and shown in Figure 8.32, is about 118 mbar at 11.4 ms using Model-3 (DFSD with EFM), 124.6 mbar at 10.98 ms using Model-4 (DFSD with DFM) and 109.5 mbar at 11.0 ms using Model-1 (AFSD), against the experimental measurements of 138 mbar at 10.3 ms. The peak pressure corresponds to the reconnection of the flame past recirculation zone over the solid square obstacle and burning of the trapped un-burnt gases around the obstacle. This is again confirmed by the novel DFSD model and therefore considered as a reference to validate other model characteristics.

The peak pressure and its timing are slightly under-predicted despite the complex nature of the DFSD models. This might be due to the over sensitivity of the models to turbulent motions during flame propagation between second and third baffle plates in chamber. Amplification of the predicted fractal dimension from Figure 8.36 between 7 and 8 ms is supporting this observation. This observation can be combined with experimental overpressure measurements presented in Figure 8.32, shows a short hump in the overpressure between 7 and 8 ms and can be attributed to jetting of the flame through second baffle plate in the chamber. LES predictions using all models including DFSD model failed to predict this short hump as shown in Figure 8.32.

Another reason might be the drop off in flame speed followed by acceleration as shown in Figures 8.34 and 8.35, after the flame encounters the square obstacle (~ between 10 and 11 ms); during this period the peak pressure is occurring. However, there is no drop off in experimental flame speed as shown in Figures 8.34 and 8.35, which might be due to the limitation of experimental data points derived from video images. Finally, ignition modelling used in the present study might have significant influence in predicting the time of incidence of the peak over pressure and other flame dynamics. Identifying the influence of the ignition modelling on flame dynamics is another subject of interest. However, flame propagation speed and position as shown in Figure 8.33 & 8.35 and flame structure at various instants after ignition as shown in Figure 8.37 are in good agreement with the experimental measurements for DFSD models.

Analysis	**Model**	**Time (ms)**	**Over pressure (mbar)**	**Flame Position (m)**	**Flame speed (m/s)**
LES	M1	11.00	109.5	0.178	81.5
	M3	11.40	118.0	0.187	78.0
	M4	10.98	124.6	0.185	80.0
Experimental	-n/a-	10.30	138.0	0.150	56.0

Table 8.5 Summary of the results from fine grid simulations and experimental measurements. (See Table 5.1 for various models used.)

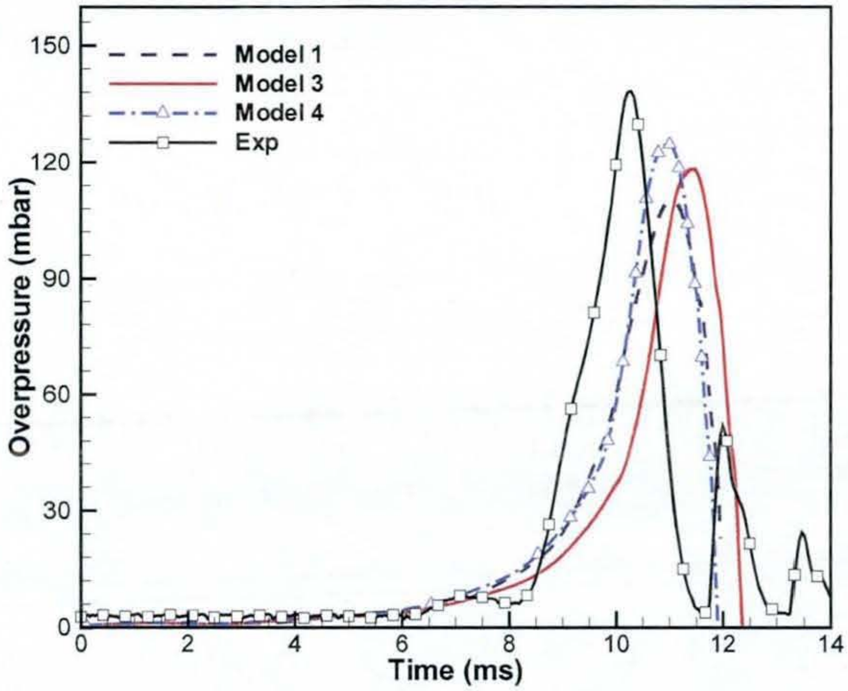

Figure 8.32 Time traces of LES simulations from AFSD and DFSD models are compared with experimental measurements (a) Peak overpressure

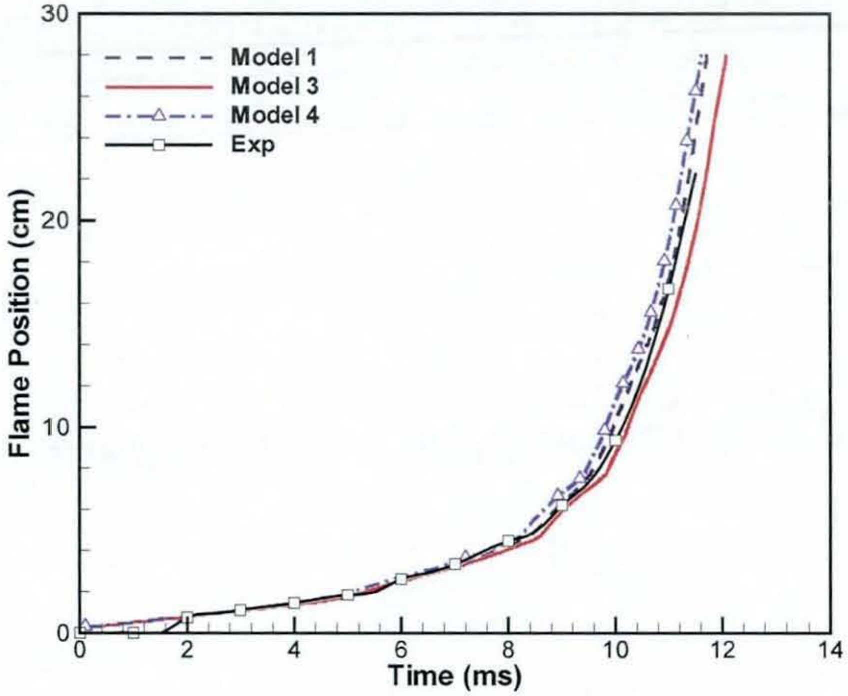

Figure 8.33 Time traces of LES simulations from AFSD and DFSD models are compared with experimental measurements (a) Flame Position

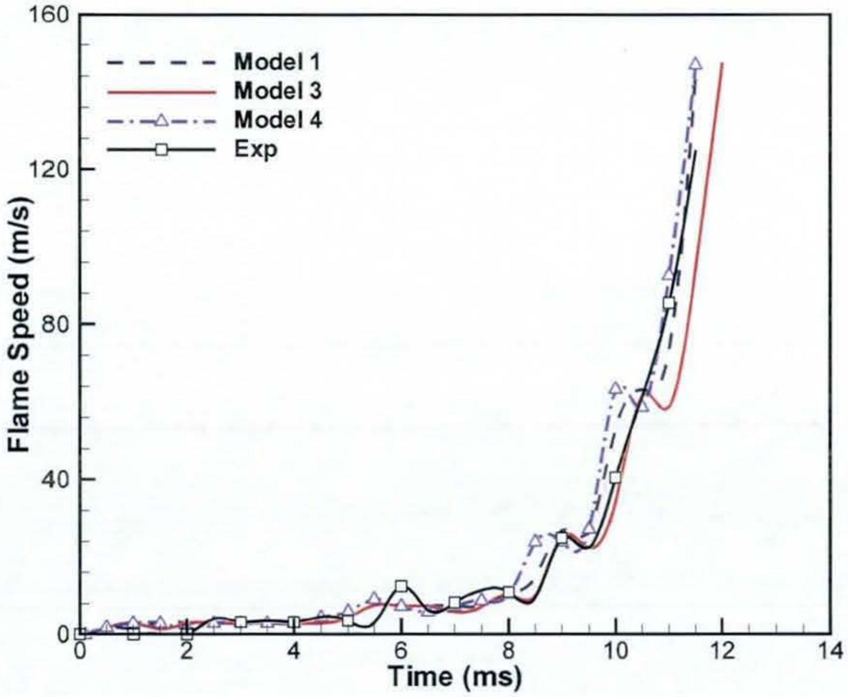

Figure 8.34 Time traces of LES simulations from AFSD and DFSD models are compared with experimental measurements (a) Flame speed

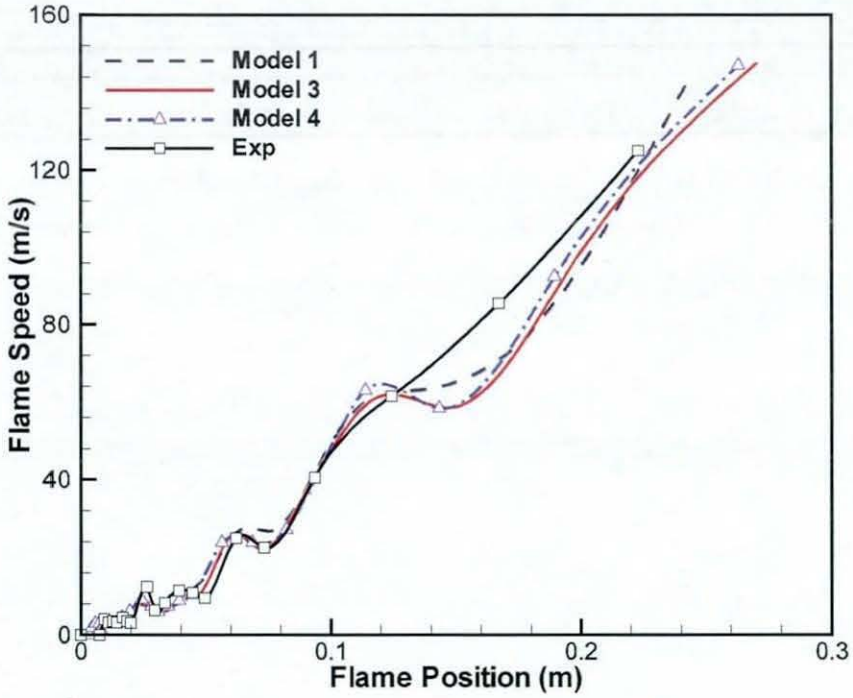

Figure 8.35 Time traces of LES simulations from AFSD and DFSD models are compared with experimental measurements (a) Flame speed vs. flame position.

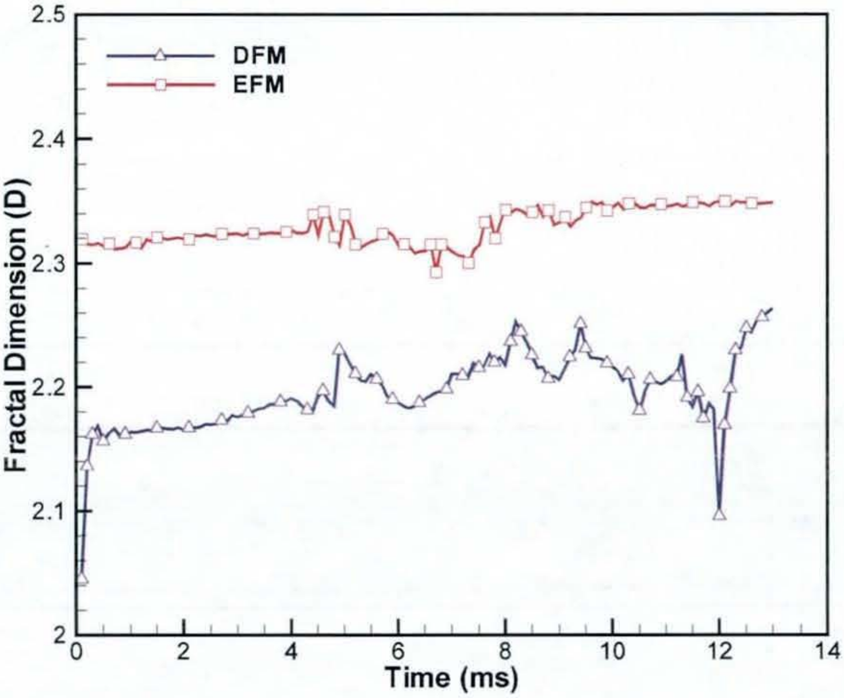

Figure 8.36 Time series of the fractal dimension at leading edge of the turbulent premixed propagating propane/air flame in a confined combustion chamber.

From the above discussion and the results presented in Figures 8.32, 8.33, 8.34 and 8.35, it is evident that, the DFSD model provides superior results as compared with the results obtained using the simple AFSD for the chemical reaction rate. Hence, further analysis is carried out in order to evaluate the reliability of the fractal models used with the DFSD model. In order to examine the results, it is sensible to choose a reference frame corresponding to the peak overpressure in all the cases, as this instance corresponds to a similar global scenario of flame reconnection past the recirculation zone, while consuming the entrapped unburned mixture in the combustion chamber.

8.4.1 Sensitivity of the Flame to the Fractal Dimension

In the present study, both models i.e. EFM & DFM are examined in Model-3 & Model-4 respectively for propane/air flames propagating over solid obstacles. In order to assess the sensitivity of the fractal dimension on the turbulent flame, time histories of the fractal dimension from both fractal models (equations 5.34 & 5.39) at the leading edge (defined here as the most downstream location of the flame, where the reaction progress variable is 0.5) of the propagating flame as shown in Figure 8.36. It is evident from Figure 8.36 that, during the early stages of the flame propagation, where the flame is expected to be quasi-laminar, the fractal dimension calculated using EFM is rather large and representing the turbulent nature of the flame. This is possible due to two reasons; firstly, due to over sensitivity of the turbulent motions and secondly, due to less sensitivity to smoothing process by laminar burning velocity at early stages of flame propagation (North and Santavicca, 1990).

Subsequently, a clear jump in the fractal dimension is observed at around 8.5 ms due to strong local flow fluctuations as a result of flame interactions with solid obstacles inside the chamber. The fractal dimension calculated using the DFM as shown in Figure 8.36 appears to be more realistic, as this model found to captures the quasi-laminar fractal dimension of the flame during early stages quite well. A gradual increase in the fractal dimension is observed due to increase in the turbulence intensity as the flame propagates from the ignition end. Fluctuations in the predicted fractal dimension are very clear from Figure 8.36, due to the presence of the solid obstacles at various stages of flame propagation. It is also evident from Figure 8.36 that the fractal dimension is always less the enforced maximum value (< 2.5) and probably limitation may not be required as it has never been reached. More detailed discussion of this with respect to turbulent premixed flame propagation is presented in the next section.

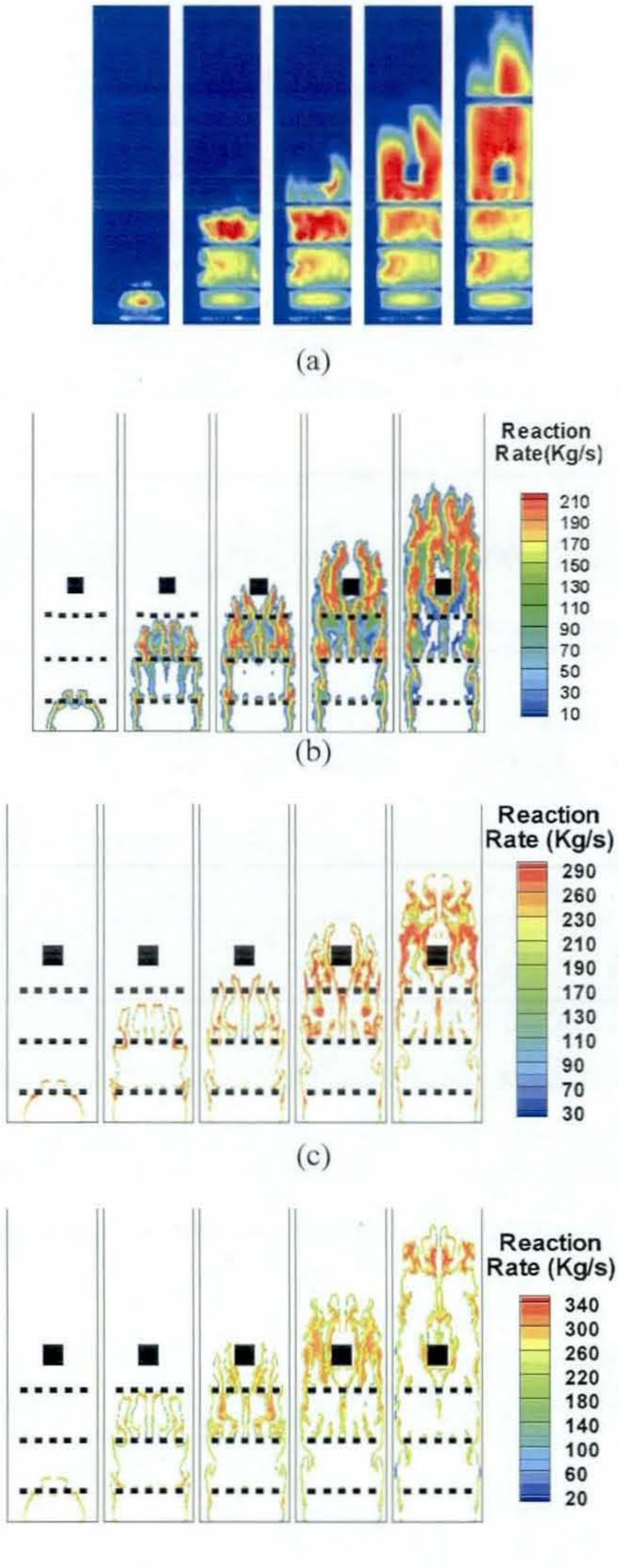
(a)

(b)

(c)

(d)

Figure 8.37 Sequence of images to show flame structure at different times after ignition at 6, 9.5, 10, 10.5 and 11.0 ms. Reaction rate contours generated from LES predictions are presented against high speed recorded video images of experiments. (a) Experiments (b) AFSD (c) DFSD with EFM (d) DFSD with DFM.

8.4.2 Evaluation of the DFSD Model

Following the budget analysis of reaction rate and flame surface density in LES by Boger et al. (1998), plotting various budgets such as reaction rate, resolved and unresolved FSD against reaction progress variable at a chosen realisation for both models i.e. AFSD & DFSD, would ideally give some insight, where further improvements can be made. For the present analysis, at peak overpressure, the mean chemical reaction rate is spatially averaged in the domain as a function of Favre filtered reaction progress variable and plotted for three models as shown in Figure 8.38. It can be evidently seen that, the SGS reaction rate is lower in case of AFSD model when compared with DFSD models (Model-3 & Model-4). From a similar analysis detailed in section 8.2.4, the stretched laminar flame thickness is identified to be within the range of 0.27-0.33 mm for AFSD and DFSD models, which is less than the LES grid resolution employed (typical grid size is 0.75 mm in case of fine grid) in the present simulations. Hence, the loss in SGS reaction rate prediction, in case of AFSD model is not due to the flame brush thickness and its insensitivity to turbulent motions. The key factor for this loss is due to the simplicity of AFSD model compared to the other two models. To clarify this fact, the Favre filtered resolved FSD profile is plotted as a function of Favre filtered reaction progress variable in Figure 8.39. Even though there is no experimental evidence to compare the reaction rate and flame surface density, it is apparent that the AFSD model under predicts even the resolved FSD compared with the other two models. This is the primary reason why the premixed flames predicted using AFSD model is not so precise. Also it can be seen that the maximum reaction rate occurs close to $\tilde{c} = 0.5$, which is the progress variable considered to identify the location of the flame front.

It is also worth mentioning from Figure 8.39 that, even though the same formulation and methodology is used to calculate the resolved part of the FSD in case of DFSD models (Model-3 & Model-4), the resolved FSD is not the same due to different fractal models i.e. EFM and DFM and has different maximum values. Similarly, the spatially averaged unresolved contributions at the same realisations are plotted with progress variable as shown in Figure 8.40. The instantaneous scattered distribution of the unresolved flame surface density accounted for by the DFSD models using dynamic fractal model and empirical fractal models are shown against filtered progress variable respectively in Figure 8.41 and 8.42. These are the contributions which are additionally calculated in this work and enhancing the accuracy of the simulations. It can be noticed from the Figure 8.40, that the maximum unresolved contributions obtained by the dynamic and empirical fractal models are different and DFM has slightly lower value, which might be one of the reasons for the lower peak pressure. Also it can be seen that the spatially averaged profile of the unresolved FSD from DFM is skewed towards burning side of flame and attaining maximum value at $\tilde{c}$ = 0.6. Similar drift can be noticed with the reaction rate profile shown in Figure 4a, and it is clear that the predicted reaction rate by both DFSD models is very close to each others.

The skewness in the spatially averaged unresolved FSD towards the burning side, as obtained with DFM, is purely due to the dynamic nature of the model in considering the local flow information to calculate the fractal dimension. As described in Section 8.4.1, in case of EFM, the fractal dimension has been calculated from an equilibrium situation of flame wrinkling due to turbulent motions and smoothing of flame due to laminar burning. Evidently, this can be identified from the model constant *Cs* given in equation (5.32), which is primarily involved with the fractal dimension, outer and inner cut-off limits. Several values are available for the inner cut-off limit and in the present analysis it is taken as three times of the laminar flame thickness width following Knikker et al. (2004). The LES filter width is considered as the outer cut-off length. The model constant *Cs*, calculated by both fractal models for the fractal dimensions are plotted against the filter width as shown in Figure 8.43. The symbols shown in Figure 8.43 are the actual values of the model constants and the line is a fitted polynomial through the symbols. It is clear from this plot that the fractal dimension has higher impact in evaluating the model constant, which in turn affects the unresolved FSD in the dynamic formulation. However, there is no experimental or DNS evidence to confirm this phenomenon.

The flame structure is represented in terms of the chemical reaction rate obtained from the three LES simulation and shown in Figure 8.37 at different times after ignition together with experimental high speed video images. The overall flame structure and speed as well as the mechanism by which the flame approach the solid obstructions, jetting through the gap around the obstacle and reconnection downstream from the solid obstacle are all well predicted. It has been found that both models successfully predict the essential features of flame/flow interactions. However, results from the DFSD model, shown in Figure 8.37 (c) and 8.37 (d), are in better agreements with experimental measurements compared with those obtained using the AFSD model as shown in Figure 8.37 (b). This may be due to contributions of the unresolved FSD to the mean chemical reaction rate.

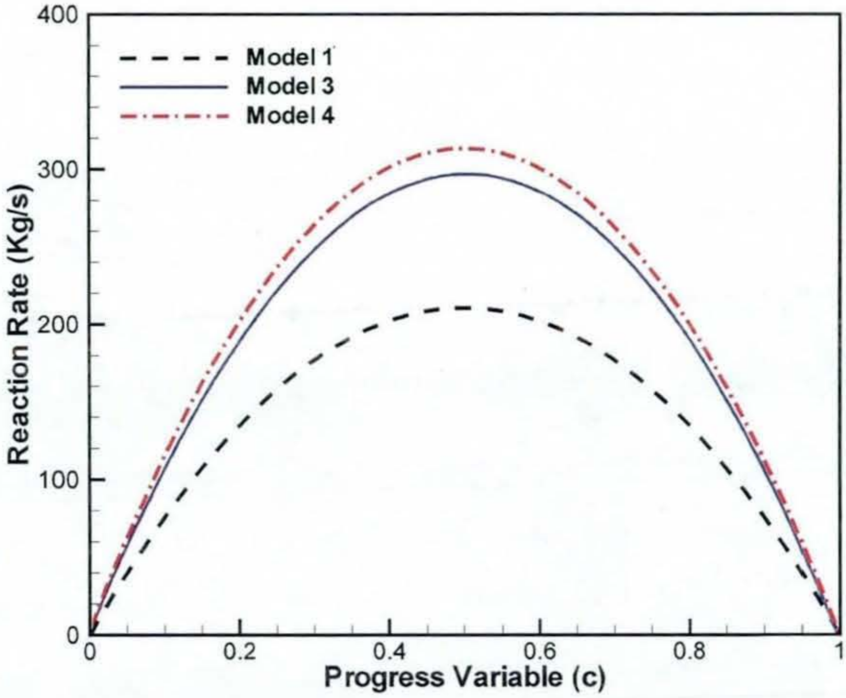

Figure 8.38 Variations of the spatially averaged reaction rate at peak overpressure from LES simulations.

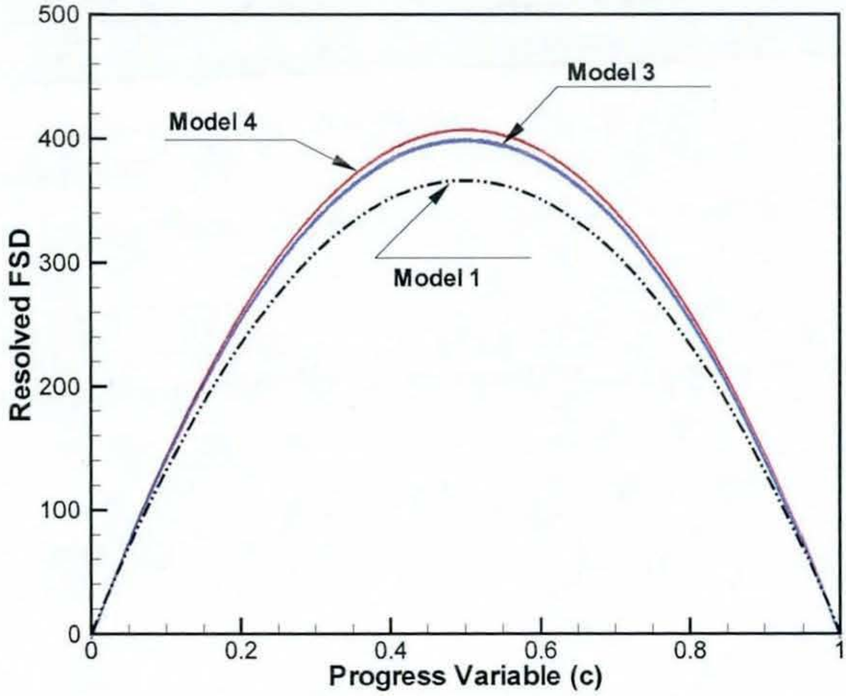

Figure 8.39 Spatially averaged resolved FSD against reaction progress variable for Model 1, 3 & 4.

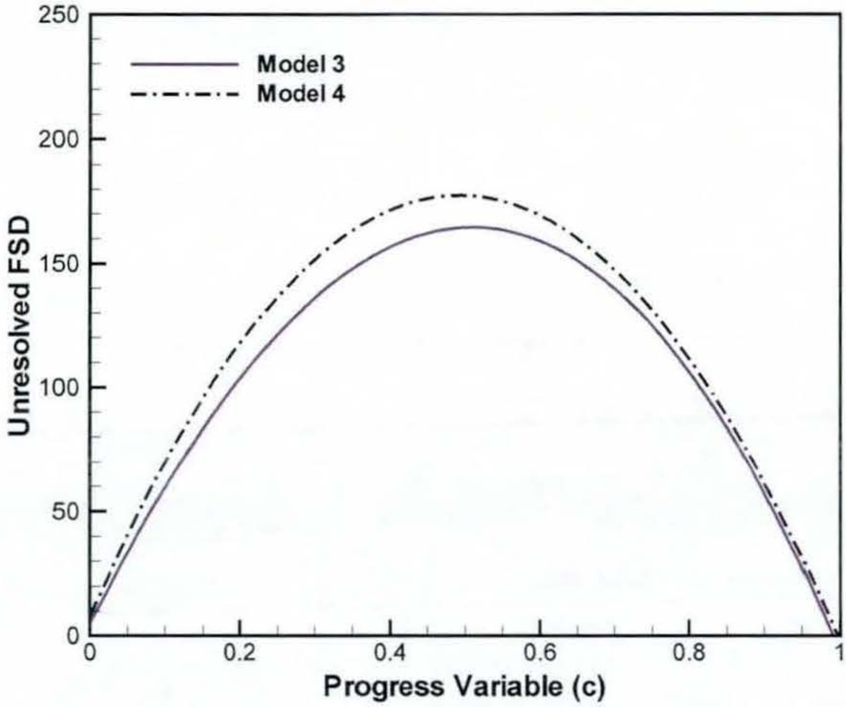

Figure 8.40 Spatially averaged unresolved FSD contributions calculated from both the DFSD models.

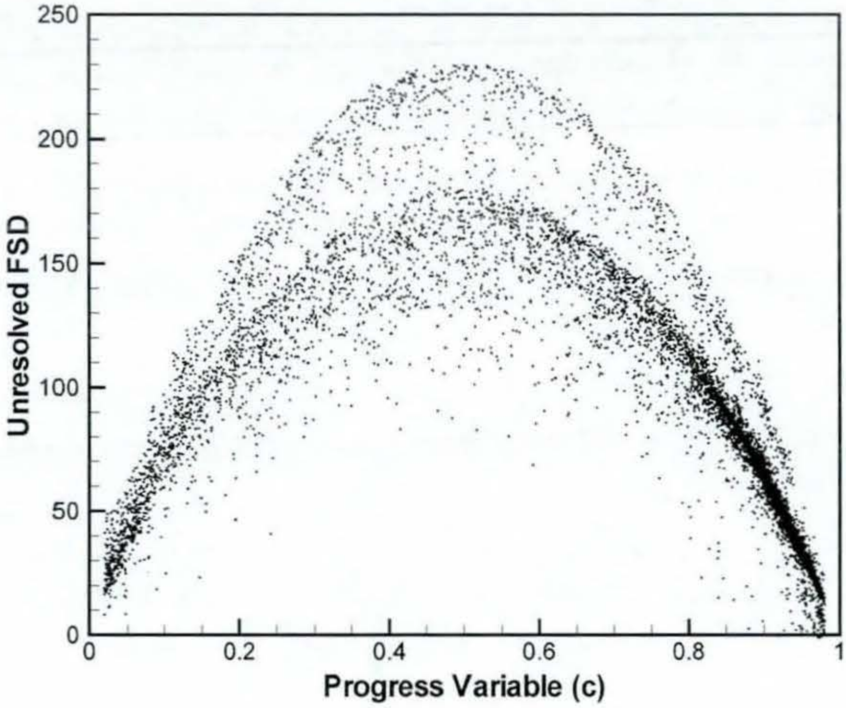

Figure 8.41 Scattered unresolved FSD contributions using DFSD model with DFM.

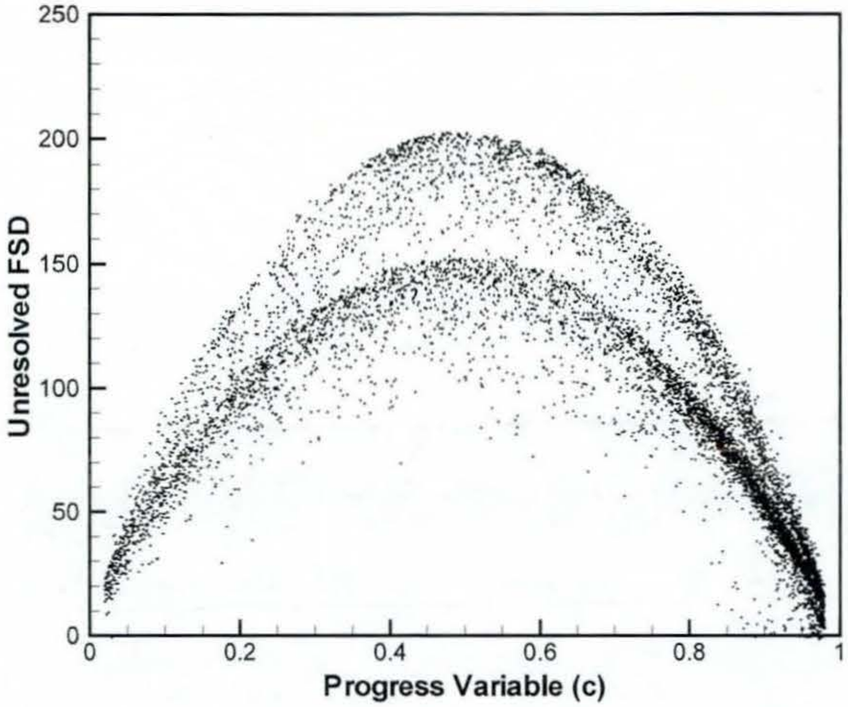

Figure 8.42 Scattered unresolved FSD contributions from DFSD model with EFM.

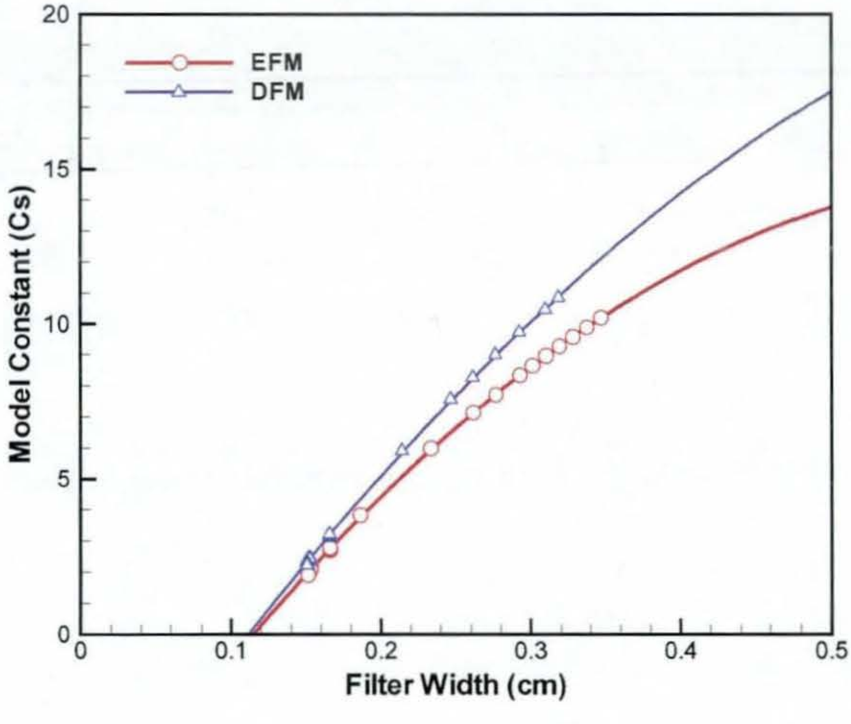

Figure 8.43 Model constant *Cs* for various filter width ($\overline{\Delta}$) employed in LES simulations. Fractal dimension is calculated using DFM and EFM.

It can be observed from Figures 8.37 (c) and 8.37 (d), that the DFSD model is able to predict regions with high sub-grid scale contribution of the flame surface density. To get more details of this, contours of the resolved and unresolved flame surface density contributions to the reaction rate from the DFSD model are presented at the time of peak pressure in Figure 8.44. Figures 8.44 (a), 8.44 (b) and 8.44 (c) show the contours of the reaction rate, resolved FSD and unresolved FSD respectively, using DFSD with EFM and DFM. Resolved flame surface density contributions to the reaction rate by both the DFSD models are close together, as both models are based on the same laminar flamelet model concepts. It can also be identified from Figures 8.44 (a), 8.44 (b) and 8.44 (c) that the unresolved FSD contributions are predicted adequately by Model-3 & Model-4 and such unresolved contributions are evidently increasing the overall mean reaction rate.

Overall, the numerical predictions from the DFSD model provide a good representation of the interactions between flame, flow and solid obstructions and are in good agreement with experimental observations. However, the magnitude and timing of occurrence of the peak overpressure are slightly under-predicted. The results can probably be improved by considering the errors associated with the calculations of the fractal dimension, especially by choosing a proper lower cut-off scale. Also it is identified earlier, that the reason for differences in peak overpressure occurrences by different models is due to the ignition radius in the model employed. A brief discussion on the influence of ignition radius on the LES results is provided in the next section.

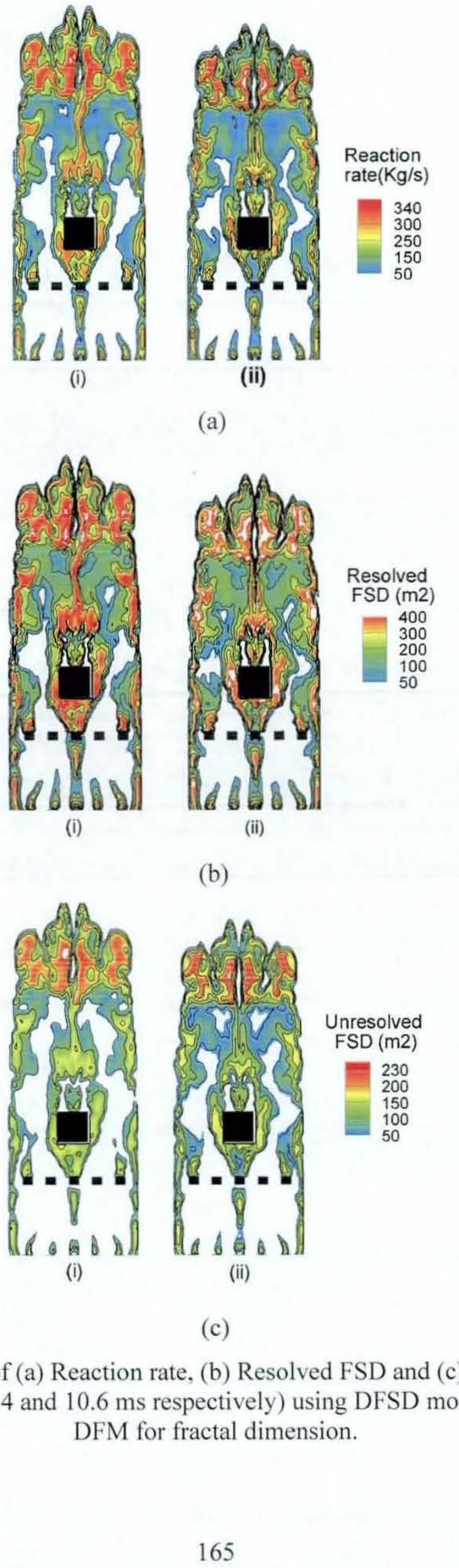

Figure 8.44 Contours of (a) Reaction rate, (b) Resolved FSD and (c) Unresolved FSD at peak over pressure (11.4 and 10.6 ms respectively) using DFSD model with (i) EFM (ii) DFM for fractal dimension.

8.5 Influence of Ignition Radius

This section describes the influence of ignition radius on overpressure trend and its timing in configuration 1. Six additional LES simulations using grid resolution C, with various ignition radiuses and initial progress variable values are carried out using Model-4 i.e. DFSD with DFM. All these simulations have been carried out using test filter ratio (γ) of 1.362. The test filter ratio 1.362 is particularly chosen, as Kirkpatrick et al. (2000) conducted parametric analysis while using 4 mm ignition radius in their numerical combustion chamber.

In the present analysis, four simulations are carried using 3, 4, 5 and 6 mm of ignition radius with a reaction progress variable of 0.5, initialised at the start of the simulation. Additionally, two extra simulations are carried with 4 and 6 mm of ignition hemi-sphere with a reaction progress variable of 0.7. The basic idea of this analysis is to verify that, which ignition radius is appropriate to choose, in order to achieve quasi-laminar phase of the premixed propagating flame. The peak overpressure and its incidence time are detailed in Table 8.6.

Figure 8.45 presents the pressure-time histories obtained from four LES simulations against experimental overpressure. Also, figures 8.46 (a) & (b) present values of the time of occurrence of peak overpressure and its magnitude, respectively, and validated against experimental measurements. It is very interesting to note from these figures, that the ignition radius of the hemi-sphere has linear relation with respect to the incidence of peak pressure. The straight horizontal line in Figure 8.46 (a) represents the time of experimental peak overpressure in configuration 1, which is roughly representing an ignition radius of about 4.5 mm. However, Figure 8.46 (b) divulges that there is no such significant influence on the magnitude of overpressure predictions.

Snap-shots of the reaction rate contours from LES simulations at peak overpressure time are presented in Figure 8.47. It reveals that irrespective of ignition radius chosen, the contours are representing similar propagating flame scenario in the combustion chamber. Though Figure 8.47 shows very few differences, at this instance in flame position, thickness, pockets, shape of recirculation zone and structure, it is quite encouraging that all LES simulations have predicted the overall flame characteristics very well. It can also be identified that, irrespective of the radius chosen to initialise ignition, overpressure predictions show a maximum of 1–2 % variation, which is quite encouraging in choosing appropriate value of ignition radius to achieve the correct timing. It should also be noticed here, that overpressure predicted by these simulations is less than 124.6 mbar, which was predicted by the LES simulation using test filter ratio 2.0. The under-prediction of overpressure is probably due to the test filter ratio, which has significant impact on LES simulations.

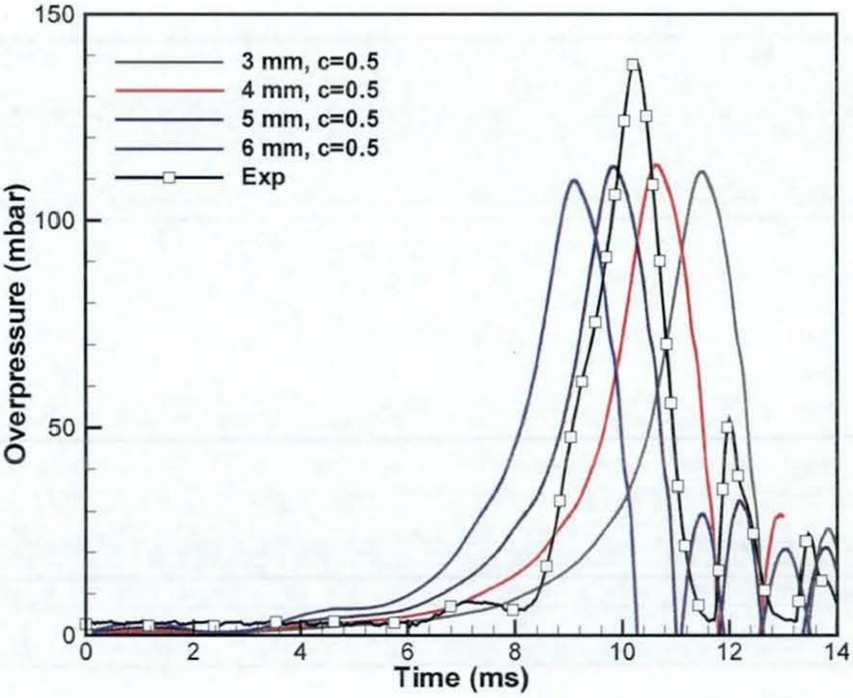

Figure 8.45 Overpressure time traces of LES simulations using various ignition radiuses, reaction progress variable of 0.7 against experimental measurements.

Radius of Ignition Hemi-sphere (mm)	Reaction Progress Variable	Peak Overpressure (mbar)	Time of Occurrence (ms)
3	0.5	111.80	11.49
4	0.5	113.59	10.64
5	0.5	113.15	9.85
6	0.5	109.73	9.11
4	0.7	112.75	11.02
6	0.7	109.94	9.70

Table 8.6 Outcome of LES simulations using various ignition radius and initial reaction progress variable values.

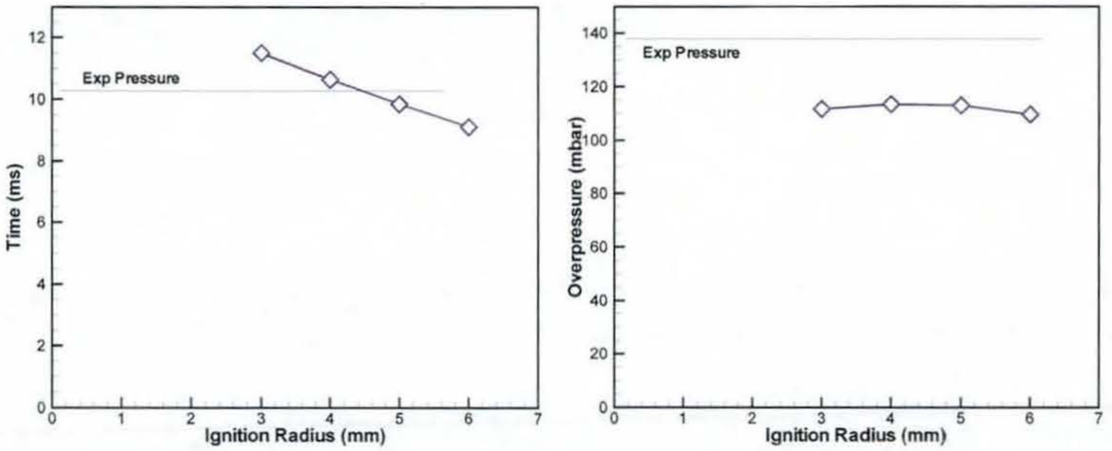

(a) (b)

Figure 8.46 (a) Peak overpressure incidence time for four LES simulations against ignition radius used (b) The magnitude of peak overpressure predicted for various ignition radiuses.

Figure 8.48 presents time histories of overpressure from two additional simulations as shown in Table 8.6 using initial reaction progress variable of 0.7 within the ignition radius. It can be noticed from Table 8.6 and Figure 8.48 that, 6 mm of ignition radius has predicted peak overpressure of 109.94 mbar at 9.7 ms against 109.73 mbar at 9.11 ms using a value of 0.7 and 0.5 for $\tilde{c}$, respectively. A similar time shift of approximately 0.4 ms can be observed while using 4 mm ignition radius, with not much impact on overpressure. It is very interesting to note that using burning ($\tilde{c}$ = 0.5) to completely burned conditions (approaching $\tilde{c}$ = 0.7 or higher) to initialise ignition, dramatically shifting the timing. This type of tuning in achieving timing of peak overpressure with chosen ignition radius may seem good option and however, physically does not represent ignition and after ignition process. Hence, it should be more appropriate to choose correct ignition radius with reaction progress variable of 0.5, which could achieve quasi-laminar phase.

Figure 8.48 also presents LES simulations using test filter ratio of 2.0 with reaction progress variable of 0.5 within 4 mm radius of ignition. This LES simulation is quite impressive in achieving most accurate pressure with a small time shift of 0.68 ms from experimental pressure reference. It is identified by Hall et al. (2008) from over hundred experimental pressure measurements at base and wall in same chamber, that this shifting is only recognized in a small number of experiments involved no more than 1-2 ms. This observation supports/justifies the present LES predictions within the experimental tolerance. The timing of peak overpressure in other configurations studied in this work as shown in next couple of sections, using DFSD with DFM model (M-4), test filter ratio 2.0, initial reaction progress variable 0.5 within ignition radius of 4 mm is coinciding with experimental measurements. Hence, the idea of fine tuning the ignition radius to achieve accurate timing, based on individual configuration is unjustifiable and not implemented here. This study supports the use of a 4 mm ignition radius in order to achieve initial quasi-laminar phase in the present turbulent premixed flame analysis.

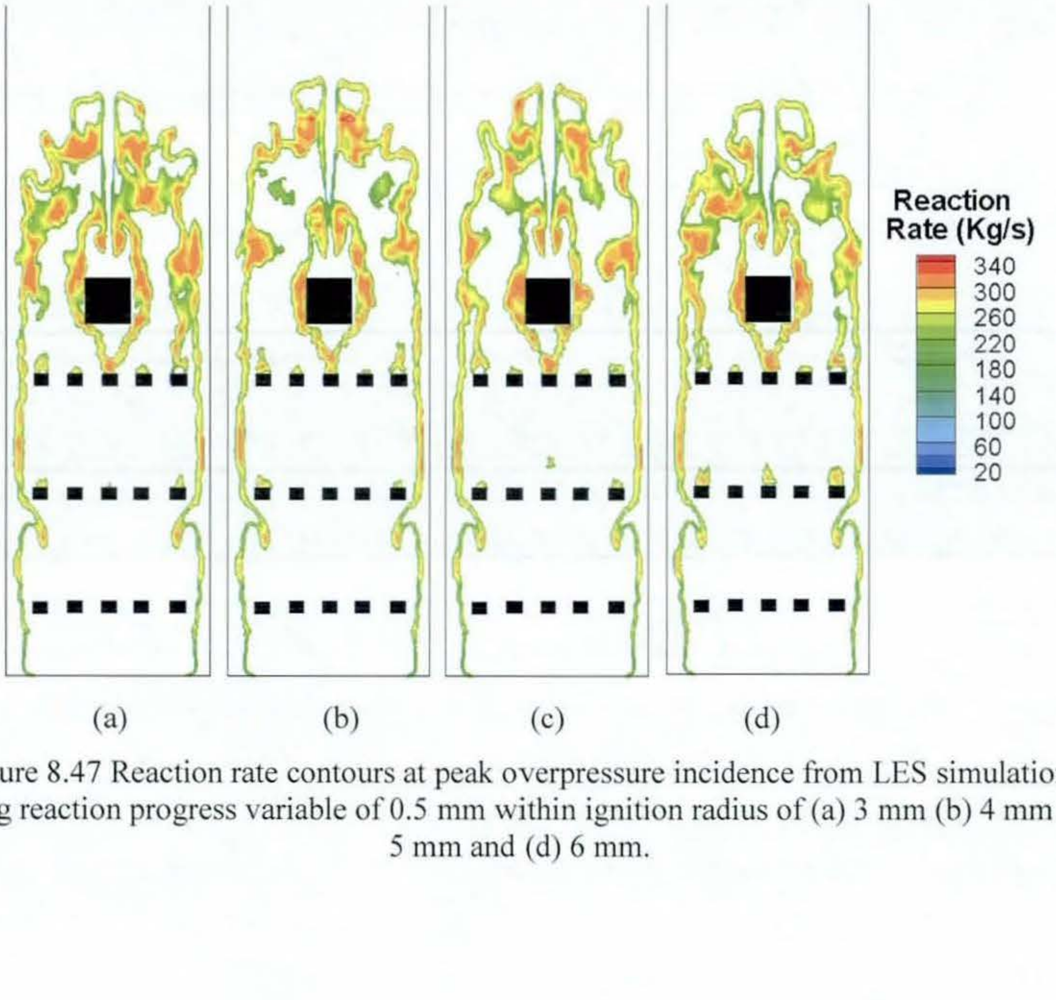

(a) (b) (c) (d)

Figure 8.47 Reaction rate contours at peak overpressure incidence from LES simulations using reaction progress variable of 0.5 mm within ignition radius of (a) 3 mm (b) 4 mm (c) 5 mm and (d) 6 mm.

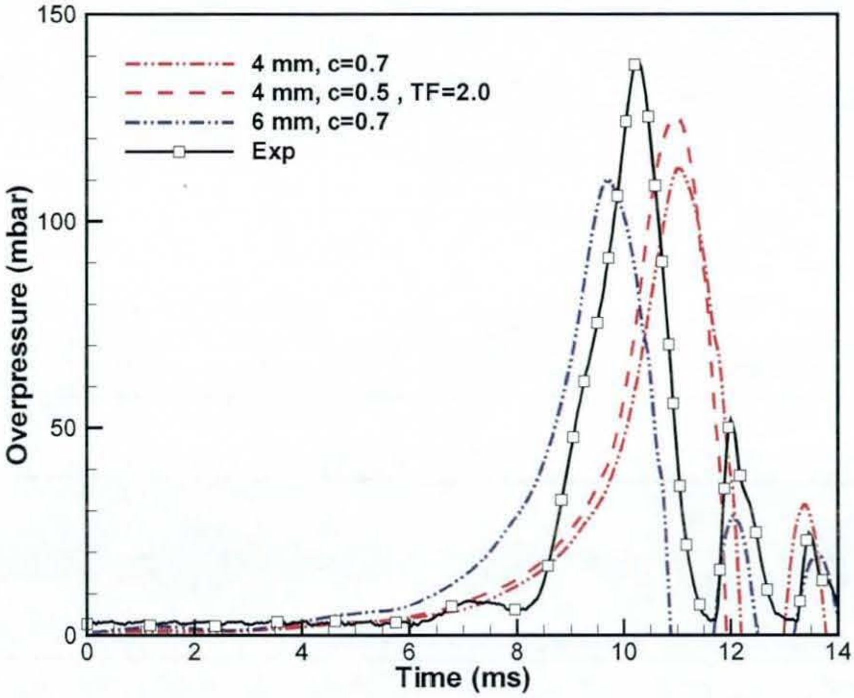

Figure 8.48 Overpressure time traces of LES simulations using various ignition radiuses, reaction progress variable of 0.7 against experimental measurements.

8.6 Influence of Solid Obstacles on Flame Characteristics

The developed dynamic FSD (DFSD) model evaluated in the preceding sections of this chapter has been identified to be more effective in predicting turbulent premixed propagating flames. To establish a higher level of confidence in using this model, various flow configurations, shown in Figure 7.3, are numerically simulated for stoichiometric propane/air mixture, ignited from stagnant condition. As described in section 8.2.5, these configurations are classified into families as shown in Figure 8.13 to facilitate efficient comparison and discussion. Furthermore, the base configuration 0 i.e. without baffles has also been simulated to validate the novel model by comparing with experimental measurements. The primary objective of the present analysis is to validate and explain the successfulness of DFSD model in predicting turbulent premixed propagating flame dynamics over a wide range of flow configurations. Secondly, influence of the position of individual baffle plate in generating overpressure, due to the interactions with deflagrating flames, with respect to the origin of ignition are examined.

8.6.1 Flame Characteristics: Configuration 0

Configuration 0 has no baffles except a solid square obstacle running through out the chamber at approximately 96 mm downstream of ignition point. Since, baffles are not presented in this chamber, the flame took longer than in any other configuration discussed in this work to encounter solid obstacle and to reach blow-down stage. This configuration is very interesting for analysis and could give some fundamental insight about the formation of flame pockets/traps, due to obstruction of the flame propagation in the chamber. Time series of overpressure and flame position from LES simulations using DFSD model (M-4) are briefly shown against experimental measurements in Figure 8.49. The overpressure trend is very encouraging, as it captures the pressure trend from ignition to blow-down much accurately, including the time of pressure rise at about 11.5 ms, slope of pressure rise, peak pressure and its incidence time at 13.5 ms and finally the pressure reflections once the main flame left the chamber.

Figure 8.49 substantiates the LES predictions of peak overpressure of 36.6 mbar at 13.5 ms against experiments measurement of 34 mbar at 13.5 ms, which is slightly over-predicted by 7.6%. However, considering the overall pressure trend from Figure 8.49, it is in excellent agreement. Similarly, the flame position shown in Figure 8.49 confirms this observation with an exact match of overpressure, up to peak overpressure and thereafter with a slight, considerable deviation. Figure 8.50 shows sequence of flame front images from LES (reaction rate contours) and experiments (false colourised images extracted from high speed video). It is evident from these images, that the LES simulations using DFSD model (M-4) is capable to reproduce turbulent flame fronts very accurately at various stages. For instance at 12 ms, the flame shape (finger shape) and its approach towards square obstacle can be immediately noticed. Similarly, at 13.5 ms (peak overpressure incidence) LES captured same shape of experimental image i.e. flame engulfs upstream of square obstacle by trapping certain amount of unburnt mixture, which can be seen to burnt before 14.5 ms. However, there is some unburnt mixture trapped in recirculation zone, which will burn after main flame left the chamber, which is causing pressure reflections.

From Figure 8.50 (a) it can be noticed that the turbulent flame thickness predicted by LES using DFSD model is about 1 to 2 grid width and the formation of wrinkles can be clearly noticed once flame starts hitting the square obstacle. However, these flame wrinkles cannot be clearly seen in experimental video images (Figure 8.50 (b)), as they are global images taken from the outside of the chamber.

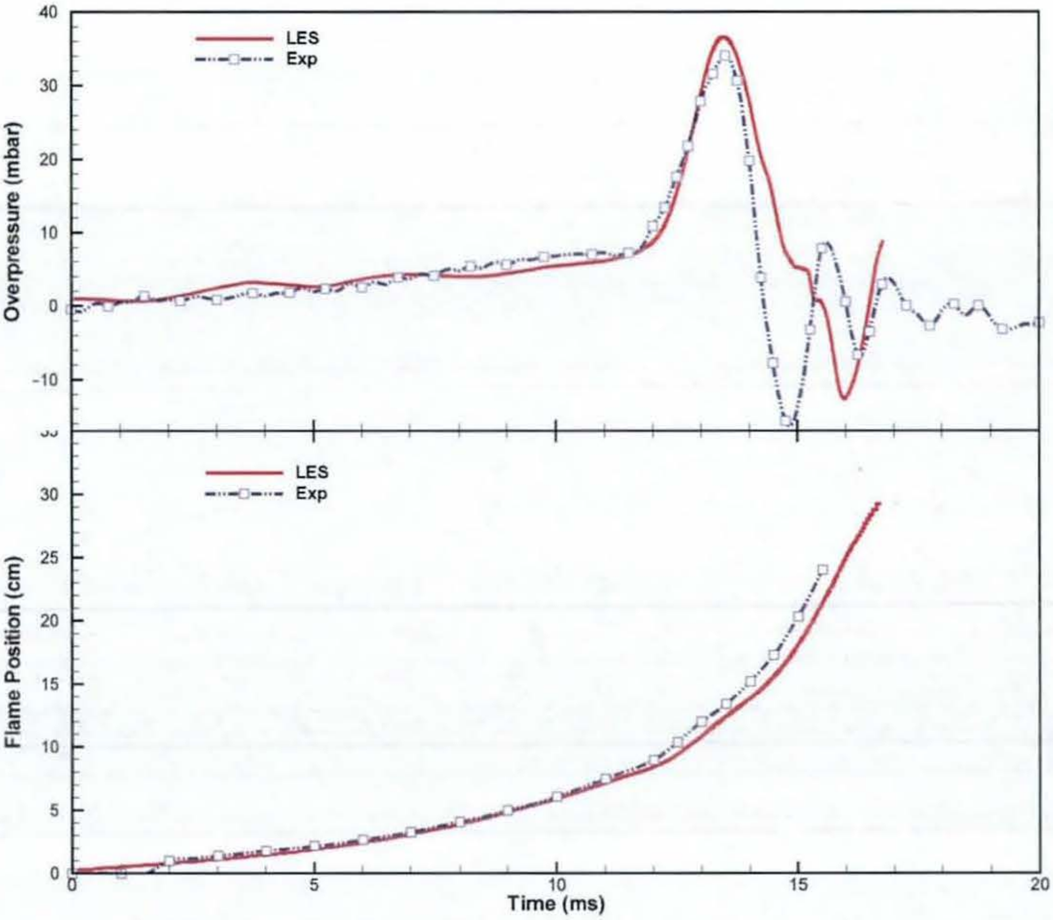

Figure 8.49 Time histories of overpressure and flame position for configuration 0.

In addition to above, experimental study recently conducted by Hall (2006) measured axial and radial flow information in the middle of the chamber (*x*-axis) and half way up the side of the square obstacle i.e. 102 mm from the base (*z*-axis) and 16 mm from the central axis (*y*-axis) using LDV technique. Laser Doppler Velocimeter measurements are available for certain configurations as detailed in Table 7.2 and are compared with LES velocity extracts to substantiate LES simulations. Experimental axial (w) and radial (v) velocity measurements shown in Figure 8.51 are the coordinates of the average polynomial fitted to the ensemble averaged velocity data from over 50 repeatable, individual experiments.

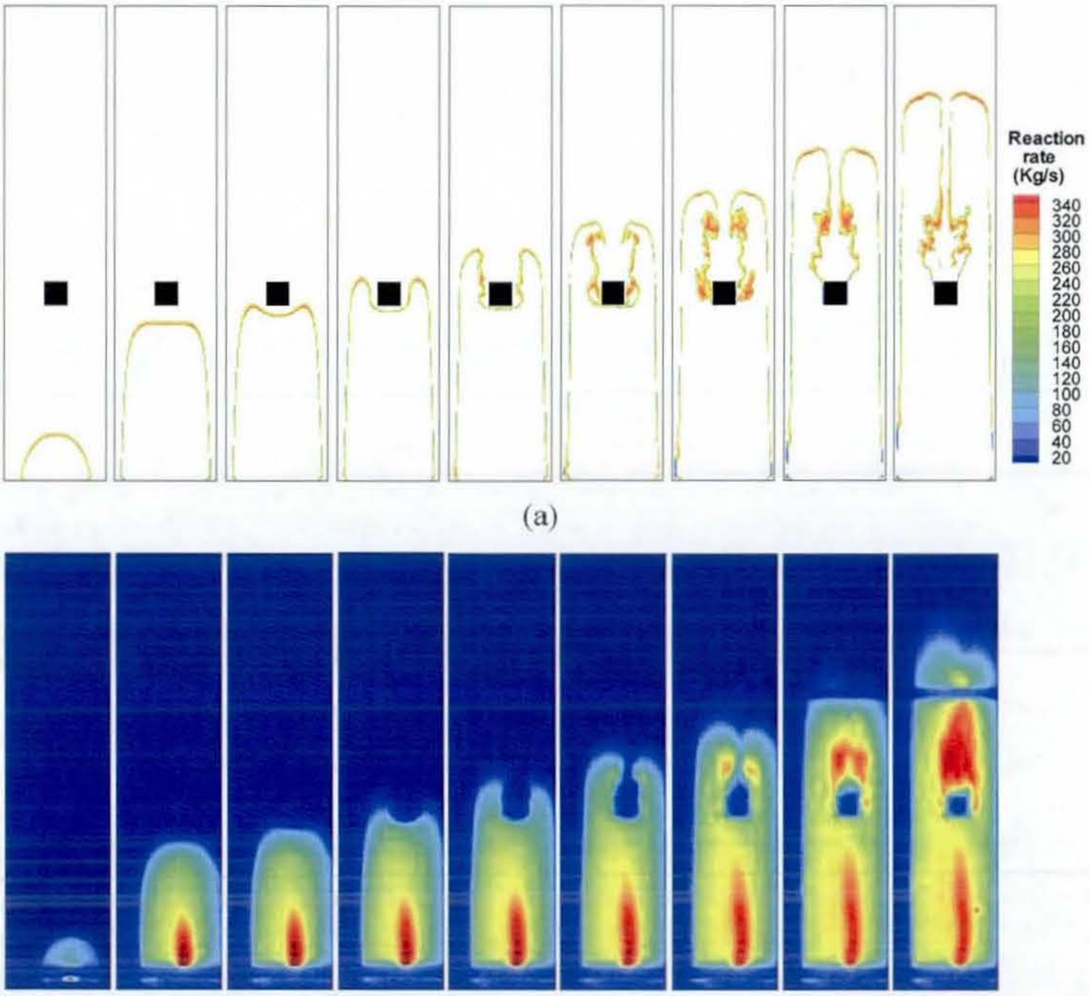

(a)

(b)

Figure 8.50 Series of flame images at 6.0, 12.0, 12.5, 13.0, 13.5, 14.0, 14.5, 15.0, 15.5 ms respectively after ignition (a) LES (b) Experimental video images (false colourised).

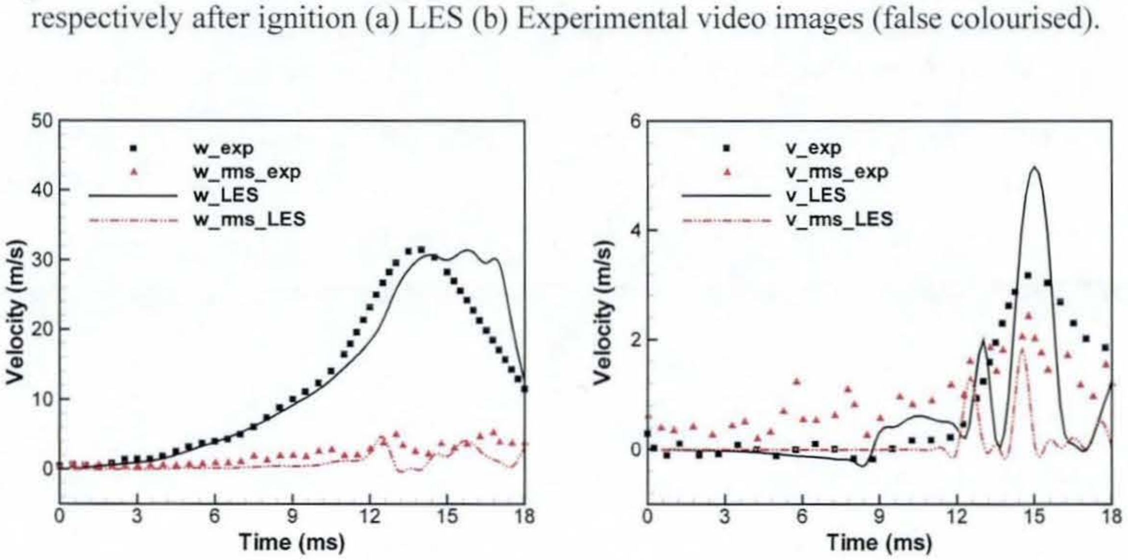

(a) (b)

Figure 8.51 Time histories of velocities and their RMS fluctuations for configuration 0 at (a) axial (b) radial velocity.

Accordingly, RMS fluctuations of w and v are calculated from the variance between a polynomial fitted to the mean velocity data. However in case of LES, the data is available from only one simulation and moreover, the flame is of totally unsteady nature, and therefore unable to obtain ensemble averaged velocity information. Hence, the only alternative choice to calculate/obtain RMS of velocity is by choosing a suitable bin size. From LES calculations, it is identified that there exist large number of data points (~100 to 500) for every one millisecond of flow due to the limitation of CFL number. Therefore, bin size of 0.25 ms has been chosen to extract average and its variance of velocity profile at 102 mm from ignition base and 16 mm from the central axis without loosing unsteady information. Averaged and RMS velocities are calculated as:

$$\bar{x} = \frac{\Sigma x_i}{n} \tag{8.4}$$

$$\text{RMS} = \left(\frac{\Sigma (x_n - \bar{x})^2}{n} \right) \tag{8.5}$$

Figure 8.51 shows the velocity mean and RMS profiles from LES and LDV measurements of turbulent propagating flame in vented chamber. It is evident from Figure 8.51 (a) that the maximum axial velocity has reached 32 m/s at approximately 14.5 ms as obtained from both experiments and LES. Velocity mean and RMS profiles of the LES are in excellent agreement up to approximately 15ms and in fair agreement with experimental measurements thereafter. The RMS fluctuations in Figure 8.51 (a) provide very good information of the turbulence levels at various stages of the flame. It can be seen that, the rate of increase in turbulence and its decay is fairly well predicted at peak pressure incidence i.e. 13.5 ms and during blow-down phase.

Considering the radial velocity mean and its RMS from Figure 8.51 (b), peaks of the mean and RMS velocities from LES are matching with experiments. It can also be noticed that, the experimental radial RMS values (red triangles) during early stages of the flame propagation (before 12 ms) measured are higher than ensemble averaged velocity (black squares) and this phenomenon is highly questionable from experimental point of view itself. Nevertheless, LES predictions of radial RMS fluctuations are found to follow the same trend of LES velocity profile. However, overall velocity mean and RMS fluctuations give a very good indication of the flame propagation in the chamber and is considered as an encouraging lead.

8.6.2 Flame Characteristics: Family 1

This section provides flame characteristics of the configurations in Family 1 using DFSD model inline with the discussion provided in section 8.2.5.1 using FSD model. This family consists of configurations 5-2-1 with progressively increasing the number of baffles from one to three and positioned farthest from ignition bottom as shown in Figure 8.13.

The time histories of overpressure and flame position from LES and experiments are plotted as shown in Figure 8.52 and 8.53 respectively. It is evident from Figure 8.52 that the overpressure trend is in excellent agreement, however, slightly under-predicted. Nevertheless, comparing the LES simulations presented in Figure 8.15 for the same family using FSD model, LES predictions using DFSD model (M-4) are very good in terms of magnitude, trend and timing, which were main drawbacks identified while using the FSD model. This is mainly due to the novel DFSD model employed, which is efficient in calculating unresolved flame surface density. Figure 8.52 highlights the impact of number of baffles and their position with respect to distance from the ignition bottom. The time elapsed in reaching the first baffle from the ignition bottom and increase in the steepness of pressure gradient due to the generated turbulence can be easily identified. Similarly, the flame position shown in Figure 8.53 is also predicted very well when compared with FSD predictions in Figure 8.17.

Figure 8.54 (a) & (b) shows flame speed and acceleration from LES and experiments derived from flame images. It can be noticed that the flame speed and acceleration from LES has matched very accurately with experimental measurements, except when the flame is located downstream of square obstacle in Region 5. One main reason for this is due to the limitation in resolution of experimental measurements. Within blow down region (R5), the flow conditions are highly turbulent and flame propagates faster with approximately about 80 - 100 m/s in this family. Hence, the available flame images within this region are limited, which eventually controls the experimental data. It is very interesting to note that irrespective of number of baffles and their position, all configurations has recorded a speed of around 100 m/s during the blow-down phase.

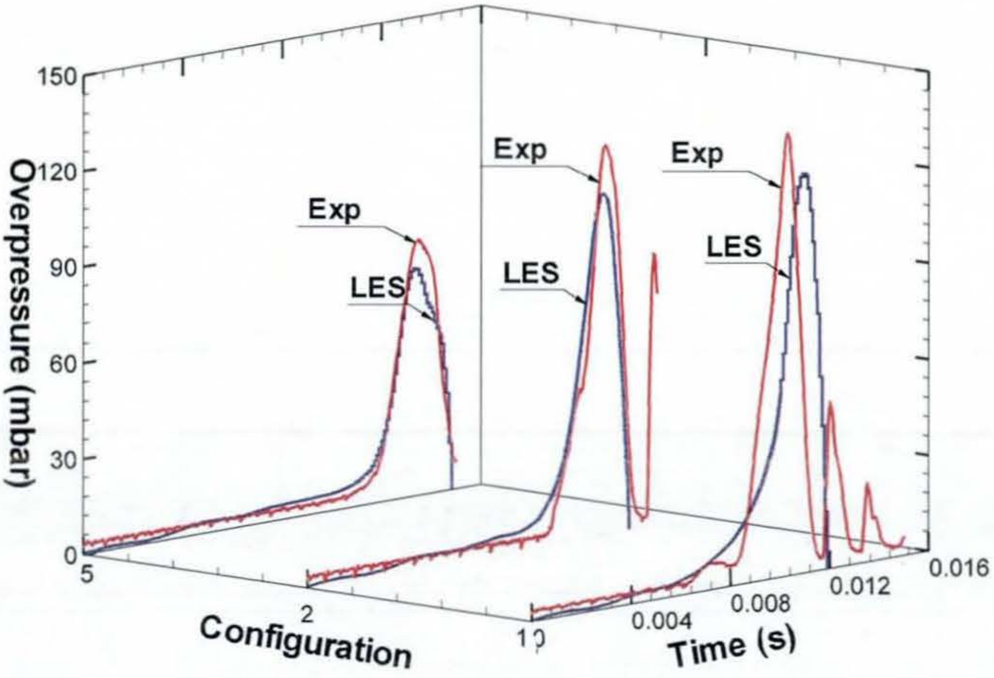

Figure 8.52 Comparison of predicted and measured overpressure time traces of Family 1.

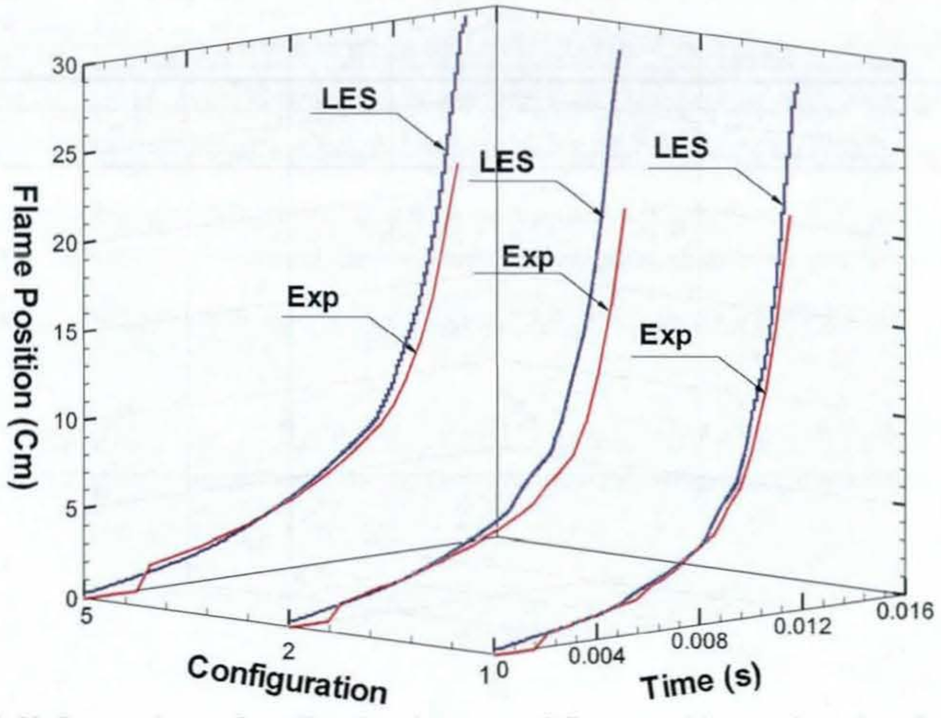

Figure 8.53 Comparison of predicted and measured flame position against time for Family 1.

Figure 8.55 presents cut-view of LES predicted reaction rate contours, showing flame structure at 6.0, 8.0, 10.0, 11.5 and 12.0 ms after ignitions for whole family. This facilitates qualitative and quantitative comparison of flame position and its structure at any given time. Figure 8.55 clearly indicates the improvement in predicted flame structure and thickness when compared with the LES flame images in Figure 8.19. It can be seen that while using flame surface density model, approximately 3 to 6 LES grid points are required to resolve the flame thickness and however using DFSD model only requires maximum of 3 grid points. The pockets or traps indicated in case of configuration 1 can be clearly seen, while using DFSD model in Figure 8.55(c) at 10.0 and 11.5 ms.

Considering an instance at 8.0 ms from Figure 8.55 (a) & (b), which illustrates the finger shaped flame structure, which is generally expected in chambers having l/d ratio greater than 3. Figure 8.55(b) at 11.5 and 12.0 ms shows a clear picture of entrapment of unburnt fuel/air mixture around solid square obstacle within recirculation zone. Similarly, Figure 8.55(c) at 11.5 and 12.0 ms shows the consumption of trapped mixture, once the main flame left the chamber. The above reaction rate contours also show the consumption of unburnt mixture within the viscous boundary layer, as evidenced in experimental flame images of Figure 8.19.

On the other hand, Figure 8.55 is also a very good indicator of the flame position, speed and turbulence levels. A quantitative comparison at any given time gives the influence of baffles on overpressure and turbulence generation. In order to facilitate further discussion, magnitude and incidence time of overpressure for four families are plotted as shown in Figure 8.56. It is evident from Figure 8.56 (a) that, as expected the overpressure generated is higher in the case of configuration 1 since it has 3 baffles with an earlier incidence time and lower in configuration 5 due to one baffle with a later incidence time. It is very interesting to note that the incidence time in this family maintains a linear relation while overpressure has a non-linear relation as seen in Figure 8.56 (a). The magnitude of the overpressure is increased 50% and 75% due to the addition of one and two baffles in configuration 2 & 1 respectively, when compared to the overpressure of configuration 5, which has one baffle at S3. However, incidence time is decreased by 11.5% and 23% in configuration 2 &1 respectively, inline with configuration 5. One reason for the non-linear relation of overpressure might be due to the position of baffles from the ignition source, even though they have the same blockage ratio. This will be further discussed in the next section.

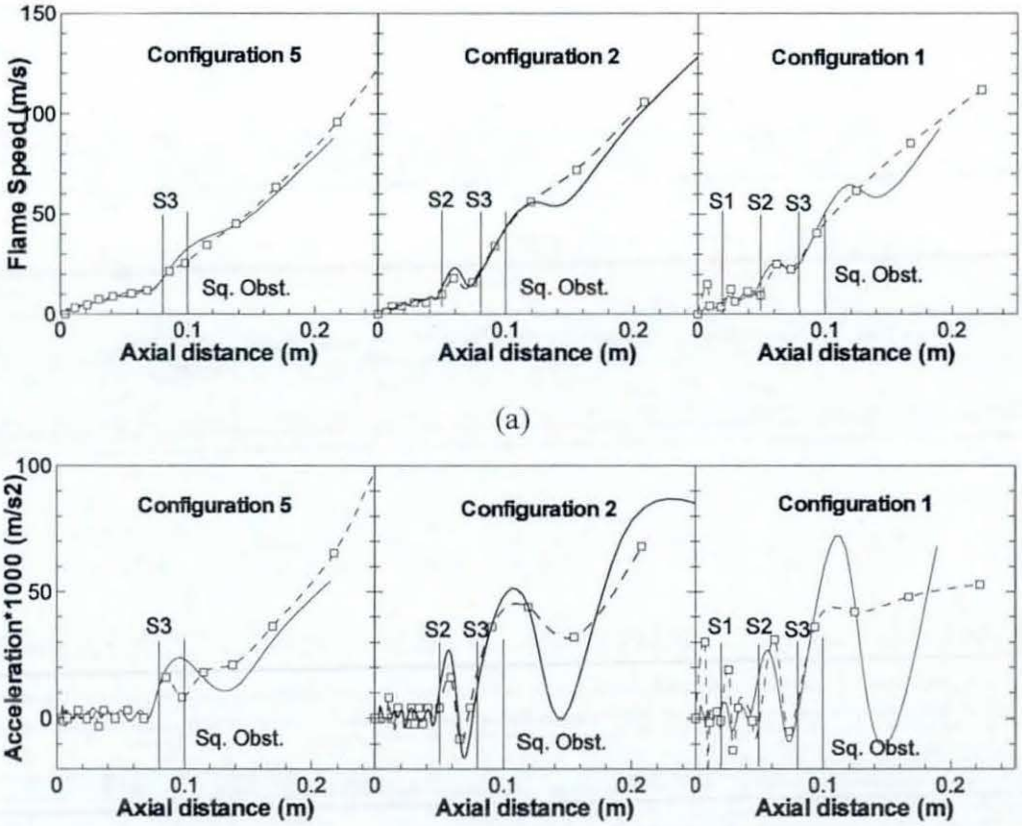

(a)

(b)

Figure 8.54 Comparisons between predicted (Solid line) and measured (Dashed lines with square symbols) (a) flame speed (b) flame acceleration vs. axial distance. The location of baffle stations (S1, S2 and S3) and the square solid obstacle are shown.

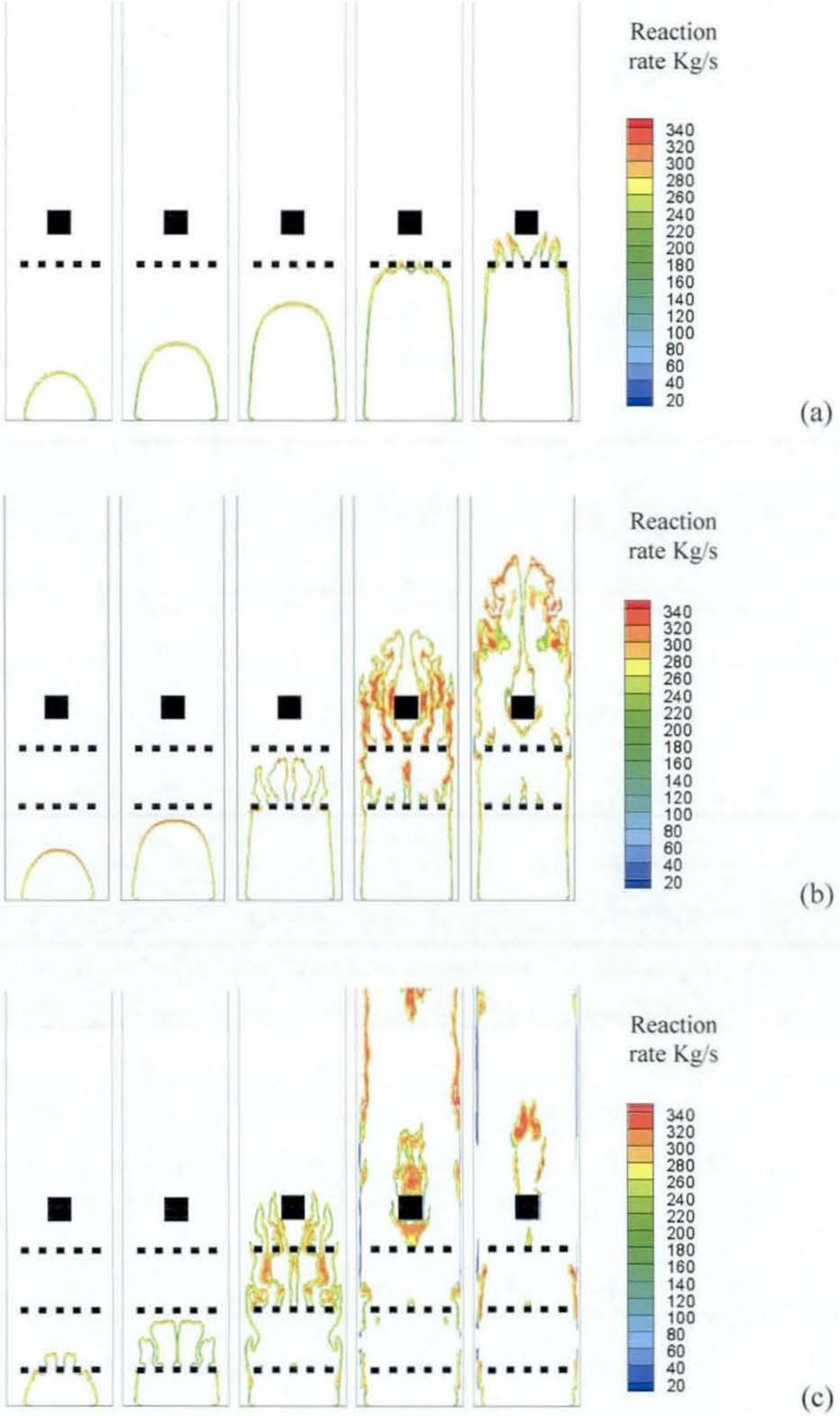

Figure 8.55 Predicted flame structure from three configurations at 6, 8, 10, 11.5 and 12.0 ms after ignition. (a) Configuration 5, (b) Configuration 2 and (c) Configuration 1.

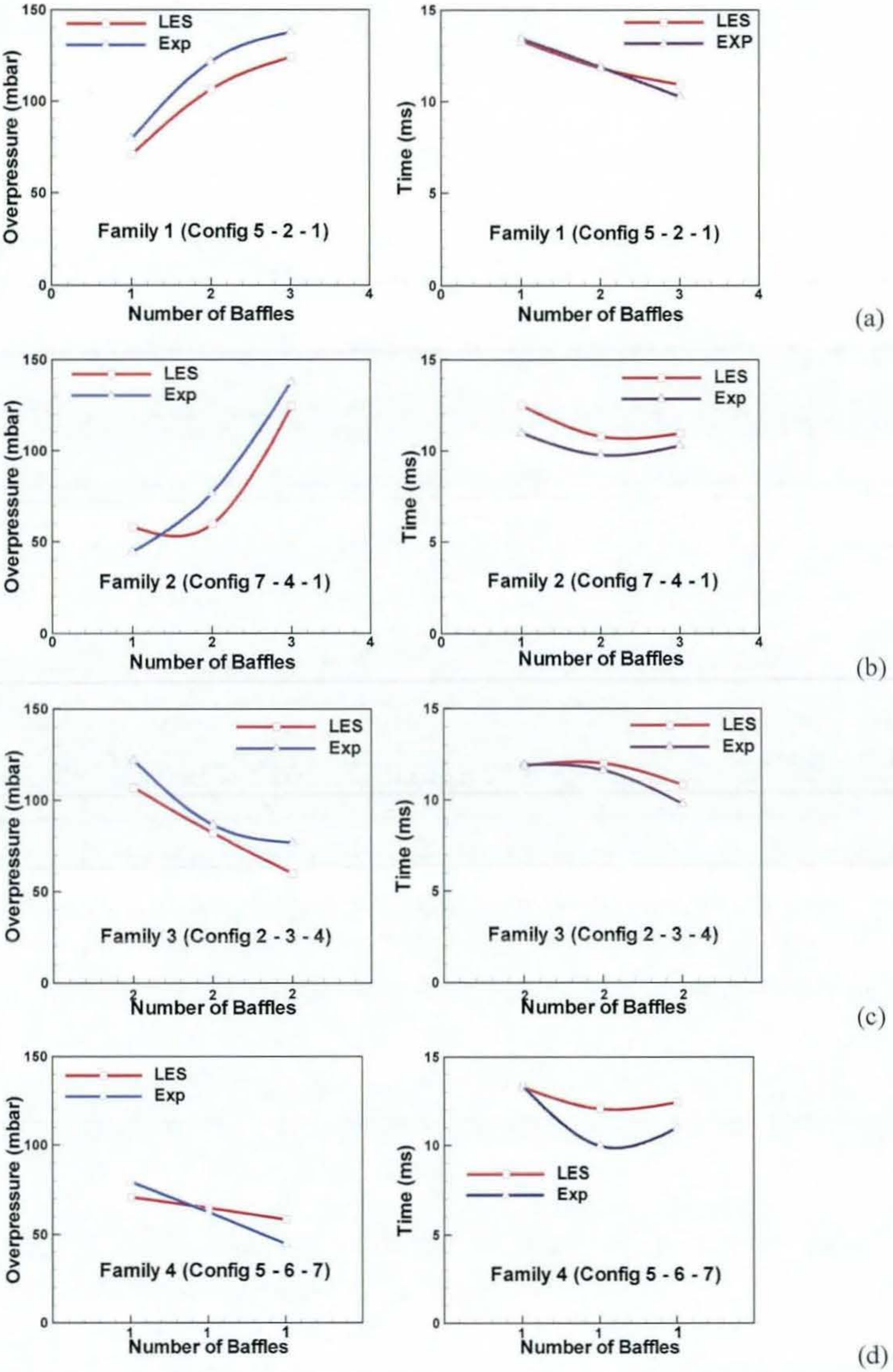

Figure 8.56 Variation of peak overpressure and its time of incidence compared from LES vs. Experiments for four families (a) Family 1 (b) Family 2 (c) Family 3 (d) Family 4.

8.6.3 Flame Characteristics: Family 2

The baffles in Family 2 are progressively increasing from one to three from ignition bottom end as shown in Figure 8.13. The configurations involved in this family are 7-4-1 and very similar to Family 1 in terms of number of baffles and however, very different in terms of position with respect to ignition source. This section does not describe the flame characteristics as it is a subset of other families. For instance, details of configuration 7 will be discussed in section 8.6.5 (Family 4) and where as configuration 4 will be discussed in section 8.6.4 (Family 3). It should also be noted here, that the detailed experimental results for configuration 7 are not available to compare with LES and however, only indicative overpressure and its time of occurrence reported by Hall et al. (2008) are used here.

The overpressure and its incidence time for the whole family of experiments is shown in Figure 8.56 (b). It is evident that both overpressure and the time are maintaining non-linear relation in this Family. The overpressure has increased 71% and 206% in configuration 4 and 1 compared to the measured overpressure in configuration 7. However, the incidence times are decreased by about 10-15%. To facilitate a comparative discussion, results for experimental families 1 and 2 are plotted together and individual configurations are mentioned as shown in Figure 8.57. The following points can be mainly derived from Figure 8.57:

- It is very interesting to note that, although the baffle plate in configuration 7 & 4 has same blockage capacity, lower overpressure is generated in configuration 7 due to the position of baffle from the ignition source. Similarly, configuration 4 & 2 have two baffles with same blockage capacity and generated less overpressure than in configuration 2. This observation confirms that the blockage with same capacity, nearer to the ignition source would generate less overpressure at an earlier time, when compared with the blockage positioned far from ignition source. In addition, it can also be observed that the timing of peak pressure in configuration 7 & 4 are less when compared to configuration 5 & 2.

- Although the overpressure increases with blockage ratio, the rate of this increase from configurations 4 to 1 and 2 to 1 is not the same, as observed in Figure 8.57.

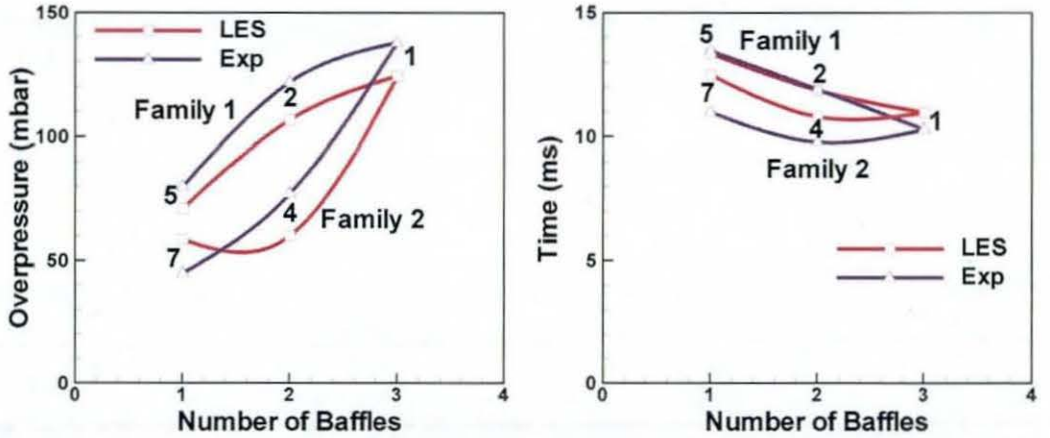

Figure 8.57 Variations of overpressure and its incidence time for various configurations in Family 1 & 2.

8.6.4 Flame characteristics: Family 3

Family 3 has three configurations (2-3-4) with two baffle plates at different stations and a solid square obstacle at a fixed position as shown in Figure 8.13. This family has been extensively investigated mainly due to three reasons. The first is consistency in the number of baffles used in individual configurations, which is very interesting for direct comparison. Secondly, availability of experimental axial and radial velocity information using LDV technique at a location downstream of square obstacle in all configurations facilitates the validation of the DFSD model developed in this work. Finally, limited OH information is available to compare with LES data.

Figures 8.58 & 8.59 present the predicted flame structure and the scattered data of reaction rate, contributions of resolved and unresolved FSD at strategic instants i.e. 6, 8, 10, 11.5 and 12.0 ms after ignition. In addition, axial, radial velocities and their RMS fluctuation from LES are compared with LDV measurements in these configurations, as shown in Figure 8.60. This facilitates the analysis of the flame position, structure and flow behaviour at any chosen time. It is identified in all these configurations that, following

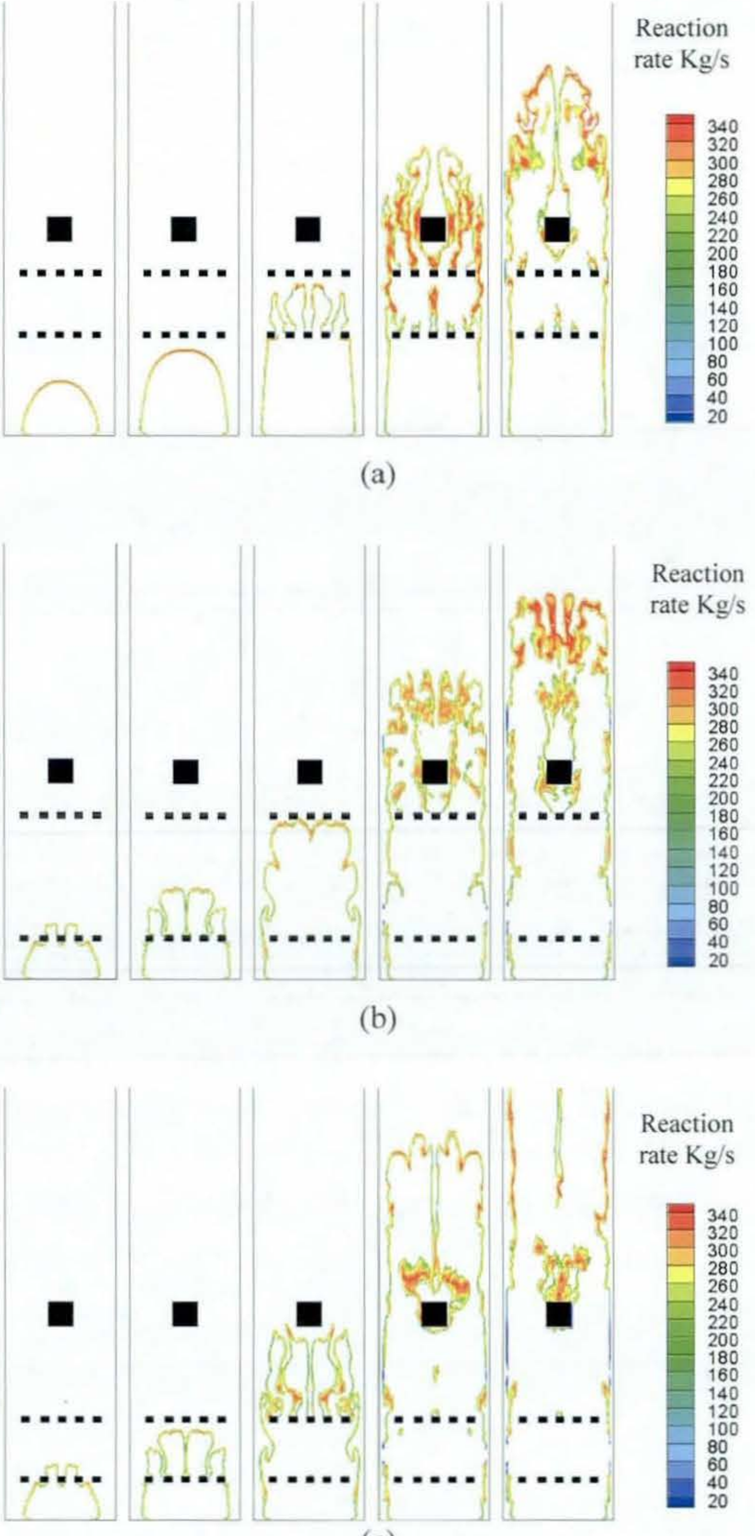

(a)

(b)

(c)

Figure 8.58. Predicted flame structure from three configurations at 6, 8, 10, 11.5 and 12.0 ms after ignition. (a) Configuration 2 (b) Configuration 3 (c) Configuration 4

ignition, flame front has expanded hemi-spherically with a velocity of Θu_L (Θ is the thermal expansion factor) in axial direction until it reaches first baffle plate and flame skirt elongates with laminar burning velocity, u_L in radial direction. The time taken by the flame front to reach solid square obstacle, to generate maximum overpressure and venting of the flame are strongly influenced by this initial laminar behaviour of the flame.

For instance at 6 ms, the flame is jetting out of the baffle plate at S1 in configuration 3 and 4, with similar flame structure. The RMS of axial velocity is computed as 2 m/s for both these configurations at 6 ms as seen in Figure 8.60 (b) & (c). However, the flame is found to be hemi-spherical and laminar with a negligible RMS fluctuation (< 0.2 m/s) in configuration 2 at 6 ms as seen in Figure 8.60 (a). Similarly, considering the reaction rate contours at 10 ms, the flame is about to interact with baffle plate at S3 with totally different flame structure and respective RMS fluctuations of 4 and 5 m/s from configuration 2 and 3. The flame in configuration 4 found to be more turbulent at 10 ms with RMS velocity of 8 m/s (at its peak in this configuration) and about to interact with solid square obstacle. Hence, the differences in flame position, flame front structure and the degree of wrinkles are found to be directly related to the axial location of baffles with respect to the origin of ignition.

The scattered data presented in Figure 8.59 at various instances provides qualitative comparison and useful in understanding the contributions of resolved and unresolved FSD in calculating reaction rate. Let us consider the plots from Figure 8.59 (a), (b) & (c) at 6 ms. It can be clearly noticed that, the top of parabola in reaction rate and unresolved FSD is clearly broken in Figure 8.59 (b) & (c), but not in Figure 8.59 (a). This is due to the presence of baffle in former configurations. Similar behaviour of unresolved FSD at 10 ms (broken or disturbed) in case of configuration 3 can be noticed from Figure 8.59 (b). At the same instance, Figure 8.59 (a) & (c) clearly shows the differences in scattered unresolved FSD, which is mainly contributing to reaction rate due to DFSD formulation. At 12 ms, it can be noticed that reaction rate is much stronger and mostly toward burning side for configurations 2 and 3 from Figure 8.59 (a) & (b) and not very strong in configuration 4 from Figure 8.59 (c) since the main flame left the chamber already.

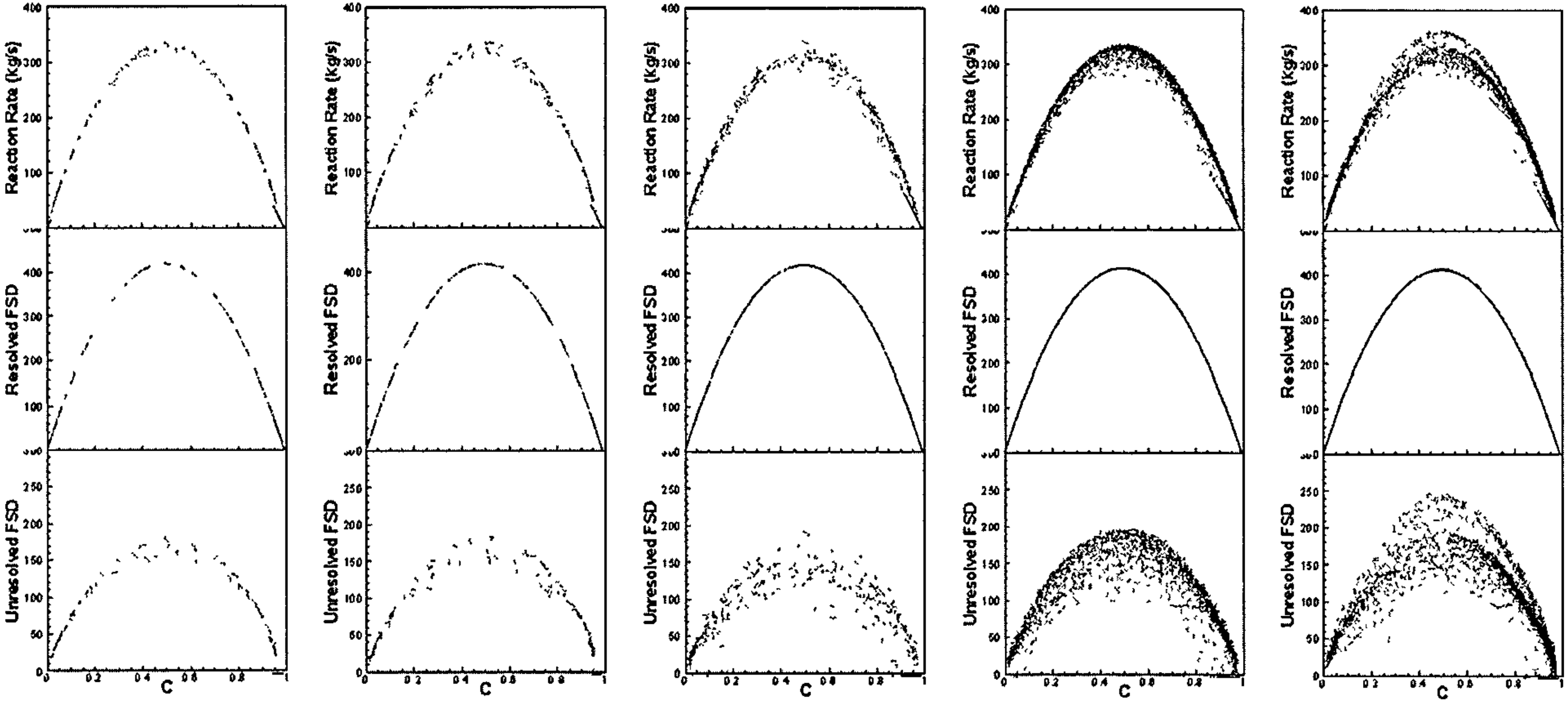

6.0 ms **8.0 ms** **10.0 ms** **11.5 ms** **12.0 ms**

Figure 8.59(a) Scattered data of reaction rate, resolved and unresolved flame surface density at chosen instants for configuration 2

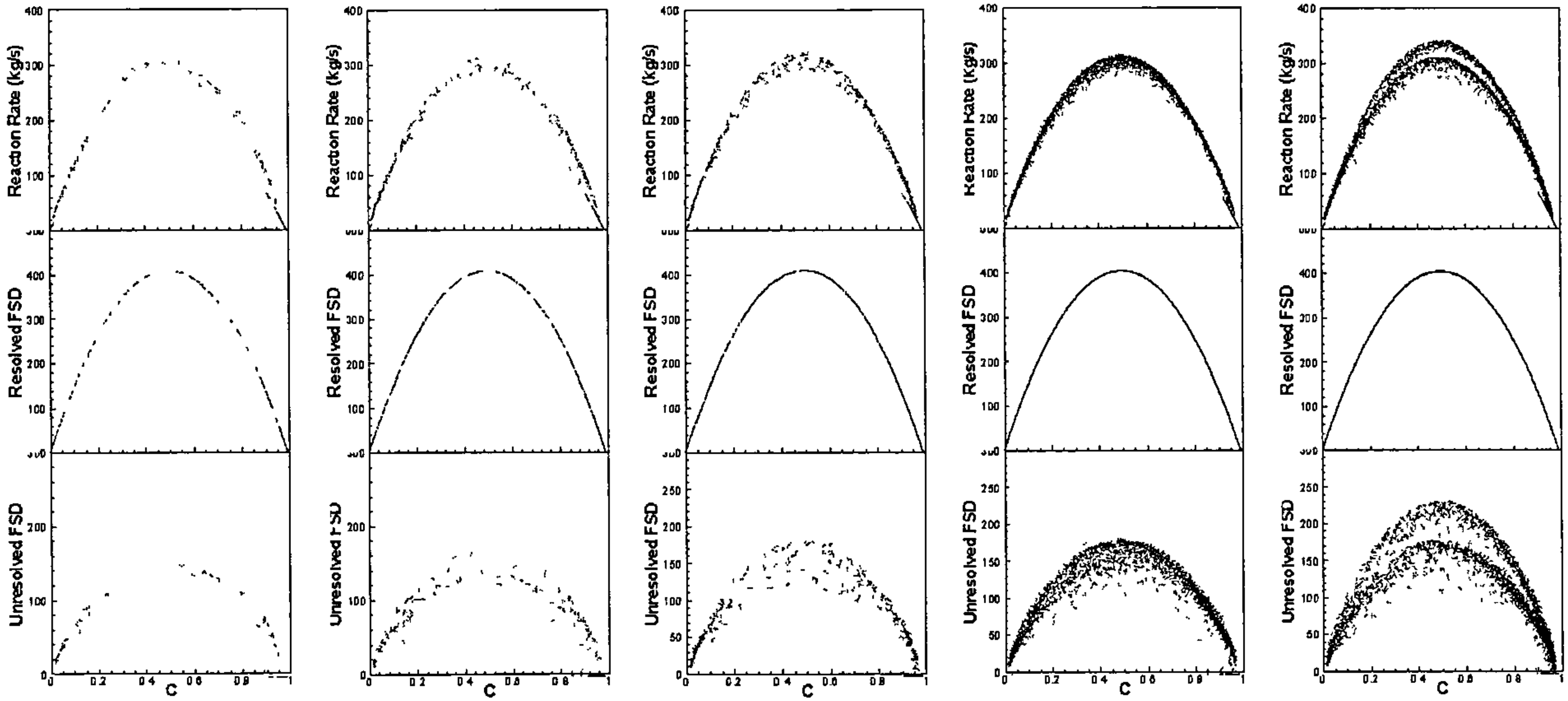

6.0 ms 8.0 ms 10.0 ms 11.5 ms 12.0 ms

Figure 8.59(b) Scattered data of reaction rate, resolved and unresolved flame surface density at chosen instants for configuration 3.

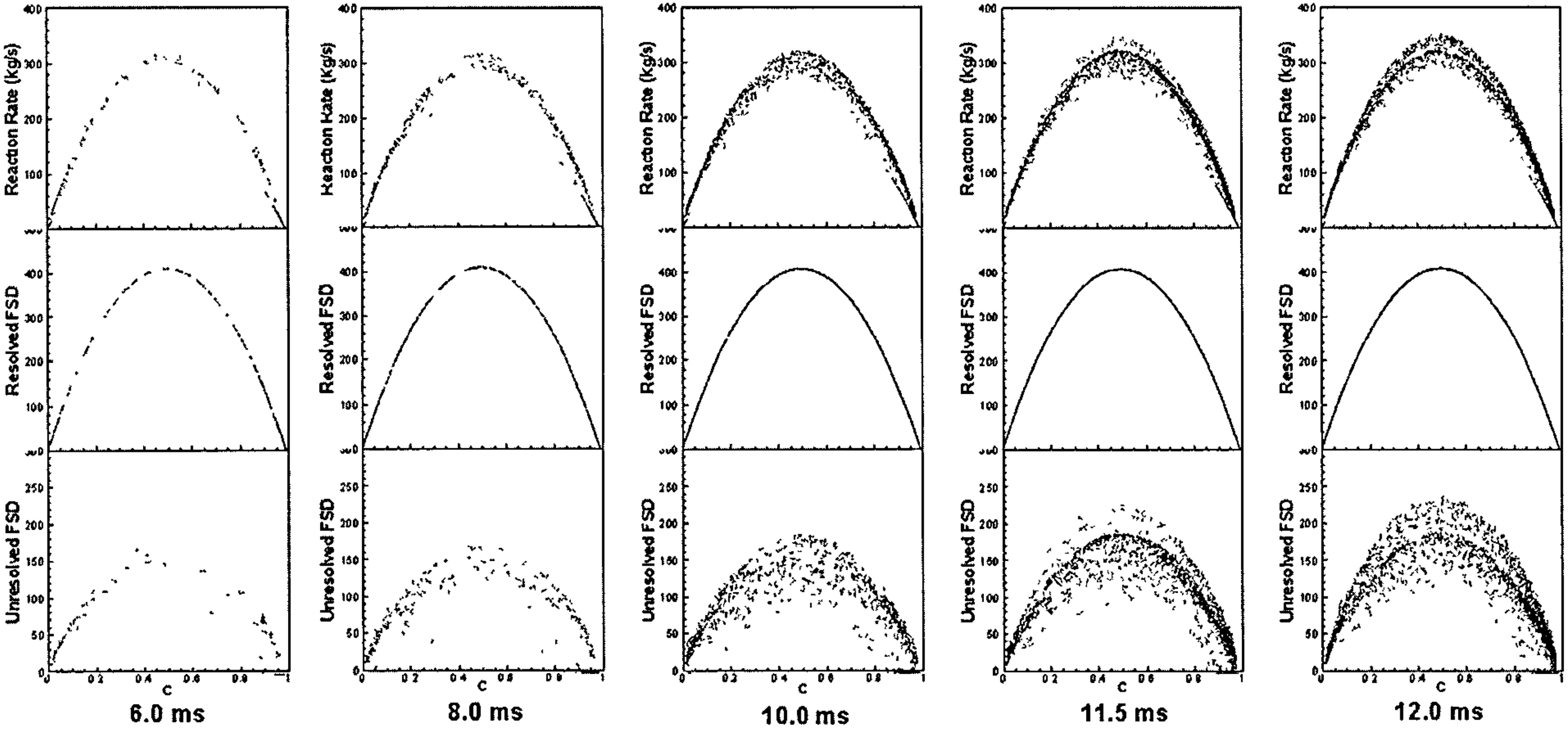

6.0 ms 8.0 ms 10.0 ms 11.5 ms 12.0 ms

Figure 8 59(c) Scattered data of reaction rate, resolved and unresolved flame surface density at chosen instants for configuration 4

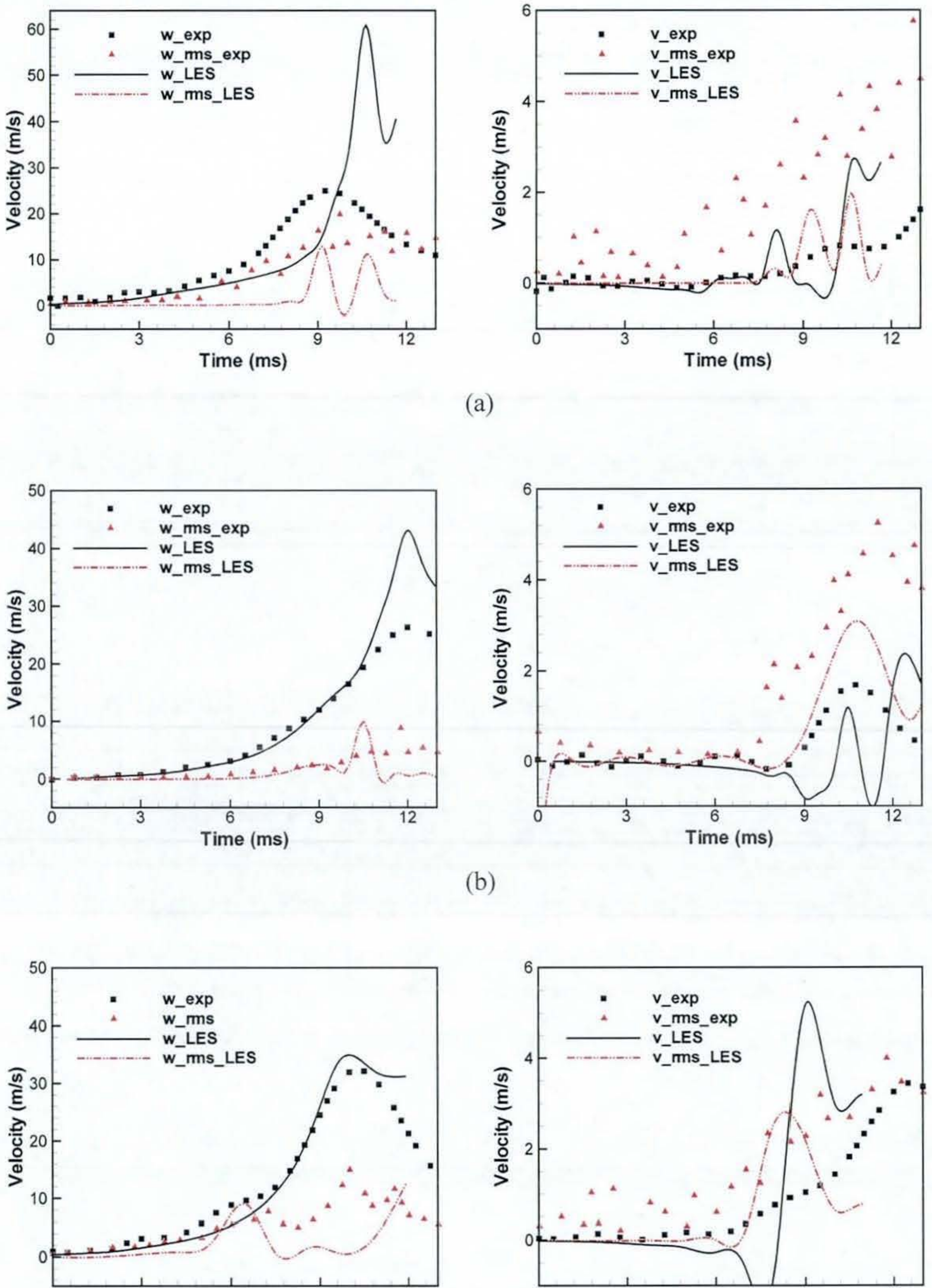

(a)

(b)

(c)

Figure 8.60 Axial and radial velocity, time histories and their RMS fluctuations of various configurations in Family 2. (a) Configuration 2 (S2 & S3) (b) Configuration 3 (S1 & S3) and (c) Configuration 4 (S1 & S2).

Figure 8.61 shows characteristic comparison of overpressure histories for three configurations, from experimental measurements and LES simulations. Due to the blockage of flow and interactions of the flame with second baffle plate in configuration 3 and 4, a small hump in pressure history is noticed at around 8 ms. It is clear that the rate of pressure rise and its trend including first hump are predicted well except for configuration 4, where the computed rate of increase of pressure is slower than measurements indicating a faster decay of turbulence between the second baffle plate and the square obstacle. It is also worth noting here that the pressures reported here are measured close to the ignition end and these may be different if measured at wall due to a possible pressure gradient within this chamber. From the experimental measurements, the overpressure is found to be oscillating after the peak overpressure, while burning the remaining trapped mixture after blow down of the main flame. It has been found in our preliminary studies, that the DFSD model is able predict the oscillating behaviour of the overpressure while burning the trapped fuel/air mixture as shown in case of configuration 0 (Figure 8.49). However, this is not repeated to verify for the present family of configurations presented in this section for two reasons. The first is, as we are more interested in flame-obstacle interactions, hence no point in carrying simulations once flame left the chamber. The second is, cost of the computational time.

A comparison of the flame position from experiments and LES predictions is shown in Figure 8.62. In case of experiments, the flame position is extracted from high speed video images by locating the farthest location of the flame front from ignition bottom end. From LES calculations, the flame position is obtained by locating the farthest location of the leading edge of the flame front from the bottom end (defined here as the most down stream location of the flame, where $\tilde{c} = 0.5$ from the ignition point). While results for configuration 3 almost fully overlap, a slightly faster rate of propagation across the chamber is computed for configurations 2 and 4. This is evident only in the last few milliseconds of propagation where the flame is experiencing the highest levels of turbulence.

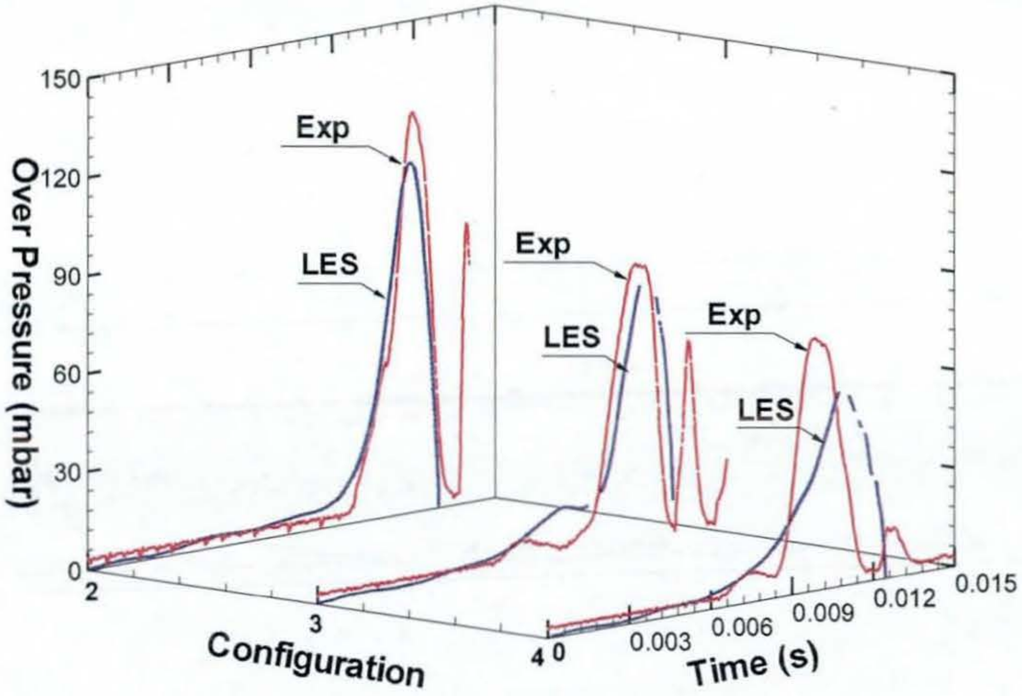

Figure 8.61 Comparisons between predicted and measured pressure vs. time

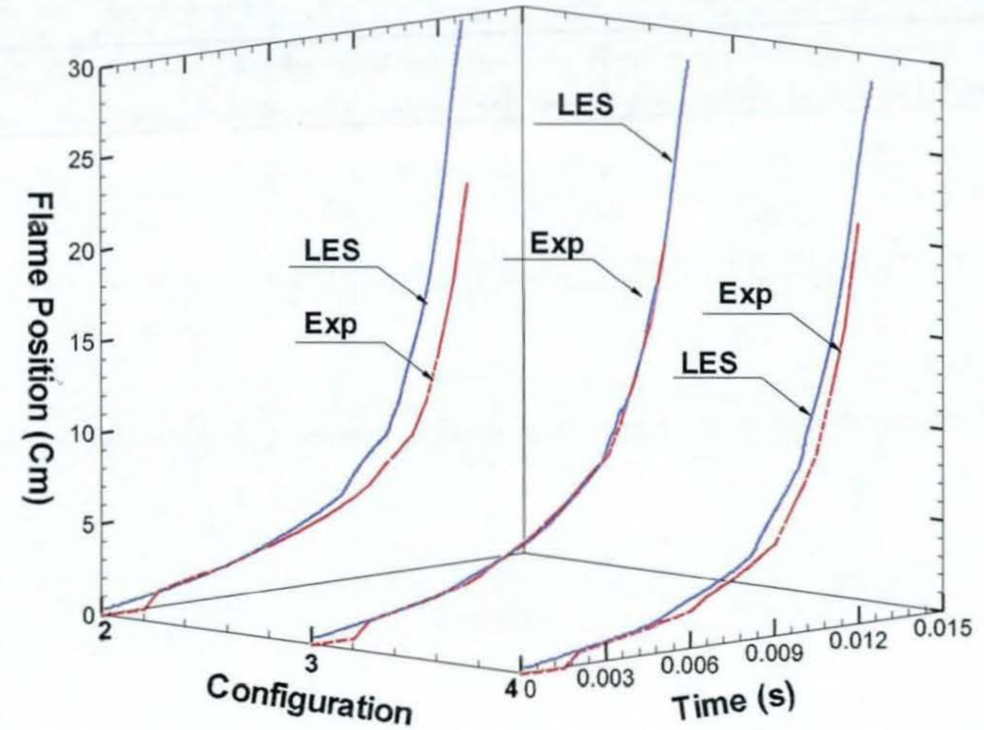

Figure 8.62 Comparisons between predicted and measured flame position vs. time

Figure 8.63 shows comparison between experimental measurements and numerical predictions of flame speed and acceleration. Also the position of baffle plates and the solid square obstacle are shown in Figure 8.63, to identify the influence of the obstacles. Flame speed is calculated from the rate of change over successive images in case of experiments and as a first derivative of the flame position with respect to time in LES. It should be noted here that in case of experimental measurements there is 2000 fps limitation on the high-speed digital camera, which eventually controls the resolution of the measurements. Due to this limitation, the drop in flame speed after the square obstacle is not captured correctly and however, predictions from LES are more continuous. For clarity, experimental measurements are represented by square symbols in Figure 8.63 (a) & (b). At the location of the square obstacle, highest flame speed is obtained for configuration 2 and this location also corresponds to the highest flame acceleration. It is interesting to note in configuration 4, the slowdown in flame speed and the reduced acceleration as the flame front travels the relatively longer distance between the second baffle plate and the square obstacle.

It is very interesting to note that using two baffles plates with a solid square obstacle having same blockage capacity in all the configurations, the recorded and predicted overpressure is maximum in configuration 2 and minimum in configuration 4 as shown in Figure 8.56 (c). Interestingly, LES predictions are showing a linear relation for generated overpressure and not by experiments. However, the predicted overpressure is very much in-line with experiments. Neither experiments, nor LES is showing a linear relation for incidence time. It is also evident from Figure 8.58 that, the flame exits the chamber faster in configuration 4 than in configuration 2. However, configuration 3 is in between the other two configurations in case of maximum overpressure and flame arrival time in the chamber. In case of configuration 2, though the flame has laminar nature until it reaches the first baffle plates at S2, quickly turn out to be highly wrinkled and turbulent due to jetting and contortion of the flame through the repeated obstacles. In this configuration the turbulent fluctuations are found to be progressively increasing and reach a maximum of 9 m/s at 11.5 ms. The laminar nature of flame front during the initial stages i.e. up to 8 ms has caused longer blow down time from the chamber at later stages. It should be noted, that the baffles and square obstacle in configuration 2 are almost all evenly spaced from bottom of ignition centre. While in configuration 4, flame found to be highly turbulent during initial stages followed by a faster decay at later stage.

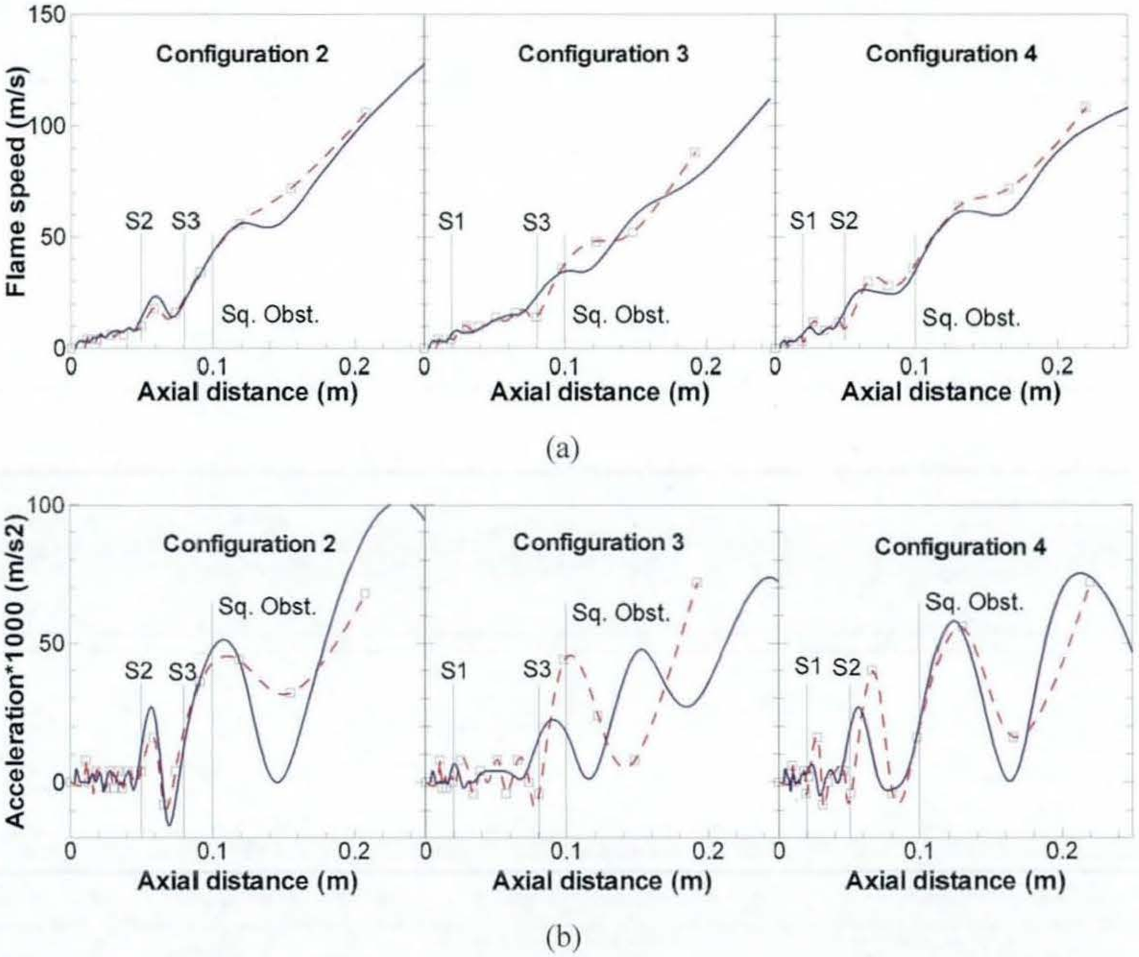

(a)

(b)

Figure 8.63 Comparisons between predicted (Solid line) and measured (Dashed lines with square symbols) (a) flame speed (b) flame acceleration vs. axial distance. The location of baffle stations (S1, S2 and S3) and the square solid obstacle are shown.

The third configuration has two baffles at S1, near to ignition centre and S3, away from the ignition centre and closed to the solid obstacle. It is noticed that, once the flame is distorted after reaching first baffle, flame front is slightly wrinkled with a higher surface area. However, re-laminarisation (reduction in speed and turbulence levels) of the flame between S1 and S3 results in approaching the square obstacle at a later stage compared to configuration 4. It is evident from the computed RMS fluctuations at 10 ms as 5 and 8 m/s and at 11.5 ms as 5 and 7 m/s respectively in configuration 3 and 4. This can be also observed by comparing the flame structure and its position between 10 and 11.5 ms from Figure 8.58 (b) and (c). Similarly, from configuration 4 it is noticed that, due to succession of baffles close to the ignition centre at S1 and S2, flame front is highly distorted and wrinkled before approaching square obstacle. However, this configuration has recorded lowest pressure due to sudden deceleration between S2 and solid square obstacle as shown in Figure 8.63 (b). The flame deceleration after S2 is also confirmed by the experimental measurements.

As a confirmation of the changing flame structure due to the location of the baffle plates upstream of the square obstacle, Figure 8.64 shows measured images of OH near the obstacle for configurations 2 and 4. Also shown in Figure 8.64 (b) are the computed reaction rates for these cases around the same region. Assuming the OH here gives an adequate representation of the flame front, it is clear that the flame is much more wrinkled in configuration 2, where the baffle plate is closer to the obstacle. This is also evident in the calculations and hence, confirming that, the turbulence generated by the baffle plates decays rather quickly, so the relative position and sequencing of obstacles is another important factor in explosions. It can be concluded that, with reference to an observer at the exit of chamber, the loss/damage due to the overpressure, is relatively less when solid obstacles are close to ignition origin, compared to that of when obstacles are relatively at longer distance.

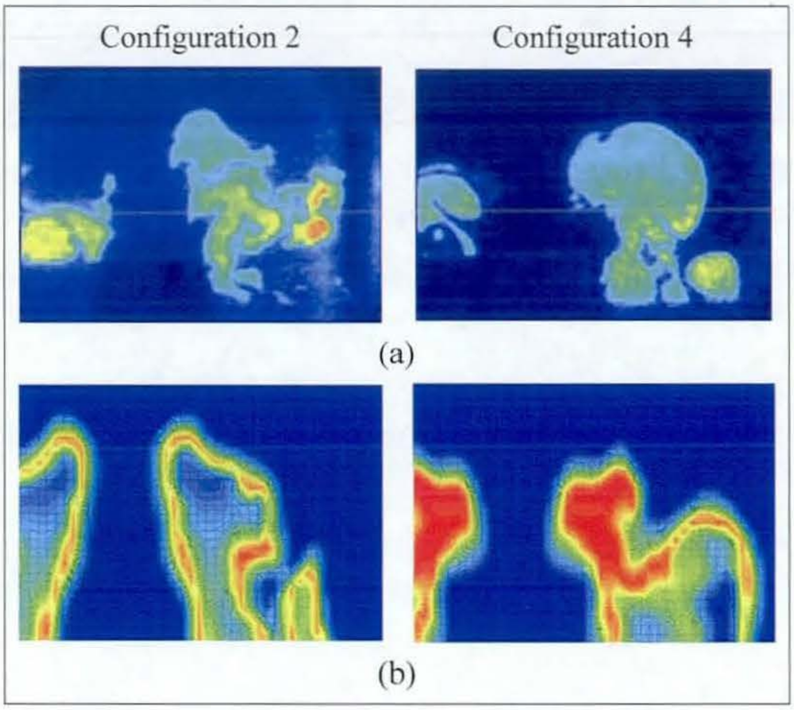

Figure 8.64 Comparison of OH images and corresponding flame fronts from LES simulations. (a) OH images (b) Reaction rate contours.

8.6.5 Flame Characteristics: Family 4

Family 4 has three interesting configurations with only one baffle positioned at different stations. Experimental measurements from configuration 6 and 7 are not available to compare. Indicative overpressure and time from work of Hall et al. (2008) using rich mixture having equivalence ratio 1.1 are used here. The time histories of overpressure for three configurations are shown in Figure 8.65(a). Experimental pressure trend collected near ignition end of configuration 5 has been plotted together to compare. As discussed earlier in case of other families, DFSD formulations is very successful in predicting turbulent premixed flames in all flow configurations. As it is evident from Figure 8.65(a) that the time traces of overpressure from LES for configuration 5 are very closely matching with the experimental measurements. It can be clearly seen that every stage of flame propagation including interacting with baffle plate and solid obstacle are reproduced very well. The time of peak overpressure occurrence is perfectly matched, however, the magnitude is slightly under predicted. It is also evident that DFSD model is successful in predicting pressure gradient at various stages of the flame propagation.

Figure 8.65 (b) and (c) presents flame position, speed against time and speed against axial distance of the chamber. Evidently it can be observed that the flame position and speed with time and flame speed with position in Figure 8.65(d) for configuration 5 are predicted very well. Reaction rate contours from LES, at five important instants are plotted in Figure 8.66 to study the flame-obstacle interactions in this family. The instants chosen are 6, 8, 10, 12 and 13 ms in all configurations, which generally matches with flame evolution, interaction with baffle plate, interactions with square obstacle, formation of recirculation zone and blow-down of flame from chamber.

The reaction rate contours at 6 and 8 ms provide a greater deal in giving information about the nature of flames. At these instants, configuration 5 & 6 has perfectly identical structure, shape with same flame thickness and the reaction rate. Since configuration 7 has a baffle plate at S1, flame has interacted and jetted through the baffle, which eventually changes the flame shape. However, the flame position at 8 ms in configuration 7 is almost all equal to the flame position in other two configurations (see Figure 8.65(d)) and just started to propagate at higher speed. At 10 ms, the flame in configuration 7 has higher surface area to consume more mixture due to its interaction with the baffle plate at 6ms.

By this time in configuration 6, the flame has evolved through baffle slits and started to form individual flame kernels. However, the flame in configuration 5 is still smooth and had a finger shaped structure propagating in axial direction proportional to gas expansion ratio.

Reaction rate contours at 12 ms are very interesting and delineating information about the flame entrapment around square obstacle. By comparing configuration 6 and 7 at this instant, it is evident that, configuration 7 has more surface area with smoother outer flame

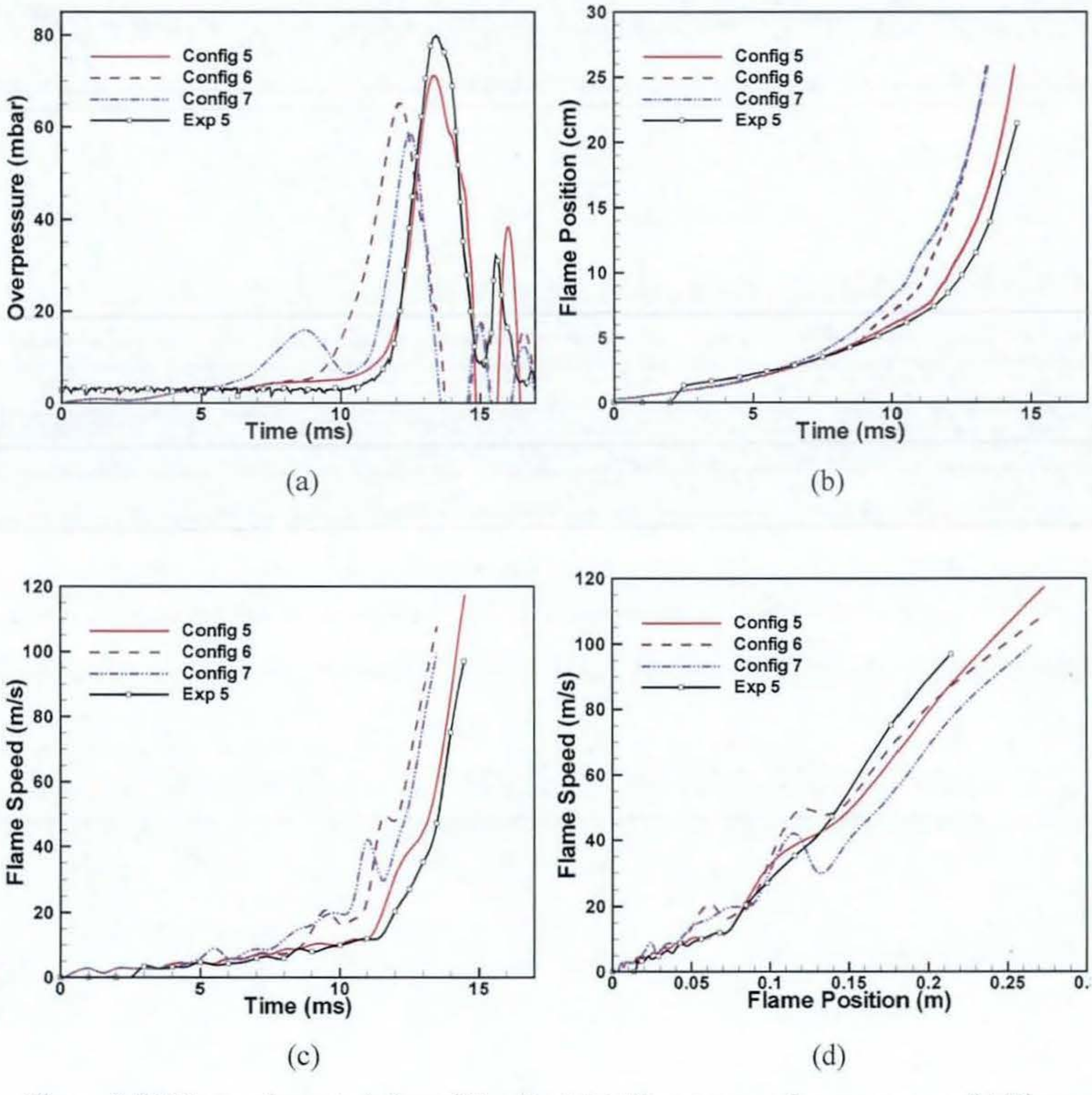

(a) (b)

(c) (d)

Figure 8.65 Flame characteristics of Family 4 (a) Time traces of overpressure (b) Time traces of flame position (c) Time traces of flame speed and (d) Flame speed with axial location of chamber.

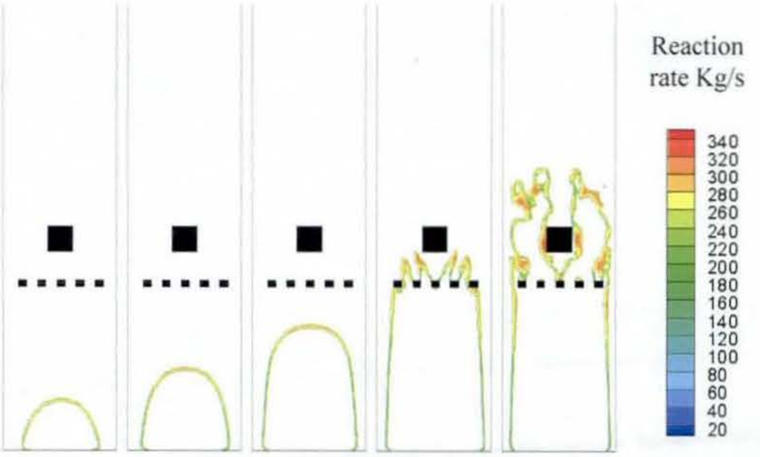

(a) Configuration 5

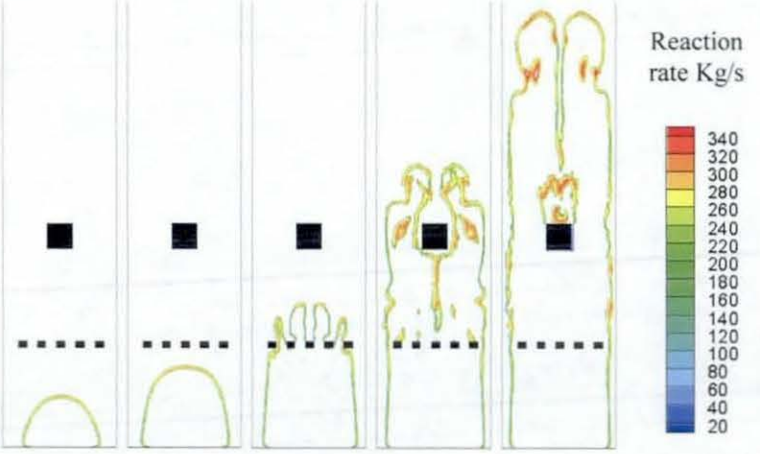

(b) Configuration 6

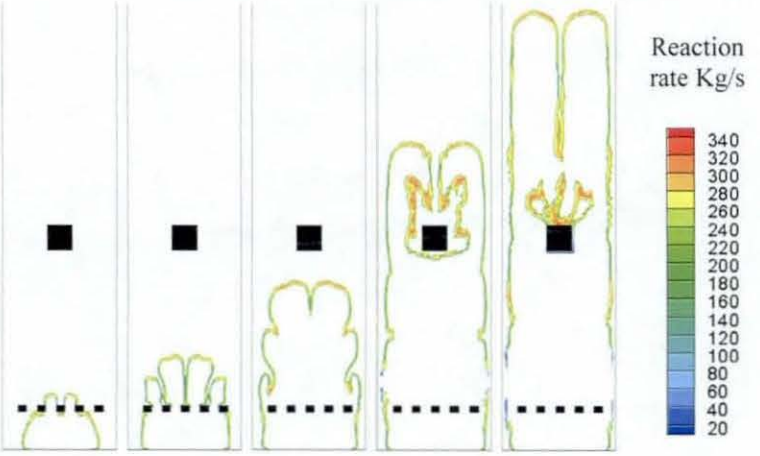

(c) Configuration 7

Figure 8.66 Snapshots of reaction rate contours at 6.0, 8.0, 10.0, 12.0 and 13 ms in various configurations.

structure and wrinkled inner flame structure. The inner flame structure is responsible for trapping of unburned mixture. Although, it is a very similar scenario in case of configuration 6, have the smoother inner flame structure, which engulfs lesser amount of mixture compared to configuration 7. Also, some flame islands can be observed in the case of configuration 6, which are responsible for slightly higher overpressure at any given time compared to configuration 7.

Comparing reaction rate contour at 13 ms from configuration 5 with contours at 12 ms of configuration 6 & 7, enhances the idea of how, individual flow configuration traps unburned mixture around obstacles It can be clearly observed that the mixture trapped in case of configuration 5 is very less compared to other configurations and the flame spreads within the boundary layer region around the square obstacle. One reason for this might be the gap between baffle and square obstacle, which is affecting the turbulence intensity of the flow within the chamber. At 13 ms from configuration 6 & 7, it can be observed that the flame position overlaps again and the both configurations shows similar nature of the flame i e consuming trapped mixture downstream of square obstacles and overlapping of the two branches of flame separated due to obstacles

Figure 8.56(d) shows peak overpressure and their incidence times from LES and experiments (indicative pressure and time only for configuration 6 and 7). It is very interesting to know that in this family, overpressure from LES is maintaining linear relation The experimental overpressure is also maintaining linear relation and however with a different slope. The incidence time in case of LES and Experiments are not maintaining linear relation as such and LES incidence times are showing slight over-prediction

It is very interesting to know that the configuration 5, having baffle at S3 (away from ignition bottom) has recorded higher overpressure of 71 2 mbar at 13.35 ms Configuration 7 having one baffle at S1, near to ignition bottom has recorded 58 6 mbar at 12.5 ms. Configuration 6 having one baffle at S2 has recorded overpressure of 65.2 mbar at 12.12 ms in between the other two. This observation evidently confirms the observation made in case of Family 3 i e farther the baffles to ignition centre, higher the overpressure at later stage. Closure the baffles to the ignition source or end, lesser the magnitude of the overpressure at an earlier stage.

Chapter 9

Conclusions and Recommendations

Flame surface density (FSD) models, based on the classical laminar flamelet theory are prominent and well accepted choice in predicting turbulent premixed flames in RANS modelling. The application of FSD models in LES is very recent and much similar to RANS models These models are gradually gaining the acceptance in industry to compute and predict a variety of turbulent premixed combustion situation in complex combustion chambers. However, there exist many issues such as their ability in calculating accurate flame surface density, applicability to a range of combustion regimes and the values of model coefficients used are to be clarified. Encouraged by the recent demand for eco-friendly combustion systems, advancements in the predictive capability of turbulent premixed combustion considered to be essential, which enhances the fundamental understanding of the entire process, is the main motivation for this research.

The work presented in this thesis has achieved three main objectives:

1 Gain confidence in using LES technique for turbulent premixed propagating flames in laboratory scale combustion chamber having built-in, solid obstacles using a simple FSD model. LES simulations have been carried out employing various grid resolutions to achieve grid-independent solution Investigations have been carried out to identify the influence of filter width and its coefficient on LES predictions Grid-independent results obtained were analysed to establish the quantity of the turbulent kinetic energy resolved using LES technique The laboratory scale combustion chamber has been divided into five regions of interest and a detailed analysis was carried out to verify the combustion regimes of the turbulent flame inside the chamber. The results from the simple FSD model were

reasonably good with some discrepancies such as under-prediction of magnitude of overpressure and its time of occurrence, resolved flame brush thickness and dependency of the results on model coefficient.

2. To improve and sophisticate the simple algebraic FSD model, in order to enhance the predicting capabilities and to identify the drawbacks if any. Investigations identified that the model coefficient generally varied based on various numerical and physical parameters such as filter width, turbulence intensity and chemistry of mixture etc A sub-model has been identified by analysing the flame as fractal surface within outer and inner cut-off scales The outer and inner cut-off scales were considered here as filter width and three times of laminar flame width respectively The LES simulations carried out using above model were identified to improve predictions slightly. Although the improvement in overpressure prediction is partial, drawbacks were identified especially due to the resolved turbulent flame thickness on LES grid. Since the flame is thinner than the LES grid employed, it has been identified that, accounting for the contributions of unresolved FSD might improve the predictions.

3 Development of a novel dynamic FSD (DFSD) model, which has enhanced the prediction capabilities of LES In order to account the unresolved FSD, a novel, complex and dynamic FSD equation proposed earlier by Knikker et al. (2004) is used and further developed. The dynamic FSD equation is involved in accounting for the resolved and unresolved FSD through the application of Germano identity to a basic FSD equation The theory is mainly based on viewing the turbulent flame surface as a fractal surface on the LES grid This procedure is involved in identifying the fractal dimension of the turbulent flame, in order to calculate model coefficient dynamically. Two sub-models were also identified to calculate the fractal dimension Firstly an empirical fractal model (EFM), which utilises sub-grid scale fluctuations and laminar burning velocity information was used. Secondly, a dynamic fractal model (DFM) involving similarity ideas and based on combination of fractal and flame wrinkling theory was developed

LES simulations using the developed DFSD model (M-4) have been performed for a series of simple to complex flow configurations having different number and position of baffles in a laboratory combustion chamber LES simulations were validated against experimental data to establish the novel DFSD model for turbulent premixed flames The flow configurations used in this study were classified into four families based on number and position of baffles and analysed the influence of baffles with respect to ignition bottom. For these experimental families, generated overpressure, other flame characteristics and reaction rate contours were generated and compared to available experimental data. LES predictions using DFSD model showed excellent agreement with experimental measurements for various configurations. However, present research has identified slight under-prediction of peak overpressure, which can be enhanced by accounting for the effects of flame curvature and strain into DFSD equation.

9.1 Conclusions

The main conclusions of the present study are as follows:

Numerical Modelling:

- The grid-independence tests conducted using four different grid resolutions have concluded that the employed grid can resolve most of the energy if it is sufficiently fine and is always independent of the filter width and grid resolution.

- The turbulent premixed regime of combustion identified in the present combustion chamber at various times after ignition at the leading edge of the flame is found to lie within the thin reaction zone, irrespective of classified regions and their interactions with obstacles This finding supports the use of the laminar flamelet modelling concept that has been in use for the modelling of turbulent premixed flames in practical applications

- The applicability of the algebraic FSD model using grid-independent results for turbulent premixed propagating flames was examined by validating the generated pressure and other flame characteristics, such as flame structure, position, speed and acceleration against experimental data. This study concludes that the predictions using FSD model provide reasonably good results.

- As a first advancement, the model coefficient has been evaluated using wrinkling flame factor between the outer and inner cut-off scales, by assuming wrinkled flame surface as fractal surface It was found that LES predictions were slightly improved in predicting higher reaction rate, which eventually increased predicted overpressure.

- Predictions using the developed dynamic FSD (DFSD) model showed significant improvement in overpressure, flame position, speed when compared to simple algebraic FSD model. This improvement is mainly due to two factors First is due to contribution from unresolved FSD and the second is due to dynamic modelling of model constant This study also shows that the DFSD model is quite effective when combined with dynamic fractal model compared to empirical fractal model. This is mainly due to automatic limitation of fractal dimension in the empirical model, which eventually lowers the model coefficient, *Cs* in DFSD model

- Accounting for the unresolved FSD in the reaction rate, is of great importance in improving the LES model predictions as demonstrated by the DFSD model The DFSD model allows for the increase in the fractal dimension as the flame progress from ignition to a fully developed turbulent flame. The model constant *Cs* found to progressively increase with the filter width employed in the simulations. However there is a need for experimental or DNS data to confirm this trend

- The agreement obtained confirms the applicability of the newly developed DFSD model to predict the dynamics of turbulent premixed flames or explosions in any flow configurations in as engineering applications or chemical/fuel process/storage industries

Flame - Flow interactions:

- This investigation demonstrates the comparison of LES predictions with experimental measurements and the effects of placing multiple obstacles at various locations in the path of the turbulent propagating premixed flames As expected, it concludes that the increase in blockage ratio increases the overpressure, however, with the same blockage ratio, the position of solid obstruction with respect to each other and ignition end has a significant impact on the magnitude of the overpressure and spatial flame structure.

- It is identified that the overpressure representing the generated energy in any individual configuration, is directly proportional to the number of baffles plates used in this study The flame speed and the development of the reaction zone are clearly dependent on the number of obstacle used and their blockage ratio.

- Extensive flame-flow interactions occur as the flame propagates past the baffle plate and the solid obstructions leading to the formation of disconnected flame islands with higher burning rates. The flame progressively accelerates as it travels through the various stages of the chamber. Turbulent burning velocities of about 12 to 14 m/s were achieved at the open end of the chamber. However there are no evidences to prove the presence of flame quenching due to elongation and stretching in the present study. This may be due to the small volume of the chamber used in this study

- Large separation between the solid baffle plates allows sufficient residence time for turbulence decay causing flow re-laminarisation and hence lowering overpressures with a much smoother flame fronts.

- Higher pressure gradient develops along the length of the chamber with more number of baffles or obstacles

- It is identified that the trapped unburnt mixtures up and down stream of obstacles are consumed once the main flame leaves the chamber leading to subsequent oscillations in pressure.

- The location of the obstacles with respect to the ignition source has a direct impact on the overpressure and the structure of the reaction zone Extending the distance between the baffles or between baffles and the downstream obstacle, allows turbulence to re-laminarise. Although with same blockage capacity, this phenomenon leads lower overpressure and less distortion in the reaction zone This new finding highlights the transient nature of the interaction between the propagating flame front and the local condition of the flow field.

The developed dynamic FSD model was found to predict the overpressure and its incidence times much more accurately than simple FSD models in turbulent premixed flames. The dynamic FSD model using dynamic fractal model (DFM) was computed unresolved FSD realistically when compared to dynamic FSD model using empirical fractal model (EFM). The predicted flame structure is very realistic in all configurations and remarkably matches with high-speed video images using Model-4. The dynamic FSD model could be further improved by implementing the recommendations provided in section 9.3

9.2 Present Contributions

The main contributions of the present research work are as follows:

- A good level of confidence has been established in using large eddy simulation technique for transient turbulent premixed propagating flames in various flow configurations by parameterising various numerical factors.

- Enhancement in the sophistication of sub-grid scale combustion modelling capability has been achieved in the in-house LES code through incorporation of newly developed self-scalable model for model coefficient based on fractal theory, in algebraic FSD model.

- A novel dynamic FSD model has been developed based on the fractal theory, which is able to predict unresolved FSD in addition to resolved FSD in order to improve the turbulent propagating premixed flame predictions This novel model has been implemented in in-house LES code and tested, validated and evaluated for a wide range of flow configurations

- Two fractal closures i e empirical and dynamic fractal models have been identified based on fractal theory and implemented in the in-house LES code, to calculate the fractal dimension dynamically to evaluate the model coefficient of the developed DFSD model

- Influence of ignition radius on LES predictions has been studied using various ignition radii with different initial reaction progress variable values The use of ignition modelling in the present LES code has been substantiated by this analysis in order to achieve the quasi-laminar phase of the early stage of flame propagation.

- A systematic study has been conducted to identify the influence of the number of baffles and their respective positions from ignition bottom

9.3 Recommendations for Future Work

- Although the dynamic FSD model has improved overall predictions, it could be further improved by identifying or developing more refined models for the inner and outer cut-off scales Especially for the inner cut-off scale, although several models are available in literature, retrieving information dynamically from flow properties could be considered from LES filtering.

- Axial and Radial velocity components and their RMS fluctuations are fairly matched with experimental measurements. However, this could be further improved by identifying more appropriate methods of averaging in transient turbulent premixed flames.

- The under-prediction of overpressure with DFSD model could possibly further improved by employing rigorous model for flame stretch

- Current in-house LES code can be further improved by implementing or adopting detailed chemistry via look-up table concept. A simple and efficient method such as intrinsic low dimensional manifold (ILDM), based on laminar flamelet modelling is suitable by generating look-up table via pre-processing tools.

- Parallelisation of the LES code is highly recommended in future, which eventually, utilises the available computational resources efficiently and could be easily extendable to predict more complex combustion scenarios

Appendix A

Implementation of Detailed Chemistry

A.1 Introduction

As described in section 4.5, implementation of detailed chemistry effects, in numerical combustion is very important in order to improve the predictions further and however, quite complex due to the nature and number of calculations involved. This chapter briefly presents Flame Prolongation of Intrinsic Low Dimensional Manifold (FP-ILDM) tabulated chemistry approach, which is being gaining popularity (Gicquel et al., 2000, Fiorina et al., 2004 & Fiorina et al., 2005) due to its efficient and simplistic implementation. Although this procedure has been successfully used in RANS, in LES it is yet to be matured. However, FP-ILDM methodology can be extendable in LES with an extra effort using FSD methodology.

In LES of FP-ILDM, the reactions rates of chosen/important chemical species are tabulated as a function of important coordinates such as Favre filtered reaction progress variable ($\tilde{c}$), Favre filtered reaction progress variable variance ($\tilde{c}''^2$), equivalence ratio (ϕ), equivalence ratio variance (ϕ''^2) and enthalpy (h) to incorporate local diffusion and heat losses if there are any. It is quite possible to add/neglect any coordinates to/from above, based on complexity/simplicity of the problem and, however requires efficient programming to retrieve the data from the pre-generated look-up tables.

A.2 FP-ILDM Using FSD Methodology

This section briefly describes the idea of FP-ILDM using FSD methodology For simplicity, we have considered only three coordinates i.e. reaction progress variable, equivalence ratio and enthalpy, on which flame structure and reaction rate depends. In FSD method, the mean reaction rate per unit volume of a species k, $\bar{\omega}_k$ is written as the product of the flame surface density and the mean reaction rate per unit surface, as:

$$\bar{\omega}_k = R_k\bar{\Sigma} \tag{A.1}$$

In the above equation, chemistry features can be implemented into the mean reaction rate per unit surface area R, by adding the reaction rate of individual species from the laminar freely propagating flame, extracted from the loop-up table, which is generated as a function of reaction progress variable, equivalence ratio and enthalpy. The look-up table also provides laminar flame speed information. The local reaction rate per unit flame surface area of species k can be extracted as:

$$R_k = \int_{-\infty}^{+\infty} R_k(\tilde{c},\phi,h)dcd\phi dh \tag{A 2}$$

From the above equation, it is evident that the mean chemical reaction rate of the individual species can be retrieved from the generated look-up table as a function of corresponding coordinates. The mean local chemical reaction rate of the flame having n number of species can be expressed as:

$$R = \sum_{k=1}^{n} R_k \tag{A 3}$$

The interactions between the flame front and turbulent motions can be described by flame surface density $\bar{\Sigma}$ (flame surface per unit volume), which can be either solved using a transport equation or implemented by an algebraic formula. From present research work, it is evident that the dynamic FSD models are much better than simple FSD models in accounting appropriate flame surface per unit volume, this formulation can be easily coupled with look-up table concept using FP-ILDM. Nevertheless, it can be noticed from equation 5.3 & 5 25, the flame surface density is mainly a function of Favre filtered reaction progress variable. The Favre filtered reaction progress variable can be expressed as the ratio of mass fractions in burned and unburned mixtures. Simply, the mass fraction Y_c can be obtained from a linear combination of mass fractions of CO and CO_2, which is sufficient to carryout preliminary studies

$$Y_c = Y_{CO} + Y_{CO2} \tag{A 4}$$

The reaction progress variable $\tilde{c}$ is defined as:

$$\tilde{c} = \frac{\tilde{Y}_c - \tilde{Y}_{cu}(\phi,h)}{\tilde{Y}_{cb}(\phi,h) - \tilde{Y}_{cu}(\phi,h)} \tag{A 5}$$

where u is for unburned mixtures and b is for burned mixtures. It is evident from the above equation that, direct substitution of reaction progress variable in equation 5 3 and 5 25 results in flame surface density of the turbulent premixed flame with detailed chemistry effects

Using equation A.3, one can express chemical reaction rate including detailed chemistry effects as:

$$\bar{\omega}_c = R\bar{\Sigma} \tag{A.6}$$

References

Abdel-Gayed, R G., Bradley, D. and Lawes, M. (1987), "Turbulent burning velocities: A general correlation in terms of straining rates", *Proceedings of the Royal Society of London Series A, Mathematical and Physical Sciences,* vol. 414, pp. 389-413.

Abu-Orf, G M and Cant, R.S. (2000), "A turbulent reaction rate model for premixed turbulent combustion in spark-ignition engines", *Combustion and Flame,* vol 122 (3), pp. 233-252.

Akkerman, V , Bychkov, V , Petchenko, A and Eriksson, L (2006), "Flame oscillations in tubes with nonslip at the walls", *Combustion and Flame,* vol. 145 (4), pp 675-687.

Aldredge, R.C , Vaezi, V. and Ronney, P D. (1998), "Premixed-flame propagation in turbulent Taylor–Couette flow", *Combustion and Flame,* vol. 115 (3), pp 395-405.

Aluri, N K , Reddy Muppala, S.P. and Dinkelacker, F. (2006), "Substantiating a fractal-based algebraic reaction closure of premixed turbulent combustion for high pressure and the Lewis number effects", *Combustion and Flame,* vol 145 (4), pp 663-674.

Angelberger, C , Veynante, D , Egolfopoulos, F and Poinsot, T. (1998), "Large eddy simulation of combustion instabilities in turbulent premixed flames", *Center for Turbulence Research, Proceedings of Summer Program, Stanford University,* pp 61-82.

Bardina, J., Ferziger, J. and Reynolds, W. (1980), "Improved subgrid scales models for large eddy simulations", *13th Fluid and Plasma Dynamics Conference*, pp. 80-90

Batty, M. (1985), *New Scientist,* vol. 1450, pp. 31-35.

Bauwens, C R L., Bauwens, L. and Wierzba, I (2007), "Accelerating flames in tubes-an analysis", *Proceedings of the Combustion Institute,* vol. 31 (2), pp 2381-2388.

Bell, J.B. and Colella, P (1989), "A second order projection method for the incompressible Navier-Stokes equations", *Journal of Computational Physics,* vol. 85, pp. 257-283

Bilger, R W. (2004), "Marker fields for turbulent premixed combustion", *Combustion and Flame,* vol 138 (1-2), pp 188-194.

Bilger, R.W , Kim, S H. and Martin, S M. (2004), "Direct numerical simulation of turbulent premixed flames with a marker field and application to RANS and LES", *Proceedings of the 2004 Summer Program, Center for Turbulence Research, Stanford University,* pp. 255-267.

Boger, M and Veynante, D (2000), "Large eddy simulations of a turbulent premixed V-shaped flame", *Advances in Turbulence VIII,* pp. 449-452.

Boger, M., Veynante, D., Boughanem, H. and Trouvé, A. (1998), "Direct numerical simulation analysis of flame surface density concept for large eddy simulation of turbulent premixed combustion", *Proceedings of the Combustion Institute,* vol. 27 (1), pp. 917-925.

Borghi, R. (1990), "Turbulent premixed combustion: Further discussions on the scales of fluctuations", *Combustion and Flame,* vol. 80 (3-4), pp. 304-312

Borghi, R. and Destriau, M. (1998), *Combustion and Flames, Chemical and Physical Priciples*

Boughanem, H. and Trouvé, A. (1998), "The domain of influence of flame instabilities in turbulent premixed combustion", *Proceedings of the Combustion Institute,* vol. 27 (1), pp. 971-978.

Boussinesq, J. (1877), *Mem Acad Sci Inst Fr ,* vol. 23 (1), pp. 252-260

Bradley, D. (2002), "Problems of predicting turbulent burning rates", *Combustion Theory and Modelling,* vol. 6, pp. 361-382.

Bradley, D., Cresswell, T.M. and Puttock, J.S. (2001), "Flame acceleration due to flame-induced instabilities in large-scale explosions", *Combustion and Flame,* vol. 124 (4), pp. 551-559.

Bradley, D., Lau, A K.C. and Lawes, M (1992), "Flame stretch rate as a determinant of turbulent burning velocity", *Philosophical Transactions of the Royal Society Physical and Engineering Sciences,* vol. 338 (1650), pp 359-387.

Bradley, D. (1992), "How fast can we burn?", *Proceedings of the Combustion Institute,* vol 24 (1), pp. 247-262.

Bradley, D. and Lung, F.K. (1987), "Spark ignition and the early stages of turbulent flame propagation", *Combustion and Flame,* vol 69 (1), pp. 71-93.

Bray, K N C. (1990), "Studies of the turbulent burning velocity", *Proceedings of the Royal Society Mathematical and Physical Sciences,* vol A431 (1882), pp. 315-335.

Bray, K.N.C. and Cant, R.S (1991), "Some applications of Kolmogorov's turbulence research in the field of combustion", *Proceedings of the Royal Society Mathematical and Physical Sciences,* vol. 434 (1890), pp 217-240.

Bray, K N C., Champion, M. and Libby, P.A. (1989), "*Flames in stagnating turbulence*" *Turbulent reacting flows*, eds R Borghi and S N Murphy, Springer Publications, New York, pp 541-563.

Bray, K N.C., Libby, P A., Masuya, G. and Moss, J B. (1981), "Turbulence production in premixed turbulent flames", *Combustion Science and Technology,* vol 25 (3), pp. 127-140.

Bray, K N.C , Libby, P.A. and Moss, J.B (1985), "Unified modelling approach for premixed turbulent combustion—Part I: General formulation", *Combustion and Flame,* vol. 61 (1), pp. 87-102.

Bray, K.N C. and Moss, J.B. (1977), "A closure model for the turbulent premixed flame with sequential chemistry", *Combustion and Flame,* vol. 30, pp. 125-131.

Bray, K N C. and Peters, N. (1993), "Laminar flamelets in turbulent flames" *Turbulent reaction flows*, eds P A Libby and F A Williams, Academic Press, pp. 63-113

Breuer, M and Rodi, W. (1994), "Large eddy simulation of turbulent flow through a straight square duct and a 180° bend" *Fluid Mechanics and its applications*, eds P R Voke, R. Kleiser and J.P. Chollet, Kulwer Publications, pp 26-36.

Butler, T D and O'Rourke, P.J (1977), "A numerical method for two dimensional unsteady reacting flows", *Proceedings of the Combustion Institute,* vol 16 (1), pp. 1503-1515.

Candel, S. and Poinsot, T. (1990), "Flame stretch and the balance equation for the flame area", *Combustion Science and Technology,* vol. 70, pp 1-15.

Cant, R.S and Bray, K.N.C. (1989), "Strained laminar flamelet calculations of premixed turbulent combustion in a closed vessel", *Proceedings of the Combustion Institute,* vol 22 (1), pp. 791-799

Cant, R.S , Pope, S B and Bray, K N C. (1991), "Modelling of flamelet surface-to-volume ratio in turbulent premixed combustion", *Proceedings of the Combustion Institute,* vol. 23 (1), pp 809-815.

Carati, D. and Wray, A.A. (2000), "Time filtering in large eddy simulations", *Proceedings of the Summer Program, Center for Turbulence Research, Stanford University,* pp. 263-270.

Castro, I P. and Jones, J M (1987), "Studies in numerical computations of recirculating flows", *International Journal for Numerical Methods in Fluids,* vol. 7, pp 793-823.

Chan, C K. and Li, X. (2005), "Flame surface density in turbulent premixed V-flame with buoyancy", *Flow, Turbulence and Combustion,* vol. 74, pp. 273-289.

Charlette, F , Meneveau, C and Veynante, D (2002), "A power-law flame wrinkling model for LES of premixed turbulent combustion Part II: dynamic formulation", *Combustion and Flame,* vol 131 (1-2), pp. 181-197

Charlette, F , Trouvé, A , Boger, M and Veynante, D. (1999), "A flame surface density model for large eddy simulations of turbulent premixed flames", *The Combustion Institute Joint Meeting of the British, German and French Sections.*

Cho, P., Law, C K , Hertzberg, J.R. and Cheng, R K (1988), "Structure and propagation of turbulent premixed flames astabilized in a stagnation flow", *Proceedings of the Combustion Institute,* vol 21 (1), pp 1493-1499

Chow, F K. and Moin, P. (2003), "A further study of numerical errors in large-eddy simulations", *Journal of Computational Physics,* vol. 184 (2), pp. 366-380.

Christophe, D. and Laszlo, F (2007), "Large eddy simulation of turbulent premixed combustion using a marker field", *Combustion Science and Technology,* vol. 179 (10), pp 2135-2152.

Colin, O , Ducros, F., Veynante, D and Poinsot, T. (2000), "Thickened flame model for large eddy simulations of turbulent premixed combustion", *Physics of Fluids,* vol. 12 (7), pp 1843-1862.

Colucci, P J , Jaberi, F.A , Givi, P. and Pope, S.B (1998), "Filtered density function for large eddy simulation of turbulent reacting flows", *Physics of Fluids,* vol 10 (2), pp 499-515.

Cook, A W. and Riley, J.J. (1998), "Subgrid-scale modeling for turbulent reacting flows", *Combustion and Flame,* vol 112 (4), pp. 593-606.

Cook, A W. and Riley, J.J. (1994), "A subgrid model for equilibrium chemistry in turbulent flows", *Physics of Fluids,* vol 6 (8), pp. 2868-2870.

Cook, A W., Riley, J.J and Kosály, G (1997), "A laminar flamelet approach to subgrid-scale chemistry in turbulent flows", *Combustion and Flame,* vol 109 (3), pp 332-341.

Correa, S M., Hu, I.Z and Tolpadi, A.K. (1996), "Combustion technology for low-emission gas-turbines some recent modelling results", *Journal of Energy Res Tech (Trans ASME),* vol. 118 (3), pp. 201-210.

Damkohler, G Z (1940), *Elektrochem,* vol 46, p. 610

Dandekar, K.V. and Gouldin, F.C (1981), "Temperature and velocity measurements in premixed turbulent flames", *Aerospace Sciences Meeting,* AIAA.

Darabiha, N , Candel, S M. and Marble, F.E. (1986), "The effect of strain rate on a premixed laminar flame", *Combustion and Flame,* vol. 64 (2), pp. 203-217.

Deardorff, J W. (1970), "A numerical study of three-dimensional turbulent channel flow at large Reynolds numbers", *Journal of Fluid Mechanics,* vol. 41 (02), pp. 453-480

Debliquy, O , Knaepen, B , Carati, D and Wray, A.A (2004), "Sampling versus filtering in large-eddy simulations", *Center for Turbulence Research, Proceedings of Summer Program, Stanford University,* pp. 133-144.

Duclos, J M , Veynante, D and Poinsot, T. (1993), "A comparison of flamelet models for premixed turbulent combustion", *Combustion and Flame,* vol. 95 (1-2), pp 101-117.

Fairweather, M , Hargrave, G K , Ibrahim, S S. and Walker, D.G. (1999), "Studies of premixed flame propagation in explosion tubes", *Combustion and Flame,* vol. 116 (4), pp 504-518.

Fairweather, M , Ibrahim, S S., Jaggers, H and Walker, D G (1996), "Turbulent premixed flame propagation in a cylindrical vessel", *Proceedings of the Combustion Institute,* vol 26 (1-2), pp. 365-371

Ferziger, J H (1993), "Sub-grid scale modelling"*Large eddy simulation of complex engineering and geophysical flows*, Galperin,B.; Orszag,S.S ; edn, Cambridge University Press, Cambridge, UK, pp. 55-78.

Ferziger, J H. (1977), "Large eddy simulation of turbulent flows", *American Institute of Aeronautics and Astronautics,* vol 15 (9), pp. 1261-1267

Ferziger, J H (1982), *State of the art in sungrid-scale modeling numerical and physical aspects of aerodynamic flows*, Springer-Verlag Publications.

Fiorina, B , Gicquel, O , Carpentier, S and Darabiha, N (2004), "Validation of the FPI chemistry reduction methods for diluted non-adiabatic premixed flames", *Combustion Science and Technology*, vol. 176 (5-6), pp. 785-797.

Fiorina, B , Gicquel, O , Vervisch, L , Carpentier, S. and Darabiha, N. (2005), "Premixed turbulent combustion modeling using tabulated detailed chemistry and PDF", *Proceedings of the Combustion Institute* vol. 30, pp. 867-874.

Flohr, P. and Pitsch, H. (2000), "A turbulent flame speed closure model for LES of industrial burner flows", *Proceedings of the Summer Program, Center for Turbulence Research, Stanford University,* pp. 169-179.

Fröhlich, J and Rodi, W. (2002), "Introduction to large eddy simulation of turbulent flows" *Closure strategies for turbulent and transitional flows*, eds B E. Launder and D N. Sandham, Cambridge University Press

Fureby, C (2000), "A computational study of combustion instabilities due to vortex shedding", *Proceedings of the Combustion Institute* vol. 28 (1), pp. 783-791

Fureby, C (1998), "Towards large eddy simulation of flows in complex geometries", *29th Fluid Dynamics conference* AIAA-98-2006.

Fureby, C. and Löfström, C. (1994), "Large-eddy simulations of bluff body stabilized flames", *Proceedings of the Combustion Institute* vol. 25 (1), pp. 1257-1264.

Fureby, C. and Moller, S.I (1995), "Large eddy simulation of reacting flows applied to bluff body stabilized flames", *American Institute of Aeronautics and Astronautics,* vol. 33 (12), pp 2339-2347.

Fureby, C., Pitsch, H., Lipatnikov and Hawkes, E (2005), "A fractal flame-wrinkling large eddy simulation model for premixed turbulent combustion", *Proceedings of the Combustion Institute,* vol. 30 (1), pp. 593-601.

Fureby, C , Tabor, G., Weller, H.G. and Gosman, A D. (1997), "A comparative study of subgrid scale models in homogeneous isotropic turbulence", *Physics of Fluids,* vol. 9 (5), pp. 1416-1429.

Gao, F. and O'Brien, E.E. (1993), "A large-eddy simulation scheme for turbulent reacting flows", *Physics of Fluids A,* vol 5, pp. 1282-1284.

Germano, M., Piomelli, U , Moin, P. and Cabot, W H. (1991), "A dynamic subgrid-scale eddy viscosity model", *Physics of Fluids A Fluid Dynamics,* vol 3 (7), pp. 1760-1765.

Ghosal, S., Lund, T.S and Moin, P. (1992), "A dynamic localization model for large-eddy simulation of turbulent flows", *Centre for Turbulence Research, Stanford University,* Manuscript 139.

Gicquel, O., Darabiha, N. and Thevenin, D (200), "Laminar premixed hydroger/air counterflow flame simulations using flame prolongation of ILDM with differential diffusion", *Proceedings of the Combustion Institute,* vol. 28, pp 1901-1908

Givi, P. (1989), "Model-free simulations of turbulent reactive flows", *Progress in Energy and Combustion Science,* vol 15 (1), pp. 1-107

Gouldin, F C. (1987), "An application of fractals to modeling premixed turbulent flames", *Combustion and Flame,* vol 68 (3), pp 249-266.

Gouldin, F C , Bray, K N.C. and Chen, J - (1989), "Chemical closure model for fractal flamelets", *Combustion and Flame,* vol. 77 (3-4), pp 241-259.

Gouldin, F.C., Hilton, S M. and Lamb, T. (1989), "Experimental evaluation of the fractal geometry of flamelets", *Proceedings of the Combustion Institute,* vol. 22 (1), pp. 541-550

Gubba, S R., Ibrahim, S.S , Malalasekera, W. and Masri, A R (2007), "LES modelling of propagating turbulent premixed flames using dynamic flame surface density model", *2^{nd} ECCOMAS Thematic Conference on Computational Combustion,* eds D. Roekaerts, P Coelho, B Boersma and K. Claramunt.

Gulati, A and Driscoll, J.F. (1986), "Velocity-density correlations and Favre averages measured in a premixed turbulent flame", *Combustion Science and Technology,* vol 48 (5), pp. 285-307

Gülder, O L. and Smallwood, G.J (1995), "Inner cutoff scale of flame surface wrinkling in turbulent premixed flames", *Combustion and Flame,* vol 103 (1-2), pp 107-114.

Hall, R (2008), *Influence of obstacle location and frequency on the propagation of premixed flames,* MEng Thesis, University of Sydney, Australia

Hall, R. (2006), *Flow field measurement in transient premixed flames,* BEng Thesis, University of Sydney, Australia

Hall, R., Masri, A R., Yaroshchyk, P. and Ibrahim, S S. (2009), "Effects of position and frequency of obstacles on turbulent premixed propagating flames", *Combustion and Flame,* vol 150, pp 439-446

Hawkes, E R (2000), *Large eddy simulations of premixed turbulent combustion,* PhD Thesis, University of Cambridge, UK

Hawkes, E R. and Cant, R S. (2001), "Implications of a flame surface density approach to large eddy simulation of premixed turbulent combustion", *Combustion and Flame,* vol 126 (3), pp 1617-1629

Hawkes, E.R and Cant, R S. (2000), "A flame surface density approach to large-eddy simulation of premixed turbulent combustion", *Proceedings of the Combustion Institute,* vol. 28 (1), pp. 51-58

Hayashi, S , Yamada, H. and Makida, M. (2000), "Short-flame/quick-quench: A unique ultralow emissions combustion concept for gas turbine combustors", *Proceedings of the Combustion Institute,* vol 28 (1), pp. 1273-1280

Hentschel, H.G.E. and Procaccia, I. (1984), "Relative diffusion in turbulent media. The fractal dimension of clouds", *Physical Review A,* vol. 29, pp 1461-1470

Hjertager, B.H , Fuhre, K. and Bjørkhaug, M. (1988), "Concentration effects on flame acceleration by obstacles in large-scale methane-air and propane-air vented explosions", *Combustion Science and Technology,* vol. 62 (4-6), pp 239-256.

Horiuti, K. (1997), "A new dynamic two-parameter mixed model for large-eddy simulation", *Physics of Fluids,* vol. 9 (11), pp 3443-3464.

Huang, y , Sung, H., Hsieh, S. and Yang, V. (2003), "Large-eddy simulation of combustion dynamics of lean-premixed swirl-stabilized combustor", *Journal of Propulsion and Power,* vol. 19 (5), pp. 782-794.

Ibrahim, S.S. and Masri, A R. (2001), "The effects of obstructions on overpressure resulting from premixed flame deflagration", *Journal of Loss Prevention in the Process Industries,* vol. 14 (3), pp. 213-221

Jones, W P (1993), "Turbulence modelling and numerical solution methods for variable density and combusting flows" *Turbulent Reacting Flows,* eds. P A. Libby and F.A Williams, Academic Press, pp. 309-368.

Kaminski, C.F., Abu-Gharbieh, R , Hamarneh, G. and Gustavsson, T. (2001), "Flame front tracking by laser induced fluorescence spectroscopy and advanced image analysis", *Optical Society of America.*

Kaminski, C F , Hult, J , Richter, M , Nygren, J., Franke, A and Alden, M (2000), "Development of high speed spectroscopic imaging techniques for the time resolved study of spark ignition phenomena", *SAE,* vol. 2000-01-2833.

Kang, Y. and Wen, J X (2004), "Large eddy simulation of a small pool fire", *Combustion Science and Technology,* vol. 176 (12), pp 2193-2223

Kempf, A , Lindstedt, R.P. and Janicka, J. (2006), "Large-eddy simulation of a bluff-body stabilized nonpremixed flame", *Combustion and Flame,* vol. 144 (1-2), pp 170-189.

Kent, J.E., Masri, A.R., Starner, S H and Ibrahim, S S. (2005), "Wrinkling scales of turbulent premixed propagating flame fronts obtained from LIF-OH imaging", *Fourth Australian Conference on Laser Diagnostics in Fluid Mechanics and Combustion,* 7-9th December, The University of Adelaide, Australia.

Kent, J E., Masri, A R and Starner, S.H (2005), "A new chamber to study premixed flame propagation past repeated obstacles", *5th Asia-Pacific Conference on Combustion,* 17-20th June, The University of Adelaide, Australia.

Kerstein, A R., Ashurst, W T. and Williams, F.A. (1988), "Field equation for interface propagation in an unsteady homogeneous flow field", *Physical Review A,* vol. 37 (7), pp 2728-2731.

Kerstein, A.R. (1991), "Linear-eddy modelling of turbulent transport. Part 6. Microstructure of diffusive scalar mixing fields", *Journal of Fluid Mechanics Digital Archive,* vol. 231 (-1), pp. 361-394

Kerstein, A.R. (1988), "Fractal dimension of turbulent premixed flames", *Combustion Science and Technology,* vol 60 (4), pp. 441-445.

Kim, W , Lienau, J J., Slooten, P.R.V., Colket III, M B , Malecki, R.E. and Syed, S (2006), "Towards modeling lean blow out in gas turbine flame holder applications", *Journal of engineering for Gas turbines and power,* vol. 128, pp. 40-48

Kim, W. and Menon, S. (2000), "Numerical modeling of turbulent premixed flames in the thin-reaction-zones regime", *Combustion Science and Technology,* vol. 160 (1), pp 119-150

Kim, W., Menon, S. and Mongia, H C (1999), "Large-eddy simulation of a gas turbine combustor flow", *Combustion Science and Technology,* vol. 143 (1), pp 25-62.

Kirkpatrick, M.P. (2002), *A large eddy simulation code for industrial and environmental flows,* PhD Thesis, The University of Sydney, Australia.

Kirkpatrick, M P., Armfield, S.W., Masri, A.R. and Ibrahim, S.S. (2003), "Large eddy simulation of a propagating turbulent premixed flame", *Flow, Turbulence and Combustion,* vol 70 (1-4), pp 1-19.

Klein, M. (2005), "An attempt to assess the quality of large eddy simulations in the context of implicit filtering", *Flow, Turbulence and Combustion,* vol 75 (1), pp. 131-147

Knikker, R., Veynante, D. and Meneveau, C. (2004), "A dynamic flame surface density model for large eddy simulation of turbulent premixed combustion", *Physics of Fluids,* vol. 16 (11), pp L91-L94.

Knikker, R., Veynante, D. and Meneveau, C. (2002), "A priori testing of a similarity model for large eddy simulations of turbulent premixed combustion", *Proceedings of the Combustion Institute,* vol 29, pp. 2105-2111.

Kollmann, W. and Schmitt, F. (1981), *Seventh Biennial Symposium on Turbulence.*

Kronenburg, A. and Bilger, R W. (2001), "Modelling differential diffusion in nonpremixed reacting turbulent flow application to turbulent jet flames", *Combustion Science and Technology,* vol. 166 (1), pp. 175-194.

Kuo, K K (1986), *Principles of Combustion (1986)* J. Wiley and Sons, New York.

Lee, T W and Lee, S J (2003), "Direct comparison of turbulent burning velocity and flame surface properties in turbulent premixed flames", *Combustion and Flame,* vol. 132 (3), pp 492-502.

Leonard, B.P. (1987), SHARP simulation of discontinuities in highly convective steady flowNASA-TM-100240.

Leonard, B.P. (1979), "A stable and accurate convective modelling procedure based on quadratic upstream interpolation", *Computer Methods in Applied Mechanics and Engineering,* vol 19, pp 59-98.

Lesieur, M and Metais, O. (1996), "New trends in large-eddy simulations of turbulence", *Annual Review of Fluid Mechanics,* vol. 28 (1), pp. 45-82.

Libby, P.A. and Bray, K.N C. (1981), "Countergradient diffusion in premixed turbulent flames", *AIAA Journal,* vol 19 (2), pp. 205-213.

Lilly, D.K (1967), "The representation of small scale turbulence in numerical simulation experiments", *proceedings of the IBM scientific computing symposium on enviromental sciences*, pp 195-210.

Lilly, D K (1992), "A proposed modification of the Germano subgrid-scale closure method", *Physics of Fluids A Fluid Dynamics,* vol 4 (3), pp. 633-635.

Lindstedt, R P. and Sakthitharan, V. (1998), "Time resolved velocity and turbulence measurements in turbulent gaseous explosions", *Combustion and Flame,* vol 114 (3-4), pp 469-483.

Lindstedt, R.P. and Váos, E.M (1999), "Modeling of premixed turbulent flames with second moment methods", *Combustion and Flame,* vol. 116 (4), pp. 461-485

Lovejoy, S (1982), "Area-perimeter relation for rain and cloud areas", *Science,* vol. 216 (4542), pp. 185-187.

Lund, T.S. and Kaltenbach, H J. (1995), "Experiments with explicit filtering for LES using a finite-difference method", *Centre for Turbulence Research, Annual Research Briefs, Stanford University*, pp. 91-105.

Madina, C K. and Givi, P. (1993), "Direct and large eddy simulation of reacting homogeneous turbulence" *Large Eddy Simulations of Complex Engineering and Geophysical Flows*, eds. B Galperin and S.A. Orszag, Cambridge University Press, Cambridge, UK, pp. 315-346.

Makarov, D , Molkov, V. and Gostintsev, Y. (2007), "Comparison between RNG and fractal combustion models for LES of unconfined explosions", *Combustion Science and Technology,* vol. 179 (1), pp 401-416.

Malalasekera, W , Dinesh, K.K.J.R., Ibrahim, S S. and Kirkpatrick, M P. (2007), "Large eddy simulaiton of isothermal turbulent swirling jets", *Combustion Science and Technology,* vol 179 (8), pp. 1481-1525.

Maly, R R. (1994), "State of the art and future needs in S.I. engine combustion", *Proceedings of the Combustion Institute,* vol. 25 (1), pp 111-124.

Mandelbrot, B.B. (1975), "On the geometry of homogeneous turbulence, with stress on the fractal dimension of the iso-surfaces of scalars", *Journal of Fluid Mechanics,* vol. 72 (2), pp. 401-416

Marble, F.E and Broadwell, J E (1977), "The coherent flame model of non-premixed turbulent combustion", TRW-9-PU

Masri, A R and Ibrahim, S.S (2007), "Recent progress in the understanding of premixed flame propagation past obstacles", *Proceedings of the Third International Conference on Thermal Engineering Theory and Applications*, May 21-23, Amman, Jordan.

Masri, A.R., Ibrahim, S S. and Cadwallader, B.J. (2006), "Measurements and large eddy simulation of propagating premixed flames", *Experimental Thermal and Fluid Science,* vol. 30 (7), pp. 687-702

Masri, A.R., Ibrahim, S S., Nehzat, N. and Green, A R. (2000), "Experimental study of premixed flame propagation over various solid obstructions", *Experimental Thermal and Fluid Science,* vol. 21 (1-3), pp 109-116

Meneveau, C. and Poinsot, T. (1991), "Stretching and quenching of flamelets in premixed turbulent combustion", *Combustion and Flame,* vol 86 (4), pp 311-332.

Menon, S. and Jou, W H (1991), "Large-eddy simulations of combustion instabilities in an axisymmetric ramjet combustor", *Combustion Science and Technology,* vol 84, pp 51-79.

Menon, S and Kerstein, A.R (1992), "Stochastic simulation of the structure and propagation rate of turbulent premixed flames", *Proceedings of the Combustion Institute,* vol 24 (1), pp 443-450.

Metghalchi, M. and Keck, J C. (1980), "Laminar burning velocity of propane-air mixtures at high temperature and pressure", *Combustion and Flame,* vol. 38, pp. 143-154.

Metghalchi, M. and Keck, J.C. (1982), "Burning velocities of mixtures of air with methanol, isooctane, and indolene at high pressure and temperature", *Combustion and Flame,* vol 48, pp 191-210

Moen, I O., Donato, M , Knystautas, R. and Lee, J H (1980), "Flame acceleration due to turbulence produced by obstacles", *Combustion and Flame,* vol 39 (1), pp 21-32.

Moen, I.O , Lee, J H.S , Hjertager, B H , Fuhre, K. and Eckhoff, R K (1982), "Pressure development due to turbulent flame propagation in large-scale methane-air explosions", *Combustion and Flame,* vol. 47, pp 31-52.

Moin, P (1997), "Numerical and physical issues in large eddy simulation of turbulent flows", *International Conference on Fluid Engineering*, Japan Society of Mechanical Engineers, vol. 1, pp. 91-100.

Moin, P. and Kim, J. (1997), "Tackling turbulence with supercomputers", *Scientific American,* vol. 276, pp. 62-68

Moin, P , Reynolds, W C. andFerziger, J.H (1978), Large eddy simulation of incompressible turbulent channel flow, NASA, NASA-CR-152190; SU-TF-12

Moin, P., Squires, K., Cabot, W. and Lee, S. (1991), "A dynamic subgrid-scale model for compressible turbulence and scalar transport", *Physics of Fluids A Fluid Dynamics,* vol 3 (11), pp 2746-2757.

Moin, P and Kim, J. (1982), "Numerical investigation of turbulent channel flow", *Journal of Fluid Mechanics,* vol. 118 (-1), pp. 341-377

Molkov, V , Makarov, D. and Grigorash, A. (2004), "Cellular structure of explosion flames. modelling and large-eddy simulation", *Combustion Science and Technology,* vol 176 (5), pp. 851-865.

Moller, S.I., Lundgren, E. and Fureby, C. (1996), "Large eddy simulation of unsteady combustion", *Proceedings of the Combustion Institute,* vol 26 (1), pp. 241-248.

Muppala, S.P R., Aluri, N.K , Dinkelacker, F. and Leipertz, A (2005), "Development of an algebraic reaction rate closure for the numerical calculation of turbulent premixed methane, ethylene, and propane/air flames for pressures up to 1 0 MPa", *Combustion and Flame,* vol 140 (4), pp. 257-266.

Murayama, M and Takeno, T (1989), "Fractal-like character of flamelets in turbulent premixed combustion", *Proceedings of the Combustion Institute,* vol 22 (1), pp. 551-559.

Naitoh, K , Itoh, T., Takagi, Y. and Kuwahara, K. (1992), "Large eddy simulation of premixed-flame in engine based on the multi-level formulation and the renormalization group theory", *SAE Paper,* vol. 920590.

North, G.L and Santavicca, D.A (1990), "The fractal nature of premixed turbulent flames", *Combustion Science and Technology,* vol. 72 (4), p. 215

Nottin, C., Knikker, R., Boger, M and Veynante, D (2000), "Large eddy simulations of an acoustically excited turbulent premixed flame", *Proceedings of the Combustion Institute,* vol. 28 (1), pp. 67-73.

Patel, S. and Ibrahim, S.S. (1999), "Burning velocities of propagating turbulent premixed flames", *Proceedings of the 1st international symposium on Turbulence and Shear Phenomena,* p. 837.

Patel, S., Ibrahim, S.S., Yehia, M.A and Hargrave, G K. (2003), "Investigation of premixed turbulent combustion in a semi-confined explosion chamber", *Experimental Thermal and Fluid Science,* vol 27 (4), pp. 355-361.

Patel, S , Jarvis, S , Ibrahim, S S. and Hargrave, G K (2002), "An experimental and numerical investigation of premixed flame deflagration in a semiconfined explosion chamber", *Proceedings of the Combustion Institute,* vol. 29 (2), pp 1849-1854.

Peters, N. (1988), "Laminar flamelet concepts in turbulent combustion", *Proceedings of the Combustion Institute,* vol. 21 (1), pp. 1231-1250.

Peters, N. (2000a), "The turbulent burning velocity for large-scale and small-scale turbulence", *Journal of Fluid Mechanics,* vol. 384 (1), pp 107-132.

Peters, N (2000b), *Turbulent Combustion,* Cambridge University Press.

Phylaktou, H. and Andrews, G E. (1991), "The acceleration of flame propagation in a tube by an obstacle", *Combustion and Flame,* vol 85 (3-4), pp. 363-379.

Piana, J , Veynante, D , Candel, S. and Poinsot, T. (1997), "Direct numerical simulation analysis of the G-equation in premixed combustion" *Direct and Large Eddy simulation II,* eds J P Chollet, P R Vole and L. Kleiser, Kluwer Academic Publishers, Amsterdam, pp. 321-330

Piomelli, U. and Liu, J (1995), "Large-eddy simulation of rotating channel flows using a localized dynamic model", *Physics of Fluids,* vol. 7 (4), pp. 839-848.

Piomelli, U., Moin, P. and Ferziger, J H. (1988), "Model consistency in large eddy simulation of turbulent channel flows", *Physics of Fluids,* vol 31 (7), pp. 1884-1891.

Piomelli, U., Yu, Y. and Adrian, R.J. (1996), "Subgrid-scale energy transfer and near-wall turbulence structure", *Physics of Fluids,* vol. 8 (1), pp. 215-224

Piomelli, U , Zang, T.A , Speziale, C.G. and Hussaini, M.Y. (1990), "On the large-eddy simulation of transitional wall-bounded flows", *Physics of Fluids A Fluid Dynamics,* vol. 2 (2), pp. 257-265.

Pitsch, H. and Duchamp de Lageneste, L. (2002), "Large-eddy simulation of premixed turbulent combustion using a level-set approach", *Proceedings of the Combustion Institute,* vol 29 (2), pp 2001-2008.

Pitsch, H. (2006), "Large-eddy simulation of turbulent combustion", *Annual Review of Fluid Mechanics,* vol 38, pp. 453-482.

Poinsot, T , Veynante, D. and Candel, S (1991), "Quenching processes and premixed turbulent combustion diagrams", *Journal of Fluid Mechanics,* vol 228, pp 561-606.

Poinsot, T and Veynante, D. (2001), *Theoretical and numerical combustion,* Edwards Publications, Philadelphia, PA

Poinsot, T , Candel, S. and Trouvé, A (1995), "Applications of direct numerical simulation to premixed turbulent combustion", *Progress in Energy and Combustion Science,* vol 21 (6), pp 531-576.

Polifke, W., Flohr, P and Brandt, M. (2000), "Modeling of inhomogeneously premixed combustion with an extended TFC model", *Proceedings of ASME TURBO EXPO,* vol. 2000-GT-0135.

Pope, S B. (1988), "The evolution of surfaces in turbulence", *International Journal of Engineering Science,* vol. 26 (5), pp. 445-469.

Pope, S B. (1985), "PDF methods for turbulent reactive flows", *Progress in Energy and Combustion Science,* vol 11 (2), pp. 119-192

Pope, S.B. (2004), "Ten questions concerning the large-eddy simulation of turbulent flows", *New Journal of Physics,* vol. 35 (6), pp. 1-24.

Porumbel, I. and Menon, S. (2006), "Large eddy simulation of bluff body stabilized premixed flame", *44th AIAA Aerospace Science Meeting and Exhibit.*

Prasad, R O S. and Gore, J P (1999), "An evaluation of flame surface density models for turbulent premixed jet flames", *Combustion and Flame,* vol. 116 (1-2), pp. 1-14.

Ranga-Dinesh, K K.J (2007), *Large eddy simulation of turbulent swirling flames,* PhD Thesis, Loughborough University, UK.

Ravikanti, S.M. (2008), *Advanced flamelet modelling of turbulent nonpremixed and partially premixed combustion,* PhD Thesis, Loughborough University, UK.

Reveillon, J and Vervisch, L. (1997), "Dynamic sub-grid PDF modelling for non-premixed turbulent combustion" *Direct and Large Eddy Simulation II,* eds. J P Chollet, P.R. Vole and L Kleiser, Kluwer Academic Publishers, Amsterdam, pp 311-320.

Richard, S , Colin, O., Vermorel, O , Benkenida, A., Angelberger, C. and Veynante, D. (2007) "Towards large eddy simulation of combustion in spark ignition engines", *Proceedings of the Combustion Institute,* vol. 31, pp. 3059–3066

Rogallo, R.S and Moin, P (1984), "Numerical simulation of turbulent flows", *Annual Review of Fluid Mechanics,* vol 16 (1), pp. 99-137.

Salvetti, M V and Banerjee, S. (1995), "A priori tests of a new dynamic subgrid-scale model for finite-difference large-eddy simulations", *Physics of Fluids,* vol 7 (11), pp. 2831-2847

Schumann, U. (1989), "Large-eddy simulation of turbulent diffusion with chemical reactions in the convective boundary layer", *Atmospheric Environment (1967),* vol. 23 (8), pp. 1713-1727.

Schumann, U. (1975), "Sub-grid scale model for finite difference simulations of turbulent flows in plane channels and annuli", *Journal of Computational Physics,* vol. 18, pp. 376-404.

Smagorinsky, J. (1963), "General circulation experiments with the primitive equations", *Monthly Weather Review,* vol. 91 (3), pp. 99-164

Spalding, D B. (1971), "Mixing and chemical reaction in steady confined turbulent flames", *Proceedings of the Combustion Institute,* vol. 13 (1), pp. 649-657.

Sreenivasan, K R. and Meneveau, C. (1986), "The fractal facets of turbulence", *Journal of Fluid Mechanics,* vol. 173 (1), pp. 357-386.

Staffelbach, G (2006), *Simulation aux grandes échelles des instabilités de combustion dans les configurations multibrûleurs,* PhD Thesis, INP Toulouse, France.

Starke, R. and Roth, P. (1989), "An experimental investigation of flame behavior during explosions in cylindrical enclosures with obstacles", *Combustion and Flame,* vol 75 (2), pp 111-121.

Tabor, G and Weller, H G. (2004), "Large eddy simulation of premixed turbulent combustion using Ξ flame surface wrinkling model", *Flow, Turbulence and Combustion,* vol 72 (1), pp 1-28.

Thibaut, D. and Candel, S (1998), "Numerical study of unsteady turbulent premixed combustion: application to flashback simulation", *Combustion and Flame,* vol. 113 (1-2), pp. 53-65.

Trouvé, A. and Poinsot, T. (1994), "The evolution equation for the flame surface density in turbulent premixed combustion", *Journal of Fluid Mechanics,* vol. 278 (1), pp. 1-31.

Turns, S.R (1996), *An introduction to combustion,* McGraw Hill.

Vankan, J. (1986), "A second order accurate pressure correction scheme for viscous incompressible flow", *SIAM Journal of Scientific and Statistical Computing,* vol. 7, pp. 870-891

Veynante, D., Piana, J , Duclos, J M and Martel, C (1996), "Experimental analysis of flame surface density models for premixed turbulent combustion", *Proceedings of the Combustion Institute,* vol 26 (1), pp 413-420.

Veynante, D. and Poinsot, T. (1997), "Large eddy simulations of the combustion instabilities in turbulent premixed burners", *Centre for Turbulence Research Annual Research Briefs, Stanford University*, pp. 253-275

Veynante, D and Vervisch, L. (2002), "Turbulent combustion modeling", *Progress in Energy and Combustion Science,* vol. 28 (3), pp 193-266.

Vreman, B , Geurts, B. and Kuerten, H. (1996), "Comparison of numerical schemes in Large-Eddy Simulations of the temporal mixing layer", *International Journal for Numerical Methods in Fluids,* vol 22 (4), pp. 297-311

Wark, K. (1977), *Thermodynamics*, 3rd edn, McGraw-Hill, New York, pp. 834-835.

Weller, H G , Tabor, G., Gosman, A.D. and Fureby, C. (1998), "Application of a flame-wrinkling LES combustion model to a turbulent mixing layer", *Proceedings of the Combustion Institute,* vol. 1, pp 899-907.

Werner, H and Wengle, H. (1991), "Large-eddy simulation of turbulent flow over and around a cube in a plate channel", *8th Symposium on Turbulent Shear Flows*

Williams, F A. (1985a), *Combustion theory the fundamental theory of chemically reacting flow systems,* Benjamin/Cummings Publications, Menlo Park, California, USA

Williams, F A (1985b), *The Mathematics of combustion,* SIAM, Philadelphia.

Yakhot, V. (1988), "Propagation Velocity of Premixed Turbulent Flames", *Combustion Science and Technology,* vol. 60 (1), pp 191-214.

Yakhot, V and Orszag, S.A. (1987), "Renormalization group and local order in strong turbulence", *Nuclear Physics B - Proceedings Supplements,* vol. 2, pp 417-440.

Yakhot, V and Orszag, S.A. (1986), "Renormalisation group analysis of turbulence I. basic theory", *Journal of Scientific Computing,* vol. 1, pp 3-51

Yoshizawa, A. (1986), "Statistical theory for compressible turbulent shear flows, with the application to subgrid modeling", *Physics of Fluids,* vol. 29 (7), pp 2152-2164.

Zang, Y., Street, R L and Koseff, J R. (1993), "A dynamic mixed subgrid-scale model and its application to turbulent recirculating flows", *Physics of Fluids A Fluid Dynamics,* vol. 5 (12), pp. 3186-3196.

Zimont, V L (2000), "Gas premixed combustion at high turbulence - turbulent flame closure combustion model", *Experimental Thermal and Fluid Science,* vol. 21 (1-3), pp 179-186.

Zimont, V L , Polifke, W , Bettelini, M and Weisenstein, W. (1997), "An efficient computational model for premixed turbulent combustion at high Reynolds numbers based on a turbulent flame speed closure", *Journal of Engineering for Gas Turbine and Power, Transactions of ASME,* vol. 120, pp. 526-532.